

UiO : **University of Oslo**

Øystein Håvard Færder

The role of resistivity in plasmoid-mediated reconnection in the solar corona and its observational imprints

Understanding how to model the solar resistivity to reproduce plasmoid instability and study the observational capabilities of future missions

Thesis submitted for the degree of Philosophiae Doctor

Institute of Theoretical Astrophysics
Faculty of Mathematics and Natural Sciences

Rosseland Centre for Solar Physics



2024

“The equations of magnetohydrodynamics, which describe the intimate subtle interaction between magnetic fields and plasma, are as beautiful and captivating as anything in nature”
–Prof. Eric R. Priest

Abstracts

English abstract

Magnetic reconnection is a fundamental mechanism in astrophysics and a promising candidate for solving the coronal heating problem. This process has been shown to produce a variety of different observable phenomena on the Sun, including Ellerman bombs, ultraviolet bursts, coronal bright points, surges, coronal jets, and flares. Achieving a better understanding on the role that reconnection plays in the heating and dynamics of the solar atmosphere requires observational data and numerical reproduction of any aspect related to reconnection, including small-scale features such as plasmoids.

A common challenge in mimicking reconnection on the Sun numerically is how to model the electrical resistivity, since this quantity is small compared to the diffusive effects caused by the discrete nature of numerical codes. To address this challenge, we ran a series of magnetohydrodynamic (MHD) simulations using the Bifrost code with its inbuilt hyper-resistivity model along with other resistivity models, for which we developed new modules especially for our research. Our experiments proved that the hyper-resistivity model of Bifrost is at least as suitable for mimicking reconnection phenomena on the Sun as other widely used resistivity models and has the advantage of being applicable in any part of the solar atmosphere without the need for re-calibration. Furthermore, we found that when simulating plasmoid-mediated reconnection with a moderate resolution, another takeaway with the hyper-resistivity model is the capability of reproducing plasmoid characteristics in closer resemblance to those attained with uniform resistivity at a significantly higher resolution.

Observing small-scale features of reconnection on the Sun, such as plasmoids, can also be demanding, due to the limited resolution provided by currently-active telescopes and spectrographs. Furthermore, plasmoids in the corona are quite dim because of the low densities, hence often difficult to detect due to an underwhelming signal-to-noise ratio. Through forward-modelling of synthetic extreme-ultraviolet (EUV) observables from simulations of plasmoid-mediated reconnection, we found that combined spectra from the upcoming Multi-slit Solar Explorer (MUSE) and Solar-C missions along with high-resolution images from the MUSE context imager and the recently-launched Solar Orbiter will together contribute strongly in providing new insights into plasmoid formation on the Sun. Those insights can be used to constrain our numerical models in terms of further development of state-of-the-art resistivity models, hence lead us one step forward in unravelling the mysteries of our life-giving star.

Norsk sammendrag

Magnetfeltsomkobling er en fundamental mekanisme i astrofysikk og en lovende kandidat til å løse koronaoppvarmingsproblemet. Denne prosessen har også blitt påvist å produsere en rekke ulike fenomener observert på Solen, slik som Ellerman-bomber, ultrafiolette lysglimt, koronalysglimt, kalde og varme utbrudd, og soleksplosjoner. Det å oppnå en bedre forståelse av den rollen som omkoblingsprosessen spiller i oppvarmingen og dynamikken i solatmosfæren krever observasjonell data og numeriske gjenskapninger av ethvert aspekt relatert til omkoblingen, inkludert småskalastrukturer slik som plasmoider.

En vanlig utfordring ved numerisk gjenskapning av magnetfeltsomkobling på Solen er hvordan man modellerer den elektriske resistiviteten, en fysisk størrelse som er svært liten sammenlignet med de diffusive effektene forårsaket av den diskrete oppførselen til numeriske koder. For å ta fatt i denne utfordringen, utførte vi en rekke magnetohydrodynamikk(MHD)-simuleringer ved hjelp av Bifrost-koden, hvor vi brukte den innebygde hyperresistivitetsmodellen i tillegg til andre resistivitetsmodeller, som vi utviklet egne moduler for spesielt tilegnet vår forskning. Våre eksperimenter viste at Bifrosts hyperresistivitetsmodell er minst like godt egnet til å gjenskape omkoblingsfenomener på Solen som andre hyppig brukte resistivitetsmodeller og har fordelen av å kunne anvendes i hvilken som helst del av solatmosfæren uten å måtte recalibreres. I tillegg fant vi at ved simulering av plasmoidemediert omkobling med en moderat oppløsning, så har denne hyperresistivitetsmodellen også den fordelen at den gjenskaper plasmoidekaraktteristikk i bedre overensstemmelse med det som ved uniform resistivitet gjenskapes under særdeles høyere oppløsning.

Observasjon av småskalastrukturer relatert til magnetfeltsomkobling på Solen, slik som plasmoider, kan også være krevende grunnet den begrensede oppløsningen som kommer med dagens teleskoper og spektrografer. I tillegg, så er plasmoider i koronaen svært lyssvake som resultat av den lave tettheten, dermed ikke så lette å oppdage grunnet et alt for lavt signal-til-støy-nivå. Ved å modellere syntetiske ekstremultrafiolette (EUV) observable fra simuleringer med plasmoidemediert omkobling, fant vi at kombinerte spektra fra fremtidige satellitter som Multi-slit Solar Explorer (MUSE) og Solar-C, sammen med høyoppløste bilder fra MUSE sin kontekstbildetaker og den nylig lanserte Solar Orbiter-satellitten, vil bidra sterkt til en økt forståelse av plasmoidedannelse på Solen. Dette kan brukes til å ytterligere forbedre våre numeriske modeller i form av videreutvikling av toppmoderne resistivitetsmodeller, ergo føre oss ett steg fremover i å løse de ulike mysteriene til våres livgivende stjerne.

Preface

This thesis is submitted in partial fulfilment of the requirements for the degree of *Philosophiae Doctor* at the University of Oslo (UiO). The research presented here was conducted at the Rosseland Centre for Solar Physics (RoCS), within the Institute of Theoretical Astrophysics (ITA) at UiO, and under the supervision of Prof. Mats Carlsson, Dr. Daniel Nóbrega-Siverio, and Prof. Viggo Hansteen. This research has been supported by the European Research Council through the Synergy Grant number 810218 (“The Whole Sun”, ERC-2018-SyG) and by the Research Council of Norway through its Centres of Excellence scheme, project number 262622. The simulations were performed on resources provided by Sigma2 - the National Infrastructure for High Performance Computing and Data Storage in Norway. In particular for Paper III, Juan Martínez-Sykora gratefully acknowledges support by NASA grants 80NSSC20K1272, 80NSSC23K0093, 80NSSC21K0737, 80NSSC21K1684, and contract NNG09FA40C (IRIS) and 80GSFC21C0011 (MUSE) and NSF ANSWERS grant 2149781.

Acknowledgements

My four-and-a-half-year time at RoCS has been an exciting voyage full of good experiences, academically and socially. Submitting this thesis is a milestone that would never have been achieved in such a successful manner without all the amazing people who surrounds me in my everyday life. Here are some credits to people who have contributed in shaping this journey, one way or another.

I wish to thank the entire **ITA**, and especially **RoCS**, for welcoming me back to academia after seven years in the industry since finishing my Master degree at the very same institute. I am also thankful for the opportunity to participate in international conferences, including the **Whole Sun** meetings in Paris, and the **American Geophysics Union** meeting in San Francisco last year, along with Rosseland Lectures, RoCS retreats and the yearly Christmas parties.

In particular, I thank my supervisor and co-author, **Prof. Mats Carlsson**, for all guidance and supervision throughout the years, not only for my articles and thesis, but also for fulfilling everything required to achieve the title of Doctor Philosophiae. Thanks for giving me both great advices and high requirements in order to ensure that I deliver the best quality possible. I also appreciate the social time with you, including travelling together in Paris and San Francisco.

I hugely thank co-supervisor and co-author **Dr. Daniel Nóbrega-Siverio**, who have done a brilliant job through supervision on a daily basis. Thank you

for constantly reminding me to read and read, for providing me with everything I need to get through my PhD projects, and for correcting my papers to the finest details. Your supreme standards are appreciated.

Furthermore, I thank **Dr. Juan Martínez-Sykora**, from the MUSE team at the Lockheed Martin Solar and Astrophysics Lab (LMSAL), for significantly contributing to my third article. Thank you for providing me access to the MUSE forward-modelling routines along with all the details needed to know about the upcoming MUSE and Solar-C missions.

I also thank co-supervisor **Prof. Viggo Hansteen** at LMSAL, for additional tips and advice during occasional meetings.

For the RoCS leadership, huge thanks goes to centre coordinator **Benedikte Fagerli Karlsen** and head-of-office **Kristine Knudsen**, for helping me with any kinds of formalities, including planning/refunding work travels and applying for paternity leave, not to mention all the nice conversations during lunch and coffee breaks. I also thank **Sara Nettum** and **Heidi Haugsand**, who did a great job stepping in for Benedikte during maternity leaves. For the ITA leadership, I thank **Brenda Apili Atubo** especially for the help with formalities during the startup phase of my PhD, and **Morsal Saba** for further help with the formalities of the completion phase. Finally, I thank **Prof. Per Barth Lilje** for being a splendid leader figure for the entire institute.

Dr. Mikolaj Szydlarski, thank you for the mentoring in Bifrost and all other code-related aid. My work would not have been half as efficient without your assistance. Also thanks to **Torben Leifsen**, **Kjell Andresen**, and **Unni Fuskeland**, for all help regarding any IT-related challenges.

To my room 216 colleagues, **Dr. Rebecca Robinson**, **Dr. Sneha Pandit**, **Dr. Helle Bakke**, **Dr. Nicolas Poirier**, **Frederik Clemmensen**, **Michaela Brchnelova**, **Elisabeth Enerhaug**, and **Mats Kirkaune**, thank you for the regular break conversations, lunches at Dana Bakeri, and movie nights. I also thank my colleague **Anna Piterskaya** for close collaboration in PhD courses.

My dear wife, **May**, thank you for patiently supporting me all the way along this journey, and for always giving me the best. I would not have been where I am without your love and support. I love you so much. And to my boys, **Johann** and **Jakob**, thank you for making all my efforts even more meaningful.

Thank you, **Mom**, for giving me all your love as a mother and raising me up to work hard for my future, and thank you, **Dad**, for building my enthusiasm in mathematics and natural sciences. Thank you, my **brother** and **sister**, for further shaping me into the person I am today. Finally, I thank all my **friends outside ITA** for all your support along the way.

• Øystein Håvard Færder

Oslo, February 2024

List of papers

Paper I

A comparative study of resistivity models for simulations of magnetic reconnection in the solar atmosphere

Øystein Håvard Færder, Daniel Nóbrega-Siverio, Mats Carlsson

In: *Astronomy & Astrophysics*. Vol. 675, no. A97 (2023)

DOI: 10.1051/0004-6361/202346447

arXiv: 2305.18895

Paper II

A comparative study of resistivity models for simulations of magnetic reconnection in the solar atmosphere. II. Plasmoid formation

Øystein Håvard Færder, Daniel Nóbrega-Siverio, Mats Carlsson

In press for publication in *Astronomy & Astrophysics*

DOI: 10.1051/0004-6361/202348046

arXiv: 2401.01177

Paper III

EUV observables of simulated plasmoid-mediated reconnection in the solar corona

Øystein Håvard Færder, Daniel Nóbrega-Siverio, Mats Carlsson, Juan Martínez-Sykora

Submitted for publication in *Astronomy & Astrophysics*

Contents

Abstracts	iii
Preface	v
List of papers	vii
Contents	ix
List of Figures	xi
1 Introduction	1
1.1 Structure of the Sun	1
2 Magnetic reconnection on the Sun	7
2.1 The magnetohydrodynamics (MHD) equations	8
2.2 Magnetic Reynolds number and Lundquist number	11
2.3 Scaling laws for reconnection with and without plasmoids	11
2.4 Examples of magnetic field configurations where reconnection takes place	14
3 Solar observations	19
3.1 Some relevant instruments for solar imaging and spectrography	19
3.2 Observed solar phenomena related to magnetic reconnection	22
4 Solar simulations	31
4.1 The massively-parallel MHD code Bifrost	31
4.2 Modelling the electrical resistivity	32
4.3 2D and 3D numerical simulations of solar atmospheric phenomena	35
5 Summary and outlook	45
Papers	57
I A comparative study of resistivity models for simulations of magnetic reconnection in the solar atmosphere	59
II A comparative study of resistivity models for simulations of magnetic reconnection in the solar atmosphere. II. Plasmoid formation	75

III EUV observables of simulated plasmoid-mediated reconnection in the solar corona	91
--	-----------

List of Figures

1.1	Sketch of the solar interior, surface, and atmosphere	2
1.2	Image from DKIST showing the solar surface granulation pattern	3
1.3	Stratification of temperature and density in the solar atmosphere	4
2.4	Sketch of the quiet-Sun magnetic field structure	8
2.5	Sketch of Sweet-Parker and Petschek reconnection	12
2.6	Sketch of plasmoid-mediated reconnection	13
2.7	Reconnection in Harris sheet with plasmoid instability	15
2.8	Reconnection in magnetic null-point configurations	16
2.9	Reconnection by magnetic flux emergence	17
3.10	Images from SST and IRIS showing an Ellerman bomb, an ultraviolet burst, and a surge	23
3.11	SST/TRIPPEL-MiHI H α image of an Ellerman bomb with a nearby-appearing plasmoid-like blob	24
3.12	SST/CHROMIS and IRIS images showing a plasmoid-like blob near an ultraviolet burst	26
3.13	Observations of a coronal bright point with SDO/AIA and SST/CRISP	27
3.14	IRIS SJI 1330 Å image series of the evolution of a coronal jet, revealing plasmoid-like blobs	28
3.15	SDO/AIA images and standard-model sketch of a flare	29
4.16	Numerical reproduction of an ultraviolet burst with plasmoid-mediated reconnection on a 2D Harris sheet	36
4.17	Fan-spine magnetic topology in 2D and 3D	37
4.18	Temperature and synthetic observables in a coronal bright point from a 2D simulation of fan-spine reconnection driven by convective motion	38
4.19	Synthetic observables and magnetic field in a coronal bright point from a 3D simulation of fan-spine reconnection driven by convective motion	38
4.20	Flux cancellation simulated in 2D and 3D	40
4.21	Evolution of the magnetic field strength in a 2D simulated flux emergence	41
4.22	Temperature maps of 2D simulated post-flux-emergence dome-structures, showing surges and jets	41
4.23	Physical properties and synthetic observables of a 3D simulated post-flux-emergence current sheet	43

Chapter 1

Introduction

Ever since Grotrian (1939) and Edlén (1943) discovered that the outer layer of the Solar atmosphere, known as the corona, holds a temperature of above 1 MK, which is 200 times warmer than the below-lying surface, it has been one of the major goals in solar physics to unravel the mechanisms behind the heating of the corona. As of today, two major theories are considered as promising candidates for solving the coronal heating problem. The first one is the wave heating theory (Alfvén 1947; Schatzman 1949; Osterbrock 1961; Hollweg 1984; Morton et al. 2012), which proposes that energy is carried from the solar interior to the chromosphere and corona by Alfvén waves and magnetosonic waves. The other one, which our study focuses on, is the theory of heating by *magnetic reconnection* (Vaiana et al. 1973b; Heyvaerts & Priest 1984; Parker 1988), a process where magnetic fields of different topologies are pushed towards each other and reshaped into a simpler topology, hence converting magnetic energy to thermal and kinetic energy. This process, as described more in detail in the following chapters, depends strongly on the resistivity of the surrounding medium. In the papers that build up this thesis, we study different models for the resistivity and compare how they affect the reconnection process differently with a special emphasis on the development of small features known as plasmoids and how future observations of those plasmoids can be used to set constraints on resistivity models.

Understanding the origin and effects of magnetic reconnection in the solar atmosphere requires a holistic picture of the Sun. With this, it is natural to start by briefly taking a look at the structure of the Sun, including 1) the solar interior, from where the solar magnetic field originates, and 2) the solar atmosphere, where the reconnection process leads to different phenomena that can be studied observationally.

1.1 Structure of the Sun

As any other main sequence star in the Universe, the Sun has a *core* with a high enough temperature (15 MK) and pressure (2.65×10^{16} Pa) to constantly fuse hydrogen into helium. The energy released from the fusion process must pass through a *radiative zone* and a *convective zone* before finally exiting the Sun in the form of photons. In the radiative zone, the energy released from the thermonuclear

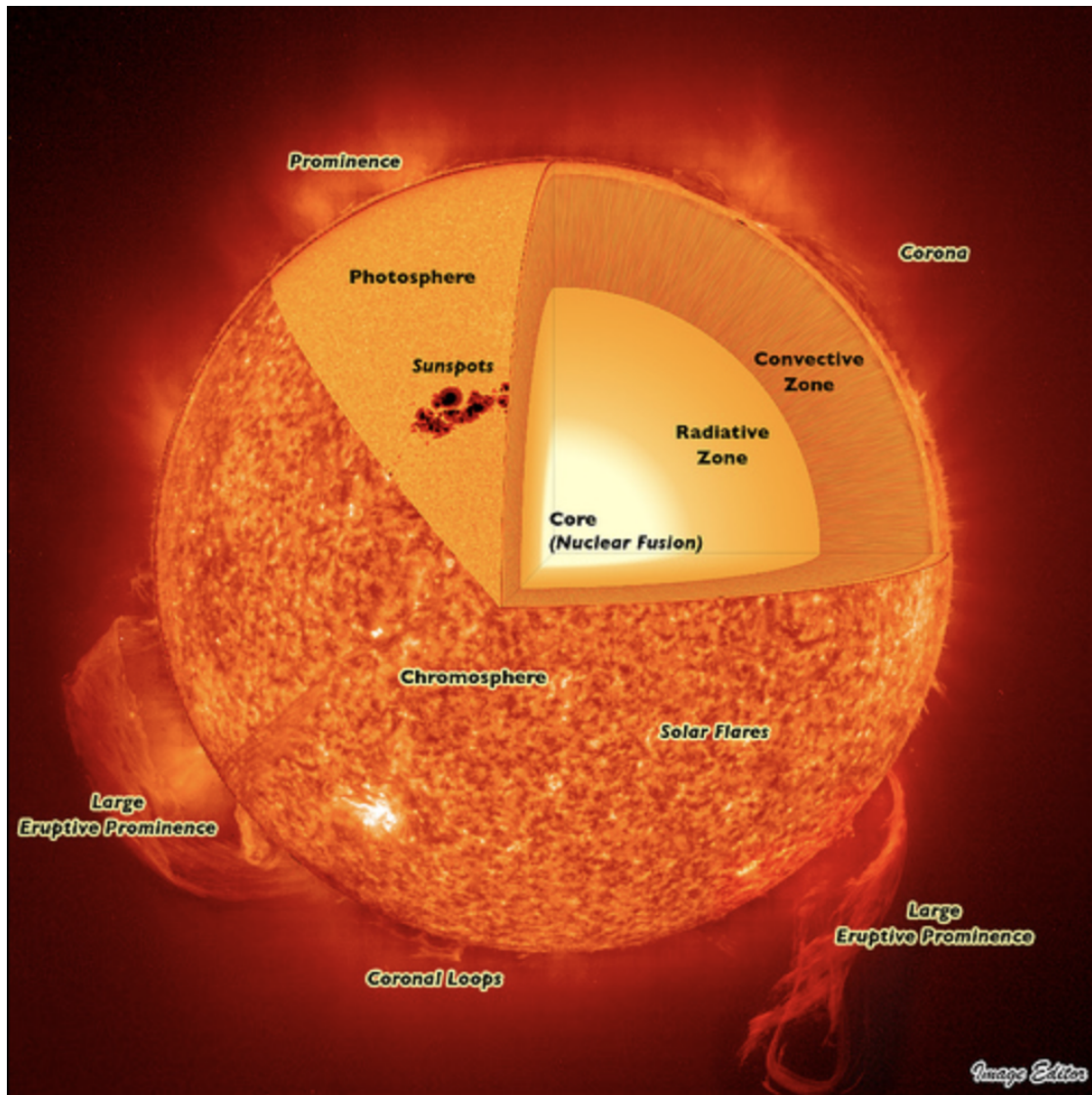


Figure 1.1: Sketch of the solar interior, surface, and atmosphere. Image credit: University of Alberta (https://sites.ualberta.ca/~pogosyan/teaching/ASTRO_122/lect8/lecture8.html).

fusion processes of the solar core travels outwards by electromagnetic radiation. The photons are here absorbed by atoms and re-emitted repeatedly, possibly billions of times, before finally leaving this part of the Sun. The convective zone is characterised by circular fluid motion due to convective instability, where blobs of ionised plasma at the bottom are heated up from below until getting buoyant enough to rise upwards, then to cool down on the top and move horizontally until getting dense enough to fall back to the bottom, and so on. It is separated from the radiative zone by a thin spherical layer known as the *tachocline*, which also separates two different rotational regimes (Spiegel & Zahn 1992; Schou et al. 1998; Brun et al. 2004). Since the Sun is a class G2 yellow dwarf star, the convective zone lies outside the radiative zone, covering the outer 30 % of the solar radius. The fact that the Sun has its convective zone right below the surface has an important consequence for the solar magnetic activity. In fact, the magnetic field in the solar

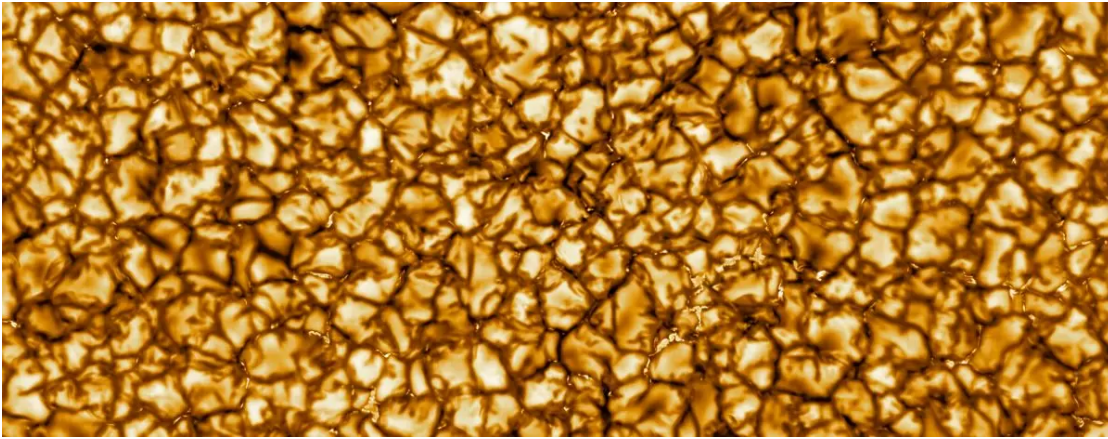


Figure 1.2: Image of the solar surface granulation pattern, taken with the Daniel K. Inouye Solar Telescope (DKIST). Image credit: National Science Foundation (<https://new.nsf.gov/news/nsfs-newest-solar-telescope-produces-first-images>).

atmosphere is partially induced by the circular motion of charged particles in the convective zone. As a matter of fact, a study by Vaiana et al. (1981) suggests that the largest main sequence stars —namely the class O, B, and A stars— which do not have surface convection, are not expected to have acoustically heated coronae. The different parts of the solar interior, along with the atmosphere, are shown in Fig. 1.1.

The innermost layer of the solar atmosphere is known as the *photosphere*. Being defined as the spherical layer around the Sun where the optical depth of light with wavelength 500 nm reaches unity ($\tau_{500\text{nm}} = 1$), it is basically seen as the solar surface when observing the Sun in visible light. The photosphere, as seen from above, is characterised by its granulation pattern, shown in Fig. 1.2, which is, together with the encompassing supergranulation pattern, an imprint of the below-lying convective zone. Here, the bright granules are characterised by upward motion, while the darker intergranular lanes are characterised by downward motion. The photosphere is approximately in local thermal equilibrium (LTE) and consists mainly of neutral atoms. The temperature is 6.6 kK at the bottom of the photosphere and decreases with height until the temperature minimum layer, located about 500 km above the photosphere, where it lies around 4.1 kK. Above this layer lies the *chromosphere*, where non-LTE and partially ionised effects get substantial. The chromosphere is optically thin in the near-ultraviolet to near-infrared spectral range (including most visible light), but optically thick in the millimeter range and in strong spectral lines¹, including the $H\alpha$ line and several UV lines. It is about 2 Mm thick with a temperature slowly increasing with height, reaching up to 20 kK in the upper parts. Further above is the *transition region* (TR) where the temperature increases from 20 kK to 1 MK in a height difference of $\sim 100 - 200$ km only (Abhyankar 1977; Vernazza et al. 1981, and references therein). Above this narrow layer is the *corona* which harbours temperatures of 1 – 20 MK and is nearly totally ionised and optically thin in most of the

¹Source: Oxford Research Encyclopedias, entry written by Dr. Shahin Jafarzadeh, <https://doi.org/10.1093/acrefore/9780190871994.013.22>

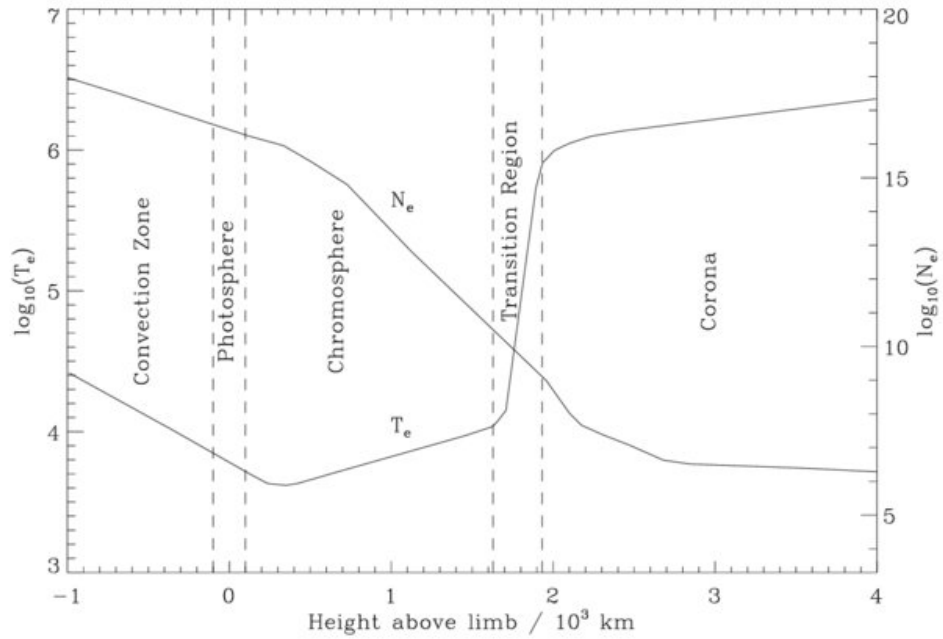


Figure 1.3: Stratification of temperature, $T(\text{K})$, and electron density, $n_e(\text{cm}^{-3})$, in the solar atmosphere. Image credit: obtained from Long (2012), originally from Gabriel & Mason (1982).

electromagnetic spectrum. In addition to the huge temperature increase, the density decreases with height with more than five orders of magnitude from the photosphere to the lower corona. Because of this, the plasma- β , defined as the ratio between gas pressure and magnetic pressure, goes from far above unity in the photosphere to below unity in the corona. Hence, while the (convective) motion of plasma in the photosphere controls the magnetic fields in the photosphere, it is in general the other way around in the corona. Beyond the corona, the atmosphere stretches out into the *solar wind*, a stream of charged particles moving out from the Sun at velocities of $250 - 750 \text{ km s}^{-1}$, causing auroras on Earth when charged particles enter its ionosphere.

A simplified, semi-empirical 1D representation of the average temperature and electron density as function of height in the solar atmosphere (including the top of the convective zone), taken from Gabriel & Mason (1982), is shown in Fig. 1.3. It is important to point out that the atmosphere of the Sun is, however, not plane-parallel. The electron density, for instance, is representatively around 10^9 cm^{-3} in the quiet-Sun lower corona, but can get at least one order of magnitude lower in regions of open magnetic fields, namely *coronal holes*. Consequently, the solar wind in those regions escapes the Sun at higher speeds than elsewhere. As another example, the height and thickness of the transition region depend strongly on the local conditions.

In the next chapter, we will delve into some basic theory of magnetic reconnection, a process that can occur in any part of the solar atmosphere. Because of the huge variations in density, temperature, ionisation degree, magnetic fields, and velocity fields, reconnection generates a variety of different observational

phenomena, depending on the location of the reconnection site. The combination of observations (see Chap. 3) and numerical simulations (see Chap. 4) of these phenomena helps us improve our knowledge on how this process contributes in heating up the solar atmosphere. A basic understanding of reconnection theory, observations, and simulations, therefore forms the basis for the papers of this thesis (see Chap. 5 and the included papers).

Chapter 2

Magnetic reconnection on the Sun

The solar atmosphere harbours remarkably strong magnetic fields. Those fields originate from below the surface, where they are generated by the solar dynamo, a mechanism which basically converts kinetic energy to electromagnetic energy. The input kinetic energy comes from two major sources: 1) the above-mentioned convective motions of the convective zone and 2) the differential rotation of the Sun, that is, the variation in the solar rotational angular velocity, which is larger in the solar equatorial regions than in the polar regions. The differential rotation is strongly correlated to a fossil magnetic field rooted in the tachocline (e.g., see Brun & Zahn 2006; Strugarek et al. 2011). The convective motion is additionally responsible for pushing the magnetic fields, generated by the dynamo, up to the solar surface, where they emerge into the atmosphere.

The solar magnetic fields are especially strong in the active regions of the photosphere, reaching up to 4 kG in sunspots and 1.5 kG in the bright regions known as plage. Reconnection events in these *active regions* can lead to explosive events such as flares and coronal mass ejections (CME) as discussed later (see Sects. 3.2.6 and 4.3.4 for references). In contrast to active regions, the *quiet-Sun regions* are characterised by the absence of any strong magnetic field concentrations, and the magnetic field of the quiet-Sun photosphere is mainly confined to the intergranular lanes of the granulation pattern. Representative values for the magnetic field strength in the quiet-Sun internetwork are of order 10 G (Faurobert & Ricort 2021). Despite such relatively low magnetic field strengths, the magnetic activity of the quiet-Sun regions have a strong impact on the dynamics of the solar atmosphere. Due to the dynamic behaviour of the convective zone, both in the quiet-Sun and active regions, the footpoints of the magnetic fields in the photosphere are continuously shifted around. Consequently, the magnetic fields in the atmosphere are twisted around each other until they break up in reconnection events known as *nanoflares*, which are considered as essential contributors in coronal heating (Parker 1988). Figure 2.4 shows a 2D sketch of the quiet-Sun magnetic field structure, with the magnetic internetwork comprising the granulation pattern and the stronger magnetic network comprising the surrounding supergranulation pattern and the above-lying canopy domain. Though a fully detailed description of the solar magnetic field topology is not part of the scope of this thesis, this figure gives a fine demonstration of its quite complex structure.

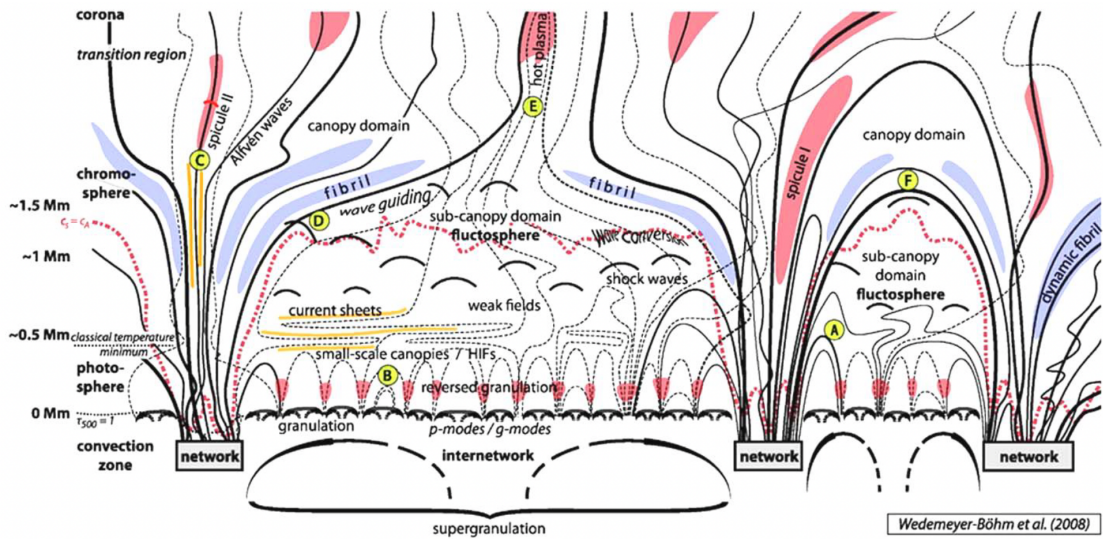


Figure 2.4: Sketch of the quiet-Sun magnetic field structure. Image credit: (Wedemeyer-Böhm et al. 2009)

2.1 The magnetohydrodynamics (MHD) equations

For studying how the magnetic fields affect the temperature and plasma motions in the solar atmosphere through numerical simulations, it is normal to apply a set of differential equations derived from physical laws. One way of modelling solar plasma is by the particle-in-cell (PIC) method, where individual particles in a Lagrangian frame are tracked in phase space, while density and current distributions are computed on an Eulerian mesh. PIC simulations have, for instance, provided detailed insights on the instabilities that occur during turbulent magnetic reconnection in the solar corona (Daughton et al. 2011; Shahraki Pour & Hosseinpour 2022). In our papers, instead, we apply numerical solutions of the equations of *magnetohydrodynamics* (MHD) to simulate magnetic reconnection on the Sun. This approach treats the solar plasma as a continuous single-fluid medium, governed by the equations of fluid dynamics and Maxwell’s equations. Basic assumptions are that any variations in the fluid are slow and large-scale, meaning that the characteristic times are much larger than the ion gyroperiod and mean free path time, and the characteristic lengths are much larger than the Larmor radius and mean free path length. Also, the fluid velocities are assumed to be non-relativistic. Despite leading to a slightly more approximate model of the solar atmosphere, the MHD approach is faster in terms of computational power, and it has successfully been used to mimic several observational phenomena in the solar atmosphere (Yokoyama & Shibata 1994, 1995, 1996, 2001; Masson et al. 2009; Nóbrega-Siverio et al. 2016, 2017, 2023; Hansteen et al. 2017, 2019; Peter et al. 2019; Cheung et al. 2019b; Guo et al. 2020; Ni et al. 2022; Liu et al. 2023; Mondal et al. 2024).

The MHD equations describe the time-evolution of the total mass density ρ , fluid velocity \mathbf{u} , magnetic field \mathbf{B} , and internal energy density e based on their spatial distributions at a given time. Derived from the assumption of mass

conservation, the first MHD equation is the *continuity equation*:

$$\frac{\partial \rho}{\partial t} = -\nabla \cdot (\rho \mathbf{u}). \quad (2.1)$$

The second MHD equation is derived from Newton's second Law, $D(\rho \mathbf{u})/Dt = \sum \mathbf{f}$, where D/Dt denotes the particle derivative and $\sum \mathbf{f}$ the net force per volume element. With the inclusion of viscosity, gas pressure, gravity, and Lorentz force, this equation, namely the *momentum equation*, can be written as

$$\frac{\partial(\rho \mathbf{u})}{\partial t} = -\nabla \cdot (\rho \mathbf{u} \otimes \mathbf{u} - \bar{\bar{\tau}}) - \nabla P + \mathbf{J} \times \mathbf{B} + \rho \mathbf{g}, \quad (2.2)$$

where $\bar{\bar{\tau}}$ is the viscosity tensor, P gas pressure, \mathbf{J} current density, and \mathbf{g} gravitational acceleration. The current density is related to the magnetic field by Ampere's Law, $\mu_0 \mathbf{J} = \nabla \times \mathbf{B}$, where μ_0 is the vacuum permeability.

The third of the MHD equations is found by combining Ohm's law $\mathbf{E} = \bar{\bar{\eta}} \mathbf{J} - \mathbf{u} \times \mathbf{B}$, with Faraday's law of induction, $\partial \mathbf{B} / \partial t = -\nabla \times \mathbf{E}$, where \mathbf{E} is the electric field induced by the variation in the magnetic field and $\bar{\bar{\eta}}$ the resistivity tensor. Written out, this equation is referred to as the *induction equation*, given by

$$\frac{\partial \mathbf{B}}{\partial t} = -\nabla \times (-\mathbf{u} \times \mathbf{B} + \bar{\bar{\eta}} \mathbf{J}). \quad (2.3)$$

One should note that the above-mentioned Ohm's law is a simplification of the *generalised Ohm's law*, which includes, for instance, ambipolar diffusion and Hall effect. Those terms can be especially important in simulations of phenomena rooted in the chromosphere, where the effects of partial ionisation have been shown to considerably affect the heating of the plasma (Nóbrega-Siverio et al. 2020b). In our simulations which focus on the corona, nevertheless, those terms are considered negligible.

Finally, the fourth MHD equation is derived from energy conservation. With the inclusion of Joule heating Q_J , viscous heating Q_V , and a thermal conductivity term Q_C , this *energy equation* can be written as

$$\frac{\partial e}{\partial t} = -\nabla \cdot (e \mathbf{u}) - P \nabla \cdot \mathbf{u} + Q_J + Q_V + Q_C. \quad (2.4)$$

In addition, this equation may include other energy source or sink terms, such as radiative cooling and optically thin losses.

Equations (2.1)-(2.4), as written out above, are referred to as *resistive MHD*, due to the presence of the resistivity (i.e. diffusive terms) in the equations and form the basis of the simulations of all three articles included here. With the absence of resistivity, this set of equations simplifies to *ideal MHD*, characterised by a conserved topology with frozen-in magnetic fields which do not reconnect. In other words, one cannot have magnetic reconnection without magnetic diffusion. The solutions of the linearised ideal MHD equations are three different plasma wave

modes: Alfvén waves, fast magnetosonic waves (or fast-mode MHD waves), and slow magnetosonic waves (or slow-mode MHD waves). For waves with frequency ω and wave vector \mathbf{k} with an angle θ relative to the background magnetic field \mathbf{B}_0 , the dispersion relation for Alfvén waves is

$$\frac{\omega}{k} = v_A \cos \theta, \quad (2.5)$$

where

$$v_A = \frac{B_0}{\sqrt{\mu_0 \rho}} \quad (2.6)$$

is the Alfvén speed. The dispersion relation for magnetosonic waves is

$$\frac{\omega}{k} = \left(\frac{1}{2}(v_A^2 + c_s^2) \pm \frac{1}{2}\sqrt{(v_A^2 + c_s^2)^2 - 4v_A^2 c_s^2 \cos^2 \theta} \right)^{\frac{1}{2}}, \quad (2.7)$$

where

$$c_s = \sqrt{\frac{\gamma P}{\rho}} \quad (2.8)$$

is the sound speed, and $\gamma = 5/3$ the ratio of specific heats. The above-solution using the positive sign corresponds to fast-mode waves, while the solution with the negative sign corresponds to slow-mode waves. Even though ideal MHD is in general not a valid approximation in the solar atmosphere (due to the non-negligible electrical resistivity), Alfvén waves, fast-mode waves and slow-mode waves are widely present in the solar atmosphere and have been shown to have a notable effect on coronal heating.

In addition to the MHD equations, in order to have a closed set of equations, it is also necessary to have an equation-of-state (EoS) which relates the gas pressure P and temperature T to the mass density and energy density. One widely used EoS is the *ideal gas law*, which gives

$$P = \frac{\rho k_B T}{\mu m_H}, \quad (2.9)$$

$$e = \frac{P}{(\gamma - 1)}, \quad (2.10)$$

where k_B is the Boltzmann constant, μ mean molecular weight, and m_H hydrogen mass. This law is valid for rarefied plasmas where particles do not interact except for elastic collisions, and the velocities can be assumed to be Maxwell-Boltzmann distributed. It is a roughly valid approximation in the corona, where the density is so low that the particles rarely interact. In general, the EoS is more complex, especially because it is necessary to take into account the ionisation and recombination of different atomic elements, the formation and dissociation of molecules, and those processes may occur out of equilibrium.

2.2 Magnetic Reynolds number and Lundquist number

Before delving into reconnection theory, we introduce two quantities often used when studying reconnection: magnetic Reynolds number and Lundquist number. The magnetic Reynolds number is defined as

$$R_M = \frac{Lu}{\eta}, \quad (2.11)$$

where L is a characteristic length scale and u a characteristic velocity scale. With L given by the characteristic length of the magnetic field, $L_B = |\mathbf{B}|/|\mathbf{J}|$, and u given by the mean fluid velocity, this number denotes how much the inductive term dominates over the diffusive term of the induction equation. The high- R_M limit is characterised by ideal MHD, with a frozen-in magnetic field, while the low- R_M limit is dominated by magnetic diffusion.

The Lundquist number, defined as

$$S_L = \frac{Lv_A}{\eta}, \quad (2.12)$$

is basically the Reynolds number with the Alfvén speed given as the characteristic velocity. In reconnection studies, the current sheet length is typically used for input value of L when estimating the Lundquist number. This quantity is often used for deriving scaling laws for several quantities related to reconnection, such as reconnection rate and plasmoid number.

2.3 Scaling laws for reconnection with and without plasmoids

Magnetic reconnection can happen along any *current sheet*, that is, any surface separating two different magnetic topologies, given a non-zero electrical resistivity (i.e., a finite Lundquist number). For instance, in 2D, the reconnection process is visualised by oppositely directed magnetic field lines being pushed towards the current sheet from each side, where they break up and rearrange in a way that causes magnetic energy to be converted into thermal and kinetic energy.

2.3.1 Steady reconnection

Several theoretical reconnection models have been evolved with analytical estimates of reconnection rates and energy conversion rates. One widely used slow-reconnection model is the Sweet (1958a,b)-Parker (1957) model, sketched in the top panel of Fig. 2.5, which assumes a layer of uniform resistivity covering the entire current sheet.¹ The *reconnection rate*, defined as the ratio between inflow

¹In the article to which that figure is credited, the authors chose to define L as the current-sheet half-length. In this thesis, we use L for the full current-sheet length and a for the full current-sheet width.

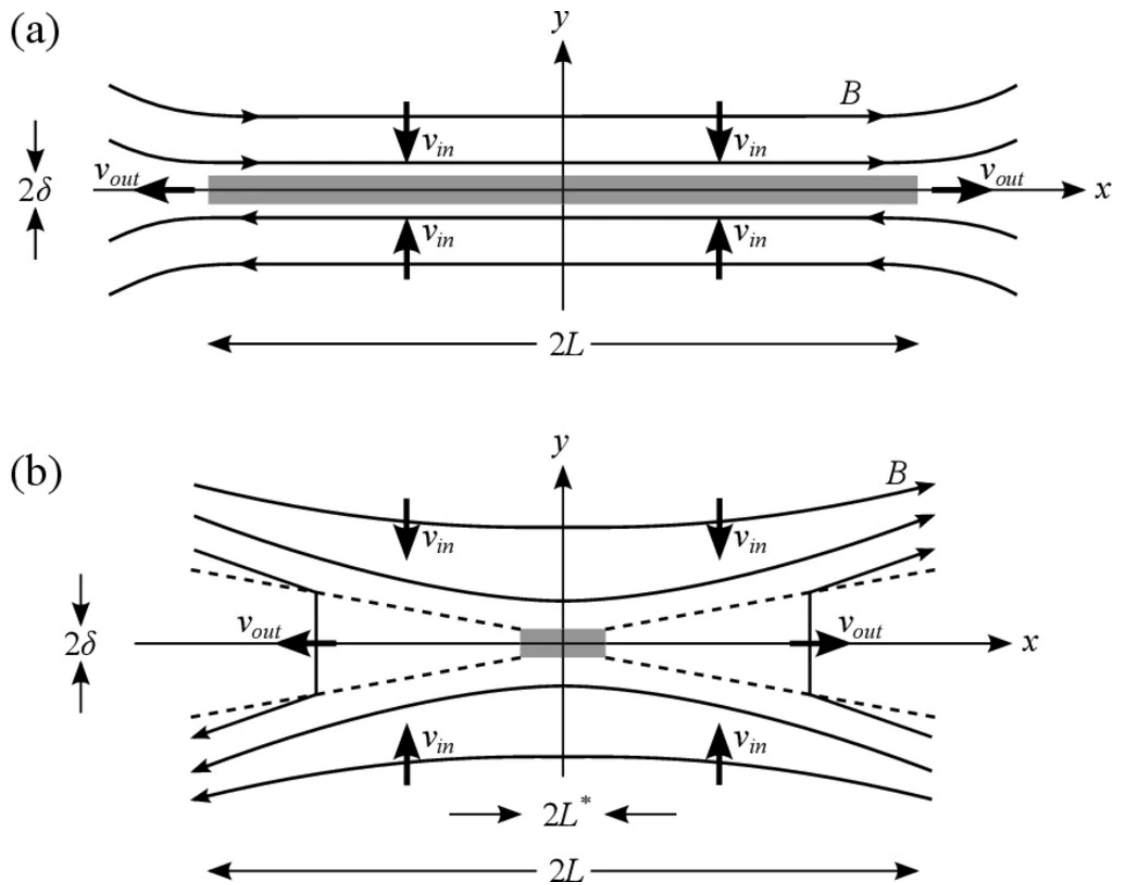


Figure 2.5: Sketch of Sweet-Parker (a) and Petschek (b) reconnection. In both cases, the grey box marks the diffusion layer. The sketches include magnetic field \mathbf{B} , inflow velocity v_{in} , outflow velocity v_{in} , current-sheet length $2L$, current-sheet width 2δ , diffusion region length $2L^*$. Image credit: Comisso & Asenjo (2014).

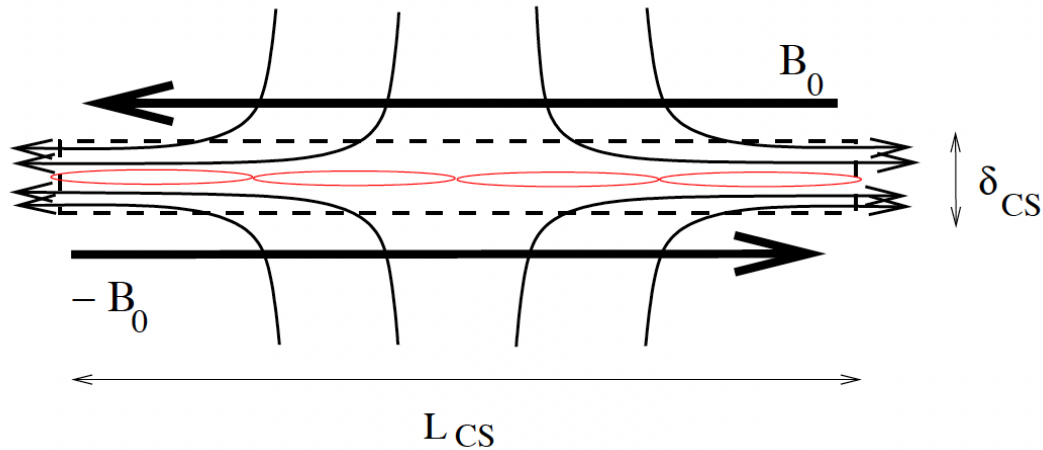


Figure 2.6: Sketch of plasmoid-mediated reconnection. Image credit: Loureiro et al. (2007).

speed and inflow Alfvén speed (i.e., the *inflow Alfvén Mach number*) $M_{Ai} \equiv v_i/v_{Ai}$, is in the Sweet-Parker model related to the Lundquist number by the following relation:

$$M_{SP} = S_L^{-1/2}. \quad (2.13)$$

In the corona, where the Lundquist numbers are normally above 10^6 , the reconnection rate predicted with this model is below 10^{-3} , which makes this reconnection model too slow for mimicking flares. Concerning the energy conversion predicted in this model, exactly one-half of the input magnetic energy is converted to thermal energy, and the remaining half to kinetic energy.

A fast-reconnection model developed by Petschek (1964), sketched in the bottom panel of Fig. 2.5, proposes a uniform diffusion layer which covers only a smaller segment of the current sheet. The outflows in this model are characterised by slow-mode MHD shocks. The reconnection rate of the Petschek model is related to the Lundquist number by

$$M_{Pet} = \frac{\pi}{8 \ln S_L}, \quad (2.14)$$

which for coronal Lundquist numbers agrees roughly with reconnection rates frequently measured in flares. In this model, two-fifths of the input magnetic energy is converted to thermal energy and the remaining three-fifths to kinetic energy.

2.3.2 Bursty reconnection mediated by plasmoids

The Sweet-Parker and Petschek reconnection models are based on a common assumption: that the current sheet remains stable throughout the reconnection process, hence ensuring *steady reconnection*. In the general case, current sheets do not remain steady. Instead, they undergo *resistive tearing instabilities* (Furth et al. 1963), leading to the appearances of small features known as *plasmoids*.

In 2D, plasmoids are seen as magnetic islands, that is, small segments of closed magnetic field appearing along the current sheet, as demonstrated in Fig. 2.6. In 3D, they appear as solenoids or helical structures (Archontis et al. 2006). Inside plasmoids, the density and temperature tends to rise, hence these small features can contribute significantly in transporting heat along the current sheet. Plasmoid instability has been shown to occur for Lundquist numbers above 10^4 (Loureiro et al. 2007), and a current sheet gets intrinsically unstable when its inverse aspect ratio a/L , where a is the current-sheet width, goes below $S_L^{-1/3}$ (Pucci & Velli 2014). For regular coronal Lundquist numbers ($>10^6$), this threshold lies at least one order of magnitude above the value of the inverse aspect ratio predicted with the Sweet-Parker model, which is $S_L^{-1/2}$, meaning that any coronal current sheet will become intrinsically unstable before reaching a Sweet-Parker-like aspect ratio. Hence, the Sweet-Parker model is not a representative model for reconnection in the corona.

A good effort has been spent on understanding the characteristics of bursty, plasmoid-mediated reconnection, including how the reconnection rate and plasmoid number depends on Lundquist number. In contrast to the above scaling laws found between reconnection rate and Lundquist number for Sweet-Parker and Petschek reconnection, the reconnection rate has been found to be nearly independent of Lundquist number under plasmoid instability (Bhattacharjee et al. 2009). In an adiabatic medium, plasmoid reconnection may occur in a linear phase and a non-linear phase, where the plasmoid number scales with the Lundquist number as $S_L^{3/8}$ in the linear phase while being linearly proportional to S_L in the non-linear phase (Loureiro et al. 2007; Huang & Bhattacharjee 2010). For the non-adiabatic cases where external heating terms are included, no scaling law for the plasmoid number has been derived analytically. In the numerical simulations of Sen & Keppens (2022), nevertheless, the maximum number of plasmoids appearing on a (non-adiabatic) current sheet was estimated to scale with the Lundquist number as $S_L^{0.223}$, which is a weaker scaling than predicted for the adiabatic case (even the linear phase). Understanding the characteristics of plasmoid instability is an important part of improving our knowledge on the dynamics of the solar atmosphere, as this bursty behaviour of the current sheet has been shown to play an essential role in several observable phenomena on the Sun, which we will look more into in the next chapter. Deriving scaling laws akin to those mentioned above is a central part of the second article of this thesis.

2.4 Examples of magnetic field configurations where reconnection takes place

In order to study reconnection, a good starting point is to have an idea about which types of magnetic field configurations where reconnection may happen. The basic idea is that this process happens at any interface between different magnetic field topologies, given a non-zero diffusivity. One of the simplest reconnecting magnetic field topologies is the *Harris current sheet*. This plane-parallel configuration consists of two oppositely directed magnetic fields with a hyperbolic tangential

2.4. Examples of magnetic field configurations where reconnection takes place

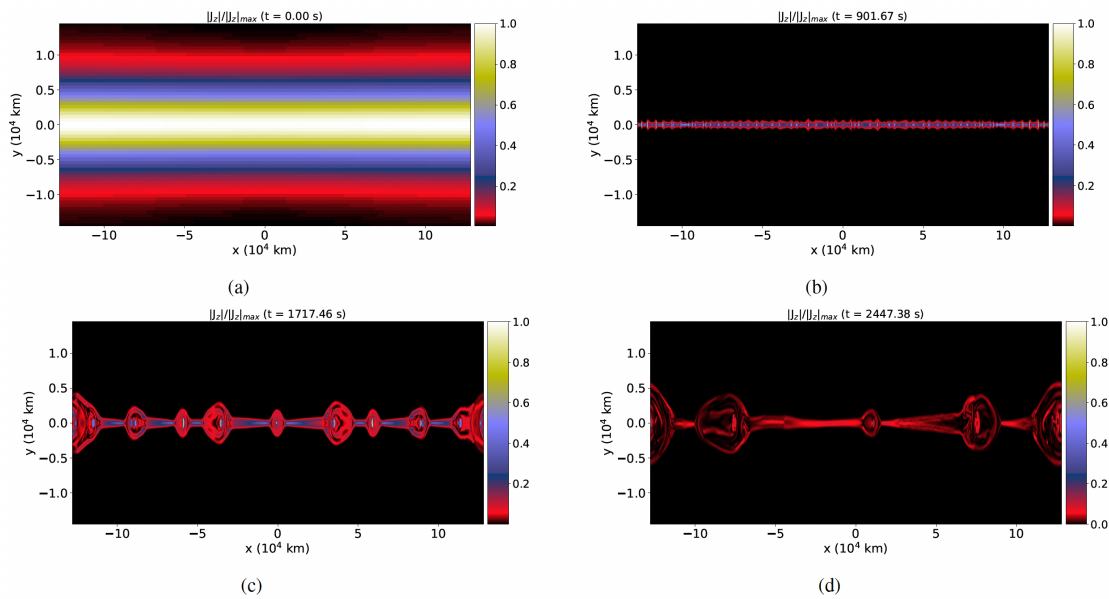


Figure 2.7: Reconnection in a Harris sheet with plasmoid instability. Panels show maps of the current density J_z from different times in the simulations of Sen & Keppens (2022, to whom the figure is credited).

transition and may be written as

$$\mathbf{B} = B_0 \tanh \frac{z}{a} \hat{\mathbf{x}}, \quad (2.15)$$

where B_0 is the field amplitude and a the current-sheet width. Reconnection may be accelerated by adding a driving velocity on each side of the current sheet. Even without such a velocity driver, the magnetic field will eventually undergo spontaneous reconnection. Plasmoid instability can be triggered by adding tiny perturbations in the Harris sheet, akin to the simulations of Sen & Keppens (2022), as shown in Fig. 2.7. Harris sheets are easy to simulate—both in 1D, 2D, and 3D—and can provide a lot of information regarding reconnection characteristics in any chosen part of the solar atmosphere, provided appropriate initial conditions based on the local plasma conditions.

Current sheets often evolve from magnetic null-points. One example of null-point configuration is a *fan-spine magnetic topology*, where the magnetic field can be written as $\mathbf{B} = \nabla \times \psi \hat{\mathbf{y}}$, with the potential field ψ given by

$$\psi(x, z) = \left[f_b \frac{L}{\pi} \sin \left(\frac{\pi x}{L} \right) \exp \left(\frac{-\pi z}{L} \right) - x \right] \bar{B}, \quad (2.16)$$

where f_b , L , and \bar{B} are free parameters (Peter et al. 2019). A fan-spine magnetic topology may occur anywhere in the solar atmosphere where a parasitic polarity moves inside a background magnetic field of opposite polarity, for instance along the moat flow between a sunspot and a pore (Chitta et al. 2017). As the fan-spine topology is stretched due to the motion of this parasitic polarity, the null-point may collapse into a current sheet where reconnection may occur, as demonstrated in the left column of Fig. 2.8. Fan-spine topologies are both associated with ultraviolet

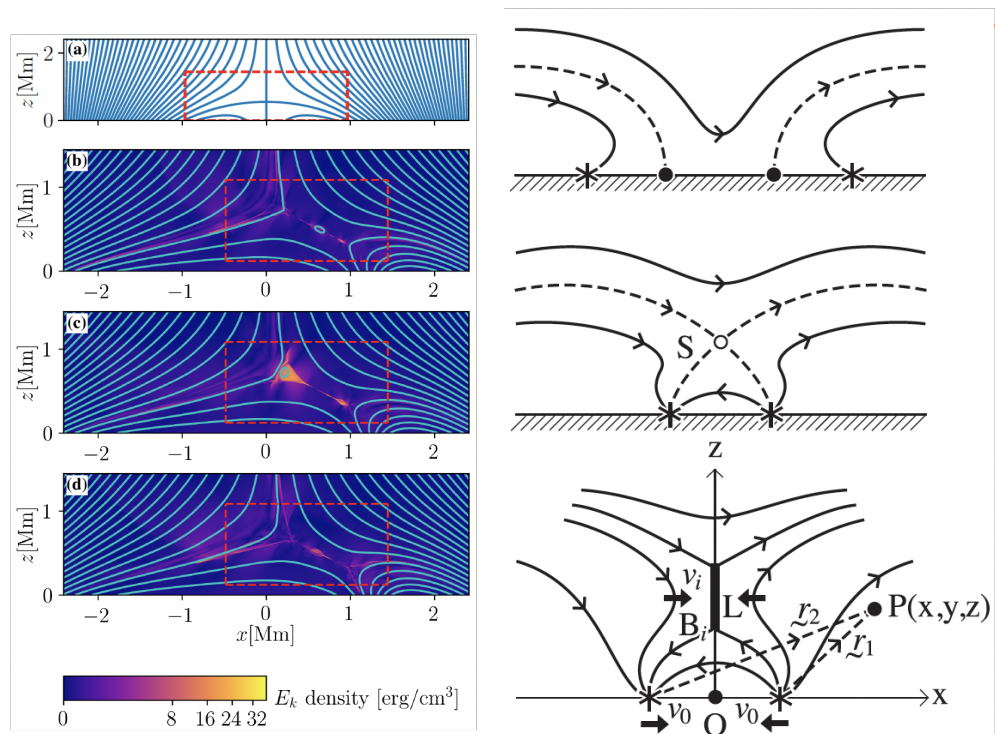


Figure 2.8: Reconnection in magnetic null-point configurations. Left: Magnetic fan-spine topology (a) where the inner spine is moved, causing the null-point to collapse into a tilted current sheet (b-d) where plasmoid-mediated reconnection occurs (image credit: Peter et al. 2019). Right: Magnetic flux cancellation, caused by two magnetic sources of opposite polarity (top) approaching each other until a null-point is formed (middle), which furthermore collapses into a vertical current sheet (c), leading to reconnection (image credit: Priest et al. 2018).

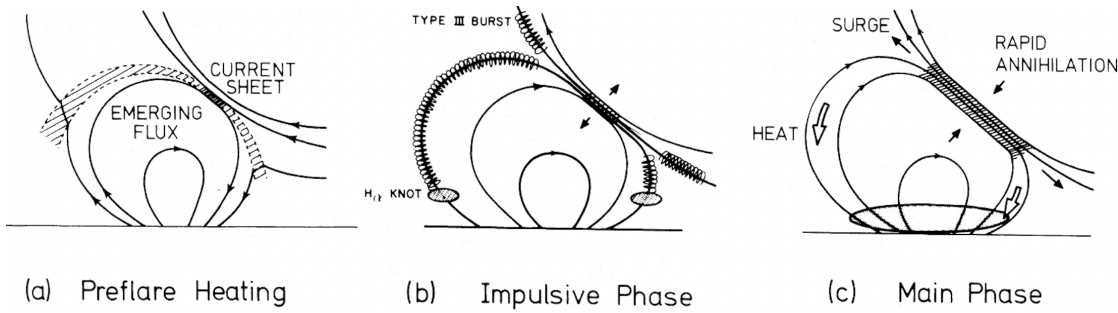


Figure 2.9: Reconnection by magnetic flux emergence. Image credit: Heyvaerts et al. (1977)

(UV) bursts and coronal bright points (CBPs) as discussed further in Sects. 3.2 and 4.3.

Another null-point configuration is one caused by *magnetic flux cancellation* (Priest et al. 2018) due to two sources of opposite magnetic topology moving towards each other, which can (in two dimensions) be written as

$$\mathbf{B}(x, z) = \frac{F_1}{\pi r_1^2} \mathbf{r}_1 - \frac{F_2}{\pi r_2^2} \mathbf{r}_2 - \mathbf{B}_0, \quad (2.17)$$

where F_1 and F_2 is flux of each source, \mathbf{r}_1 and \mathbf{r}_2 the distance from any given point (x, z) to each of the sources, and \mathbf{B}_0 the background field. As the sources move towards each other, the null-point collapses into a current sheet where reconnection takes place. A simplified flux-cancellation scheme is sketched out in the right column of Fig. 2.8. If the sources are located in the photosphere and the null-point in the corona, the reconnection caused by the flux cancellation may provide a considerable amount of coronal heating, with hot structures resembling coronal loops and cool structures resembling surges (discussed in Sects. 3.2 and 4.3) or spicules (Syntelis et al. 2019).

Since magnetic reconnection events in the solar atmosphere are often due to magnetic fields emerging from the surface as a result of the convective motion, it is very common to simulate reconnection on the Sun through the process of *magnetic flux emergence* (Heyvaerts et al. 1977), as demonstrated in Fig. 2.9. In this process, current sheets are formed on the borderline between an emerging magnetic field and a background field, allowing reconnection to occur. Reconnection through flux emergence can lead to several different observable phenomena, including Ellerman bombs, ultraviolet bursts, and surges, as discussed further in Sects. 3.2 and 4.3.

In addition to fan-spine reconnection, flux cancellation, and flux emergence, there are numerous ways that reconnection may self-consistently occur in the solar atmosphere. As an example, nanoflare events can easily be triggered by coronal flux ropes that are gradually built up from coalescence of several current-carrying flux-tubes, occurring as a result of numerous component reconnection events driven by the flows of the underlying convective zone (Robinson et al. 2023).

Chapter 3

Solar observations

Solar observations provide important information about dynamics, thermodynamic properties as well as radiative processes. All this information is relevant not only to understand the Sun, but also to constrain numerical models. Correspondingly, simulations can also predict how any solar features will look like in observations (e.g., see predicted IRIS, Hinode, AIA, and future MUSE observations of a C-class flare by Bose et al. 2023). Since plasmoid instability has been numerically shown to affect the characteristics of the reconnection process in a non-negligible manner (e.g., Bhattacharjee et al. 2009), it is highly interesting to get an idea on how plasmoids in the solar atmosphere can be analysed observationally to provide groundbreaking new insights in solar physics. In the third article of this thesis, we used forward-modelling to produce synthetic observables from simulations of plasmoid-mediated reconnection to examine how coronal plasmoids may be seen through different currently-active and upcoming instruments. For this, a certain amount of background knowledge in solar observations is crucial. In the following section, we therefore give a brief overview of some instruments that provide imaging and spectrography in *extreme-ultraviolet* (EUV) wavelengths, in which the corona is best viewed, especially those with sufficient resolution for detecting plasmoids. Since similar plasmoids can also be seen in the photosphere, chromosphere, and TR through high-resolution observations in *visible* and *ultraviolet* (UV) wavelengths (e.g., Rouppe van der Voort et al. 2017, 2023), we also give some details of a few instruments capable of observing plasmoids in those inner layers of the solar atmosphere. In the last section of this chapter, we give an overview of different observable phenomena where plasmoids have been detected.

3.1 Some relevant instruments for solar imaging and spectrography

The corona is mostly observed through EUV or X-ray filters, using space missions, since photons in this part of the spectrum are completely absorbed in Earth's atmosphere and cannot be received by ground-based instruments. One widely-used space instrument for imaging of the solar corona is the *Atmospheric Imaging Assembly* (AIA, Lemen et al. 2012; Boerner et al. 2012) onboard the *Solar Dynamics Observatory* (SDO, Pesnell et al. 2012), which was launched in 2010.

With its four telescopes, AIA performs narrow-band imaging in seven EUV filters focused on lines with wavelengths from 94 to 335 Å, in addition to the C IV 1600 Å and nearby 1700 Å continuum observed by one of the telescopes, covering temperatures of 0.06 – 20 MK. It provides 24-hours-a-day, full-disk imaging of the solar corona with a satisfactorily high cadence (12 s). Its spatial resolution is 1.5'' (with a spatial pixel size of 0.6'') which may not be optimal for observing plasmoids, except for those larger than ~ 1 Mm, but still higher than that of any other Earth-orbiting instrument which currently provides imaging of the corona, including the *X-Ray Telescope* (XRT, with a spatial resolution of 2'', Golub et al. 2007) onboard the *Hinode* satellite (the Solar-B mission, Kosugi et al. 2007). Apart from AIA, the SDO mission contains two other instruments: the EUV Variability Experiment (EVE, Woods et al. 2012), designed to study the Sun's EUV irradiance with improved spectral resolution, and the Helioseismic and Magnetic Imager (HMI, Scherrer et al. 2012; Schou et al. 2012), which produces Doppler images and magnetograms for the entire solar disk.

The recent launch of the *Solar Orbiter* (García Marirrodriga et al. 2021) satellite, with its elliptic orbit reaching within the orbit of Mercury, has paved the way for higher-resolution imaging of the solar corona. Its *Extreme Ultraviolet Imager* (EUI, Rochus et al. 2020) consists of three telescopes: one Full Sun Imager (FSI) and two High Resolution Imagers (HRIs). One of the HRIs (HRI_{EUV}) takes images in a filter comprising the Fe x 174 Å line with a spatial pixel size of 0.5'' and a cadence of 1 s. At its perihelion distance of 0.3 AU from the Sun, this allows for resolving objects on the solar disk as small as ~ 0.11 Mm, making it the most promising opportunity for direct imaging of coronal small-scale plasmoids as of today, at least for temperatures around 1 MK.

Though high-resolution imaging of the Sun is an important tool for detecting bright features which may be driven by reconnection or other processes, the total intensity maps as received through imaging give only limited information regarding the local density and temperature distributions. More detailed diagnostics in temperature, electron density, and velocity along the line-of-sight (LOS) can be gained through spectrography of a chosen emission line. This technique provides full spectral information of the given emission line, from which one may map the total intensity, Doppler shift, and line width as a function of spatial coordinate. Among currently-active EUV spectrographs, the *EUV Imaging Spectrometer* (EIS, Culhane et al. 2007) onboard *Hinode* and the *Spectral Imaging of the Coronal Environment* (SPICE, SPICE Consortium et al. 2020) onboard *Solar Orbiter* perform spectrography in a wide range of EUV lines with temperature ranges of 1 – 20 MK and 0.01 – 10 MK, respectively. With this, they are together able to do diagnostics in temperature, density, and LOS velocity over the whole corona and TR. With their quite moderate resolutions of 2'' and 1.2'', respectively, they are, similarly to SDO/AIA and *Hinode*/XRT, still not optimal for studying small-scale plasmoids.

The future holds promising opportunities for coronal plasmoid spectrography. Slated to launch in 2027, the *Multi-slit Solar Explorer* (MUSE, Cheung et al. 2019a, 2022; De Pontieu et al. 2020, 2022) mission includes a 35-slit spectrograph set to perform spectrography in the Fe ix 171 Å, Fe xv 284 Å, Fe xix 108 Å, and Fe xxii

108 Å lines —hence covering temperatures from 0.8 to 12 MK— at unprecedented cadences. With a spatial pixel size of $0.167'' \times 0.4''$ and a spectral pixel size of 14.6 mÅ, this spectrograph (SG) can produce two-dimensional full-raster images with full spectral information (of the given spectral lines) and with a resolution high enough to study relatively small plasmoids. To supplement these spectrographical studies, MUSE will also be equipped with a context imager (CI) that provides imaging of the corona in two different filters comprising the Fe XII 195 Å and He II 304 Å lines with a spatial resolution of $0.33''$.

The upcoming *Solar-C* mission will provide additional opportunities in coronal spectrography with its *EUV High-Throughput Spectroscopic Telescope* (EUVST, Suematsu et al. 2021). Being a single-slit spectrograph, in contrast to MUSE, this instrument is designed to obtain spectra from a wider range of EUV wavelengths, hence covering a wider range of temperatures with a slightly higher spatial ($0.16''$ along the slit axis) and spectral pixel size. *Solar-C* and MUSE do therefore complement each other and can together be used for providing ground-breaking, new insights into the small-scale structures of the corona, including plasmoids.

The heating of the solar corona depends strongly on the dynamics of the below-lying photosphere and chromosphere. Because of this, observing these inner regions of the solar atmosphere is also an important part of unravelling the mechanisms that heats up the corona. The photosphere can be observed from both space missions and ground-based telescopes. Among the space-based ones, the *Solar Optical Telescope* (SOT, Tsuneta et al. 2008) onboard Hinode observes the photosphere in visible light with a satisfactorily high spatial resolution of $0.2''$, though, as of today (with only the spectrograph left working), taking images in its full field-of-view (FOV) of $400'' \times 400''$ can only be done with a quite low temporal resolution.

For imaging and spectrography of the photosphere and chromosphere with the highest possible resolution, ground-based telescopes are preferable, and the *Swedish 1-m Solar Telescope* (SST, Scharmer et al. 2003a,b) provides both. Located on La Palma in the Canary Islands and operational since May 2002 with a lens diameter of 39 inches (~ 109 cm), it is the largest refracting telescope in the world. With a spatial resolution near to the diffraction limit of $0.1''$, this telescope offers unique opportunities to resolve the finest structures in the lower parts of the solar atmosphere, including plasmoids. To correct for any aberrations caused by the distortion of light passing through the atmosphere, multi-object multiframe blind deconvolution (MOMFBD, Van Noort et al. 2005) is applied for restoring images taken with SST. For imaging, SST uses two different Fabry-Pérot based filters: 1) CHROMospheric Imaging Spectrometer (CHROMIS, Scharmer 2017) in the blue parts of the spectrum (380 – 500 nm; and 2) CRisp Imaging SpectroPolarimeter (CRISP, Scharmer et al. 2008) in the red (510 – 860 nm). For spectrography, the TRI-Port Polarimetric Echelle-Littrow (TRIPPEL, Kiselman et al. 2011) spectrograph is used, which exploits the full spatial resolution of SST and covers a wavelength range of 380 – 1100 nm. Apart from SST, more detailed imaging of plasmoids (at least in the sub-coronal regions) should be possible with the newly-built *Daniel K. Inouye Solar Telescope* (DKIST Rimmele et al. 2020), and the upcoming *European Solar Telescope* (EST, Quintero Noda et al. 2022),

both being reflecting telescopes in the 4-meter class with spatial resolutions of $\sim 0.03''$.

The decade-ago launch of the *Interface Region Imaging Spectrograph* (IRIS, De Pontieu et al. 2014) has opened up for high-resolution imaging and spectrography also for the solar chromosphere and TR. The spectrograph has two far-ultraviolet (FUV) channels covering wavelength ranges of 1333–1358 Å and 1389–1407 Å and one near-ultraviolet (NUV) channel covering 2783–2834 Å, including the TR lines of C II 1334/1335 Å and Si IV 1394/1403 Å along with the chromospheric lines of Mg II 2796/2803 Å. The slit-jaw imager (SJI) has four different passbands: C II 1330 Å, Si IV 1400 Å, Mg II 2796 Å, and Mg II wing 2830 Å. With a spatial resolution of 0.33'' for FUV and 0.4'' for NUV, IRIS is highly suitable of providing temperature, density, and LOS velocity diagnostics of chromospheric and TR plasmoids and other small structures.

3.2 Observed solar phenomena related to magnetic reconnection

The process of magnetic reconnection on the Sun produces a wide range of different observable phenomena on the solar disk. It is therefore a common practice to study such observational phenomena and mimic them numerically in order to gain knowledge on the role that the reconnection process plays in the heating and dynamics of the solar atmosphere. In this section, we give a brief overview over phenomena on the solar disk that has been shown to be related to magnetic reconnection, some of these in which plasmoids have been observed, or are expected to be seen with future instruments. Some examples of numerical reproductions of these phenomena triggered by (plasmoid-mediated) reconnection are given in Sect. 4.3.

3.2.1 Ellerman bombs (EBs)

Originally observed in 1915 and documented two years later by Ellerman (1917), EBs have been under scrutiny by solar physicists for more than a century. By definition, EBs are seen as brightenings of the H α line wings where the H α line core remains unperturbed, with typical lifetimes of 10 – 20 min and sizes of 0.5 – 1.0'' (e.g., Kurokawa et al. 1982; Dara et al. 1997). As an example, top-left panel of Fig. 3.10 contains an SST/CRISP image of the H α line wing, where a brightening is marked by a red circle. The same area is not brightened in the H α line core, as seen in top-right panel, confirming that this brightening is an EB. It also coincides with regions of opposite magnetic polarity as shown in the SST/CRISP Ca II 8542 Å Stokes V wings image (bottom-right), indicating the occurrence of magnetic reconnection. In recent ultra-high-resolution images from SST/TRIPPEL, using a Microlensed Hyperspectral Imager (MiHI), plasmoid-like blobs have been observed near EBs (Roupe van der Voort et al. 2023), as seen in Fig. 3.11.

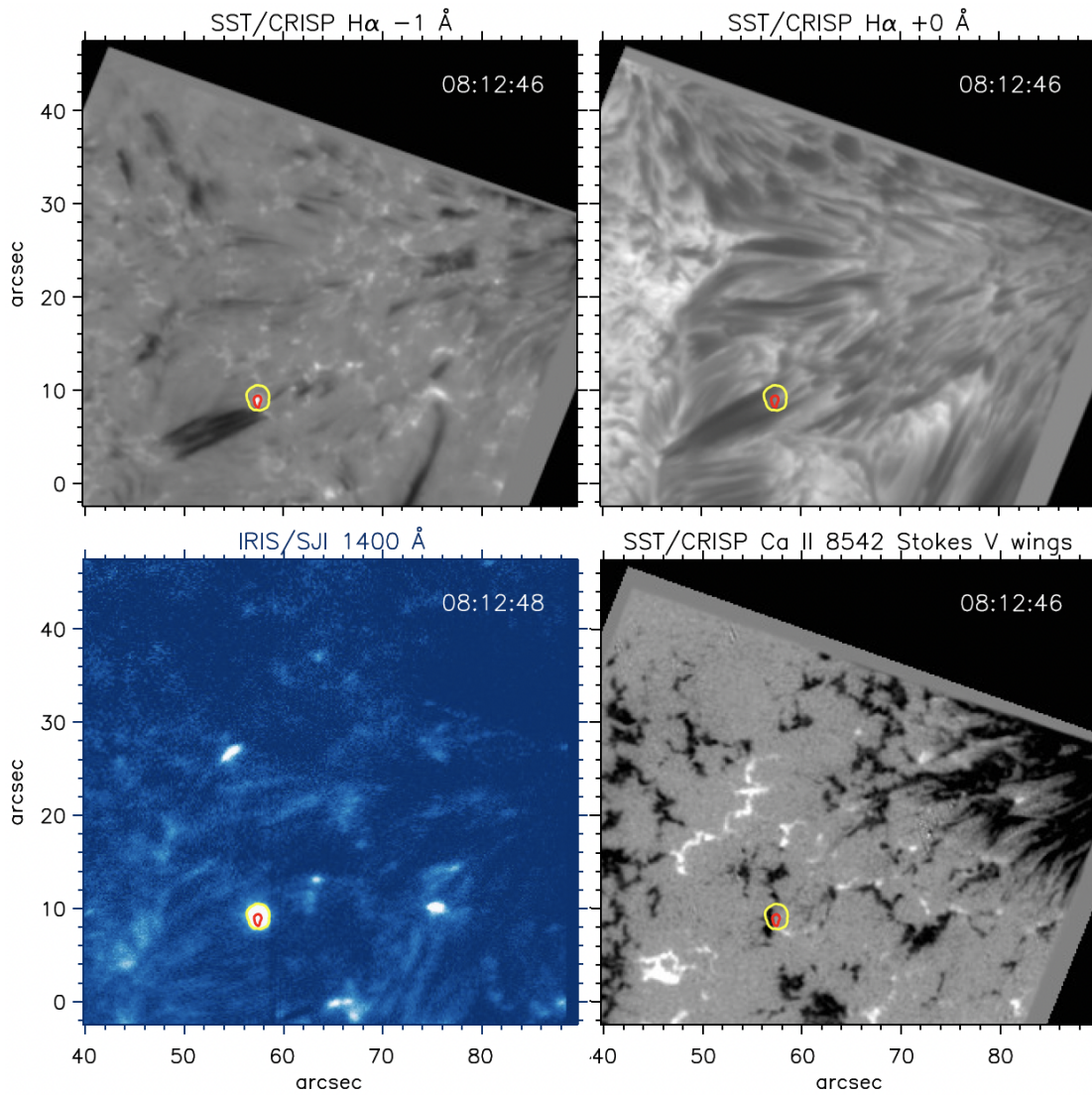


Figure 3.10: Images from SST and IRIS taken September 6, 2016, showing an Ellerman bomb (EB), an ultraviolet (UV) burst, and a surge. The EB, delimited by a red circle, is seen as a brightening in the SST/CRISP $H\alpha$ line wing (top-left), whereas not in the line core (top-right). It coexists with a UV burst, delimited by the yellow circle, seen in IRIS/SJI 1400 \AA (bottom-left). Both features coincide with the borderline between regions of opposite polarity, as seen in the SST/CRISP $\text{Ca II } 8542 \text{ \AA}$ Stokes V wings (bottom-right). The surge is also seen next to the EB in the SST/CRISP $H\alpha$ line wing (top-left). Image credit: Ortiz et al. (2020).

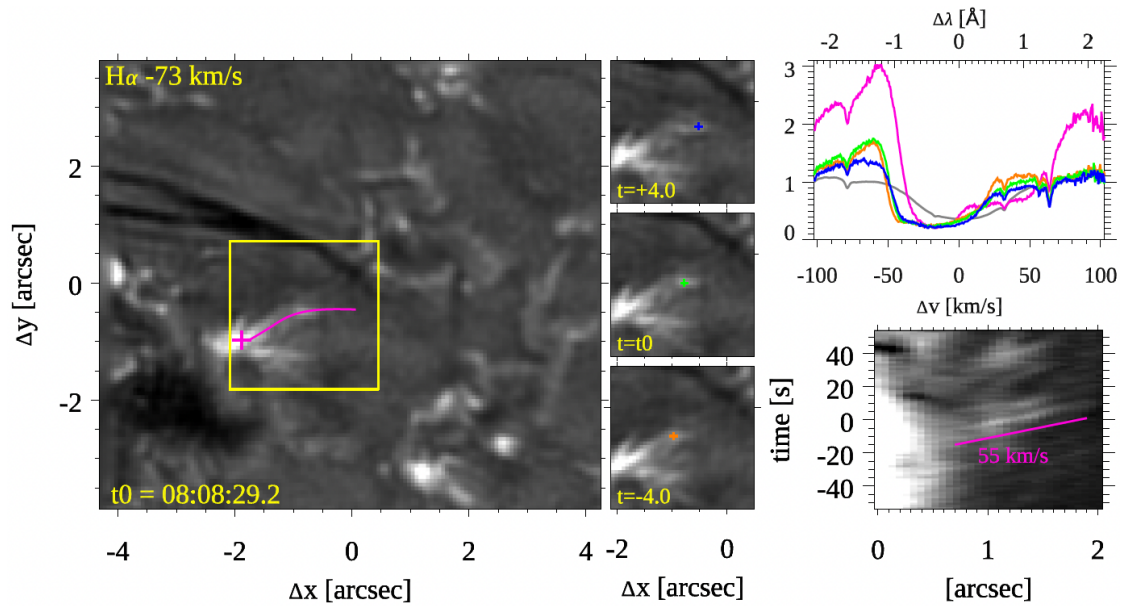


Figure 3.11: SST/TRIPPEL-MiHI $H\alpha$ image of an Ellerman bomb (EB) with a nearby-appearing plasmoid-like blob. Left panel is an overview image with the EB marked by the pink cross, and the trajectory of the blob marked by the pink curve. The yellow square marks a zoom-in region from where a time-series of images are shown in the middle column. In those three (smaller) images, the location of the blob is marked by coloured crosses, from where the light-curves are measured and shown in the top-right panel with the same colour, showing that the left wing of the line profile is brighter than the average over the full FOV (grey curve) and coincides with the corresponding brightening of the EB (pink curve). An st diagram of the blob trajectory is shown in the bottom-right panel. Image credit: Rouppe van der Voort et al. (2023).

3.2.2 Ultraviolet (UV) bursts

As described in the review by Young et al. (2018), UV bursts are defined as brightenings in the intensity of UV lines (can get up to 100-1000 brighter than the median), which are short-lived ($\sim 10 \text{ s} - 1 \text{ hr}$) and small in size ($1 - 2''$), moving slowly ($\leq 10 \text{ km s}^{-1}$), and are not related to flares. With their original discovery dating back to the 1970s (Brueckner et al. 1976), UV bursts have more recently been observed both by IRIS in Si IV 1400 Å and Mg II 2796 Å, as well as by AIA in its 1600 and 1700 Å channels (Peter et al. 2014). As an example, bottom-left panel of Fig. 3.10 shows a UV burst, delimited by a yellow circle, seen in an IRIS SJI Si IV 1400 Å image. The location of the UV burst is also shown in the other panels of the figure, indicating coexistence with the Ellerman bomb and the borderline between opposite magnetic polarities. As a matter of fact, four out of five EBs studied by Ortiz et al. (2020) were found to coexist with a UV burst. Plasmoids have also been observationally reported to appear near UV bursts (Roupe van der Voort et al. 2017, in agreement with plasmoid-mediated UV burst simulation by Nóbrega-Siverio et al. 2017), as shown in Fig. 3.12, and the triangular line profiles observed in UV bursts do also agree with those numerically predicted by reconnection models that reproduce plasmoid instability (e.g., Guo et al. 2020).

3.2.3 Surges

With their detection dating back to the late 1930s (McMath & Pettit 1937; Newton 1942; Ellison 1942), surges are characterised as dark elongated structures visible in the blue or red wings of the H α line with typical lengths of 10 – 50 Mm and typical LOS velocities between 20 and 40 km s $^{-1}$ (e.g., Kirshner & Noyes 1971; Roy 1973; Cao et al. 1980; Schmieder et al. 1984). Surges also tend to appear near EBs and UV bursts (e.g., Ortiz et al. 2020, and references therein), with an example of this seen in the top-left panel of Fig. 3.10, indicating strongly that this phenomenon can be related to plasmoid-mediated reconnection as well.

3.2.4 Coronal bright points (CBPs)

The discovery of CBPs with the Skylab satellite (Vaiana et al. 1973b,a, 1976) was a game changer for coronal physics, as it revealed that the solar corona is not quiet and homogeneous as previously believed, but rather highly structured with numerous point-like, bright sources of X-ray (and EUV) emission. These bright spots comprises several small-scale coronal loops which connect magnetic fluxes of opposite polarities. They are found to have diameters ranging between 4 and 40 Mm, lifetimes up to 20 h, and their magnetic bipoles can reach a total flux strength of 10^{20} Mx (see the recent review by Madjarska 2019). Figure 3.13 shows observations from SDO and SST of a CBP taken at 2022 July 01 (Nóbrega-Siverio et al. 2023). The magnetic topologies derived for such structures (e.g., see Galsgaard et al. 2017) tend to contain a null-point where reconnection expectedly occur (e.g., see Cheng et al. 2023). Therefore, one might also expect to see

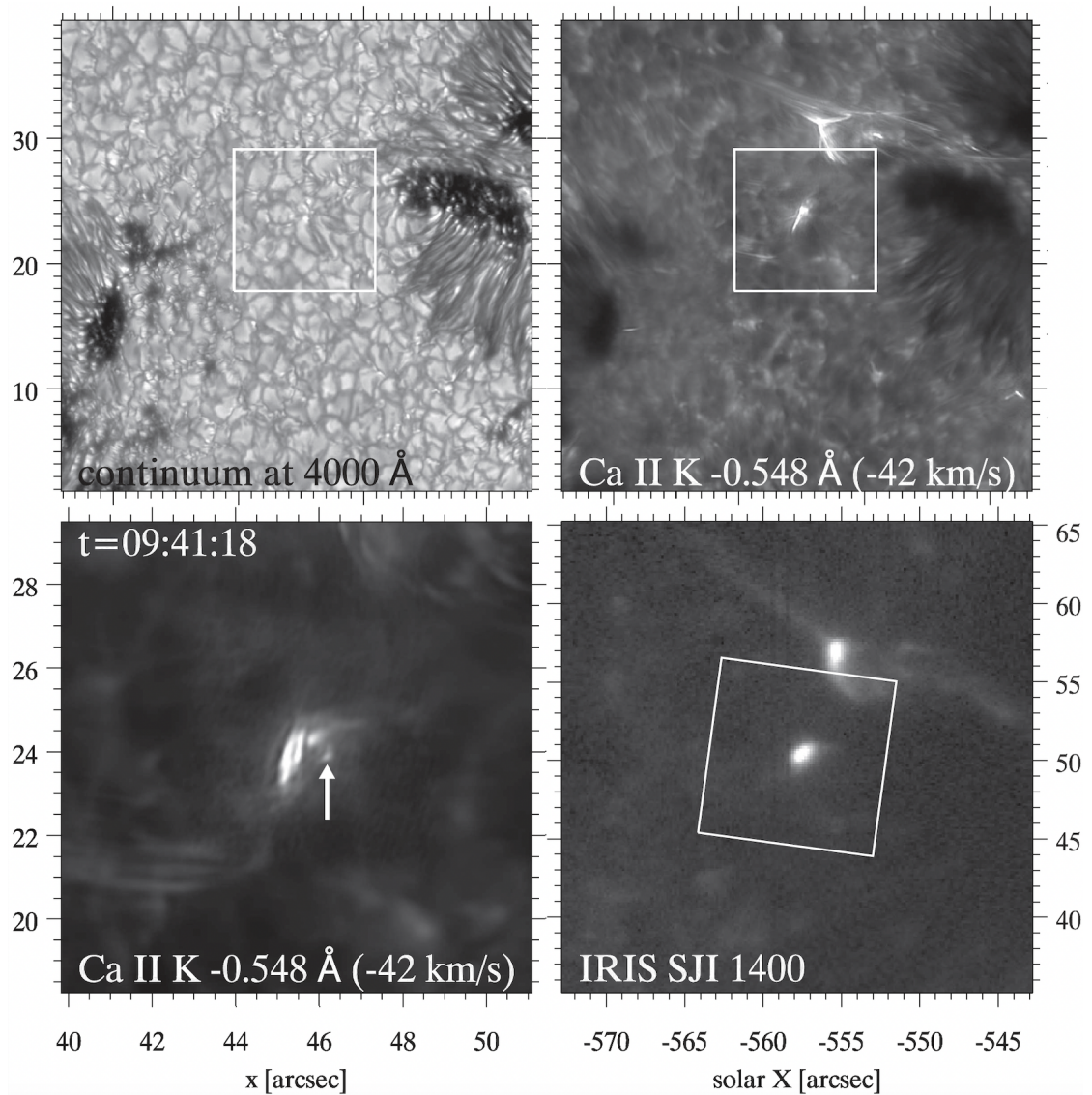


Figure 3.12: SST/CHROMIS and IRIS images showing a plasmoid-like blob near an ultraviolet (UV) burst. For context, top-left panel is a SST CHROMIS 4000 Å continuum image of the photosphere below the location of the UV burst, and top-right panel images the same region seen in the Ca II K 3934 Å line. A zoom-in on the region delimited by the white square is shown in bottom-left panel, with an arrow pointing at the plasmoid next to the UV burst. The same UV burst is seen in IRIS SJI 1400 Å (bottom-right). Image credit: Rouppe van der Voort et al. (2017).

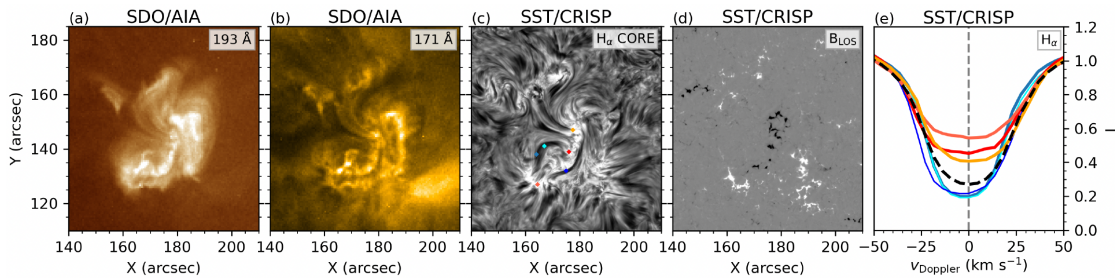


Figure 3.13: Observations of a CBP taken at 2022 July 01, seen in SDO/AIA 193 Å (a), SDO/AIA 171 Å (b), and SST/CRISP H α core (c), including an SST/CRISP magnetogram (d) and SST/CRISP H α line profiles (e) from locations marked in panel (c) with the same colour. Image credit: Nóbrega-Siverio et al. (2023)

plasmoids related to CBPs, which still remains to be observationally proven, due to the limited availability of high-resolution coronal imaging as of today.

3.2.5 Coronal jets

Since the early observations with the Naval Research Laboratory’s High Resolution Spectrograph and Telescope (HRTS) in EUV wavelengths (Brueckner & Bartoe 1983) and with the Soft X-ray Telescope (SXT, Tsuneta et al. 1991) on the Yohkoh satellite (Solar-A, Ogawara et al. 1991) in X-ray wavelengths (Shibata et al. 1992a; Shimojo et al. 1996), coronal jets have been deeply studied. By definition, they are collimated high-speed hot ejections seen in EUV and X-ray lines mainly associated with small flares (microflares) in CBPs, emerging flux regions, and active regions, with lengths ranging from 10 to 400 Mm, widths of 5 – 100 Mm, velocities of 10 – 1000 km s $^{-1}$, and lifetimes of up to 10 hours. Recent observations of coronal jets with IRIS have revealed plasmoid-like blobs (Kumar et al. 2019), as seen in Fig. 3.14, furthermore strengthening the significance of plasmoid instability in reconnection as a coronal heating mechanism.

3.2.6 Flares

Recorded for the first time in the enormous Carrington (1859) event, flares are explosive events in the solar corona seen in many parts of the spectrum including visible light, EUV, and X-ray with duration from tens of seconds up to several hours, energy releases of up to 10^{32} erg, and temperatures of up to 20 MK (Hirayama 1974). An example is shown in the left panel of Fig. 3.15. They tend to occur around sunspots, and therefore the frequency of flares vary with the 11-year solar cycle. Though several theories for the mechanism behind flares have been suggested, they are as of today widely believed to be driven by huge reconnection events in emerging coronal loops, described by the so-called standard flare model developed by Carmichael (1964), Sturrock (1966), Hirayama (1974), and Kopp & Pneuman (1976), with a simplified sketch given in the right panel of Fig. 3.15. Plasmoid instability has a visible effect on flares as well, as observationally indicated (e.g., Nishizuka et al. 2010; Takasao et al. 2012; Yan

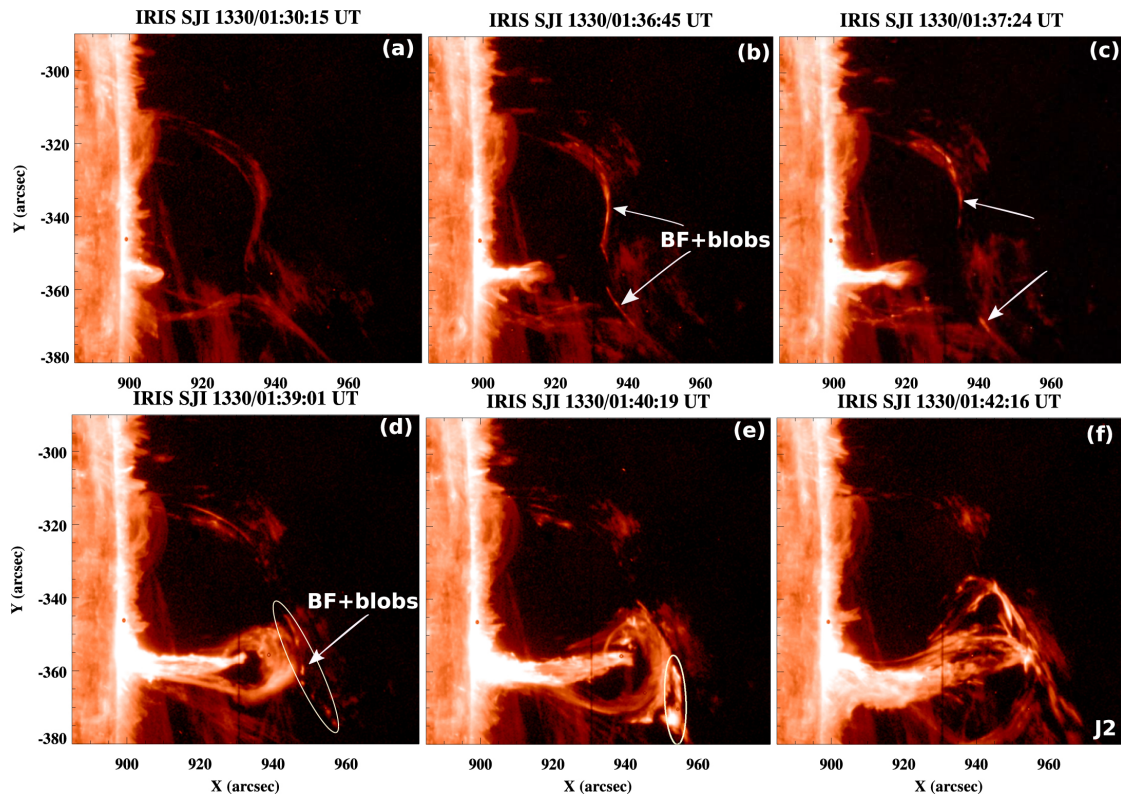


Figure 3.14: IRIS SJI 1330 Å image series of the evolution of a coronal jet, revealing plasmoid-like blobs. Image credit: Kumar et al. (2019).

et al. 2022). In fact, large-scale plasmoids formed in the null-points of flares can evolve into coronal mass ejections (CMEs, for instance see Antiochos et al. 1999; Gou et al. 2019), which can have a noticeable effect on space weather on Earth in the form of auroras.

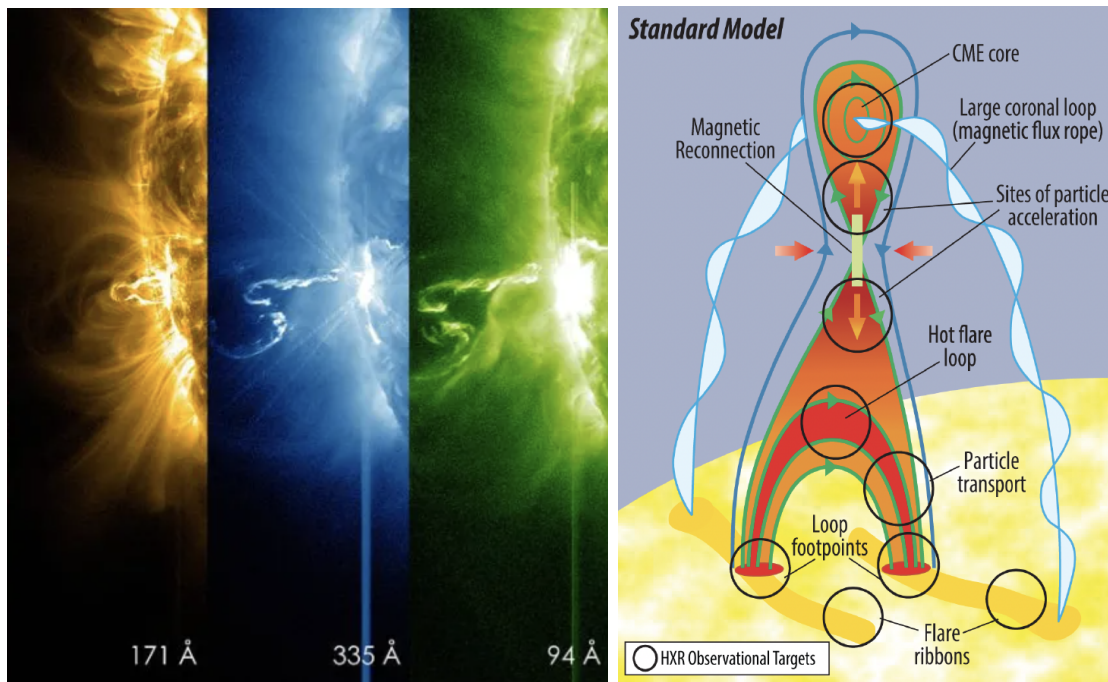


Figure 3.15: Left: SDO/AIA images of a flare seen in different wavelengths. Image credit: NASA (<https://scied.ucar.edu/learning-zone/sun-space-weather/solar-flare>). Right: Sketch of the standard flare model. Image credit: Christie et al. (2017).

Chapter 4

Solar simulations

Numerical simulations of plasma in the solar atmosphere are performed by discretising a chosen set of differential equations, that is, approximating all spatial and temporal derivatives by finite differences, in order to calculate the distributions of the relevant quantities at a given timestep in the simulation based on their values at the previous timestep. In the following section, we will briefly describe how this is done with the Bifrost code (Gudiksen et al. 2011). Furthermore, we will take a closer look at different models for the electrical resistivity, which is a central part of our thesis, especially the first two papers. In the final section of this chapter, we will give a few examples of 2D and 3D simulations of magnetic reconnection (in some cases plasmoid-mediated) where previously-observed phenomena, as mentioned in Sect. 3.2, have been successfully mimicked.

4.1 The massively-parallel MHD code Bifrost

Bifrost is a massively-parallel code that numerically solves the radiative magnetohydrodynamic (RMHD) equations, as described in Sect. 2.1 (but including radiative transfer), on a 3D Cartesian grid. For spatial discretisation, Bifrost applies a staggered mesh, where the mass density and energy density are cell-centered variables, magnetic field and fluid velocity are face-centered, and electric field and current density are edge-centered. Sixth-order differential operators are used for discretising the spatial derivatives, supported by fifth-order interpolation operators. For temporal discretisation, Bifrost can use either a third-order Runge-Kutta or Hyman (1979) time-stepping scheme. Different modules can be included in the code depending on which physical terms that need to be taken into account in the simulations. This includes solving the equations of radiative transfer (Hayek et al. 2010) for taking into account the effects of radiation in the energy equation, along with calculating chromospheric radiative losses (Carlsson & Leenaarts 2012), optically thin losses (based on atomic data from CHIANTI, e.g. see Dere et al. 2023, and references therein), and thermal conduction, or expanding the induction equation by including Hall effect and ambipolar diffusion (Martínez-Sykora et al. 2012, 2017; Nóbrega-Siverio et al. 2020a). In addition, one may include non-equilibrium calculations of hydrogen (Leenaarts et al. 2011), helium (Golding et al. 2016), and heavier elements relevant for the transition region (Olluri et al. 2015).

4.2 Modelling the electrical resistivity

One challenge in numerically mimicking magnetic reconnection processes is the modelling of the electrical resistivity, η , defined as the ratio between the electric field and the current density in the rest frame of the fluid (which is, by definition, the reciprocal of the conductivity). Derived from kinetic theory where particle collisions are taken into account, the resistivity is given by

$$\eta = \frac{m_e(\tau_{ei}^{-1} + \tau_{en}^{-1})}{\mu_0 n_e q_e^2}, \quad (4.1)$$

where m_e , n_e , and q_e are the electron mass, electron density, and elementary charge, respectively, and τ_{ei} and τ_{en} are the electron-ion and electron-neutral collision times. For fully-ionised collision-dominated plasma, this can be approximated with the *Spitzer resistivity*, given by

$$\eta = 5.2 \times 10^7 \ln \Lambda T^{3/2} \text{ m}^2 \text{ s}^{-1}, \quad (4.2)$$

where $\ln \Lambda$ is the Coulomb logarithm. Representative values for the Spitzer resistivity in the photosphere, chromosphere (at 10 kK), and corona (at 1 MK) are 10^4 , 10^3 , and $1 \text{ m}^2 \text{ s}^{-1}$, respectively (Priest 2014, and references therein).

The Spitzer resistivity is not always a valid approximation of the resistivity in the solar atmosphere. In regions of strong magnetic field gradients, for instance, the dynamics of charged particles is strongly affected by plasma instabilities, causing the resistivity to rise far beyond the Spitzer value, an effect referred to as *anomalous resistivity* (Roussev et al. 2002). In fact, when modelling the dissipation of direct currents (Heyvaerts & Priest 1984) as an efficient source for coronal heating, the Spitzer resistivity is too small for dissipating such strong currents, making anomalous resistivity an essential component (Adamson et al. 2013). Furthermore, the diffusive effects caused by the discrete nature of numerical codes can often get substantially larger than those caused by the physical diffusivity, unless an ultra-high numerical resolution is applied, which can be computationally expensive, especially in 3D. In some high-resolution 2D cases with adaptive mesh refinement (AMR), resistivity given by Eq. (4.1) or (4.2) have successfully been used, for instance in some reproductions of EBs and UV bursts with plasmoid-mediated reconnection (Ni et al. 2021, 2022; Liu et al. 2023). In the general case with more limited resolution, like 3D models covering a huge area of the solar atmosphere, large magnetic field gradients require typically a diffusivity considerably larger than that provided by the Spitzer resistivity in order to become numerically resolvable. This is why a reasonable amount of effort has been put into developing ad hoc models for anomalous resistivity terms (Sato & Hayashi 1979; Nordlund & Galsgaard 1995; Roussev et al. 2002; Vögler et al. 2005; Felipe et al. 2010; Adamson et al. 2013; Rempel 2014; Przybylski et al. 2022). These terms are defined to be sufficiently large around current sheets in order to make them numerically resolvable but stay small elsewhere to minimise the deviations between the simulated and the physical plasma.

To mimic steady Sweet-Parker or Petschek reconnection in a simplified model where the location of the current sheet is fixed, a localised enhancement of the

resistivity in a fixed location is normally sufficient (Innes & Tóth 1999). More dynamic reconnection models with plasmoid instability can be simulated with an adaptive anomalous resistivity, for instance given by an enhancement that scales with the current density or the electron drift velocity (Sato & Hayashi 1979) or hyper-diffusive operators consisting of global and local diffusion terms (Nordlund & Galsgaard 1995). In the following paragraphs, we describe the resistivity models that have been deeply analysed in this thesis.

4.2.1 Uniform resistivity

The simplest way to model the resistivity is by keeping it uniform,

$$\eta = \eta_0. \quad (4.3)$$

With a moderate resolution, this resistivity model typically requires high values of η_0 in order to maintain numerical stability, hence resulting in Lundquist numbers too low for simulating plasma on the Sun in a realistic way. Given a sufficiently high resolution, nevertheless, this model is efficient for deriving scaling laws for different reconnection characteristics or other simplified studies of reconnection on the Sun (Syntelis & Priest 2020; Sen & Keppens 2022; Sen et al. 2023).

4.2.2 Resistivity scaled by current density

Used by Syntelis et al. (2019) in a cancellation nanoflare model for chromospheric and coronal heating, anomalous resistivity linearly proportional to the current density,

$$\eta = \begin{cases} \eta_0, & |\mathbf{J}| < J_{\text{crit}} \\ \eta_0 + \eta_1 |\mathbf{J}|/J_{\text{crit}}, & |\mathbf{J}| \geq J_{\text{crit}} \end{cases}, \quad (4.4)$$

with η_0 , η_1 , and J_{crit} as free scaling parameters, is satisfactorily efficient for making current sheets numerically resolvable while maintaining a low resistivity far from those current sheets. Though being more efficient than uniform resistivity in ensuring numerical resolvability of current sheets while maintaining satisfactorily high Lundquist numbers, this resistivity model is not optimal for more complex simulations with different magnetic field topologies, since the ideal values for the scaling parameters depend strongly on the local mean values of the current density in the vicinity of current sheets. Given the proper scaling, though, it is still a fine model for mimicking reconnection with fairly Petschek-like characteristics.

4.2.3 Resistivity scaled quadratically by electron drift velocity

Dating back to the late 70s (Sato & Hayashi 1979), anomalous resistivity quadratically proportional with the electron drift velocity, $v_d \equiv |\mathbf{J}|/(n_e q_e)$, given by

$$\eta = \begin{cases} 0, & v_d \leq v_c \\ \min(\alpha(\frac{v_d}{v_c} - 1)^2, \eta_{\text{max}}), & v_d > v_c \end{cases}, \quad (4.5)$$

with v_c , α , and η_{\max} as free scaling parameters, has been used in several papers, including simulations of magnetic flux emergence leading to surges and coronal jets (Shibata et al. 1992b, 1993; Yokoyama & Shibata 1994, 1995, 1996; Matsumoto et al. 2004). This resistivity model is even more efficient in ensuring numerical stability while maintaining high Lundquist numbers than the above current-density-scaled model due to its quadratic dependence on the drift velocity. Despite of this, the ideal values for the scaling parameters of this model do nevertheless depend strongly on the local plasma conditions, hence essentially different in the corona compared to the photosphere. It is still an adequate resistivity model for mimicking (non-steady) Petschek reconnection, as long as the current sheet is confined within regions with roughly the same background density.

4.2.4 Hyper-resistivity

The default way of modelling the resistivity in Bifrost is by hyper-resistivity (Nordlund & Galsgaard 1995), which can be written as a 3×3 diagonal tensor, $\bar{\eta}$, with elements given by

$$\begin{aligned}\eta_{xx} &= \frac{\eta_3}{2} \left[U_{m,y} \Delta y Q_y \left(\frac{\partial B_z}{\partial y} \right) + U_{m,z} \Delta z Q_z \left(\frac{\partial B_y}{\partial z} \right) \right], \\ \eta_{yy} &= \frac{\eta_3}{2} \left[U_{m,z} \Delta z Q_z \left(\frac{\partial B_x}{\partial z} \right) + U_{m,x} \Delta x Q_x \left(\frac{\partial B_z}{\partial x} \right) \right], \\ \eta_{zz} &= \frac{\eta_3}{2} \left[U_{m,x} \Delta x Q_x \left(\frac{\partial B_y}{\partial x} \right) + U_{m,y} \Delta y Q_y \left(\frac{\partial B_x}{\partial y} \right) \right], \\ \eta_{xy} &= \eta_{yx} = \eta_{yz} = \eta_{zy} = \eta_{xz} = \eta_{zx} = 0.\end{aligned}\tag{4.6}$$

Here, \mathbf{U}_m is an electrical diffusive speed with the x_i component defined by

$$U_{m,i} \equiv \nu_1 c_f + \nu_2 |u_i| + \eta_3 \Delta x_i |\nabla_{\perp} u_i|,\tag{4.7}$$

and $c_f \equiv \sqrt{c_s^2 + v_A^2}$, with c_s and v_A denoting the sound speed and Alfvén speed, respectively, and Δx_i denoting the grid spacing in x_i direction. Thus, the hyper-resistivity term scales with the fast-mode wave speed, bulk velocity, and gradients (shocks) in the velocity perpendicular to the magnetic field. Usual input values for the scaling parameters are $\nu_1 = 0.03$, $\nu_2 = 0.2$, and $\eta_3 = 0.2$. The positive-definite *quenching operator* in (4.6) is defined by

$$Q_i(g) \equiv \frac{\left| \frac{\partial^2 g}{\partial x_i^2} \right| \Delta x_i^2}{|g| + \frac{1}{q_{\max}} \left| \frac{\partial^2 g}{\partial x_i^2} \right| \Delta x_i^2},\tag{4.8}$$

where Δ_i^2 denotes the second-order difference operator in x_i -direction, and g can be any first-order spatial derivative of an MHD variable. For the maximum quenching factor, $q_{\max} = 8$ is often used by default, which empirically has been shown to work well when solving standard test problems. Given any perturbation with a wavenumber k , the quenching term approaches q_{\max} in the high-wavenumber limit

and decreases as k^2 in the low-wavenumber limit. This puts a heavy damping on any perturbation with wavelength of same order of magnitude as the grid size, while only a negligibly small damping is applied on perturbations with wavelengths of more than one order of magnitude higher.

With this, the hyper-resistivity of Bifrost is designed to be a more general resistivity model which can be applied on more holistic models of the solar atmosphere, from the top of the convection zone to the upper corona, using only the default values for the scaling parameters. It ensures that the resistive term of the induction equation is large only in regions where the diffusive speed is large—due to a large fast-mode speed, bulk velocity, or velocity shock—and where the gradients in the magnetic field are strong, while elsewhere maintaining a sufficiently high Lundquist number.

4.3 2D and 3D numerical simulations of solar atmospheric phenomena

One can gain deep insights into solar physics both from 2D and 3D simulations. 2D simulations are much faster to perform, allowing for applying a quite high resolution without demanding extremely large amounts of computational power. Solar simulations in 3D, on the other hand, takes in general much longer time to run, but are better for developing more holistic models of the solar atmosphere. In this final section before delving into the three papers that build up this thesis, we will give some examples of 2D and 3D simulations of magnetic reconnection, in some cases plasmoid-mediated, where different phenomena seen in solar observations have been mimicked. Several of these simulations have been sources of inspiration for the setups studied in this thesis.

4.3.1 Harris sheet-like simulations

Harris sheets, as given by Eq. (2.15), are efficient for studying basic reconnection theory. They can also be used for mimicking observable reconnection phenomena from a specific region of the solar atmosphere by simply using a representative mass density and temperature for that region as initial condition. As an example, Guo et al. (2020) mimicked UV bursts by simulating plasmoid-mediated reconnection on a Harris sheet, located in the upper chromosphere. With an initial temperature of 30 kK, the plasmoids are heated up to temperatures near the formation temperature of the Si iv 1400 Å line, which is around 80 kK. The synthesised Si iv 1400 Å line profile started out with a bi-directional shape in the slow-reconnection phase and evolved into a triangular shape in the plasmoid-mediated fast-reconnection phase, in agreement with IRIS observations. This is demonstrated in Fig. 4.16.

Similarly, Ni et al. (2022) simulated plasmoid-mediated reconnection, using the MHD code NIRVANA (Ziegler 2011), on a low- β Harris sheet located in the temperature minimum region ($T = 4.4$ kK) and showed that UV bursts could also be generated in the low chromosphere, just as EBs, given reconnecting magnetic

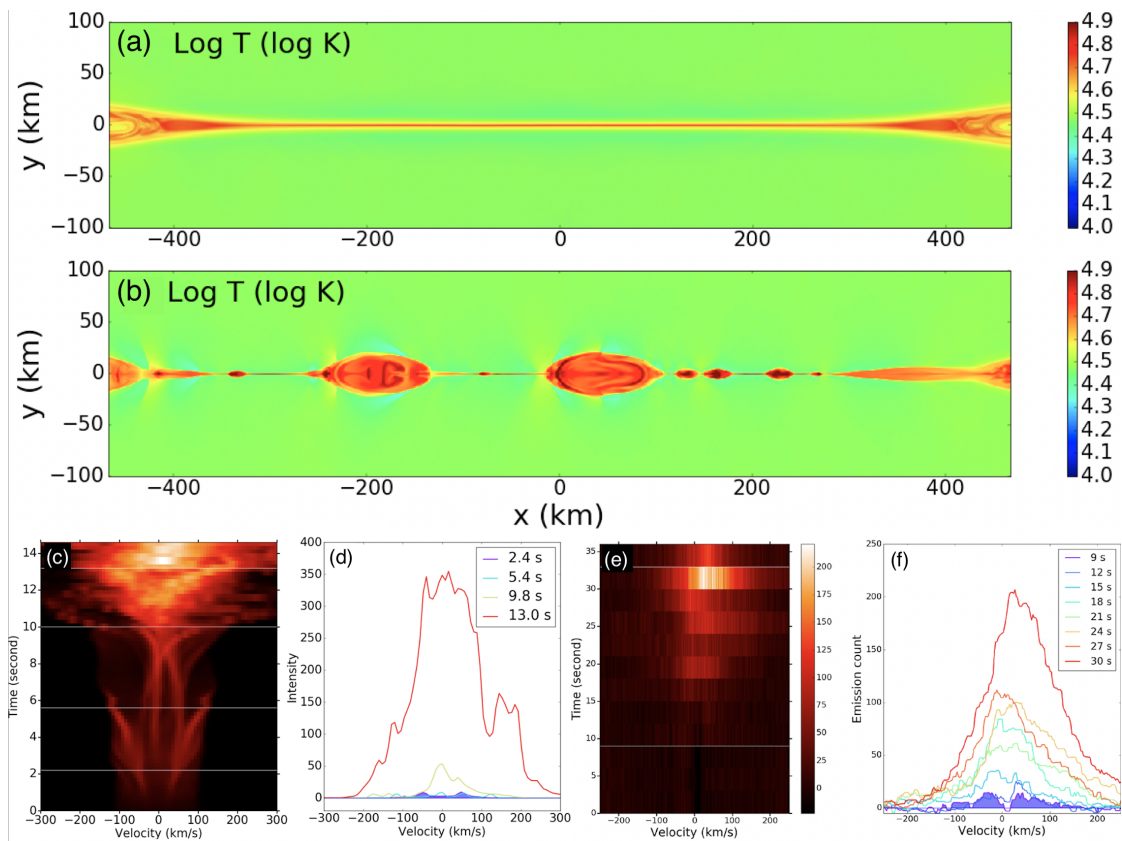


Figure 4.16: Numerical reproduction of a UV burst with plasmoid-mediated reconnection on a 2D Harris sheet (Guo et al. 2020, to whom the figure is credited). Panels (a) and (b) maps the temperature in the simulated Harris sheet at the early slow-reconnection phase and the late fast-reconnection phase mediated by plasmoids, respectively. Panel (c) maps the time evolution of the synthesised Si IV 1400 Å profile, and (d) plots the line profile at given times marked by white lines in panel (c). Panels (e) and (f) are observational counterparts, taken with IRIS.

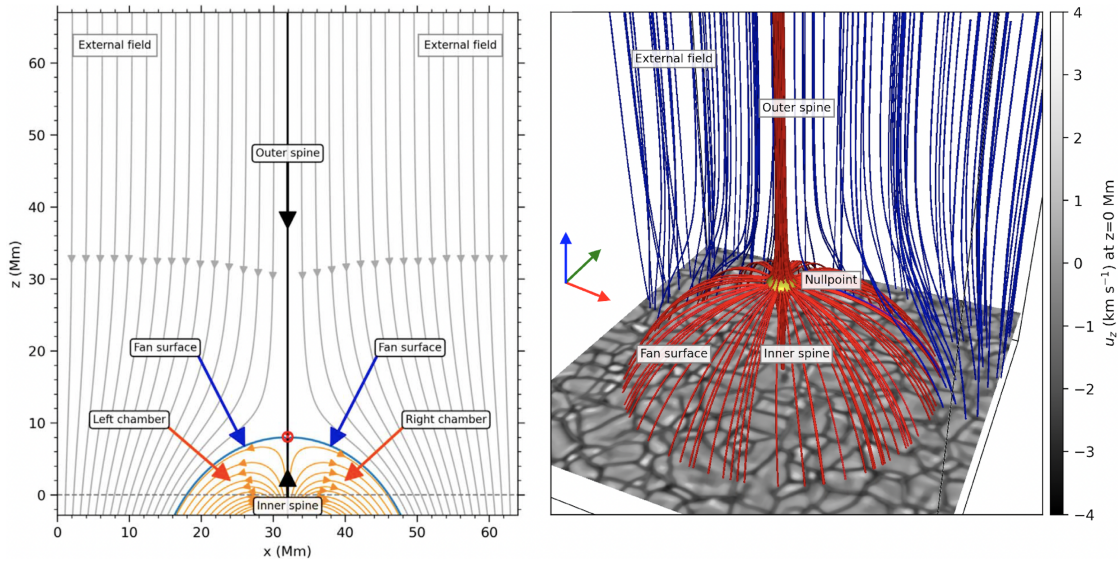


Figure 4.17: Fan-spine magnetic topology in 2D (left) and 3D (right). Image credit: Nóbrega-Siverio & Moreno-Insertis (2022); Nóbrega-Siverio et al. (2023).

fields of $\sim 500\text{G}$. They found that the heating increases rapidly at the onset of plasmoid instability, with plasmoid temperatures reaching 20 kK and synthetic Si iv 1400 \AA line profiles in good agreement with observations. In a follow-up paper, Liu et al. (2023) simulated high- β reconnection in the temperature minimum region using the same initial condition but with a Harris sheet field strength of only 100 G , resulting in EB-like events. There, they found that the reconnection rate increases rapidly from below 0.01 to above 0.05 as soon as plasmoid instability takes place, where magnetic diffusion caused by electron-neutral collisions, along with the motion of plasmoids, contributes to this fast reconnection. They also found that the radiative cooling effect plays an important role in constraining the temperature increase to reasonable values, in agreement with the temperatures found in EBs. More recently, the coronal Harris sheet simulations of Mondal et al. (2024), performed with the MPI-AMRVAC code (Keppens et al. 2012; van der Holst et al. 2012; Porth et al. 2014; Xia et al. 2018), showed that coronal plasmoids are accelerated to velocities of $105 - 303\text{ km s}^{-1}$ and heated up to temperatures of 8 MK with average plasmoid densities of twice the coronal background density, in a promising agreement with the observed characteristics of plasmoids in coronal jets and flares (Takasao et al. 2012; Zhang et al. 2016; Lu et al. 2022).

4.3.2 Fan-spine topology simulations

Fan-spine magnetic topologies are easy to set up both in 2D (as given by Eq. (2.16)) and 3D. With reconnection obtained through the collapse of the associated null-point by motions affecting the fan-spine structure, this topology is suitable for reconnection studies both with stratified and non-stratified atmospheric models. As an example, Peter et al. (2019) mimicked UV burst-like events in their simulation of plasmoid-mediated reconnection in a 2D fan-spine topology located in the chromosphere using an ad-hoc driving mechanism to move the fan-spine

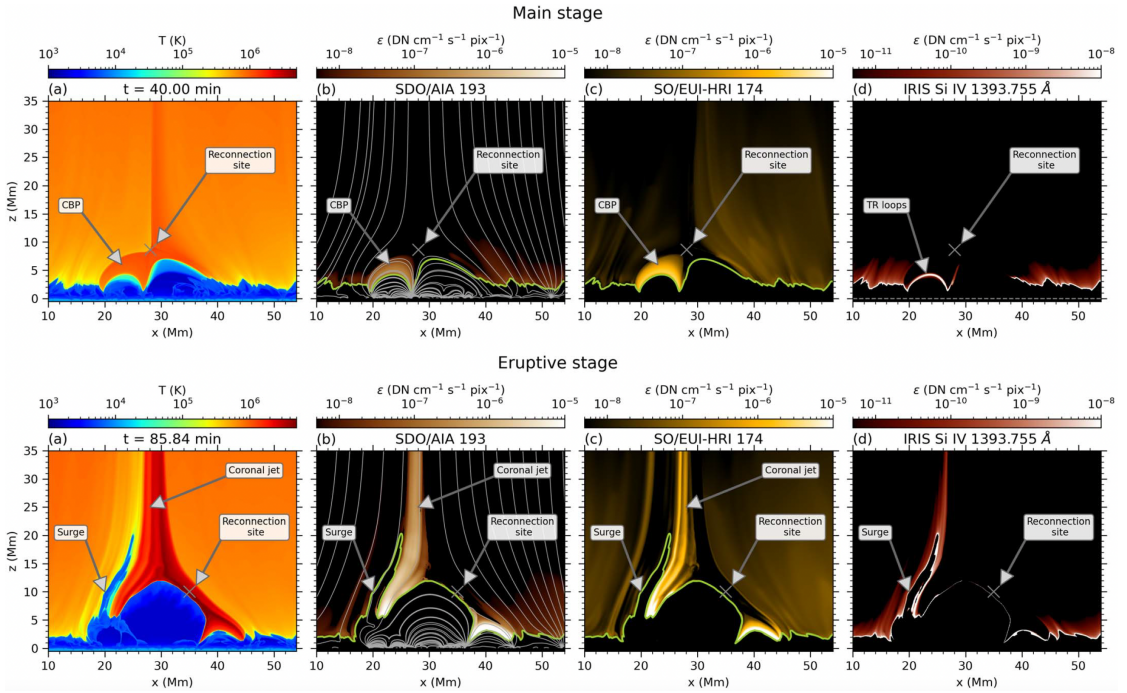


Figure 4.18: Temperature along with synthetic SDO/AIA 193 Å, SO/EUI-HRI 174 Å, and IRIS Si iv 1394 Å intensities during the main stage (top) and the eruptive stage (bottom) of a CBP from a 2D simulation of fan-spine reconnection driven by convective motion. Image credit: Nóbrega-Siverio & Moreno-Insertis (2022).

structure, as demonstrated in the left column of Fig. 2.8. The plasmoids in their case accelerates the reconnection process, leading to the formation of bi-directional jets, consistent with what is expected for UV bursts.

In the Bifrost simulations of Nóbrega-Siverio & Moreno-Insertis (2022) and Nóbrega-Siverio et al. (2023), a fan-spine magnetic topology is set up in a stratified solar atmosphere within a coronal hole environment, the former in 2D and the latter in 3D, with initial conditions displayed in Fig. 4.17. In both cases, the inner spine is rooted in the convective zone, while the null-point lies in the lower corona, hence the fan surface reaches from the top of the convective zone up to the lower corona, and the outer spine goes out far into the upper corona. The inner spine is

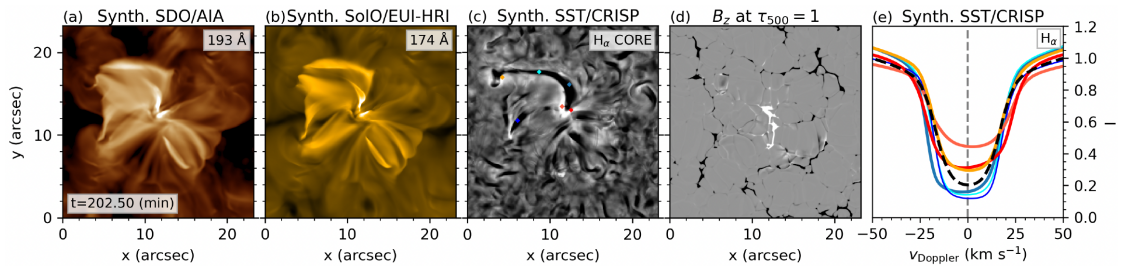


Figure 4.19: Synthetic intensities in SDO/AIA 193 Å, SO/EUI-HRI 174 Å, and SST/CRISP H α core, along with photospheric vertical magnetic field component and synthetic H α line profiles of a CBP from a 3D simulation of fan-spine reconnection driven by convective motion. Image credit: Nóbrega-Siverio et al. (2023).

moved around by convective motions, causing the null-point to collapse, leading to the formation of a current sheet, along where reconnection takes place. In the 2D case (Nóbrega-Siverio & Moreno-Insertis 2022), a CBP evolves in the left chamber of the fan-spine topology, as seen in the top panels of Fig. 4.18 (visible in SDO/AIA 193 Å and SO/EUI-HRI 174 Å), due to the reconnection driven self-consistently by the stochastic granular motion of the photosphere. In the final, eruptive stage of the simulation (bottom panels), the CBP is disrupted by magnetic flux emergence due to the granular motion. As a result, both UV bursts, surges, and coronal jets can be seen.

In the corresponding 3D case (Nóbrega-Siverio et al. 2023), a CBP is formed similarly, this time covering nearly the whole dome structure below the fan surface, since this 3D dome is not divided into two separate chambers, in contrast to the 2D case. Also in contrast to the 2D case, the CBP is here maintained solely by the viscous and Joule heating due to the stochastic convective motion, with only a secondary heating contribution from the reconnection site. This major difference between the 2D and 3D case is related to the fact that the braiding of field lines can only occur in 3D reconnection simulations, where it has an essential effect on the heating of the CBP. The synthetic EUV observables, displayed in Fig. 4.19, show striking similarities with the observation shown in Fig. 3.13. Visible in those observables are also upflows resembling dark coronal jets previously seen with Hinode/EIS. The fundamental differences seen between these 2D and 3D simulations highlights the fact that only 3D simulations of a stratified solar atmosphere can give a holistic understanding of the dynamics that causes the different observable phenomena. Still, 2D simulations are efficient especially for preliminary studies.

4.3.3 Flux cancellation simulations

Following up the theory established by Priest et al. (2018) for a cancellation nanoflare model for solar chromospheric and coronal heating, Syntelis et al. (2019) performed simulations of reconnection by magnetic flux cancellation in a 2D stratified atmosphere using the Lare3D code (Arber et al. 2001). This was done by setting up a null-point configuration given by a superposition of two sources of opposite magnetic polarity below the photosphere and an overlying horizontal background field, with initial condition akin to Eq. (2.17), then moving the two polarities towards each other with a driving velocity boundary condition. Five simulations were run with different background magnetic field, leading to different initial null-point locations. The first of these cases is mimicked in the first article of this thesis. In all cases, the motion of the polarities towards each other causes the null-point to collapse, leading to the formation of a vertical current sheet which moves downwards as the polarities approaches each other (until they cancel out). Reconnection takes place along the current sheet, heating up the surrounding plasma. They found that several of the reconnection characteristics, including the current-sheet length, inflow velocity, and energy release, agreed well with the established flux cancellation theory, and that the energy conversion rate was nearly Petschek-like. Depending on the initial height of the null-point, the flux

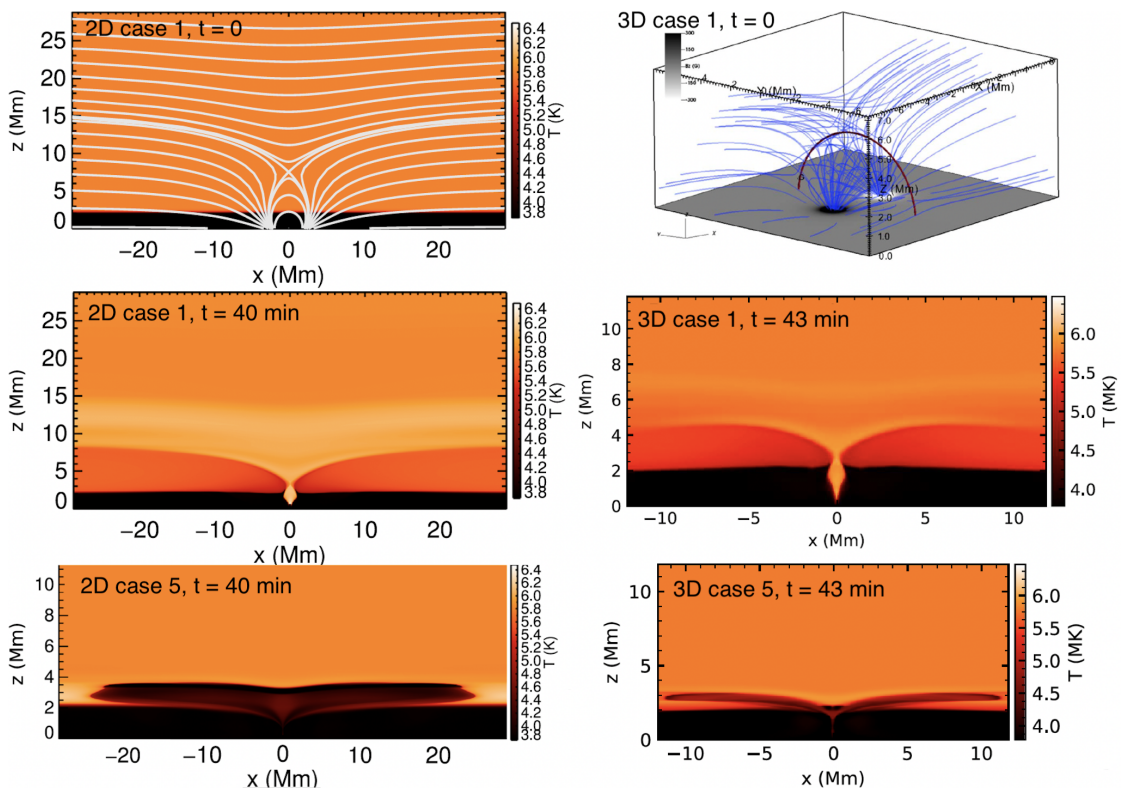


Figure 4.20: Flux cancellation simulations in 2D (left) and 3D (right). Top: initial condition. Middle and bottom: final temperature profile from different cases (in the 3D cases, evaluated at the xz -midplane). Panels are taken from different figures, hence some inconsistency in the aspect ratios. Image credit: Syntelis et al. (2019); Syntelis & Priest (2020).

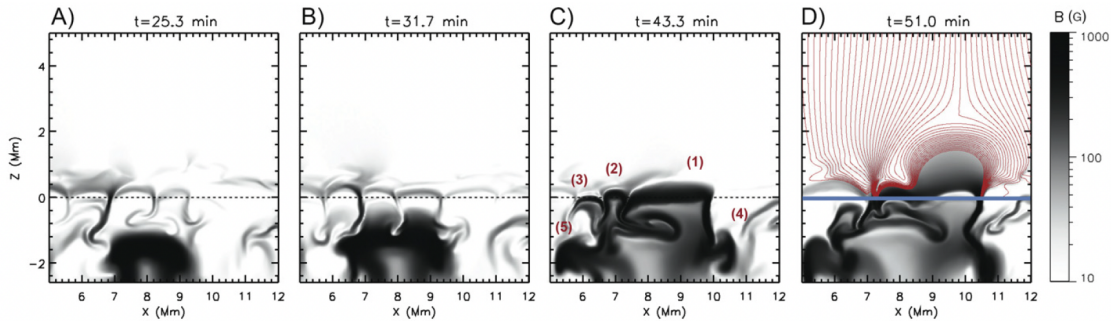


Figure 4.21: Evolution of the magnetic field strength in the 2D flux-emergence simulation of Nóbrega-Siverio et al. (2016, to whom the figure is credited). Field lines are plotted into the last panel to demonstrate the current sheets forming between the newly-emerged field and the background field.

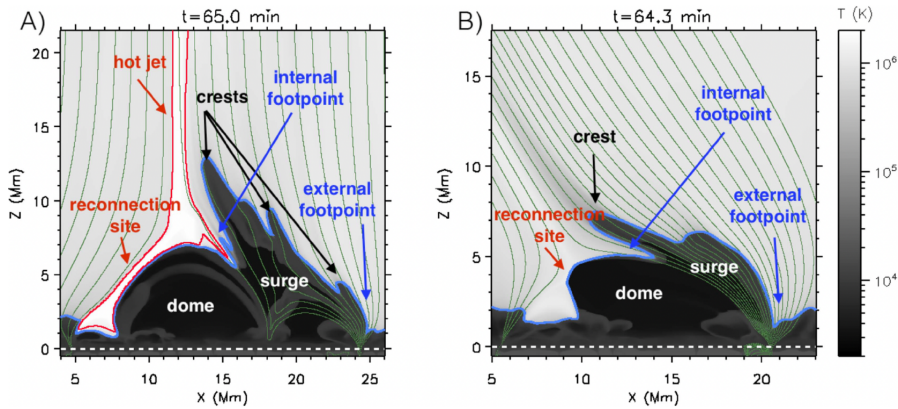


Figure 4.22: Temperature maps of the 2D post-flux-emergence dome structures with magnetic field lines superimposed, showing surges and jets, from the two simulations of Nóbrega-Siverio et al. (2017, to whom the figure is credited): the one with a vertical background field (A) and the one with a slanted background field (B).

cancellation process leads to hot ejections resembling coronal loops and/or cold ejections resembling surges. Examples are shown in the left column of Fig. 4.20. Very similar results were found in the 3D reproduction (Syntelis & Priest 2020), as shown in the right column of the figure, though the null-point was here expanded into a semicircular separator line, and they concluded that, depending on the properties of the cancelling region, the flux cancellation can generate a large variety of multi-thermal ejections associated with EBs, UV bursts, and spicules.

4.3.4 Flux-emergence simulations

Though simulations with magnetic null-point topologies are good for studying the evolution of current sheets as well as they successfully mimic several observable features, the aforementioned models have the drawback that the null-point topology is imposed as an initial condition. In magnetic flux emergence simulations, on the other hand, the null-point and the reconnection sites are naturally created as a consequence of strong concentrations of magnetic fields, generated in the convective zone by the solar dynamo, emerging into the solar

atmosphere. This allows reconnection to occur at any heights along the interface between the emerging field and the background field, leading to a wide range of different observable phenomena.

Among the most fundamental examples are the 2D flux emergence simulations of Yokoyama & Shibata (1994, 1995, 1996), being the first numerical simulations of coronal jets, as previously observed with the Yohkoh satellite, along with surges. Over the next decade, improved models of flux emergence leading to jets and surges have been evolved with a more adequate treatment of the physical mechanisms and quantities. In the papers by Nóbrega-Siverio et al. (2016, 2017), surges and jets were reproduced in 2D flux emergence simulations with Bifrost including a more realistic equation of state and taking radiative transfer, heat conduction, and optically thin radiative cooling into account. To demonstrate the flux emergence process (which is quite similar in both papers), Fig. 4.21 maps the magnetic field strength at different phases of the flux emergence, taken from the 2016 paper, and to demonstrate the resulting reconnection site which gives rise to surges and hot jets, Fig. 4.22 shows this in its temperature maps with magnetic field lines superimposed, taken from the 2017 paper. Especially, the simulations of the latter paper reproduced a UV burst with plasmoids nearby and was used to as theoretical support to the corresponding observations reported in the letter by Rouppe van der Voort et al. (2017). Among other noteworthy 2D flux emergence simulations with plasmoid-mediated reconnection are those of Ni et al. (2017), which demonstrated that the blob structures observed near coronal jets can be related to plasmoid instability and Kelvin-Helmholtz instability, along with Ni et al. (2021), with further demonstrations of EBs and UV bursts being capable of occurring at the same heights.

Three-dimensional flux emergence simulations have contributed fundamentally in linking different observed events on the Sun with each other and with the process of magnetic reconnection. Fundamental example are the MURaM (Vögler et al. 2005; Rempel et al. 2009) simulations of Danilovic (2017) and the Bifrost simulations of Hansteen et al. (2017, 2019), both reaching similar results concerning EB formation. Especially in the latter (2019) paper, they found EBs and UV bursts to be formed at opposite ends of the same current sheet which extends over several scale heights through the chromosphere. This is demonstrated in Fig. 4.23, which shows a selection of figures from that paper. In the top row, yz -cuts of selected physical quantities are mapped, showing clearly the location of the vertical current sheet. The middle row shows that the EB, as seen by the brightening of the Ca II 8542 Å line wing but not core, is located along the current sheet, and similar for the UV burst (Si IV 1394 Å brightening) in the bottom row. Throughout the simulation, plasmoids appear frequently along the current sheet, hence providing further theoretical support for plasmoid-mediated reconnection as the central mechanism behind EBs and UV bursts.

The largest observed solar events that have been numerically re-created by simulations of magnetic reconnection as a result of magnetic flux emergence are the flares. In the recent few decades, comprehensive 3D simulations of the evolution of flares have been performed, from the emergence of colliding sunspots to the eruptive phase, explaining several of the observed flare characteristics and shedding

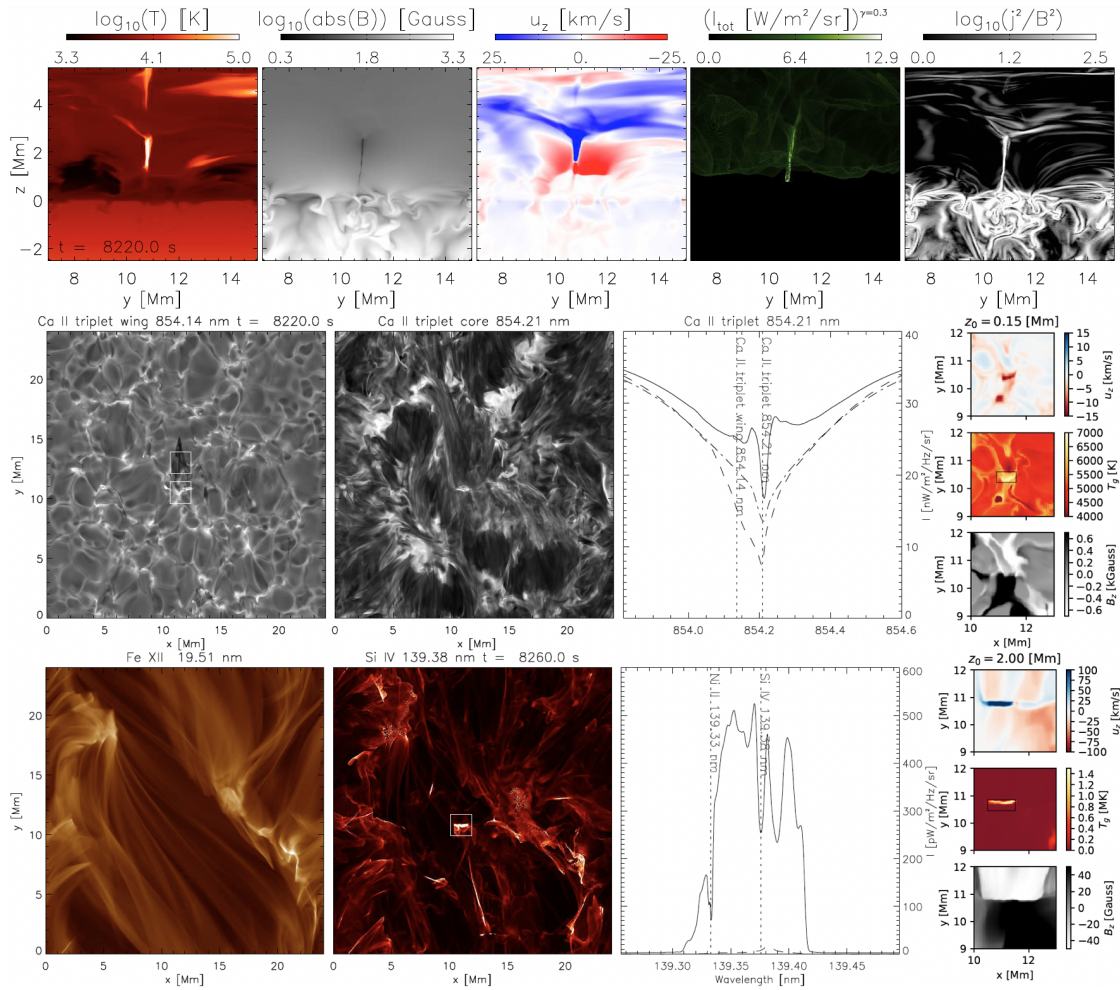


Figure 4.23: Physical properties and synthetic observables of the post-flux-emergence current sheet in the 3D simulations of Hansteen et al. (2019, to whom the figure is credited). Top: vertical cuts at $x = 10.78$ Mm of the temperature, magnetic field strength, vertical velocity, Si IV 1394 Å intensity, and inverse magnetic characteristic length, taken at $t = 8220$ s. Middle: properties of the EB, including mosaics of synthetic Ca II 8542 Å line wing (first panel, with squares marking EB and surge) and core (second), line profiles (third) from EB (solid) and surge (dashed), and xy -cuts of selected quantities (small panels). Bottom: Properties of the UV burst, including synthetic Fe XII 195.1 Å (first panel) and Si IV 1394 Å (second) intensities, Si IV 1394 Å line profile (third) from UV burst (solid) and average spectrum (dashed), and xy -cuts of selected quantities (small panels).

light on questions concerning how and when magnetic flux ropes are evolved during the flare (Masson et al. 2009; Cheung et al. 2019b; Chen et al. 2023; Rempel et al. 2023). This also includes proving plasmoid instability as a strong candidate for explaining the impulsive phase of confined flares (MacTaggart & Fletcher 2019).

Chapter 5

Summary and outlook

In the preceding chapters, we have seen examples showing, observationally and numerically, how magnetic reconnection is related to a variety of observable phenomena on the Sun. All of those phenomena are, to a certain degree, affected by plasmoid instability, as indicated in several of the examples. A central part of this thesis is to study and compare different resistivity models used for simulating reconnection in the solar atmosphere, which includes comparing the plasmoid characteristics that they reproduce. Observations of plasmoids can therefore be used for constraining the modelling of the electrical resistivity, and because of this, using forward-modelling to determine how plasmoids can be seen with different telescopes and spectrographs is also part of the scope here. In the following, we give a brief summary on how the three papers of this thesis together achieve the above-mentioned goals.

In Paper I, we used the Bifrost code to mimic the 2D flux cancellation simulation (Case 1) of Syntelis et al. (2019). For this, we applied the three anomalous resistivity models described in Sect. 4.2: 1) the inbuilt hyper-resistivity model of Bifrost; 2) the current-density-scaled resistivity used in the original experiment; and 3) the frequently-used resistivity scaled quadratically with the electron drift velocity. To use the latter two resistivity models, we developed new Bifrost modules especially made for this comparative study. We found that all three resistivity models, given proper values for the scaling parameters, were capable of reproducing similar large-scale reconnection characteristics, especially in terms of current-sheet length, inflow velocity, inflow magnetic field strength, and Poynting influx. With the current-density-scaled resistivity model, a steady, Petschek-like reconnection process was reproduced, akin to the original experiment. In contrast, the drift-velocity-dependant resistivity model and the hyper-resistivity model both reproduced plasmoid-mediated reconnection but with different energy conversion rates. The study was complemented with an MHD simulation of a 1D Harris current sheet, located in roughly the same coronal environment (i.e., with similar temperature and density) as near the null-point of the 2D experiment, using the same three resistivity models. In order to attain consistent results in terms of Joule heating and final current sheet width (after a certain diffusion time), we found that the current-density-proportional resistivity model needed a re-scaling of several orders of magnitude due to its strong dependence on the local magnetic field topology. The other two resistivity models needed only a slight re-scaling

in order to ensure consistent results. While the scaling parameter of the drift-velocity-dependent resistivity model in our two experiments (both dealing with coronal current sheets) was set to a value of many orders of magnitude lower than the one used in previous experiments with current sheets located in the lower solar atmosphere (Yokoyama & Shibata 1994, 1996), the free parameters of the hyper-resistivity model were set to standard values previously applied for the entire solar atmosphere. From this, we concluded that the hyper-resistivity model of Bifrost, being as suitable for simulating reconnection on the Sun as other previously used resistivity models, has the advantage of being applicable in any region of the solar atmosphere without the need for any considerable re-calibration.

In Paper II, we performed a deeper analysis of the reconnection characteristics reproduced with the anomalous resistivity models used in Paper I and compared them with the characteristics attained using uniform resistivity at different resolutions. To that end, we ran Bifrost simulations of a fan-spine magnetic topology located in a quiet-Sun coronal hole, using a driving velocity boundary condition to simulate reconnection. In total, 44 experiments were run, using the different resistivity models and resolutions with various values for the scaling parameters in order to study how the reconnection characteristics scaled with Lundquist number. Most of those cases resulted in plasmoid-mediated reconnection. In the cases of uniform resistivity, the frequency of plasmoids was found to converge towards higher values with a weaker scaling to the Lundquist number when increasing the resolution, reaching values of 7.9-12 plasmoids per minute for $S_L \in [1.8 \times 10^4, 2.6 \times 10^5]$ in the highest-resolution cases with a scaling of $S_L^{0.210}$, strikingly close to the scaling relation (of $S_L^{0.223}$) found by Sen & Keppens (2022) in their Harris sheet experiments. For Lundquist numbers below this range, Sweet-Parker reconnection was reproduced, and for Lundquist numbers above, a (nearly) shock-mediated Petschek-like reconnection occurred, as confirmed in the reconnection rates. The cases with anomalous resistivity showed similar behaviour even with lower resolution. The cases with drift-velocity-scaled resistivity were characterised by non-steady Petschek reconnection, and a scaling relation between plasmoid frequency and Lundquist number very close to that ($\sim S_L^{0.375}$) found by Loureiro et al. (2007) for plasmoid reconnection in an adiabatic medium. Similar results were seen with the current-density-scaled resistivity, though with slightly lower plasmoid frequencies and reconnection rates. The hyper-resistivity cases, on the other hand, were the only ones, for the given resolution, to reproduce the relatively high plasmoid frequencies with the weaker scaling to Lundquist number as seen in the higher-resolution cases. This led us to conclude that, when simulating magnetic reconnection with a moderate numerical resolution, the hyper-resistivity model of Bifrost has the advantage of being capable of reproducing plasmoid characteristics in closer resemblance to those attained with uniform resistivity at a significantly higher resolution.

In Paper III, we examined the possibility of observing coronal plasmoids, akin to those seen in the Paper II simulations, with currently-active and upcoming instruments. To that end, we used two simulations of plasmoid-mediated fan-spine reconnection, with the same setup as in paper II but with different mass densities (hence different emission measures), and performed forward-modelling

of observables with SDO/AIA and SO/EUI-HRI_{EUV} along with the upcoming MUSE (SG and CI) and Solar-C/EUVST. Here, we found that the short-lived ($\sim 10\text{--}20$ s) small-scale ($\sim 0.2\text{--}0.5$ Mm) plasmoids seen in our simulations cannot be detected with the moderate resolution of SDO/AIA, but should be possible to capture with SO/EUI-HRI_{EUV}. Among future instruments, MUSE/SG, with its planned high spatial and temporal resolution, will be adequate for acquiring full spectral information of these plasmoids. Achieving a sufficient signal-to-noise ratio for ~ 0.8 MK plasmoids in the MUSE/SG Fe IX 171 Å line should be doable on full-raster mode for regions of electron density higher than 10^9 cm^{-3} whereas on sit-and-stare mode for lower-density regions. The plasmoids should also be possible to capture with SOLAR-C/EUVST, where the plasmoid motions should leave detectable traces also in the form of rapid changes in the Doppler shift and line width of different EUV lines. The combination of spectra from MUSE/SG and Solar-C/EUVST of different EUV lines and high-resolution images from SO/EUI-HRI_{EUV} and MUSE/CI should therefore provide us with a promising possibility of gaining new insights into coronal plasmoid characteristics. Those insights can furthermore be used for putting constraints on future simulations, for instance in terms of determining which resistivity model reproduces plasmoid characteristics in best agreement with the observed ones.

We have hereby demonstrated the capability of different resistivity models in recreating the same reconnection phenomena which look similar on larger scales but with considerably different reconnection characteristics on smaller scales. In particular, we have shown how anomalous resistivity models, when applied on moderate resolutions, can mimic results seen with uniform resistivity only at higher resolutions, and especially the advantages of hyper-resistivity models in optimising those results as seen in the reproduced plasmoid characteristics. Our forward-modelling showing how Solar Orbiter along with the future MUSE and Solar-C missions can observe those plasmoids is a good starting point in demonstrating that future observational plasmoid analyses have a great potential for constraining numerical models in terms of evolving state-of-the-art resistivity models. For future research, it would be interesting to extend this analysis to 3D and perform forward-modelling on coronal plasmoids with a larger variety in temperature, density, and velocity. This could be an essential tool in preparing for future observations aimed to gain ground-breaking, new insights in solar physics.

Bibliography

- Abhyankar, K. D. 1977, *Bulletin of the Astronomical Society of India*, 5, 40
- Adamson, E., Büchner, J., & Otto, A. 2013, *A&A*, 557, A118
- Alfvén, H. 1947, *MNRAS*, 107, 211
- Antiochos, S. K., DeVore, C. R., & Klimchuk, J. A. 1999, *ApJ*, 510, 485
- Arber, T. D., Longbottom, A. W., Gerrard, C. L., & Milne, A. M. 2001, *Journal of Computational Physics*, 171, 151
- Archontis, V., Galsgaard, K., Moreno-Insertis, F., & Hood, A. W. 2006, *ApJ*, 645, L161
- Bhattacharjee, A., Huang, Y.-M., Yang, H., & Rogers, B. 2009, *Physics of Plasmas*, 16, 112102
- Boerner, P., Edwards, C., Lemen, J., et al. 2012, *Sol. Phys.*, 275, 41
- Bose, S., Hansteen, V., & Testa, P. 2023, in *AAS/Solar Physics Division Meeting*, Vol. 55, 54th Meeting of the Solar Physics Division, 106.41
- Brueckner, G. E. & Bartoe, J. D. F. 1983, *ApJ*, 272, 329
- Brueckner, G. E., Patterson, N. P., & Scherrer, V. E. 1976, *Sol. Phys.*, 47, 127
- Brun, A. S., Miesch, M. S., & Toomre, J. 2004, *ApJ*, 614, 1073
- Brun, A. S. & Zahn, J. P. 2006, *A&A*, 457, 665
- Cao, T.-j., Xu, A.-a., & Tang, Y.-h. 1980, *Chinese Astronomy*, 4, 143
- Carlsson, M. & Leenaarts, J. 2012, *A&A*, 539, A39
- Carmichael, H. 1964, in *NASA Special Publication*, Vol. 50, 451
- Carrington, R. C. 1859, *MNRAS*, 20, 13
- Chen, F., Rempel, M., & Fan, Y. 2023, *ApJ*, 950, L3
- Cheng, X., Priest, E. R., Li, H. T., et al. 2023, *Nature Communications*, 14, 2107
- Cheung, M. C. M., De Pontieu, B., Martínez-Sykora, J., et al. 2019a, *ApJ*, 882, 13

- Cheung, M. C. M., Martínez-Sykora, J., Testa, P., et al. 2022, *ApJ*, 926, 53
- Cheung, M. C. M., Rempel, M., Chintzoglou, G., et al. 2019b, *Nature Astronomy*, 3, 160
- Chitta, L. P., Peter, H., Young, P. R., & Huang, Y. M. 2017, *A&A*, 605, A49
- Christe, S., Krucker, S., Glesener, L., et al. 2017, arXiv e-prints, arXiv:1701.00792
- Comisso, L. & Asenjo, F. A. 2014, *Phys. Rev. Lett.*, 113, 045001
- Culhane, J. L., Harra, L. K., James, A. M., et al. 2007, *Sol. Phys.*, 243, 19
- Danilovic, S. 2017, *A&A*, 601, A122
- Dara, H. C., Alissandrakis, C. E., Zachariadis, T. G., & Georgakilas, A. A. 1997, *A&A*, 322, 653
- Daughton, W., Roytershteyn, V., Karimabadi, H., et al. 2011, *Nature Physics*, 7, 539
- De Pontieu, B., Martínez-Sykora, J., Testa, P., et al. 2020, *ApJ*, 888, 3
- De Pontieu, B., Testa, P., Martínez-Sykora, J., et al. 2022, *ApJ*, 926, 52
- De Pontieu, B., Title, A. M., Lemen, J. R., et al. 2014, *Sol. Phys.*, 289, 2733
- Dere, K. P., Del Zanna, G., Young, P. R., & Landi, E. 2023, *ApJS*, 268, 52
- Edlén, B. 1943, *ZAp*, 22, 30
- Ellerman, F. 1917, *ApJ*, 46, 298
- Ellison, M. A. 1942, *MNRAS*, 102, 22
- Faurobert, M. & Ricort, G. 2021, *A&A*, 651, A21
- Felipe, T., Khomenko, E., & Collados, M. 2010, *ApJ*, 719, 357
- Furth, H. P., Killeen, J., & Rosenbluth, M. N. 1963, *Physics of Fluids*, 6, 459
- Gabriel, A. H. & Mason, H. E. 1982, in *Applied Atomic Collision Physics, Volume 1: Atmospheric Physics and Chemistry*, Vol. 1, 346
- Galsgaard, K., Madjarska, M. S., Moreno-Insertis, F., Huang, Z., & Wiegmann, T. 2017, *A&A*, 606, A46
- García Marirrodriga, C., Pacros, A., Strandmoe, S., et al. 2021, *A&A*, 646, A121
- Golding, T. P., Leenaarts, J., & Carlsson, M. 2016, *ApJ*, 817, 125
- Golub, L., DeLuca, E., Austin, G., et al. 2007, *Sol. Phys.*, 243, 63

- Gou, T., Liu, R., Kliem, B., Wang, Y., & Veronig, A. M. 2019, *Science Advances*, 5, 7004
- Grottrian, W. 1939, *Naturwissenschaften*, 27, 214
- Gudiksen, B. V., Carlsson, M., Hansteen, V. H., et al. 2011, *A&A*, 531, A154
- Guo, L. J., De Pontieu, B., Huang, Y. M., Peter, H., & Bhattacharjee, A. 2020, *ApJ*, 901, 148
- Hansteen, V., Ortiz, A., Archontis, V., et al. 2019, *A&A*, 626, A33
- Hansteen, V. H., Archontis, V., Pereira, T. M. D., et al. 2017, *ApJ*, 839, 22
- Hayek, W., Asplund, M., Carlsson, M., et al. 2010, *A&A*, 517, A49
- Heyvaerts, J. & Priest, E. R. 1984, *A&A*, 137, 63
- Heyvaerts, J., Priest, E. R., & Rust, D. M. 1977, *ApJ*, 216, 123
- Hirayama, T. 1974, *Sol. Phys.*, 34, 323
- Hollweg, J. V. 1984, *ApJ*, 277, 392
- Huang, Y.-M. & Bhattacharjee, A. 2010, *Physics of Plasmas*, 17, 062104
- Hyman, J. M. 1979, in *Advances in Computer Methods for Partial Differential Equations - III*, 313–321
- Innes, D. E. & Tóth, G. 1999, *Sol. Phys.*, 185, 127
- Keppens, R., Meliani, Z., van Marle, A. J., et al. 2012, *Journal of Computational Physics*, 231, 718
- Kirshner, R. P. & Noyes, R. W. 1971, *Sol. Phys.*, 20, 428
- Kiselman, D., Pereira, T. M. D., Gustafsson, B., et al. 2011, *A&A*, 535, A14
- Kopp, R. A. & Pneuman, G. W. 1976, *Sol. Phys.*, 50, 85
- Kosugi, T., Matsuzaki, K., Sakao, T., et al. 2007, *Sol. Phys.*, 243, 3
- Kumar, P., Karpen, J. T., Antiochos, S. K., Wyper, P. F., & DeVore, C. R. 2019, *ApJ*, 885, L15
- Kurokawa, H., Kawaguchi, I., Funakoshi, Y., & Nakai, Y. 1982, *Sol. Phys.*, 79, 77
- Leenaarts, J., Carlsson, M., Hansteen, V., & Gudiksen, B. V. 2011, *A&A*, 530, A124
- Lemen, J. R., Title, A. M., Akin, D. J., et al. 2012, *Sol. Phys.*, 275, 17
- Liu, M., Ni, L., Cheng, G.-C., Ziegler, U., & Lin, J. 2023, *Research in Astronomy and Astrophysics*, 23, 035006

- Long, D. M. 2012, PhD thesis, University of Dublin Trinity College, Ireland
- Loureiro, N. F., Schekochihin, A. A., & Cowley, S. C. 2007, *Physics of Plasmas*, 14, 100703
- Lu, L., Feng, L., Warmuth, A., et al. 2022, *ApJ*, 924, L7
- MacTaggart, D. & Fletcher, L. 2019, *MNRAS*, 486, L96
- Madjarska, M. S. 2019, *Living Reviews in Solar Physics*, 16, 2
- Martínez-Sykora, J., De Pontieu, B., Carlsson, M., et al. 2017, *ApJ*, 847, 36
- Martínez-Sykora, J., De Pontieu, B., & Hansteen, V. 2012, *ApJ*, 753, 161
- Masson, S., Pariat, E., Aulanier, G., & Schrijver, C. J. 2009, *ApJ*, 700, 559
- Matsumoto, R., Machida, M., & Nakamura, K. 2004, *Progress of Theoretical Physics Supplement*, 155, 124
- McMath, R. R. & Pettit, E. 1937, *ApJ*, 85, 279
- Mondal, S., Srivastava, A. K., Pontin, D. I., Yuan, D., & Priest, E. R. 2024, arXiv e-prints, arXiv:2401.07048
- Morton, R. J., Verth, G., Jess, D. B., et al. 2012, *Nature Communications*, 3, 1315
- Newton, H. W. 1942, *MNRAS*, 102, 2
- Ni, L., Chen, Y., Peter, H., Tian, H., & Lin, J. 2021, *A&A*, 646, A88
- Ni, L., Cheng, G., & Lin, J. 2022, *A&A*, 665, A116
- Ni, L., Zhang, Q.-M., Murphy, N. A., & Lin, J. 2017, *ApJ*, 841, 27
- Nishizuka, N., Takasaki, H., Asai, A., & Shibata, K. 2010, *ApJ*, 711, 1062
- Nóbrega-Siverio, D., Martínez-Sykora, J., Moreno-Insertis, F., & Carlsson, M. 2020a, *A&A*, 638, A79
- Nóbrega-Siverio, D., Martínez-Sykora, J., Moreno-Insertis, F., & Rouppe van der Voort, L. 2017, *ApJ*, 850, 153
- Nóbrega-Siverio, D. & Moreno-Insertis, F. 2022, *ApJ*, 935, L21
- Nóbrega-Siverio, D., Moreno-Insertis, F., Galsgaard, K., et al. 2023, *ApJ*, 958, L38
- Nóbrega-Siverio, D., Moreno-Insertis, F., & Martínez-Sykora, J. 2016, *ApJ*, 822, 18
- Nóbrega-Siverio, D., Moreno-Insertis, F., Martínez-Sykora, J., Carlsson, M., & Szydlarski, M. 2020b, *A&A*, 633, A66
- Nordlund, Å. & Galsgaard, K. 1995, A 3D MHD Code for Parallel Computers

- Ogawara, Y., Takano, T., Kato, T., et al. 1991, *Sol. Phys.*, 136, 1
- Olluri, K., Gudiksen, B. V., Hansteen, V. H., & De Pontieu, B. 2015, *ApJ*, 802, 5
- Ortiz, A., Hansteen, V. H., Nóbrega-Siverio, D., & Rouppe van der Voort, L. 2020, *A&A*, 633, A58
- Osterbrock, D. E. 1961, *ApJ*, 134, 347
- Parker, E. N. 1957, *J. Geophys. Res.*, 62, 509
- Parker, E. N. 1988, *ApJ*, 330, 474
- Pesnell, W. D., Thompson, B. J., & Chamberlin, P. C. 2012, *Sol. Phys.*, 275, 3
- Peter, H., Huang, Y. M., Chitta, L. P., & Young, P. R. 2019, *A&A*, 628, A8
- Peter, H., Tian, H., Curdt, W., et al. 2014, *Science*, 346, 1255726
- Petschek, H. E. 1964, *Magnetic Field Annihilation*, Vol. 50, 425
- Porth, O., Xia, C., Hendrix, T., Moschou, S. P., & Keppens, R. 2014, *ApJS*, 214, 4
- Priest, E. 2014, *Magnetohydrodynamics of the Sun*
- Priest, E. R., Chitta, L. P., & Syntelis, P. 2018, *ApJ*, 862, L24
- Przybylski, D., Cameron, R., Solanki, S. K., et al. 2022, *A&A*, 664, A91
- Pucci, F. & Velli, M. 2014, *ApJ*, 780, L19
- Quintero Noda, C., Schlichenmaier, R., Bellot Rubio, L. R., et al. 2022, *A&A*, 666, A21
- Rempel, M. 2014, *ApJ*, 789, 132
- Rempel, M., Chintzoglou, G., Cheung, M. C. M., Fan, Y., & Kleint, L. 2023, *ApJ*, 955, 105
- Rempel, M., Schüssler, M., & Knölker, M. 2009, *ApJ*, 691, 640
- Rimmele, T. R., Warner, M., Keil, S. L., et al. 2020, *Sol. Phys.*, 295, 172
- Robinson, R. A., Aulanier, G., & Carlsson, M. 2023, *A&A*, 673, A79
- Rochus, P., Auchère, F., Berghmans, D., et al. 2020, *A&A*, 642, A8
- Rouppe van der Voort, L., De Pontieu, B., Scharmer, G. B., et al. 2017, *ApJ*, 851, L6
- Rouppe van der Voort, L. H. M., van Noort, M., & de la Cruz Rodríguez, J. 2023, *A&A*, 673, A11

- Roussev, I., Galsgaard, K., & Judge, P. G. 2002, *A&A*, 382, 639
- Roy, J. R. 1973, *Sol. Phys.*, 32, 139
- Sato, T. & Hayashi, T. 1979, *Physics of Fluids*, 22, 1189
- Scharmer, G. 2017, in *SOLARNET IV: The Physics of the Sun from the Interior to the Outer Atmosphere*, 85
- Scharmer, G. B., Bjelksjo, K., Korhonen, T. K., Lindberg, B., & Petterson, B. 2003a, in *Society of Photo-Optical Instrumentation Engineers (SPIE) Conference Series*, Vol. 4853, *Innovative Telescopes and Instrumentation for Solar Astrophysics*, ed. S. L. Keil & S. V. Avakyan, 341–350
- Scharmer, G. B., Dettori, P. M., Lofdahl, M. G., & Shand, M. 2003b, in *Society of Photo-Optical Instrumentation Engineers (SPIE) Conference Series*, Vol. 4853, *Innovative Telescopes and Instrumentation for Solar Astrophysics*, ed. S. L. Keil & S. V. Avakyan, 370–380
- Scharmer, G. B., Narayan, G., Hillberg, T., et al. 2008, *ApJ*, 689, L69
- Schatzman, E. 1949, *Annales d’Astrophysique*, 12, 203
- Scherrer, P. H., Schou, J., Bush, R. I., et al. 2012, *Sol. Phys.*, 275, 207
- Schmieder, B., Mein, P., Martres, M. J., & Tandberg-Hanssen, E. 1984, *Sol. Phys.*, 94, 133
- Schou, J., Antia, H. M., Basu, S., et al. 1998, *ApJ*, 505, 390
- Schou, J., Scherrer, P. H., Bush, R. I., et al. 2012, *Sol. Phys.*, 275, 229
- Sen, S., Jenkins, J., & Keppens, R. 2023, *A&A*, 678, A132
- Sen, S. & Keppens, R. 2022, *A&A*, 666, A28
- Shahraki Pour, M. & Hosseinpour, M. 2022, *Frontiers in Astronomy and Space Sciences*, 8, 237
- Shibata, K., Ishido, Y., Acton, L. W., et al. 1992a, *PASJ*, 44, L173
- Shibata, K., Nozawa, S., & Matsumoto, R. 1992b, *PASJ*, 44, 265
- Shibata, K., Nozawa, S., & Matsumoto, R. 1993, in *Astronomical Society of the Pacific Conference Series*, Vol. 46, *IAU Colloq. 141: The Magnetic and Velocity Fields of Solar Active Regions*, ed. H. Zirin, G. Ai, & H. Wang, 500
- Shimojo, M., Hashimoto, S., Shibata, K., et al. 1996, *PASJ*, 48, 123
- SPICE Consortium, Anderson, M., Appourchaux, T., et al. 2020, *A&A*, 642, A14
- Spiegel, E. A. & Zahn, J. P. 1992, *A&A*, 265, 106

- Strugarek, A., Brun, A. S., & Zahn, J. P. 2011, *A&A*, 532, A34
- Sturrock, P. A. 1966, *Nature*, 211, 695
- Suematsu, Y., Shimizu, T., Hara, H., et al. 2021, in *Society of Photo-Optical Instrumentation Engineers (SPIE) Conference Series*, Vol. 11852, *International Conference on Space Optics — ICSO 2020*, ed. B. Cugny, Z. Sodnik, & N. Karafolas, 118523K
- Sweet, P. A. 1958a, in *Electromagnetic Phenomena in Cosmical Physics*, ed. B. Lehnert, Vol. 6, 123
- Sweet, P. A. 1958b, *Il Nuovo Cimento*, 8, 188
- Syntelis, P. & Priest, E. R. 2020, *ApJ*, 891, 52
- Syntelis, P., Priest, E. R., & Chitta, L. P. 2019, *ApJ*, 872, 32
- Takasao, S., Asai, A., Isobe, H., & Shibata, K. 2012, *ApJ*, 745, L6
- Tsuneta, S., Acton, L., Bruner, M., et al. 1991, *Sol. Phys.*, 136, 37
- Tsuneta, S., Ichimoto, K., Katsukawa, Y., et al. 2008, *Sol. Phys.*, 249, 167
- Vaiana, G. S., Cassinelli, J. P., Fabbiano, G., et al. 1981, *ApJ*, 245, 163
- Vaiana, G. S., Davis, J. M., Giacconi, R., et al. 1973a, *ApJ*, 185, L47
- Vaiana, G. S., Krieger, A. S., & Timothy, A. F. 1973b, *Sol. Phys.*, 32, 81
- Vaiana, G. S., Krieger, A. S., Timothy, A. F., & Zombeck, M. 1976, *Ap&SS*, 39, 75
- van der Holst, B., Keppens, R., Meliani, Z., et al. 2012, *MPI-AMRVAC: MPI-Adaptive Mesh Refinement-Versatile Advection Code*, *Astrophysics Source Code Library*, record ascl:1208.014
- Van Noort, M., Rouppe Van Der Voort, L., & Löfdahl, M. G. 2005, *Sol. Phys.*, 228, 191
- Vernazza, J. E., Avrett, E. H., & Loeser, R. 1981, *ApJS*, 45, 635
- Vögler, A., Shelyag, S., Schüssler, M., et al. 2005, *A&A*, 429, 335
- Wedemeyer-Böhm, S., Lagg, A., & Nordlund, Å. 2009, *Space Sci. Rev.*, 144, 317
- Woods, T. N., Eparvier, F. G., Hock, R., et al. 2012, *Sol. Phys.*, 275, 115
- Xia, C., Teunissen, J., El Mellah, I., Chané, E., & Keppens, R. 2018, *ApJS*, 234, 30
- Yan, X., Xue, Z., Jiang, C., et al. 2022, *Nature Communications*, 13, 640
- Yokoyama, T. & Shibata, K. 1994, *ApJ*, 436, L197

Yokoyama, T. & Shibata, K. 1995, *Nature*, 375, 42

Yokoyama, T. & Shibata, K. 1996, *PASJ*, 48, 353

Yokoyama, T. & Shibata, K. 2001, *ApJ*, 549, 1160

Young, P. R., Tian, H., Peter, H., et al. 2018, *Space Sci. Rev.*, 214, 120

Zhang, Q. M., Ji, H. S., & Su, Y. N. 2016, *Sol. Phys.*, 291, 859

Ziegler, U. 2011, *Journal of Computational Physics*, 230, 1035

Papers

Paper I

A comparative study of resistivity models for simulations of magnetic reconnection in the solar atmosphere

Øystein Håvard Færder, Daniel Nóbrega-Siverio, Mats Carlsson

A&A 675, A97 (2023)

DOI: [10.1051/0004-6361/202346447](https://doi.org/10.1051/0004-6361/202346447)

A comparative study of resistivity models for simulations of magnetic reconnection in the solar atmosphere[★]

Ø. H. Færder^{1,2} , D. Nóbrega-Siverio^{3,4,1,2} , and M. Carlsson^{1,2} 

¹ Rosseland Centre of Solar Physics, University of Oslo, PO Box 1029, Blindern 0315, Oslo, Norway
e-mail: o.h.farder@astro.uio.no

² Institute of Theoretical Astrophysics, University of Oslo, PO Box 1029, Blindern 0315, Oslo, Norway

³ Instituto de Astrofísica de Canarias, 38205 La Laguna, Tenerife, Spain

⁴ Universidad de La Laguna, Dept. Astrofísica, 38206 La Laguna, Tenerife, Spain

Received 17 March 2023 / Accepted 18 May 2023

ABSTRACT

Context. Magnetic reconnection is a fundamental mechanism in astrophysics. A common challenge in mimicking this process numerically in particular for the Sun is that the solar electrical resistivity is small compared to the diffusive effects caused by the discrete nature of codes.

Aims. We aim to study different anomalous resistivity models and their respective effects on simulations related to magnetic reconnection in the Sun.

Methods. We used the Bifrost code to perform a 2D numerical reconnection experiment in the corona that is driven by converging opposite polarities at the solar surface. This experiment was run with three different commonly used resistivity models: 1) the hyper-diffusion model originally implemented in Bifrost, 2) a resistivity proportional to the current density, and 3) a resistivity proportional to the square of the electron drift velocity. The study was complemented with a 1D experiment of a Harris current sheet with the same resistivity models.

Results. The 2D experiment shows that the three resistivity models are capable of producing results in satisfactory agreement with each other in terms of the current sheet length, inflow velocity, and Poynting influx. Even though Petschek-like reconnection occurred with the current density-proportional resistivity while the other two cases mainly followed plasmoid-mediated reconnection, the large-scale evolution of thermodynamical quantities such as temperature and density are quite similar between the three cases. For the 1D experiment, some recalibration of the diffusion parameters is needed to obtain comparable results. Specifically the hyper-diffusion and the drift velocity-dependent resistivity model needed only minor adjustments, while the current density-proportional model needed a rescaling of several orders of magnitude.

Conclusions. The Bifrost hyper-diffusion model is as suitable for simulations of magnetic reconnection as other common resistivity models and has the advantage of being applicable to any region in the solar atmosphere without the need for significant recalibration.

Key words. magnetohydrodynamics (MHD) – magnetic reconnection – methods: numerical – Sun: atmosphere – Sun: corona – Sun: magnetic fields

1. Introduction

Magnetic reconnection plays a crucial role in a wide range of phenomena in the Universe. For instance, it sparks high-energetic bursts in the accretion disc around the black hole in active galactic nuclei (Liu et al. 2002), it is the basis of thermonuclear power devices, such as the tokamak (Furth et al. 1973), and it strongly affects space weather (Paschmann et al. 1979). On the Sun in particular, this physical process has been shown through numerical experiments to cause several remarkable solar events, such as Ellerman bombs (EBs) and ultraviolet (UV) bursts (e.g., Hansteen et al. 2017, 2019; Danilovic 2017; Nóbrega-Siverio et al. 2017; Peter et al. 2019; Ni et al. 2021), surges and coronal jets (e.g., Yokoyama & Shibata 1995, 1996; Nishizuka et al. 2008; Pariat et al. 2009; Moreno-Insertis & Galsgaard 2013; Archontis & Hood 2013; Fang et al. 2014; Toriumi et al. 2015; Nóbrega-Siverio et al. 2016; Wyper et al. 2016, 2017; Karpen et al. 2017; Luna & Moreno-Insertis 2021;

Nóbrega-Siverio & Moreno-Insertis 2022), and flares (e.g., Yokoyama & Shibata 2001; Masson et al. 2009; Cheung et al. 2019; Rempel et al. 2023; Chen et al. 2023), to mention some.

Theoretical reconnection models are commonly divided into two types: slow-reconnection and fast-reconnection. The slow-reconnection model developed by Sweet (1958a,b) and Parker (1957) assumes constant diffusivity over the whole reconnection site and predicts exactly one-half of the inflowing magnetic energy to be converted into heat and the other half into kinetic energy. Nonetheless, the Sweet-Parker model is not efficient enough to reproduce the relatively high reconnection rate observed in flares (e.g., Priest 2014, and references therein). The fast-reconnection model developed by Petschek (1964) instead assumes a diffusion layer limited to a small segment of the boundary layer between the opposing magnetic fields with slow-mode shock waves propagating from the diffusion region. Most of the energy conversion in this model takes place at the shocks, and for a specific heat ratio of $\gamma = \frac{5}{3}$, two-fifths of the inflowing magnetic energy is turned into heat and the remaining three-fifths into kinetic energy. This model predicts a reconnection rate that is high enough to reproduce flares. The Sweet-Parker

[★] Movie associated to Fig. 3 is available at <https://www.aanda.org>

model and the Petschek model are both steady-state models that assume that the current sheets are stable and do not break. However, reconnection theory has shown that current sheets tend to undergo different resistive instabilities, such as the tearing instability (Furth et al. 1963), causing plasmoids (magnetic islands) to appear and move along the current-flow lines. As a consequence, the reconnection rate and energy conversion rate may deviate from the values predicted analytically with the Sweet-Parker and the Petschek model, and careful analysis is therefore required when studying non-stationary reconnection through numerical simulations.

Mimicking magnetic reconnection processes from a numerical perspective is challenging due to the complex behaviour of the electrical resistivity, η , which appears in Ohm's law as the ratio of the electric field strength and the current density in the rest frame of the fluid. In the solar atmosphere, this coefficient is commonly derived from kinetic theory of particle collisions and given by Spitzer resistivity (Spitzer 1962). However, under some conditions, such as regions of strong magnetic field gradients, plasma instabilities can affect the dynamics of the charged particles and can cause the resistivity to rise beyond the Spitzer value (Roussev et al. 2002). This effect, known as anomalous resistivity, is also a necessary component to support the theory of dissipation of direct currents (Heyvaerts & Priest 1984) as a significant source of coronal heating because the collisional Spitzer resistivity is too small to dissipate such strong currents (Adamson et al. 2013). In addition, we need to take into account the diffusive effects caused by the discrete nature of numerical codes, which are often significantly greater than those caused by the physical resistivity. Especially in numerical models of the solar atmosphere, regions of large magnetic field gradients require a diffusivity that is much larger than the Spitzer resistivity in order to become numerically resolvable. Because of this, it is common to apply ad hoc terms for anomalous resistivity (Sato & Hayashi 1979; Nordlund & Galsgaard 1995; Roussev et al. 2002; Vögler et al. 2005; Felipe et al. 2010; Adamson et al. 2013; Rempel 2014, 2017; Przybylski et al. 2022) that are set to be large around current sheets in order to dissipate them until they become numerically resolvable, but stay small elsewhere in order to keep the Reynolds and Lundquist numbers relatively high.

For a steady Sweet-Parker- or Petschek-like reconnection model, it is sufficient to use a localised anomalous resistivity model, which means that the resistivity is set to a non-zero value (or to a function of spatial coordinates) in a specific location and zero elsewhere (Innes & Tóth 1999). Non-steady reconnection models with a plasmoid instability can be simulated by using a more adaptive anomalous resistivity model, for instance by enhancing the resistivity when the electron drift velocity or the current density surpass a given threshold value (e.g., Sato & Hayashi 1979), or by applying a fourth-order hyper-diffusive operator consisting of a small global diffusive term and a location-specific diffusion term (e.g., Nordlund & Galsgaard 1995; Gudiksen et al. 2011). However, if the numerical resolution is sufficiently high in areas of strong magnetic field gradients, it is even possible to successfully simulate reconnection with a plasmoid instability without adding any anomalous resistivity terms and only using the actual resistivity in the solar atmosphere (e.g., Ni et al. 2021).

In this paper, three different resistivity models are applied on two numerical experiments for the purpose of analysing their effects on magnetic reconnection. The first experiment mimics a 2D simulation by Syntelis et al. (2019). This enables us to compare our results with already published results that were obtained

using a different numerical code. The second experiment simulates a 1D Harris current sheet. We can therefore study the diffusive effects that the resistivity models have in a simple setup.

The structure of the paper is as follows. Section 2 describes the numerical code and the model equations (Sect. 2.1) we used for our experiments, the resistivity models (Sect. 2.2), and the setup for the numerical experiments (Sect. 2.3). Section 3 gives a detailed analysis of the results for the 2D experiment (Sect. 3.1) and the 1D experiment (Sect. 3.2). Finally, Sect. 4 contains a brief discussion of the key results of our study and summarises the conclusions.

2. Numerical model

The simulations of this paper were performed with the Bifrost code (Gudiksen et al. 2011). Bifrost is a massively parallel 3D code that solves the equations of magnetohydrodynamics (MHD) on a staggered grid using a sixth-order differential operator to discretise the spatial derivatives, supported by fifth-order interpolation operators. For the time-stepping, we chose a third-order method (Hyman 1979). The code is modular and can take various physical ingredients into account depending on the experiment.

2.1. Model equations

The model equations for our experiments are given by

$$\frac{\partial \rho}{\partial t} = -\nabla \cdot (\rho \mathbf{u}), \quad (1)$$

$$\frac{\partial (\rho \mathbf{u})}{\partial t} = -\nabla \cdot (\rho \mathbf{u} \otimes \mathbf{u} - \bar{\tau}) - \nabla P + \mathbf{J} \times \mathbf{B} + \rho \mathbf{g}, \quad (2)$$

$$\frac{\partial \mathbf{B}}{\partial t} = -\nabla \times (-\mathbf{u} \times \mathbf{B} + \bar{\eta} \mathbf{J}), \quad (3)$$

$$\frac{\partial e}{\partial t} = -\nabla \cdot (e \mathbf{u}) - P \nabla \cdot \mathbf{u} + Q_J + Q_V + Q_C, \quad (4)$$

where ρ , \mathbf{u} , e , and \mathbf{B} are the mass density, fluid velocity, internal energy per unit volume, and the magnetic field, respectively. $\bar{\tau}$, P , \mathbf{J} , \mathbf{g} , $\bar{\eta}$, Q_J , Q_V , and Q_C are the viscous stress tensor, gas pressure, electric current density, gravitational acceleration, electrical resistivity tensor, Joule heating, viscous heating, and the Spitzer thermal conductivity term, respectively. Other terms such as non-equilibrium ionisation, ambipolar diffusion, Hall effect, radiative cooling, and optically thin losses are neglected in our experiments. The gravitational term $\rho \mathbf{g}$, with $g = 0.274 \text{ km s}^{-2}$, and the Spitzer thermal conductivity term Q_C are only included in the first experiment of this paper (Sect. 2.3.1).

For the equation-of-state, we used the same equation as Syntelis et al. (2019), that is, an electrically neutral ideal gas with a specific heat ratio of $\gamma = \frac{5}{3}$ and a mean molecular weight of $\mu = 1.2$, where P and e are related to the mass density, ρ , and temperature, T , as follows:

$$P = \frac{\rho k_B T}{\mu m_H}, \quad (5)$$

$$e = \frac{P}{(\gamma - 1)}, \quad (6)$$

where k_B and m_H are the Boltzmann constant and mass of hydrogen, respectively.

2.2. Electrical resistivity models

For the purpose of analysing the effects of the electrical resistivity model on the reconnection in the corona, three different approaches were compared: 1) the default way of handling magnetic resistivity in Bifrost, by means of hyper-diffusion (Gudiksen et al. 2011), hereafter referred to as the Gudiksen-11 model (see Sect. 2.2.1), 2) a resistivity that scales linearly with the current density as was used by Syntelis et al. (2019) for their 2D flux cancellation simulation, which is mimicked in this paper (see Sect. 2.3.1), hereafter referred to as the Syntelis-19 model (see Sect. 2.2.2); and 3) a resistivity that scales quadratically with the electron drift velocity employed by Yokoyama & Shibata (1994) for their simulation of an emerging coronal loop, hereafter referred to as the YS-94 model. Inspired by Sato & Hayashi (1979), the latter resistivity model has been used in several other papers (e.g., Shibata et al. 1992, 1993; Yokoyama & Shibata 1996; Matsumoto et al. 2004).

For later reference, we introduce here the definitions of the Reynolds number, Re , and Lundquist number, S_L ,

$$Re \equiv \frac{|\mathbf{u}|L_B}{\eta}, \quad (7)$$

$$S_L \equiv \frac{v_A L_B}{\eta}, \quad (8)$$

where $L_B \equiv (|\mathbf{J}|/|\mathbf{B}|)^{-1}$ is the characteristic length of the magnetic field, and $v_A \equiv |\mathbf{B}|/\sqrt{\mu_0\rho}$ is the Alfvén speed of the plasma, where μ_0 is the vacuum permeability.

2.2.1. Gudiksen-11 model

Based on the resistivity model developed by Nordlund & Galsgaard (1995), the Gudiksen-11 resistivity consists of two major terms. The first term is an electrical diffusive speed, U_m , with the x_i component defined by

$$U_{m,i} = \nu_1 c_f + \nu_2 |u_i| + \eta_3 \Delta x_i |\nabla_{\perp} u_i|, \quad (9)$$

where ν_1 , ν_2 , and η_3 are scaling factors for the fast-mode wave velocity, bulk velocity, and gradients in the velocity perpendicular to the magnetic field, respectively; and $c_f \equiv \sqrt{c_s^2 + v_A^2}$ is the fast-mode speed, with the sound speed c_s given by $c_s \equiv \sqrt{\gamma P/\rho}$. In our experiments, we set $\nu_1 = 0.03$, $\nu_2 = 0.2$, and $\eta_3 = 0.2$, which are typical values used in Bifrost simulations. In Sect. 3.1.5 we discuss how modifying these free parameters affects the results.

The second term is a positive definite quenching operator defined by

$$\mathbb{Q}_i(g) \equiv \frac{|\Delta_i^2 g|}{|g| + |\Delta_i^2 g|/q_{\max}}, \quad (10)$$

where Δ_i^2 is the second-order difference operator in the x_i -direction, g is the first-order derivative (with respect to any spatial coordinate) of any MHD variable, and q_{\max} is the maximum quenching factor. For any perturbation of the wavenumber k , this term quickly approaches q_{\max} as $k \rightarrow \infty$ and decreases with k^2 as $k \rightarrow 0$, hence ensuring that perturbations with a wavelength of same order as the grid size are heavily damped, while perturbations with wavelengths that are more than one order of magnitude larger than the grid size are only slightly damped. We used $q_{\max} = 8$ because this has been empirically shown to work well when Bifrost was used to solve standard test problems.

Thus, the hyper-diffusive resistivity of Bifrost can be written as a diagonal tensor, $\bar{\eta}_{G11}$, given by

$$\begin{aligned} \eta_{G11,xx} &= \frac{\eta_3}{2} \left[U_{m,y} \Delta y \mathbb{Q}_y \left(\frac{\partial B_z}{\partial y} \right) + U_{m,z} \Delta z \mathbb{Q}_z \left(\frac{\partial B_y}{\partial z} \right) \right], \\ \eta_{G11,yy} &= \frac{\eta_3}{2} \left[U_{m,z} \Delta z \mathbb{Q}_z \left(\frac{\partial B_x}{\partial z} \right) + U_{m,x} \Delta x \mathbb{Q}_x \left(\frac{\partial B_z}{\partial x} \right) \right], \\ \eta_{G11,zz} &= \frac{\eta_3}{2} \left[U_{m,x} \Delta x \mathbb{Q}_x \left(\frac{\partial B_y}{\partial x} \right) + U_{m,y} \Delta y \mathbb{Q}_y \left(\frac{\partial B_x}{\partial y} \right) \right], \\ \eta_{G11,xy} &= \eta_{G11,yx} = \eta_{G11,yz} = \eta_{G11,zy} = \eta_{G11,xz} = \eta_{G11,zx} = 0. \end{aligned} \quad (11)$$

This resistivity model ensures that the resistive terms in the induction and energy equation become significant only in the regions in which the diffusive velocity is high because of the high fast-mode velocity, advective velocity, or strong magnetic shocks along with strong gradients in the magnetic field, which allow the Reynolds number to stay high outside these regions.

2.2.2. Syntelis-19 model

The Syntelis-19 resistivity, η_{S19} , is a scalar function given by

$$\eta_{S19} = \begin{cases} \eta_0, & |\mathbf{J}| < J_{\text{crit}} \\ \eta_0 + \eta_1 |\mathbf{J}|/J_{\text{crit}}, & |\mathbf{J}| \geq J_{\text{crit}} \end{cases} \quad (12)$$

Syntelis et al. (2019) used $\eta_0 = 3.78 \times 10^{-2} \text{ km}^2 \text{ s}^{-1}$, $\eta_1 = 3.78 \times 10^{-1} \text{ km}^2 \text{ s}^{-1}$, and $J_{\text{crit}} = 5.00 \times 10^{-4} \text{ G km}^{-1}$. In our experiments, we instead chose $\eta_1 = 7.56 \text{ km}^2 \text{ s}^{-1}$ in order to obtain approximately the same inflow Alfvén Mach number as when applying the Gudiksen-11 model on the 2D flux cancellation experiment (Sect. 3.1), as well as an average current sheet length similar to that of Syntelis et al. (2019). This change was needed because the MHD solver scheme of Bifrost and the Lare3D code employed by Syntelis et al. (2019) are different. The Lare3D code is a Lagrangian-Eulerian Remap code (Arber et al. 2001).

2.2.3. YS-94 model

The YS-94 resistivity, η_{YS94} , is defined as

$$\eta_{YS94} = \begin{cases} 0, & v_d \leq v_c \\ \min \left(\alpha \left(\frac{v_d}{v_c} - 1 \right)^2, \eta_{\max} \right), & v_d > v_c \end{cases} \quad (13)$$

where $v_d = \frac{J}{n_e e}$ is the electron drift velocity, and v_c , α , and η_{\max} are free parameters. Yokoyama & Shibata (1994) used $v_c \in [4.16 \times 10^{-7}, 8.32 \times 10^{-6}] \text{ km s}^{-1}$, $\alpha \in [0.20, 2000] \text{ km}^2 \text{ s}^{-1}$, and $\eta_{\max} = 2000 \text{ km}^2 \text{ s}^{-1}$ (normalisation units and formulae are extracted from Nozawa et al. 1992 and Yokoyama & Shibata 1996).

In our simulations, we used $v_c = 8.3 \times 10^{-6} \text{ km s}^{-1}$, $\alpha = 4.0 \times 10^{-8} \text{ km}^2 \text{ s}^{-1}$, and $\eta_{\max} = 2000 \text{ km}^2 \text{ s}^{-1}$ in order to obtain a similar inflow Alfvén Mach number in the 2D flux cancellation simulation as when using the other resistivity models. With this, we applied a much lower value of the scaling factor α than Yokoyama & Shibata (1994) used in their study of current sheets located in the convection zone. Our case deals with reconnection in current sheets that are located in the corona, where the density is several orders of magnitude lower. This causes the drift velocity in current sheets to become several orders of magnitude higher. It is therefore logical that a weaker scaling factor between resistivity and drift velocity is needed here. In addition to the resistivity given by Eq. (13), we added a background uniform resistivity of $\eta_0 = 4.00 \times 10^{-2} \text{ km}^2 \text{ s}^{-1}$ when using this model, similar to that of Syntelis-19.

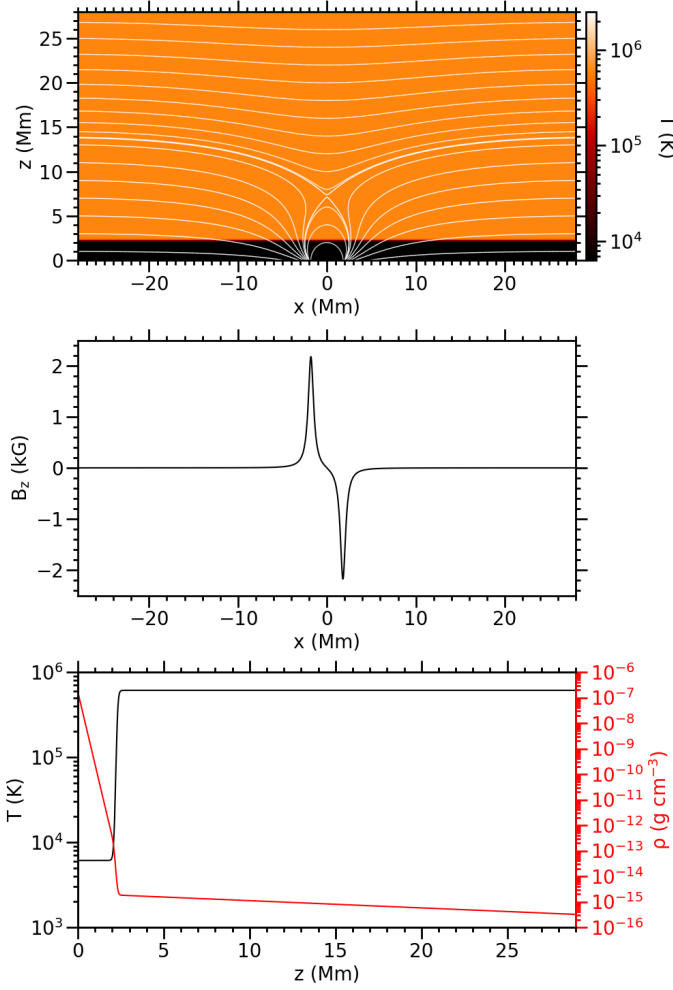


Fig. 1. Initial conditions for the 2D flux cancellation experiment mimicking (Syntelis et al. 2019). Top: map of the temperature with the magnetic field topology superimposed. Middle: vertical component of the magnetic field, B_z , at $z = 0$. Bottom: stratification of the temperature (black) and mass density (red).

2.3. Numerical experiments

2.3.1. 2D flux cancellation experiment

The first experiment mimics the case 1 simulation by Syntelis et al. (2019), in which reconnection is driven by converging opposite polarities at the solar surface, leading to flux cancellation in a 2D atmosphere. The computational domain was given by $x \in [-30, 30]$ Mm and $z \in [0, 30]$ Mm, and it was discretised over 2048×1024 grid points. The initial magnetic field was a superposition of two sources of opposite polarity placed below the photosphere, along with a horizontal uniform background magnetic field. In 2D, the magnetic field strength from one source with a flux of F at a given distance \mathbf{r} is $F/(\pi r)$, with the direction given by unit vector $\hat{\mathbf{r}} = \mathbf{r}/r$. Thus, the initial magnetic field is given by

$$\mathbf{B}(x, z, t = 0) = \frac{F}{\pi} \frac{\mathbf{r}_1}{r_1^2} - \frac{F}{\pi} \frac{\mathbf{r}_2}{r_2^2} - B_0 \hat{\mathbf{x}}, \quad (14)$$

where $F = 2500$ G Mm is the flux of each source, $B_0 = 45$ G is the magnetic field strength of the horizontal background,

and

$$\mathbf{r}_1 = (x + d_s) \hat{\mathbf{x}} + (z - z_0) \hat{\mathbf{z}}, \quad (15)$$

$$\mathbf{r}_2 = (x - d_s) \hat{\mathbf{x}} + (z - z_0) \hat{\mathbf{z}}, \quad (16)$$

where $d_s = 1.8$ Mm is the initial half-separation distance between the sources, and $z_0 = -0.36$ Mm is the height at which the sources are located.

The initial temperature profile of Syntelis et al. (2019), set to mimic the C7 model of Avrett & Loeser (2008), is given by

$$T(x, z, t = 0) = T_{\text{pho}} + \frac{T_{\text{cor}} - T_{\text{pho}}}{2} \left[\tanh\left(\frac{z - z_{\text{cor}}}{w_{\text{tr}}}\right) + 1 \right], \quad (17)$$

with $T_{\text{pho}} = 6109$ K and $T_{\text{cor}} = 0.61$ MK. For the location of the bottom of the corona and the width of the transition region, we used $z_{\text{cor}} = 2.31$ Mm and $w_{\text{tr}} = 0.09$ Mm in our simulations. The initial mass density was found by requiring hydrostatic equilibrium, $\partial P/\partial z = -\rho g$, and a photospheric density of $\rho_{\text{pho}} = 1.67 \times 10^{-7}$ g cm $^{-3}$. With P given by the ideal gas law and T given by Eq. (17), the following analytical solution was found:

$$\rho(x, z, t = 0) = \rho_{\text{pho}} e^{-2\chi_0(z+z_c)} \left(\frac{T_{\text{pho}} + T_{\text{cor}} e^{2z}}{T_{\text{pho}} + T_{\text{cor}} e^{-2z_c}} \right)^{\chi_0 - \chi_1} \frac{T_{\text{pho}}}{T(z)}, \quad (18)$$

where

$$\tilde{z} \equiv \frac{z - z_{\text{cor}}}{w_{\text{tr}}}, \quad \tilde{z}_c \equiv \frac{z_{\text{cor}}}{w_{\text{tr}}}, \quad \chi_0 \equiv \frac{\mu m_{\text{H}} g w_{\text{tr}}}{2 k_{\text{B}} T_{\text{pho}}}, \quad \chi_1 \equiv \frac{\mu m_{\text{H}} g w_{\text{tr}}}{2 k_{\text{B}} T_{\text{cor}}}. \quad (19)$$

Initial magnetic field, temperature, and mass density computed from the above equations are shown in Fig. 1. The figure shows that the initial conditions of Syntelis et al. (2019) have indeed been successfully mimicked.

For the bottom boundary conditions, we used a driving mechanism where the horizontal velocity u_x is defined as

$$u_x(x, z = 0, t) = \begin{cases} v_0(t) & x < 0 \\ 0 & x = 0 \\ -v_0(t) & x > 0 \end{cases}, \quad (20)$$

where

$$v_0(t) = \frac{1}{2} v_{\text{max}} \left[\tanh\left(\frac{t - t_0}{w}\right) + 1 \right], \quad (21)$$

$v_{\text{max}} = 1$ km s $^{-1}$, $t_0 = 10.1$ min, and $w = 1.4$ min; and the magnetic field \mathbf{B} is given by

$$\mathbf{B}(x, z = 0, t) = \frac{F}{\pi} \frac{\mathbf{r}_1(t)}{r_1^2(t)} - \frac{F}{\pi} \frac{\mathbf{r}_2(t)}{r_2^2(t)} - B_0 \hat{\mathbf{x}}, \quad (22)$$

where

$$\mathbf{r}_1(t) = (x + d(t)) \hat{\mathbf{x}} + (z - z_0) \hat{\mathbf{z}}, \quad (23)$$

$$\mathbf{r}_2(t) = (x - d(t)) \hat{\mathbf{x}} + (z - z_0) \hat{\mathbf{z}}, \quad (24)$$

and

$$d(t) = d_s - \left(v_{\text{max}} \frac{w}{2} \left[\ln\left(\cosh\left(\frac{t - t_0}{w}\right)\right) - \ln\left(\cosh\left(\frac{t_0}{w}\right)\right) \right] + \frac{1}{2} v_{\text{max}} t \right). \quad (25)$$

In addition, an absorbing layer was applied on u_x , ρ , and e to ensure that waves hitting the boundaries were not reflected. With respect to the top boundary, we set $u_x = 0$, \mathbf{B} to be line-tied to the flow, and applied an absorbing layer for u_x , ρ , and e .

Because Bifrost is designed to use periodic side-boundaries, we superimposed additional terms to the initial and bottom boundary conditions for \mathbf{B} , Eqs. (14) and (22), which corresponds to magnetic sources located in neighbouring domains identical to our computational domain. This adjustment had a negligible effect on the central parts of the domain, where the reconnection takes place, but it ensured that the field was horizontal and $\nabla \cdot \mathbf{B}$ -free at the periodic side-boundaries. For u_x , ρ , and e , we also applied an absorbing layer, thus keeping a periodic side-boundary.

As an additional note regarding the boundaries, the Syntelis-19 and YS-94 resistivity models in this experiment were applied within $x \in [-28, 28]$ Mm $\wedge z \in [2, 28]$ Mm. The resistivity was set uniformly to η_0 outside these regions to avoid conflicts near the boundary layers.

2.3.2. 1D Harris current sheet

Our second experiment was a 1D Harris current sheet that was set up in a computational domain of $z \in [-2, 2]$ Mm and was discretised over 4096 grid points. To keep this experiment relatively simple, we neglected the gravitational term, $\rho\mathbf{g}$, and the Spitzer thermal conductivity term, Q_C , when solving Eqs. (1)–(4). The initial condition for the magnetic field was

$$\mathbf{B}(z, t = 0) = B_0 \tanh((z - z_0)/w) \hat{\mathbf{x}}. \quad (26)$$

When we assume a uniform total pressure (the sum of gas pressure and magnetic pressure) with a uniform temperature $T(z, t = 0) = T_0$, the initial density is given by

$$\rho(z, t = 0) = \rho_0 + \frac{\mu m_H}{k_B T_0} \frac{B_0^2}{\sqrt{8\pi}} \left(1 - \tanh^2((z - z_0)/w)\right), \quad (27)$$

where ρ_0 is the density far away from the current sheet. In our simulations, we used $T_0 = 0.61$ MK, $\rho_0 = 10^{-15}$ g cm $^{-3}$, and $B_0 = 1$ G (as well as $w = 20$ km and $z_0 = 0$) in order to approximately match the temperature, mass density, and magnetic field strength in the inflow region of the current sheet of the 2D flux cancellation experiment (Sect. 2.3.1). This ensured that the Alfvén velocity and current density in the 1D and 2D experiment were of the same order of magnitude in the regions near the current sheets, which facilitated performing the same comparisons between the same resistivity models in the two experiments.

The boundary condition was handled by applying an absorbing layer for all variables near the two boundaries to ensure that no waves hitting the boundaries were reflected back into the physical domain. The Syntelis-19 and YS-94 resistivities in this experiment were applied within $z \in [-0.5, 0.5]$ Mm and were set uniformly to η_0 elsewhere to avoid conflicts near the boundary layers.

3. Results

3.1. 2D flux cancellation experiment

3.1.1. Overview

The simulation was run for 40 min, and the results show that the large-scale evolution of the main quantities such as the magnetic field, temperature, and density agrees relatively well with the case 1 simulation of Syntelis et al. (2019) for the three resistivity models.

The two sources of opposite magnetic polarity located immediately below the photosphere move towards each other with the

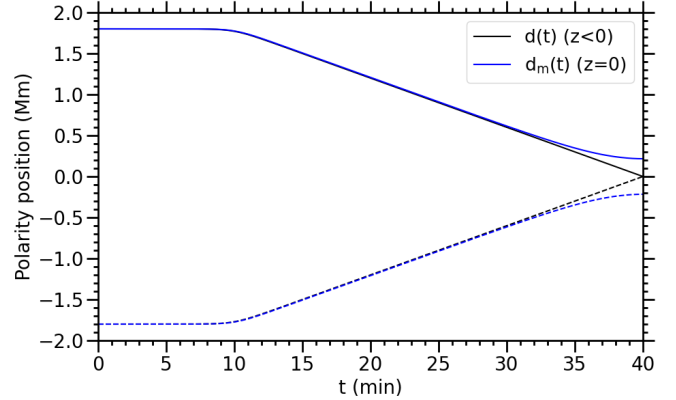


Fig. 2. Evolution of the magnetic polarities in the 2D flux cancellation experiment. The black lines show the horizontal position of each source, given by Eq. (25). The blue lines show the horizontal position of the photospheric polarities, that is, the location along $z = 0$ where B_z reaches its maximum value. The results here are from the simulation with the Gudiksen-11 resistivity model, but nearly identical results are obtained with the other two resistivity models.

driving velocity given by Eq. (21) until they meet at $x = 0$ at $t = 40$ min. Figure 2 shows that the above-lying photospheric polarities do indeed follow the driver very well throughout the simulation time, until they start to slow down after $t = 35$ min, similar to Syntelis et al. (2019).

As a consequence of the motion of the photospheric polarities towards each other, the null-point, initially located 7.6 Mm above the photosphere, is stretched into a vertical current sheet with a length of up to ~ 0.6 Mm. The reconnection site moves slowly downwards along $x = 0$ during the cancellation phase, that is, from $t = 10$ min to $t = 40$ min. Thermal energy from the reconnection is transported outwards from the current sheet along the magnetic field lines and heats up a wide nearly horizontal open reconnection loop above it and a narrow closed reconnection loop below it. The top panels of Fig. 3 show maps of the temperature in the atmosphere at $t = 40$ min for each resistivity model. The magnetic field topology is superimposed. The bottom panels show the corresponding maps of the mass density in the region surrounding the null-point¹. The resistivity models are indeed capable of producing a large-scale atmospheric response that agrees among the models, except for some differences in terms of final null-point height and maximum temperature. The height of the elongated null-point (here defined as the centre of the current sheet) at $t = 40$ min lies at 4.05 Mm above the photosphere in the Syntelis-19 case, 4.0 Mm in the YS-94 case, and 3.85 Mm in the Gudiksen-11 case. The maximum temperature in the heated region at this time is 1.49 MK in the Syntelis-19 case, 1.38 MK in the YS-94 case, and 1.78 MK in the Gudiksen-11 case.

A movie of Fig. 3 is available [online](#). It shows the evolution of the temperature, magnetic field, and density throughout the whole simulation time for the three cases. While all cases eventually have temperature profiles of the same structural shape, despite some differences in terms of maximum temperature and null-point height, the plasma inside the current sheet behaves notably differently in each case. In the Syntelis-19 model, the current sheet moves steadily downwards without any sign of plasmoid generation. In the other two resistivity models, plasmoids are generated rapidly. The current sheet in the YS-94 case

¹ These plots mimic the style of Syntelis et al. (2019) to facilitate comparison.

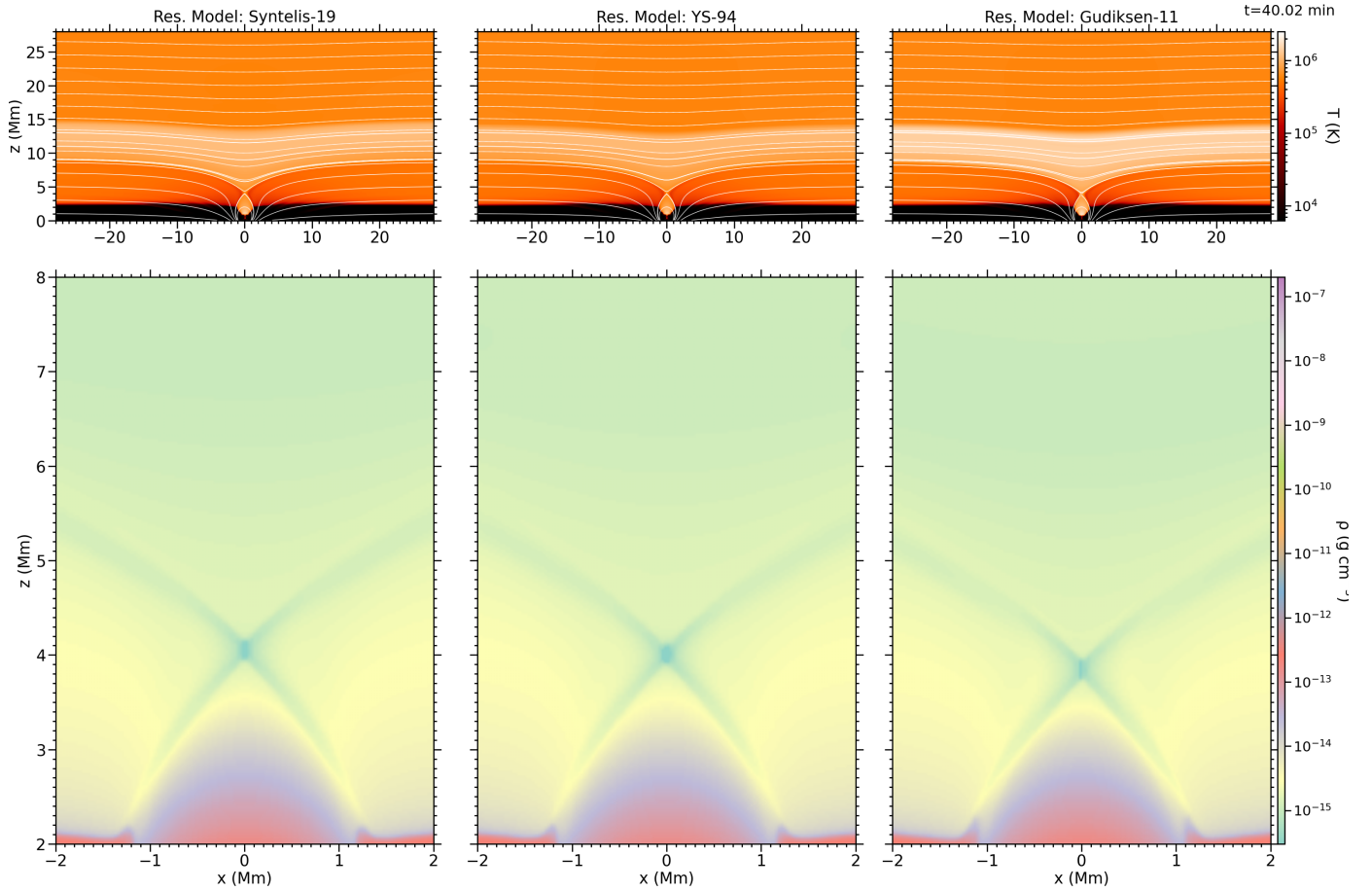


Fig. 3. Atmospheric response in the 2D flux cancellation experiment for the three resistivity models (columns) at $t = 40$ min. Top: maps of the temperature with the magnetic field topology superimposed. Bottom: maps of the mass density around the reconnection site. A movie of the full evolution from $t = 0$ to $t = 40$ min of these maps is available [online](#).

is different from the other two cases by its remarkably lower mass density. In the Gudiksen-11 case, the current sheet coincides with a thin stripe of increased mass density. This is also visible in the Syntelis-19 case, but to a lesser extent.

The Lundquist number at the centre of the current sheet is ~ 5 in the Gudiksen-11 case, ~ 10 in the Syntelis-19 case, and ~ 20 – 100 in the YS-94 case, while the Reynolds number inside the current sheet approaches unity in all three cases (but it is slightly higher in the YS-94 case). At a horizontal distance of 0.1 Mm from the current sheet, the Reynolds and Lundquist numbers are $\sim 10^4$ or higher in all three models. This is as expected because the resistivity models were scaled so that the simulation was able to obtain roughly the same Alfvén velocities in the inflow region. The plasma- β inside the current sheet reaches maximum values (in the top and bottom points of the current sheet) of ~ 2 – 5 in the Gudiksen-11 case, ~ 1 in the Syntelis-19 case, and ~ 0.5 in the YS-94 case. At a distance of 0.1 Mm from the current sheet, $\beta \sim 0.1$ in all three cases.

To demonstrate that the three resistivity models work differently on the current sheet, maps of the resistivity along $x = 0$ as function of height relative to the vertical midpoint of the current sheet and time for each resistivity model are shown in Fig. 4. The dashed lines in each panel mark the top and bottom of the current sheet. The relatively smooth behaviour of the resistivity of the Syntelis-19 model agrees well with the fact that the current sheet in this case evolves steadily without any sign of plasmoid instability. Based on this, it is plausible to expect the

current sheet in this case to follow a Petschek-like reconnection scheme, especially in terms of energy conversion, which is analysed in Sect. 3.1.4. The resistivity of the Gudiksen-11 and YS-94 models, on the other hand, varies more rapidly in its magnitude due to the frequent plasmoid generation, and therefore we expect the energy conversion rates in these cases to deviate more significantly from the Petschek theory. While the Gudiksen-11 and Syntelis-19 resistivities inside the current sheet mostly stay within the range of 100 – $1000 \text{ km}^2 \text{ s}^{-1}$, the YS-94 resistivity has a lower average value that reaches below $100 \text{ km}^2 \text{ s}^{-1}$ within the boundaries of the current sheet. Along with the fact that the diffusive layer is shorter than in the other cases, this explains why the atmosphere in this case has the lowest maximum temperature: the Joule heating scales directly with the resistivity. Although the diffusive layer in the Gudiksen-11 case is of similar size as in the Syntelis-19 case, the average resistivity of the current sheet in the Gudiksen-11 case is slightly higher because the resistivity is enhanced in the plasmoids that appear relatively frequently. This explains why the atmosphere receives the highest amount of heating in the Gudiksen-11 case.

3.1.2. Comparison method

We performed the same comparison between simulations and theory as Syntelis et al. (2019) by locating the current sheet and measuring some inflow values near it and comparing them with values predicted from analytical formulae. To demonstrate the

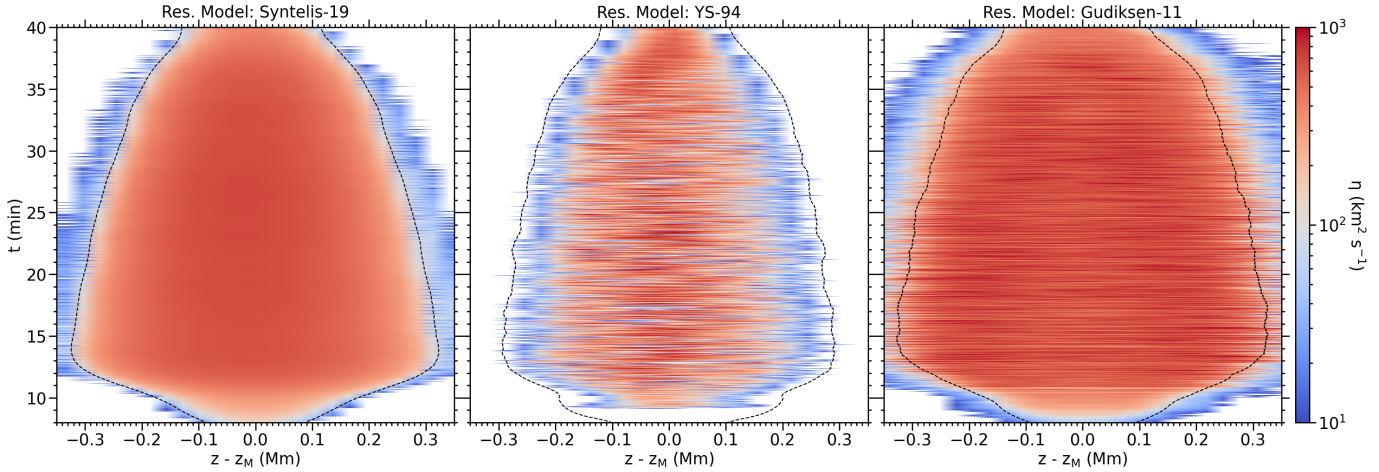


Fig. 4. Evolution of the resistivity η along the current sheet for each resistivity model. The resistivity is measured at $x = 0$ and is shown as function of the height relative to the current sheet midpoint, z_M . The dashed lines mark the top and bottom of the current sheet, which are annotated as S_h and S_l , respectively, in Fig. 5.

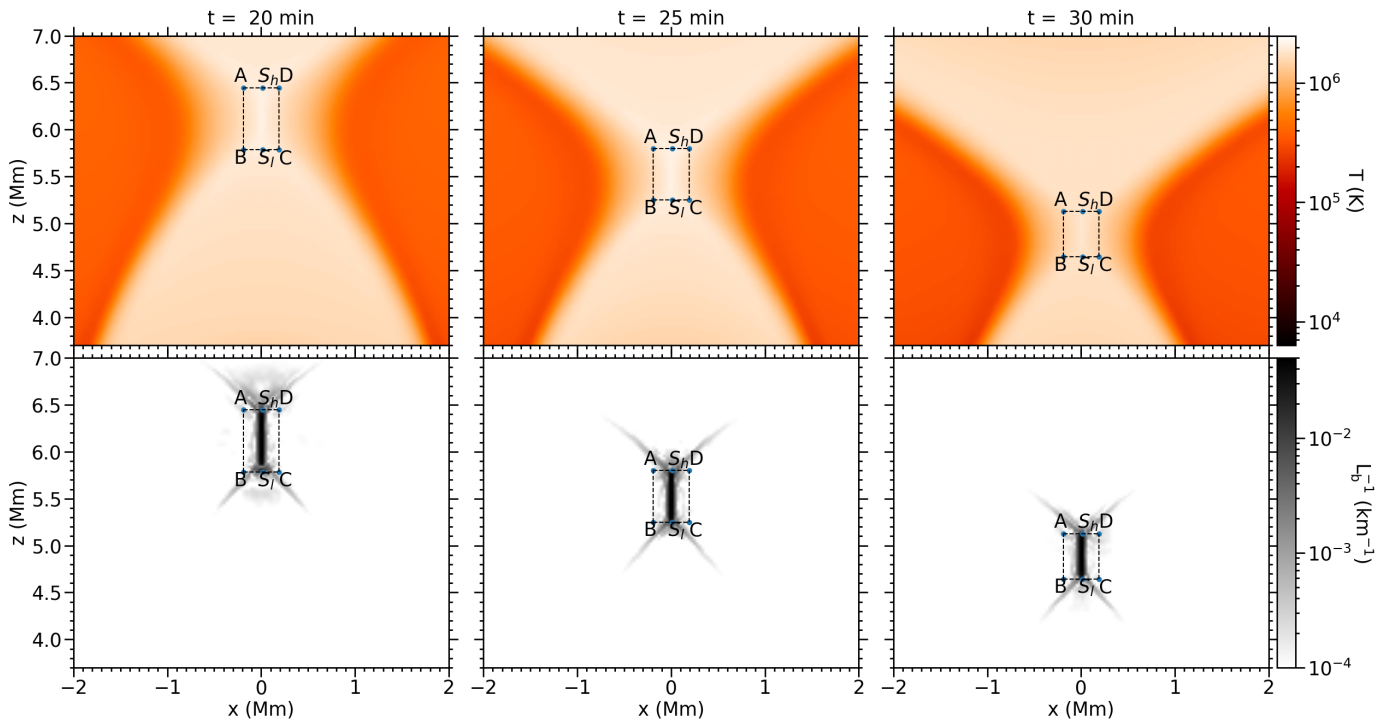


Fig. 5. Evolution of the current sheet in the 2D flux cancellation experiment for the Gudiksen-11 resistivity model at different times (columns). Top: temperature maps zoomed in on the region around the elongated current sheet. Bottom: corresponding maps of the inverse characteristic length L_B^{-1} . The rectangle marks the region around the current sheet, and the inflow parameters are measured at the line segments AB and CD. S_h and S_l are the top and bottom of the current sheet, respectively.

localisation of the current sheet and the regions in which the inflow values are measured, Fig. 5 shows maps of the temperature and inverse characteristic length of the magnetic field, L_B , in the surroundings of the null-point with the inflow region delimited by a rectangle of points A, B, C, and D. We defined the current sheet as the oblong vertical region along $x = 0$ where the characteristic length for magnetic field, L_b , is shorter than a chosen threshold value of 100 km, which is roughly three grid cells because the numerical resolution of the experiments is ~ 30 km. The extremes of the current sheet are indicated in the plots with S_h (top) and S_l (bottom). The corresponding current sheet length L_m is measured as the vertical distance between

these two points. The index m denotes that it is a numerically measured value. This indexation was applied to several numerically measured values in order to distinguish them from their analytical counterparts. Points A, B, C, and D are defined such that the AB and CD segments form vertical lines parallel to the current sheet at 0.2 Mm to the left and right of the current sheet, respectively. The choice of this location of the line segments was made so that the segments lay within the range in which the analytical formulae for the inflow values used by Syntelis et al. (2019) are valid. We found that placing AB and CD at any horizontal distance between 0.1 and 0.2 Mm was suitable. We used 0.2 Mm to also be consistent with the criterion employed by

Syntelis et al. (2019). The figure shows that the inflow rectangle ABCDA does indeed follow the current sheet as it moves downwards throughout the cancellation phase.

The inflow magnetic field strength B_{im} and velocity v_{im} were measured as the mean absolute value of the magnetic field and the velocity, respectively, along the line segments AB and CD. The Poynting influx $\Phi_{S_{im}}$ was measured by integrating the Poynting vector component perpendicular to these line segments, $S_x = [\mathbf{E} \times \mathbf{B}]_x / \mu_0 = E_y B_z / \mu_0$, over AB and CD. The average density along AB and CD, ρ_{im} , was also measured because it is needed in the calculations of the analytical estimate for the Poynting influx.

Knowing the numerical measures B_{im} , v_{im} , L_m , and $\Phi_{S_{im}}$, we compared them with analytical estimates for B_i , v_i , L , and Φ_{S_i} , as derived by Syntelis et al. (2019). The analytical expression for the inflow magnetic field strength B_i is

$$B_i(d, d_0, L) = B_0 \sqrt{\frac{d_0}{d} - 1} \frac{L}{d_0}, \quad (28)$$

where d and d_0 are the source separation distance and the critical source separation distance, respectively. Two different analytical estimates were made for B_i : 1) $B_i(d(t), d_0, L_m)$, based on the source positions with $d(t)$ given by Eq. (25) and $d_0 = \frac{2F_m}{\pi B_0}$; and 2) $B_i(d_m(t), d_{0m}, L_m)$, based on the photospheric polarity positions, where $d_m(t)$ is the half-separation distance between the photospheric polarities, shown as the blue curve in Fig. 2, and $d_{0m} = \frac{2F_m}{\pi B_0}$, where $F_m = 2200 \text{ G Mm}$ is the flux of each photospheric polarity.

The analytical expression for the inflow velocity is

$$v_i(v_0, d_0, L) = f(d, d_0, z_0) v_0 \frac{d_0}{L}, \quad (29)$$

where

$$f(d, d_0, z_0) = 1 - d_0 \frac{z_{\max} - z_0}{(z_{\max} - z_0)^2 + d^2} \frac{1}{\sqrt{d_0/d - 1}} \quad (30)$$

is a flux correction factor, as explained in detail in the appendix of Syntelis et al. (2019), with $z_{\max} = 30 \text{ Mm}$ as the top of the computational domain. The factor was initially $f \approx 0.72$ when $d = 1.8 \text{ Mm}$, then approached 1 as $d \rightarrow 0$. Again, two analytical estimates were made for the inflow velocity: 1) $v_i(v_0(t), d_0, L_m)$, based on the sources, with $v_0(t)$ given by Eq. (21); and 2) $v_i(v_{0m}(t), d_{0m}, L_m)$, based on the photospheric polarities, using $f(d_m, d_{0m}, 0)$, and where $v_{0m}(t) \equiv \dot{d}_m(t)$ is the absolute value of the velocity of the photospheric polarities given by the time derivative of the blue curve in Fig. 2.

The analytical current sheet length is

$$L(M_A, d, d_0, v_0, v_{A0}) = \sqrt{f(d, d_0, z_0)} d_0 \sqrt{\frac{M_{A0}}{M_A} \frac{1}{\sqrt{d_0/d - 1}}}, \quad (31)$$

where M_A is the inflow Alfvén Mach number, and $M_{A0} \equiv v_0/v_{A0}$ is a hybrid Alfvén Mach number based on the hybrid Alfvén speed $v_{A0} \equiv B_0/\sqrt{\mu_0 \rho_i}$, a quantity introduced by Syntelis et al. (2019) which is based on the external magnetic field B_0 but the inflow mass density ρ_i (therefore ‘‘hybrid’’). We estimated 1) $L(M_{Am}, d(t), d_0, v_0(t), v_{A0m})$ based on sources, with $v_{A0m} = B_0/\sqrt{\mu_0 \rho_{im}}$, and 2) $L(M_{Am}, d_m(t), d_{0m}, v_{0m}(t), v_{A0m})$ based on photospheric polarities.

The analytical Poynting influx is

$$\Phi_{S_i}(M_A, d, d_0, v_0, v_{A0}) = 2f^2(d, d_0, z_0) \frac{v_0 B_0^2}{\mu_0} d_0 \sqrt{d_0/d - 1} \frac{M_{A0}}{M_A}, \quad (32)$$

where we estimated 1) $\Phi_{S_i}(M_{Am}, d(t), d_0, v_0(t), v_{A0m})$ based on the sources and 2) $\Phi_{S_i}(M_{Am}, d_m(t), d_{0m}, v_{0m}(t), v_{A0m})$ based on the photospheric polarities.

We also calculated the fractions of the Poynting influx that were converted into kinetic energy and into heat. According to Gauss’ theorem, we have

$$\Phi_{S_i} \equiv \oint_C \frac{1}{\mu_0} \mathbf{E} \times \mathbf{B} \cdot d\mathbf{C} = \int_A \frac{1}{\mu_0} \nabla \cdot (\mathbf{E} \times \mathbf{B}) dA, \quad (33)$$

where C is the curve over the points $ABCD$, and A is its enclosed area. This simply states that the energy increase in the system equals the energy added into it. The above equation can, with the help of vector calculus as well as Faraday’s law, Ohm’s law, and Ampère’s law, be rewritten as

$$|\Phi_{S_i}| \approx \left| \int_A \eta \mathbf{J}^2 dA \right| + \left| \int_A \mathbf{J} \cdot (\mathbf{v} \times \mathbf{B}) dA \right|, \quad (34)$$

which indeed tells us that the input magnetic energy is converted into heat (first right-hand-side term) and kinetic energy (second right-hand-side term) through reconnection. A third right-hand-side term, $\int_A \frac{\partial}{\partial t} \left(\frac{B^2}{2\mu_0} \right)$, was neglected here as Syntelis et al. (2019) did the same (we measured this term in our simulations, and it is indeed small compared to the other right-hand side terms in the above equation). To compare the simulated energy conversion with Petschek (1964) theory, we measured the $\mathbf{J} \cdot (\mathbf{v} \times \mathbf{B})$ term and the Joule heating term integrated over the rectangle A and compared it to three-fifths and two-fifths of the Poynting influx, respectively. For this comparison, we used both the numerical measure $\Phi_{S_{im}}$ and the analytical estimate Φ_{S_i} .

3.1.3. Inflow magnetic field, velocity, and current sheet length

Figure 6 shows the comparison between the numerical results (solid lines) and the analytical estimates based on the dynamics of the sources (dashed curves) and the photospheric polarities (dash-dotted curves) for the inflow magnetic field (top panels), the inflow velocity (middle panels), and the current sheet length (bottom panels). The quantities shown in the figure were averaged over 100 s to obtain smooth lines, which reduced their rapid fluctuations as a consequence of the non-stationary nature of the current sheet.

It is clear from the figure that the numerical measures for B_{im} , v_{im} , and L_m in each model satisfactorily agree with each other and with the analytical estimates, especially those based on the photospheric response (dash-dotted curves), but they are not identical. The current sheet length in the YS-94 case is slightly shorter than in the other cases, which means that it deviates more strongly from the analytical estimate. The current sheet length in the Syntelis-19 case is similar to that of the Gudiksen-11 case in the first 10 min of the cancellation phase, but it then declines faster. The agreement is best in the Gudiksen-11 model for the numerical measure for L_m and the analytical estimate for L based on photospheric polarities. The inflow velocity in the Syntelis-19 case is more or less the same as in the YS-94 case, both numerically and analytically, while the inflow velocity in the Gudiksen-11 case has a lower maximum value, and the numerical measure and the analytical estimate based on photospheric polarities agree better. The inflow magnetic field in the Gudiksen-11 case has a slightly higher maximum field strength than in the other two cases and simulation and theory agree best, while the field strength in the YS-94 case is weakest and simulation and theory deviate most.

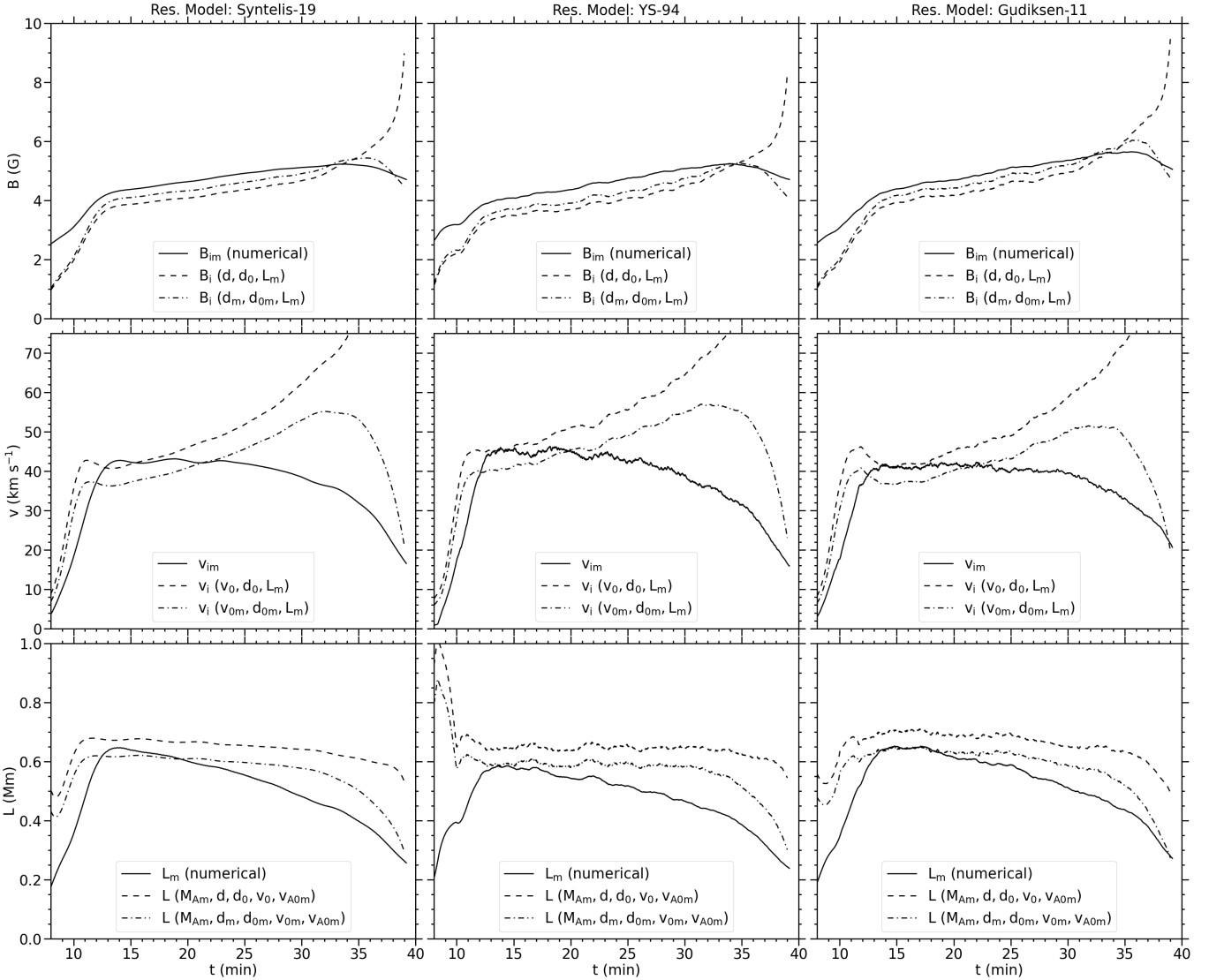


Fig. 6. Evolution of the relevant quantities in the 2D flux cancellation experiment for each resistivity model (columns). Top: inflow magnetic field, both numerical measures (solid curves) and analytical estimates (dashed and dash-dotted curves). Middle: inflow velocity. Bottom: length of the current sheet. The quantities are averaged over 100 s to reduce their rapid fluctuations.

The analytical estimates for L in each model agree very well with each other from $t = 15$ min and throughout the simulations because the Alfvén Mach number, on which the analytical current sheet length is directly dependent, agrees well. We adjusted the input values of the diffusion scaling parameters of each model (η_1 for the Syntelis-19 model, α for the YS-94 model, and η_3 for the Gudiksen-11 model) on purpose in order to obtain this agreement between the analytical estimates. The analytical estimates for B_i and v_i agree less well when comparing the resistivity models because these estimates depend on the numerical measures for L_m , which are slightly different in each case.

3.1.4. Energy release

Figure 7 shows the energy release in the three models. The quantities here are also averaged over 100 s to reduce their rapid fluctuations. The first row shows the numerical measures of the Poynting influx $\Phi_{S_{im}}$ (solid line), and the analytical estimates for Φ_S , based on the source positions (dashed curve) and based

on the photospheric polarity positions (dash-dotted curve). In all three cases, the numerical measures approach the analytical estimate at $t = 13$ min, which is approximately the time at which the current sheet length reaches its maximum value. After this time, the numerical Poynting influx stays constant in each case for the next 15 min, instead of increasing, as analytically predicted, before it slowly decreases. These numerical measures roughly follow the same evolution in all the three cases, however, but they reach a slightly lower maximum value in the YS-94 case, and are roughly of same order of magnitude as the analytical estimates based on photospheric polarities.

The second and third rows show the fraction of the energy that is released through reconnection that is transformed into kinetic energy and thermal energy, respectively, compared to three-fifths and two-fifths, respectively, of the numerical measures and analytical estimates for the Poynting influx. The energy conversion with the Syntelis-19 model is more Petschek-like than with the other two models, with almost exactly three-fifths of the energy input converted into kinetic energy, and slightly less than two-fifths converted into heat. In the

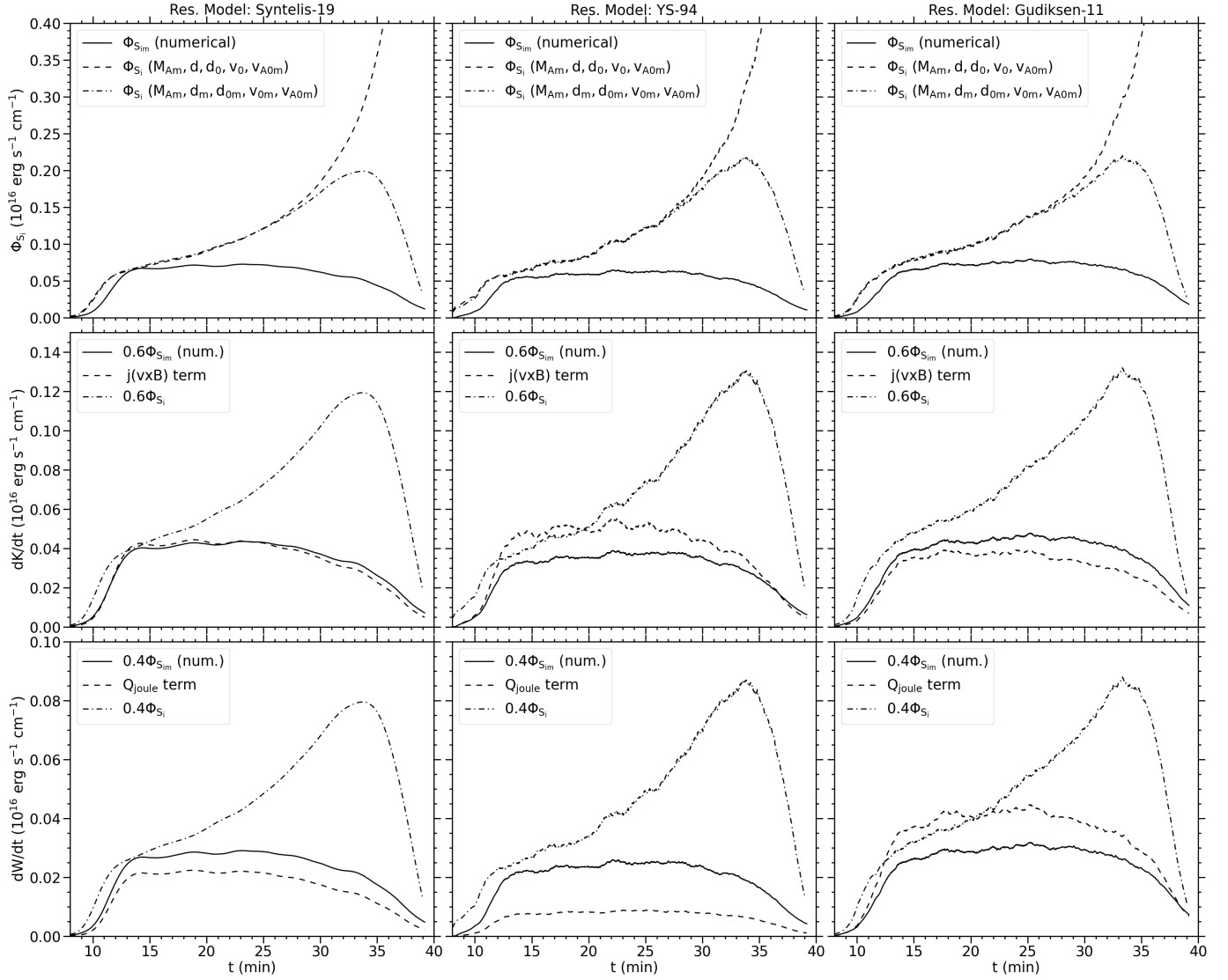


Fig. 7. Evolution of the energy release in the 2D flux cancellation experiment for each resistivity model (columns). Top: poynting influx, both numerical measures (solid curves) and analytical estimates (dashed and dash-dotted curves). Middle: three-fifths of the numerical measure for the released energy (solid lines), compared to the numerical value for the kinetic energy output (dashed curves) and three-fifths of the analytical estimate for the released energy (dash-dotted curves). Bottom: two-fifths of the numerical measure for the released energy (solid lines), compared to the numerical value for the heat output (dashed curves) and two-fifths of the analytical estimate for the released energy (dash-dotted curves). The quantities are averaged over 100 s to reduce their rapid fluctuations.

Gudiksen-11 model, significantly more than two-fifths of the input energy is converted into heat. It gains more heat than the other two models, and therefore, the agreement between the numerically measured and analytically predicted heat output is best. The YS-94 model deviates most from the Petschek theory: less than one-fifth of the energy is converted into heat. This agrees with Fig. 3, in which the Gudiksen-11 case resulted in the warmest atmosphere. The maximum temperature was almost 0.3 MK higher than in the Syntelis-19 case, while the YS-94 model had the coldest atmosphere with a maximum temperature 0.1 MK lower than in the Syntelis-19 case.

The Syntelis-19 case follows a nearly perfect Petschek-like energy conversion. This agrees with the fact that this simulation has nearly no sign of plasmoid generation in the current sheet, as seen in the movie of Fig. 3. This means that this resistivity model allows the current sheet to undergo Petschek reconnection. In the YS-94 and Gudiksen-11 models, the current

sheet undergoes plasmoid-mediated reconnection, which explains why the kinetic and thermal energy released through reconnection is not necessarily equal to three-fifths and two-fifths, respectively, of the input magnetic energy. Still, it is noteworthy that these two cases, while they are plasmoid-mediated, follow completely different energy conversion schemes. While in the Gudiksen-11 case, more of the magnetic energy is converted into heat than predicted with Petschek theory and less into kinetic energy, in the YS-94 case, less magnetic energy is converted into heat and more into kinetic energy. As we described above, this is caused by the significantly stronger diffusive layer in the Gudiksen-11 model than in the YS-94 model, as shown in Fig. 4, where the Gudiksen-11 model clearly has the highest mean resistivity along the centre of the current sheet. The frequency of plasmoids in current sheets as a result of different resistivity models and how this affects the heating of the surrounding plasma will be studied more in detail in an upcoming paper.

3.1.5. Dependence on the choice of diffusion parameters

The results of the above section were obtained by setting the free parameters of the resistivity models to specific values to ensure that the inflow Alfvén speed has roughly the same value in all simulation cases. In this way, we ensured that we solved a very similar physical problem even though we used different numerical approaches. In this section, we study the dependence of the results on an adjustment of these parameters.

For the Gudiksen-11 model (Sect. 2.2.1), we originally used $\nu_1 = 0.03$, $\nu_2 = 0.2$, and $\eta_3 = 0.2$. The parameter ν_1 affects the electrical resistivity as well as the viscous terms, and it scales up all the diffusive terms in the MHD equations over the entire computational domain. Therefore, this parameter should be kept as low as possible. It has been shown empirically that $\nu_1 > 0.02$ is needed to obtain stable solutions in several standard test problems to which Bifrost has been applied for a numerical solution (Gudiksen et al. 2011). We studied different choices for this parameter for the 2D flux cancellation experiment and found that $\nu_1 = 0.03$ is a suitable choice because decreasing ν_1 below this value leads to numerical instability in the current sheet, and increasing it much beyond this value will make the whole problem over-diffused.

Furthermore, it has been shown empirically that $\nu_2 = 0.2$ is about the minimum for numerically stable solutions in several standard test problems (Gudiksen et al. 2011). In our case, the length of the current sheet is only slightly affected when this parameter was decreased below that value. However, running the experiment with a higher value of ν_2 led to a reduction of the current sheet length, and therefore, to a considerable deviation between the numerical measures and analytical estimates shown in Figs. 6 and 7.

The only free parameter of the Gudiksen-11 model that is interesting to adjust for our purposes is η_3 because it directly scales the electrical resistivity and has no effect on the viscosity. We tested running the experiment with different values of η_3 and obtained that values below 0.2 are numerically unstable, while values much higher than 0.2 increase the deviation between the numerical measures and the analytical estimates for the inflow values.

The simulation was also run using different values of η_1 for the Syntelis-19 resistivity model. We found that this parameter can be decreased by an order of magnitude from the value used for the results in the above sections without losing numerical stability. However, this reduction of this diffusion parameter causes the current sheet length to be too long compared to the results of Syntelis et al. (2019), thus deviating more from the analytically predicted current sheet length. A further decrease in η_1 will lead to numerical instability. When we instead increase this parameter by an order of magnitude, the current sheet length is too small compared to the analytical estimate. Decreasing the threshold value J_{crit} has almost the same effect as increasing η_1 .

The results obtained with the YS-94 resistivity model seem to be weakly dependent on the scaling parameters: The current sheet length and Poynting influx barely increase when α is decreased by a factor ten. In addition, there is no significant change in the plasmoid behaviour. Decreasing this parameter further causes numerical instability. When the threshold value v_{crit} is modified, it creates roughly the same effect as adjusting α the opposite way.

For each of the three resistivity models used in this experiment, we observed that the current sheet becomes numerically unstable when the anomalous resistivity is scaled down too strongly. This also shows that the experiment cannot be run

without an anomalous resistivity for the given resolution because the current sheet would not be numerically resolvable, unless we were to use a uniform resistivity that is many orders of magnitude greater than the Spitzer resistivity, leading to very unphysical results, or if we were to increase the resolution by several orders of magnitude, causing the experiment to become expensive in terms of compute resources.

3.2. 1D Harris current sheet

In the previous section, we showed that we could use three different resistivity models in a 2D flux cancellation experiment and obtain relatively consistent results in terms of current sheet length and energy release by adjusting the diffusion parameters of each resistivity model. In this section, we begin to study the effects of applying the same resistivity models and parameters to the 1D Harris current sheet experiment introduced in Sect. 2.3.2.

The results of the experiment for the magnetic field B_x , resistivity η , Joule heating Q_J , and temperature T are shown in the first two columns of Fig. 8 at two selected times: one time close to the beginning (0.25 min), and another time at the moment we stopped the simulation (15 min). Even though we applied the same diffusion parameters that ensured relatively consistent results for the 2D flux cancellation experiment, the results for this 1D Harris sheet vary significantly depending on the resistivity model. At $t = 0.25$ min, the Syntelis-19 model has already had a huge impact in terms of diffusing out the current sheet width and heating up the plasma. The YS-94 model has a significant diffusive effect on the current sheet at $t = 15$ min, but it is still small compared to the Syntelis-19 model. The Gudiksen-11 model has apparently no diffusive effect on the current sheet with the given values for its free parameters. By fitting the B_x profile to a hyperbolic tangent, $\tanh(z/w)$, and finding the width w through the least-squares method, we find that the width of the current sheet, which initially is 20 km, has at $t = 15$ min increased to 217 km with the Syntelis-19 model and to 30 km with the YS-94 model, but it remained at 20 km with the Gudiksen-11 model. The reason is that the resistivity (second row of the figure) in the Syntelis-19 model is highest: it is up to two orders of magnitude higher than in the YS-94 model. At the end of the simulation, in the Syntelis-19 case, its maximum is $\sim 15 \text{ km}^2 \text{ s}^{-1}$, while for the YS-94 model, it is $\sim 0.20 \text{ km}^2 \text{ s}^{-1}$. The resistivity stays $< 0.01 \text{ km}^2 \text{ s}^{-1}$ in the Gudiksen-11 model. As a result of this, the Joule heating, as seen in the third row, has a maximum value more than one order of magnitude higher in the Syntelis-19 case than in the YS-94 case at the early stages of the simulation, and then this difference decreases over time as the magnetic field is diffused and the currents are smaller. Since the resistivity is really low for the Gudiksen-11 case, the associated Joule heating in this case is negligible. Consequently, the temperature profile in the current sheet, which is initially uniform with a value of 0.61 MK, has risen to a maximum value above 1.1 MK in the Syntelis-19 case at $t = 15$ min, but only to 0.69 MK in the YS-94 case. It is unchanged in the Gudiksen-11 case. The large asymmetry seen in the temperature profile for the Syntelis-19 case at $t = 15$ min is due to the tiny asymmetries in the staggered mesh, which are rapidly magnified by the relatively high diffusivity of this resistivity model (with the given values for the diffusion parameters).

For comparison, the third and fourth columns of Fig. 8 show the results after adjusting the scaling parameter of each resistivity model to ensure that they have roughly the same diffusive effect on this 1D Harris sheet. The new values for the adjusted parameters are $\eta_3 = 1.0$ for the Gudiksen-11

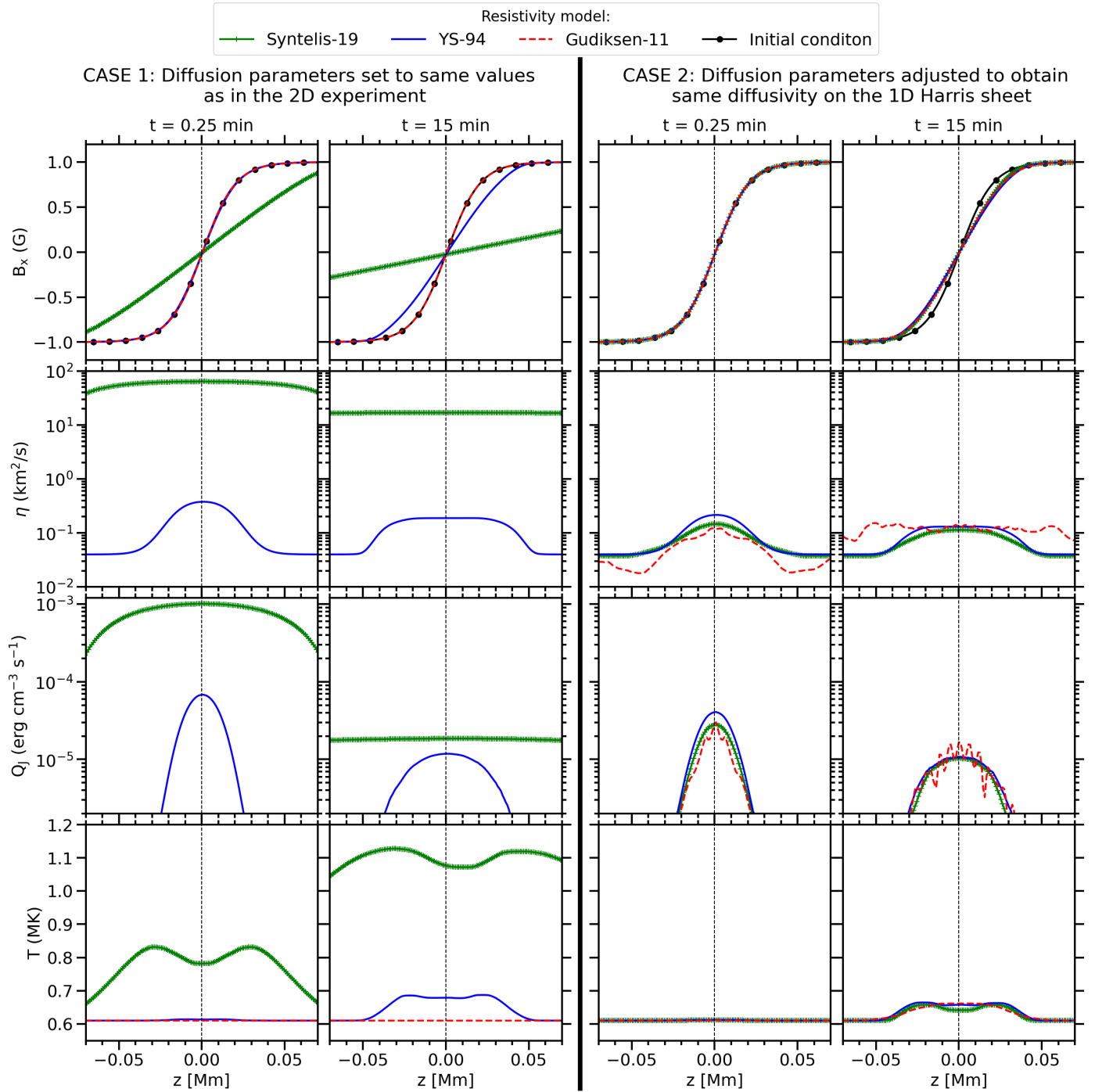


Fig. 8. Evolution of the 1D Harris current sheet. From top to bottom: the magnetic field B_x , the resistivity η , the Joule heating Q_J , and the temperature T are plotted as obtained by using the Syntelis-19 (green), YS-94 (blue), and Gudiksen-11 (red) resistivity models. The first and second columns show the results, measured at different times, setting the diffusion parameters to the same values as used in the 2D experiment. The third and fourth columns show the results obtained after adjusting these diffusion parameters to obtain the same behaviour on this 1D Harris sheet for the three resistivity models.

model, $\eta_1 = 3.78 \times 10^{-3} \text{ km}^2 \text{ s}^{-1}$ for the Syntelis-19 model, and $\alpha = 2.0 \times 10^{-8} \text{ km}^2 \text{ s}^{-1}$ for the YS-94 model. With the adjusted values, all three resistivity models diffuse the current sheet out to a final width of $\sim 26 \text{ Mm}$ at $t = 15 \text{ min}$. The resistivity at the centre of the current sheet lies at slightly above $\sim 0.10 \text{ km}^2 \text{ s}^{-1}$ in all three cases, causing the final Joule heating profiles to be nearly identical and the final maximum temperature to reach about 0.66 MK in all three cases. One noticeable difference is seen in the resistivity

in the regions outside the current sheet, where the magnetic field is nearly constant. The Gudiksen-11 model is nearly an order of magnitude higher than the other two models because the resistivity of this model depends, among other factors, on third derivatives of the magnetic field as well as on the gradients in the velocity perpendicular to the field. This makes it relatively sensitive to tiny perturbations in the current density that are enhanced by the velocity perturbations that arise during the diffusion of the current sheet. However, this enhancement of the resistivity

outside the current sheet does not affect the temperature profile at all because the current density, and hence the Joule heating, is here several orders of magnitude lower than at the centre of the current sheet. Additionally, the Lundquist number in the Gudiksen-11 case is above 10^4 at any distance greater than 0.01 Mm away from the current sheet. This agrees well with the other two resistivity models. This shows indeed that the resistivity outside the current sheet has no effect on the evolution of the plasma.

We have shown that the resistivity models resulted in completely different levels of the diffusive effect when they were applied in this 1D Harris current sheet experiment when the same diffusion parameter values were used that in the 2D flux cancellation experiment gave results that agreed well. We also demonstrated that we can easily adjust the diffusion parameters to obtain roughly the same diffusive behaviour in this relatively simple experiment. The free parameters of the YS-94 and Gudiksen-11 models only needed adjustments within roughly the same order of magnitude to obtain these results, as shown in the second two columns of Fig. 8, but the η_1 value of the Syntelis-19 model needed to be decreased by more than three orders of magnitude. This is due to its direct scaling with the current density, which causes the diffusivity of this resistivity model to be strongly dependent on the magnetic field topology.

4. Discussion

This comparative study of resistivity models has demonstrated that we can use different types of resistivity models in the same numerical experiment and still obtain results that agree relatively well with each other. We successfully mimicked a 2D flux cancellation experiment from Syntelis et al. (2019) and found that using Bifrost's hyper-diffusive resistivity model (Gudiksen et al. 2011, referred to in this paper as Gudiksen-11) results in a current sheet length that more or less follows the same evolution as when using the current density-proportional resistivity model of the original experiment (Syntelis-19), given the right input values for the diffusion parameters. The magnetic field and velocity measured in the inflow region of the current sheet also develop in a similar way when the experiment is performed with each of these two resistivity models. As a result of this, the Poynting influx evolves similarly in both cases. The energy conversion, on the other hand, follows different schemes in each case. While the energy conversion in the Syntelis-19 case agrees with the Petschek theory, the current sheet in the Gudiksen-11 case undergoes plasmoid-mediated reconnection and a significantly higher portion of the magnetic energy is converted into heat. As a result, the maximum temperature is higher in this last case. The drift velocity-dependent resistivity model (YS-94), previously applied by Yokoyama & Shibata (1994), among others, was also applied for the same experiment. The results obtained when using this resistivity model also agree satisfactorily with the results from the other two resistivity models. The current sheet is slightly shorter and the inflow magnetic field is slightly weaker, however, leading to a significantly lower Poynting influx. Despite undergoing plasmoid-mediated reconnection, a lower portion of the input magnetic energy is converted into heat in this case than in the Petschek-conform Syntelis-19 case, in contrast to the Gudiksen-11 case, in which the conversion rate of magnetic energy to heat is higher. Therefore, the heated region has a lower temperature than in the other two cases. Except for the differences in terms of plasmoid generation and energy conversion, the temperature and mass density profiles of all three cases have a similar structural shape.

Furthermore, we observed that when we numerically solved the same model equations for a 1D Harris current sheet, the results in terms of diffusive rates and Joule heating obtained using each of the three resistivity models were significantly different from each other, given the same input values for the diffusion parameters as in the 2D experiment. Running the same experiment with adjusted values for the diffusion parameters showed that two of these resistivity models, namely Gudiksen-11 and YS-94, needed only adjustments within the same order of magnitude for their scaling parameters in order to obtain the same diffusive rate on the Harris sheet. The scaling parameter η_1 in the Syntelis-19 resistivity model, on the other hand, needed to be scaled down by more than three orders of magnitude from its value applied in the 2D experiment in order to obtain the same diffusive rate in this 1D Harris sheet experiment as the other two resistivity models.

One of the free parameters of the resistivity model used by Syntelis et al. (2019) requires an adjustment of several orders of magnitude when jumping between these two experiments because the resistivity scales linearly with the current density. This causes the ideal value for the scaling parameter to be strongly dependent of the magnetic field topology of the experiment when a satisfactory result is to be obtained. Moreover, its linear proportionality to the current density causes the resistivity to stay relatively high in relatively large areas around the current sheet. The Lundquist number therefore increases relatively slowly with distance from the current sheet compared to the other two resistivity models that were tested in this paper. Finally, because η scales with the current density, the anomalous resistivity in regions near to magnetic sources needed to be turned off. This resistivity model works in a satisfactory way for several numerical experiments when the scaling parameter is adjusted properly, however.

We observed that the electron drift velocity-dependent resistivity model that was previously used by Yokoyama & Shibata (1994) might be used to obtain results in both experiments of this paper that agree satisfactorily with the corresponding results obtained with Bifrost's hyper-diffusion model without adjusting the scaling parameter drastically. However, both our experiments dealt with coronal plasma with approximately the same temperature and density as well as similar magnetic field strength. The experiment of Yokoyama & Shibata (1994), on the other hand, which used the same resistivity model to handle current sheets in the upper convection zone, required the scaling parameter to be larger by several orders of magnitude. As the typical electron drift velocity and electron thermal velocity (which typically determines the threshold velocity at which this type of anomalous resistivity is to be activated) differs by several orders of magnitude from the upper convection zone to the upper corona, the ideal values for the free parameters of this resistivity model strongly depend on the local plasma conditions. We were therefore also able to activate the anomalous resistivity of this model only in the coronal region of our 2D experiment (as the scaling parameter was set to handle coronal plasmas) and had to apply a relatively low uniform resistivity below. Despite this, we were fully able to use this resistivity model and obtain results in both our experiments that agreed relatively well with the results obtained with the other two resistivity models, after the free parameters were adjusted properly.

The hyper-diffusive resistivity model of Bifrost (Gudiksen et al. 2011), on the other hand, depends not only on the magnitude of magnetic field gradients, but also on the local fast-mode wave velocity, fluid velocity, and velocity gradients along magnetic field lines. This ensures that the resistivity of this model

becomes large only when it is really needed to be large in order to make current sheets numerically resolvable and stay relatively low elsewhere. With a default set of input values for the diffusion parameters, this resistivity model can be applied on anything from coronal plasmas to convection zone plasmas with any type of magnetic field topology without adjusting the parameters drastically. Therefore, this resistivity model does not need to be turned off and replaced by uniform resistivity in specific areas of the computational domain, but can rather be applied on the whole domain.

It is important to point out that several simplifications were made in this study, which is only a rough representation of driven reconnection in the solar atmosphere. For a more detailed study of the reconnection in the Sun, partially ionised effects such as ambipolar diffusion (Zweibel 1989) and the Hall effect (Huang et al. 2011) cannot be ignored, especially when studying the energy balance in the chromosphere (Wargnier et al. 2023) and the heating mechanisms for EBs (Liu et al. 2023) and UV bursts (Ni et al. 2022). These effects also play a significant role in the structure of the inflow current density (Snow et al. 2018), plasmoid formation (Singh et al. 2019; Murtas et al. 2021), and reconnection-driven slow-mode shocks (Hillier et al. 2016). A detailed study of the reconnection rate in plasmoid-mediated reconnection may be performed with high-resolution simulations of a 2D current sheet (Bhattacharjee et al. 2009). More realistic studies of the turbulent energy cascade that occurs in flux ropes generated along the current sheets where the reconnection takes place can be made through high-resolution 3D MHD simulations (Dong et al. 2022) or particle-in-cell simulations (Daughton et al. 2011). We acknowledge that the details of the reconnection physics cannot be revealed through MHD models with anomalous resistivity, and this is not what we attempted to achieve with our study. With the simplifications and assumptions that were made, however, we achieved the insight that three relatively different anomalous resistivity models can be applied on a well-known physical problem to obtain results that agree relatively well with each other. The main gain in knowledge with the hyper-diffusive resistivity model of Bifrost from the results of our experiments is that it is not that strongly dependent on local plasma conditions and magnetic field topology and can therefore be applied on the whole solar atmosphere as well as to upper convection zone in numerical models without using different values for the free parameters in different areas of the computational domain.

Acknowledgements. This research has been supported by the European Research Council through the Synergy Grant number 810218 (“The Whole Sun”, ERC-2018-SyG) and by the Research Council of Norway through its Centres of Excellence scheme, project number 262622. The simulations were performed on resources provided by Sigma2 – the National Infrastructure for High Performance Computing and Data Storage in Norway. The authors are grateful to the referee for his/her constructive comments to improve the paper.

References

- Adamson, E., Büchner, J., & Otto, A. 2013, *A&A*, **557**, A118
- Arber, T. D., Longbottom, A. W., Gerrard, C. L., & Milne, A. M. 2001, *J. Comput. Phys.*, **171**, 151
- Archontis, V., & Hood, A. W. 2013, *ApJ*, **769**, L21
- Avrett, E. H., & Loeser, R. 2008, *ApJS*, **175**, 229
- Bhattacharjee, A., Huang, Y., Yang, H., & Rogers, B. 2009, in *AGU Fall Meeting Abstracts*, 2009, SM24B-07
- Chen, F., Rempel, M., & Fan, Y. 2023, *ApJ*, **950**, L3
- Cheung, M. C. M., Rempel, M., Chintzoglou, G., et al. 2019, *Nat. Astron.*, **3**, 160
- Danilovic, S. 2017, *A&A*, **601**, A122
- Daughton, W., Roytershteyn, V., Karimabadi, H., et al. 2011, *Nat. Phys.*, **7**, 539
- Dong, C., Wang, L., Huang, Y.-M., et al. 2022, *Sci. Adv.*, **8**, eabn7627
- Fang, F., Fan, Y., & McIntosh, S. W. 2014, *ApJ*, **789**, L19
- Felipe, T., Khomenko, E., & Collados, M. 2010, *ApJ*, **719**, 357
- Furth, H. P., Killeen, J., & Rosenbluth, M. N. 1963, *Phys. Fluids*, **6**, 459
- Furth, H. P., Rutherford, P. H., & Selberg, H. 1973, *Phys. Fluids*, **16**, 1054
- Gudiksen, B. V., Carlsson, M., Hansteen, V. H., et al. 2011, *A&A*, **531**, A154
- Hansteen, V. H., Archontis, V., Pereira, T. M. D., et al. 2017, *ApJ*, **839**, 22
- Hansteen, V., Ortiz, A., Archontis, V., et al. 2019, *A&A*, **626**, A33
- Heyvaerts, J., & Priest, E. R. 1984, *A&A*, **137**, 63
- Hillier, A., Takasao, S., & Nakamura, N. 2016, *A&A*, **591**, A112
- Huang, Y.-M., Bhattacharjee, A., & Sullivan, B. P. 2011, *Phys. Plasmas*, **18**, 072109
- Hyman, J. M. 1979, in *Advances in Computer Methods for Partial Differential Equations - III*, 313
- Innes, D. E., & Tóth, G. 1999, *Sol. Phys.*, **185**, 127
- Karpen, J. T., DeVore, C. R., Antiochos, S. K., & Pariat, E. 2017, *ApJ*, **834**, 62
- Liu, B. F., Mineshige, S., & Shibata, K. 2002, *ApJ*, **572**, L173
- Liu, M., Ni, L., Cheng, G.-C., Ziegler, U., & Lin, J. 2023, *Res. Astron. Astrophys.*, **23**, 035006
- Luna, M., & Moreno-Insertis, F. 2021, *ApJ*, **912**, 75
- Masson, S., Pariat, E., Aulanier, G., & Schrijver, C. J. 2009, *ApJ*, **700**, 559
- Matsumoto, R., Machida, M., & Nakamura, K. 2004, *Prog. Theor. Phys. Suppl.*, **155**, 124
- Moreno-Insertis, F., & Galsgaard, K. 2013, *ApJ*, **771**, 20
- Murtas, G., Hillier, A., & Snow, B. 2021, *Phys. Plasmas*, **28**, 032901
- Ni, L., Chen, Y., Peter, H., Tian, H., & Lin, J. 2021, *A&A*, **646**, A88
- Ni, L., Cheng, G., & Lin, J. 2022, *A&A*, **665**, A116
- Nishizuka, N., Shimizu, M., Nakamura, T., et al. 2008, *ApJ*, **683**, L83
- Nóbrega-Siverio, D., & Moreno-Insertis, F. 2022, *ApJ*, **935**, L21
- Nóbrega-Siverio, D., Moreno-Insertis, F., & Martínez-Sykora, J. 2016, *ApJ*, **822**, 18
- Nóbrega-Siverio, D., Martínez-Sykora, J., Moreno-Insertis, F., & Rouppe van der Voort, L. 2017, *ApJ*, **850**, 153
- Nordlund, Å., & Galsgaard, K. 1995, *A 3D MHD Code for Parallel Computers*, Tech. Rep., Astronomical Observatory, Copenhagen University
- Nozawa, S., Shibata, K., Matsumoto, R., et al. 1992, *ApJS*, **78**, 267
- Pariat, E., Antiochos, S. K., & DeVore, C. R. 2009, *ApJ*, **691**, 61
- Parker, E. N. 1957, *J. Geophys. Res.*, **62**, 509
- Paschmann, G., Papamastorakis, I., Scokpe, N., et al. 1979, *Nature*, **282**, 243
- Peter, H., Huang, Y. M., Chitta, L. P., & Young, P. R. 2019, *A&A*, **628**, A8
- Petschek, H. E. 1964, *Magn. Field Annihilation*, **50**, 425
- Priest, E. 2014, *Magnetohydrodynamics of the Sun* (Cambridge, UK: Cambridge University Press)
- Przybylski, D., Cameron, R., Solanki, S. K., et al. 2022, *A&A*, **664**, A91
- Rempel, M. 2014, *ApJ*, **789**, 132
- Rempel, M. 2017, *ApJ*, **834**, 10
- Rempel, M., Chintzoglou, G., Cheung, M. C. M., Fan, Y., & Kleint, L. 2023, *ApJ*, submitted [arXiv:2303.05299]
- Roussev, I., Galsgaard, K., & Judge, P. G. 2002, *A&A*, **382**, 639
- Sato, T., & Hayashi, T. 1979, *Phys. Fluids*, **22**, 1189
- Shibata, K., Nozawa, S., & Matsumoto, R. 1992, *PASJ*, **44**, 265
- Shibata, K., Nozawa, S., & Matsumoto, R. 1993, *ASP Conf. Ser.*, **46**, 500
- Singh, K. A. P., Sakaue, T., Nakamura, N., et al. 2019, *ApJ*, **884**, 161
- Snow, B., Botha, G. J. J., McLaughlin, J. A., & Hillier, A. 2018, *A&A*, **609**, A100
- Spitzer, L. 1962, *Physics of Fully Ionized Gases* (New York: Interscience)
- Sweet, P. A. 1958a, in *Electromagnetic Phenomena in Cosmical Physics*, ed. B. Lehnert, **6**, 123
- Sweet, P. A. 1958b, *Il Nuovo Cimento*, **8**, 188
- Syntelis, P., Priest, E. R., & Chitta, L. P. 2019, *ApJ*, **872**, 32
- Toriumi, S., Cheung, M. C. M., & Katsukawa, Y. 2015, *ApJ*, **811**, 138
- Vögler, A., Shelyag, S., Schüssler, M., et al. 2005, *A&A*, **429**, 335
- Wargnier, Q. M., Martínez-Sykora, J., Hansteen, V. H., & De Pontieu, B. 2023, *ApJ*, **946**, 115
- Wyper, P. F., DeVore, C. R., Karpen, J. T., & Lynch, B. J. 2016, *ApJ*, **827**, 4
- Wyper, P. F., Antiochos, S. K., & DeVore, C. R. 2017, *Nature*, **544**, 452
- Yokoyama, T., & Shibata, K. 1994, *ApJ*, **436**, L197
- Yokoyama, T., & Shibata, K. 1995, *Nature*, **375**, 42
- Yokoyama, T., & Shibata, K. 1996, *PASJ*, **48**, 353
- Yokoyama, T., & Shibata, K. 2001, *ApJ*, **549**, 1160
- Zweibel, E. G. 1989, *ApJ*, **340**, 550

Paper II

A comparative study of resistivity models for simulations of magnetic reconnection in the solar atmosphere. II. Plasmoid formation

Øystein Håvard Færder, Daniel Nóbrega-Siverio, Mats Carlsson

Forthcoming article in A&A

DOI: 10.1051/0004-6361/202348046

A comparative study of resistivity models for simulations of magnetic reconnection in the solar atmosphere.

II. Plasmoid formation

Ø. H. Færder^{1,2}, D. Nóbrega-Siverio^{3,4,1,2} and M. Carlsson^{1,2}

¹ Rosseland Centre for Solar Physics, University of Oslo, PO Box 1029, Blindern, NO-0315 Oslo, Norway

e-mail: o.h.farder@astro.uio.no

² Institute of Theoretical Astrophysics, University of Oslo, PO Box 1029, Blindern, NO-0315 Oslo, Norway

³ Instituto de Astrofísica de Canarias, E-38205 La Laguna, Tenerife, Spain

⁴ Universidad de La Laguna, Dept. Astrofísica, E-38206 La Laguna, Tenerife, Spain

January 3, 2024

ABSTRACT

Context. Plasmoid-mediated reconnection plays a fundamental role in different solar atmospheric phenomena. Numerical reproduction of this process is therefore essential for developing robust solar models.

Aims. Our goal is to assess plasmoid-mediated reconnection across various numerical resistivity models in order to investigate how plasmoid numbers and reconnection rates depend on the Lundquist number.

Methods. We used the Bifrost code to drive magnetic reconnection in a 2D coronal fan-spine topology, carrying out a parametric study of several experiments with different numerical resolution and resistivity models. We employed three anomalous resistivity models: (1) the original hyper-diffusion from Bifrost, (2) a resistivity proportional to current density, and (3) a resistivity quadratically proportional to electron drift velocity. For comparisons, experiments with uniform resistivity were also run.

Results. Plasmoid-mediated reconnection is obtained in most of the experiments. With uniform resistivity, increasing the resolution reveals higher plasmoid frequency with weaker scaling to the Lundquist number, obtaining 7.9-12 plasmoids per minute for $S_L \in [1.8 \times 10^4, 2.6 \times 10^5]$ with a scaling of $S_L^{0.210}$ in the highest-resolution resistivity cases, transcending into Petschek reconnection in the high- S_L limit (where the diffusive effects of the resistivity become small compared to the non-uniform viscosity) and Sweet-Parker reconnection in the low- S_L limit. Anomalous resistivity leads to similar results even with lower resolution. The drift-velocity-dependent resistivity excellently reproduces Petschek reconnection for any Lundquist number, and similar results are seen with resistivity proportional to current-density though with slightly lower reconnection rates and plasmoid numbers. Among the different resistivity models applied on the given numerical resolution, the hyper-diffusion model reproduced plasmoid characteristics in closest resemblance to those obtained with uniform resistivity at a significantly higher resolution.

Key words. magnetohydrodynamics (MHD) – magnetic reconnection – methods: numerical – Sun: atmosphere – Sun: corona – Sun: magnetic fields

1. Introduction

Magnetic reconnection is a promising candidate as a mechanism for heating up the solar corona (e.g. Vaiana et al. 1973; Heyvaerts & Priest 1984; Parker 1988). In addition, this process has been shown to unleash some of the important phenomena in the solar atmosphere that have been successfully modelled in numerical experiments; these include Ellerman bombs (EBs) and ultraviolet (UV) bursts (e.g. Hansteen et al. 2017, 2019; Danilovic 2017; Nóbrega-Siverio et al. 2017; Peter et al. 2019; Ni et al. 2021), surges and coronal jets (e.g. Yokoyama & Shibata 1995, 1996; Nóbrega-Siverio et al. 2016; Wyper et al. 2016, 2017; Nóbrega-Siverio & Moreno-Insertis 2022), as well as flares (e.g. Yokoyama & Shibata 2001; Rempel et al. 2023).

This fundamental mechanism can either be modelled as steady reconnection or non-steady, plasmoid-mediated reconnection. In the former case, one may analytically predict how the reconnection rate, among other quantities, depends on the Lundquist number $S_L \equiv Lv_{Ai}/\eta$, where L is the length of the current sheet, v_{Ai} the inflow Alfvén speed, and η the resistivity of the medium. In the slow-reconnection model developed by

Sweet (1958a,b) and Parker (1963), where a uniform diffusion layer is assumed to cover the entire current sheet, the reconnection rate is predicted to be equal to $S_L^{-1/2}$. In the fast reconnection model by Petschek (1964), which assumes a Sweet-Parker diffusion layer that covers only a limited segment of the current sheet, the reconnection rate is found to be roughly equal to $\pi/(8 \ln S_L)$.

Non-steady reconnection is characterised by resistive tearing instability (see Furth et al. 1963), where magnetic islands, or plasmoids, appear rapidly along the current sheet. Plasmoid instability occurs when $S_L > 10^4$ (Loureiro et al. 2007), where the current sheet gets intrinsically unstable when its inverse aspect ratio a/L —where a is the current-sheet width—passes below a threshold value of $S_L^{-1/3}$ (Pucci & Velli 2014), which for coronal Lundquist numbers is significantly higher than the Sweet-Parker inverse aspect ratio of $S_L^{-1/2}$. Therefore, Sweet-Parker reconnection is not expected to occur commonly in the upper solar atmosphere, given that any current sheet becomes unstable long before obtaining a Sweet-Parker-like aspect ratio. The Sweet-Parker reconnection rate, given a coronal Lundquist number, is also far too slow to reproduce any flare (see Priest 2014, and ref-

erences therein). Petschek-like reconnection rates have, on the other hand, been successfully reproduced numerically when applying a local enhancement of the resistivity in the current sheet (Yokoyama & Shibata 1994) or a very low, uniform resistivity (Baty et al. 2009), even in the case of non-steady reconnection.

For plasmoid-mediated reconnection in an adiabatic medium, the number of plasmoids has been analytically predicted to scale with the Lundquist number as $S_L^{0.375}$ (Loureiro et al. 2007). For the non-adiabatic case, Sen & Keppens (2022) numerically found the maximum plasmoid number in a 2D Harris current sheet to scale as $S_L^{0.223}$. In both cases, the number of plasmoids increases slowly with the Lundquist number. Plasmoids can therefore be expected to be quite numerous in coronal current sheets due to the relatively high Lundquist number. The presence of plasmoids in EBs, UV bursts, surges, and coronal jets has been shown both observationally (e.g., Rouppe van der Voort et al. 2017, 2023; Kumar et al. 2019) and numerically (Ni et al. 2017; Nóbrega-Siverio et al. 2017; Hansteen et al. 2019; Peter et al. 2019; Guo et al. 2020; Ni et al. 2022; Liu et al. 2023). Numerical studies of plasmoid-mediated reconnection are therefore key to understanding any reconnection event that may occur in the solar atmosphere.

In our previous paper (Færder et al. 2023, hereafter F2023), we compared three different anomalous resistivity models by applying them on a 2D magnetohydrodynamics (MHD) simulation with flux cancellation. There, we found that the models were all capable of reproducing roughly the same large-scale results in terms of current-sheet length and Poynting influx. In the present paper, we analyse the details of the plasmoid instability of these resistivity models during magnetic reconnection at the null-point of a 2D fan-spine topology and compare the results to cases with uniform resistivity. To this end, we perform a parametric study, employing different resistivity magnitudes and resolutions. The structure of the paper is as follows. Section 2 describes the code and model equations used for our simulations, the different resistivity models, and the setup for the numerical experiments. In Section 3, we look into the results of the experiments by measuring and comparing the plasmoid frequency, aspect ratio, and reconnection rate of each simulation case. Finally, in Sect. 4 we briefly discuss our results and summarise our conclusions.

2. Numerical model

2.1. Model equations

The simulations of this paper were performed with the 3D MHD code Bifrost (Gudiksen et al. 2011). This code uses a sixth-order operator for the spatial derivatives and a third-order scheme for the time derivatives, allowing us to minimise the numerical diffusion due to the discretisation of the equations. In particular, we carried out different 2D simulations focusing on magnetic reconnection at coronal heights. We therefore included Joule heating, viscous heating, and Spitzer conductivity, while excluding radiative heating and cooling terms. Regarding the equation of state, we assume a fully singly ionised ideal gas with a mean molecular weight of 0.616. In addition, gravity is neglected as the whole computational domain lies in the corona.

2.2. Resistivity models

To study reconnection, we employed the three anomalous resistivity models described in the F2023 paper, which are summarised below.

2.2.1. Gudiksen-11 model

The Gudiksen-11 model (Gudiksen et al. 2011; Nordlund & Galsgaard 1995) is the default resistivity model of Bifrost. This hyper-diffusive model dynamically scales up the resistivity around gradients in the magnetic field \mathbf{B} and velocity \mathbf{u} and can be written as a diagonal tensor, $\bar{\eta}_{G11}$, given by

$$\begin{aligned}\eta_{G11,xx} &= \frac{\eta_3}{2} \left[U_{m,y} \Delta y Q_y \left(\frac{\partial B_z}{\partial y} \right) + U_{m,z} \Delta z Q_z \left(\frac{\partial B_y}{\partial z} \right) \right], \\ \eta_{G11,yy} &= \frac{\eta_3}{2} \left[U_{m,z} \Delta z Q_z \left(\frac{\partial B_x}{\partial z} \right) + U_{m,x} \Delta x Q_x \left(\frac{\partial B_z}{\partial x} \right) \right], \\ \eta_{G11,zz} &= \frac{\eta_3}{2} \left[U_{m,x} \Delta x Q_x \left(\frac{\partial B_y}{\partial x} \right) + U_{m,y} \Delta y Q_y \left(\frac{\partial B_x}{\partial y} \right) \right], \\ \eta_{G11,xy} &= \eta_{G11,yx} = \eta_{G11,yz} = \eta_{G11,zy} = \eta_{G11,xz} = \eta_{G11,zx} = 0,\end{aligned}\quad (1)$$

where

$$U_{m,i} \equiv v_1 c_f + v_2 |u_i| + \eta_3 \Delta x_i |\nabla_{\perp} u_i|, \quad (2)$$

$$Q_i(g) \equiv \frac{\left| \frac{\partial^2 g}{\partial x_i^2} \right| \Delta x_i^2}{|g| + \frac{1}{q_{\max}} \left| \frac{\partial^2 g}{\partial x_i^2} \right| \Delta x_i^2}, \quad (3)$$

and $c_f \equiv \sqrt{c_s^2 + v_A^2}$, with c_s and v_A denoting the sound speed and Alfvén speed, respectively. v_1 , v_2 , and η_3 are free scaling parameters. For this paper, we varied the input value of η_3 while using fixed $v_1 = 0.03$ and $v_2 = 0.2$, which should be kept as low as possible as discussed in Sect. 3.1.5 of F2023.

2.2.2. Syntelis-19 model

The Syntelis-19 model (Syntelis et al. 2019) applies a scalar resistivity η_{S19} proportional to the current density \mathbf{J} as follows:

$$\eta_{S19} = \begin{cases} \eta_0, & |\mathbf{J}| < J_{\text{crit}} \\ \eta_0 + \eta_1 |\mathbf{J}| / J_{\text{crit}}, & |\mathbf{J}| \geq J_{\text{crit}} \end{cases}, \quad (4)$$

where η_0 , η_1 , and J_{crit} are free parameters. We used $\eta_0 = 3.78 \times 10^{-2} \text{ km}^2 \text{ s}^{-1}$ and $J_{\text{crit}} = 5.00 \times 10^{-4} \text{ G km}^{-1}$ while varying the input value of η_1 .

2.2.3. YS-94 model

In the YS-94 model (Yokoyama & Shibata 1994), the resistivity η_{YS94} scales with the electron drift velocity $v_d = |\mathbf{J}| / (n_e q_e)$, given the electron density n_e and elementary charge q_e , as follows,

$$\eta_{YS94} = \begin{cases} 0, & v_d \leq v_c \\ \min(\alpha (v_d / v_c - 1)^2, \eta_{\max}), & v_d > v_c \end{cases}, \quad (5)$$

where v_c , α , and η_{\max} are free parameters. We used $v_c = 8.3 \times 10^{-6} \text{ km s}^{-1}$ and $\eta_{\max} = 2000 \text{ km}^2 \text{ s}^{-1}$ while varying the input value of α .

2.2.4. Uniform resistivity

In addition to the three aforementioned anomalous resistivity models, we also used uniform resistivity for comparison purposes,

$$\eta_u = \eta_0, \quad (6)$$

with various input values for η_0 .

2.3. Viscosity in Bifrost

While the resistivity $\bar{\eta}$ in our simulations is given by one of the four resistivity models mentioned above, the viscosity tensor $\bar{\tau}$ is always given by Bifrost's in-built description, namely

$$\tau_{ij} = \begin{cases} \rho \Delta x_i U_{v,i} \frac{\partial u_i}{\partial x_i} Q_i \left(\frac{\partial u_i}{\partial x_i} \right), & i = j \\ \rho \left[\Delta x_j U_{v,j} \frac{\partial u_i}{\partial x_j} Q_j \left(\frac{\partial u_i}{\partial x_j} \right) + \Delta x_i U_{v,i} \frac{\partial u_j}{\partial x_i} Q_i \left(\frac{\partial u_j}{\partial x_i} \right) \right], & i \neq j, \end{cases} \quad (7)$$

where

$$U_{v,i} \equiv v_1 c_f + v_2 |u_i| + v_3 \Delta x_i |\nabla u_i|, \quad (8)$$

and v_3 is a free scaling parameter, which is set to 0.3 in our simulations.

2.4. Model setup

For the initial condition, we imposed a 2D fan-spine topology in a similar fashion to Peter et al. (2019) and Nóbrega-Siverio & Moreno-Insertis (2022). In particular, the horizontal and vertical components of the magnetic field are respectively given by

$$B_x = B_1 e^{-kz} \sin(kx), \quad (9)$$

$$B_z = B_0 + B_1 e^{-kz} \cos(kx), \quad (10)$$

where $B_1 = 10$ G, $k = \pi/16$ Mm⁻¹, and $B_0 = 3$ G. The external field B_0 was set to resemble that of a typical quiet-Sun coronal hole (Hofmeister et al. 2019). Panels (a) and (b) of Fig. 1 contain the initial magnetic field topology and $B_z(x, z = 0)$, respectively. These panels show that the imposed field has a negative parasitic polarity in a positive background, which leads to a null-point at $z = 6.13$ Mm. The initial temperature and mass density were uniformly set to $T_0 = 0.61$ MK and $\rho_0 = 3 \times 10^{-16}$ g cm⁻³ to resemble typical values of the lower corona.

Concerning the boundary conditions, the side boundaries were periodic. The top boundary was treated by an absorbing layer on all MHD variables in order to ensure that any wave that hits the boundary is not reflected. At the bottom boundary, an absorbing layer was applied on the mass density ρ , internal energy density e , and the vertical velocity u_z . For the horizontal velocity u_x , a driving condition was imposed to move the inner spine of our fan-spine topology with a velocity up to 1 km s⁻¹. More specifically, u_x is a product of two components, similar to Peter et al. (2019), defined as

$$u_x(x, z = 0, t) = v_d(t)v_0(x). \quad (11)$$

The spatial component $v_0(x)$ is given by

$$v_0(x) = \left(\frac{1 + \cos(\pi(x - L_x)/L_x)}{2} \right)^{10}, \quad (12)$$

where $L_x = 16$ Mm, which is the half-width of the computational domain. The temporal component $v_d(t)$ is as follows

$$v_d(t) = v_p \begin{cases} \sin(0.5\pi t/t_r) & t \in [0, t_r] \\ 1.0 & t \in [t_r, t_d - t_r] \\ \sin(0.5\pi(t_d - t)/t_r) & t \in [t_d - t_r, t_d] \end{cases}, \quad (13)$$

with a peak velocity of $v_p = 1$ km s⁻¹, a ramping time of $t_r = 10$ min, and a total driving time of $t_d = 40$ min. The spatial and temporal components of this driving velocity are shown in panels (c) and (d) of Fig. 1. The magnetic field at the bottom

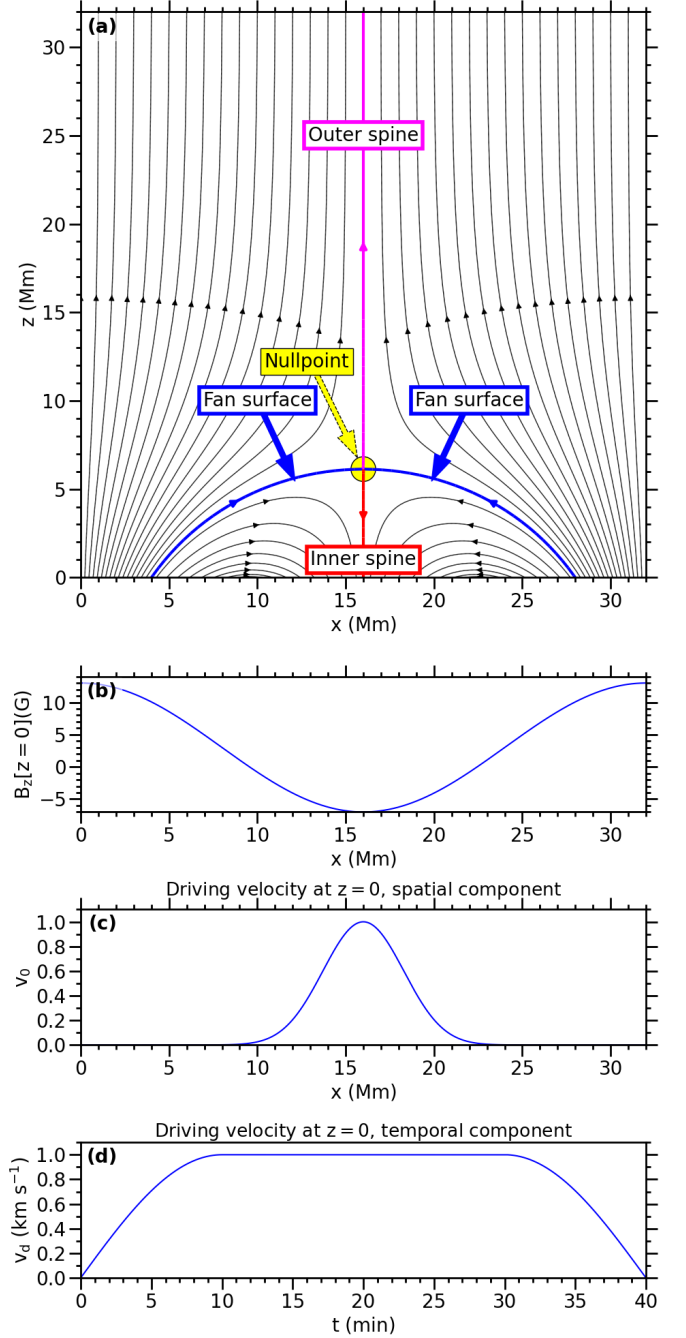


Fig. 1: Model setup. Panel (a) shows the initial magnetic field topology. Panel (b) displays the vertical component of this field measured at $z = 0$. The inner spine of the magnetic field topology is moved in positive x -direction with a driving velocity given by a product of a spatial factor, plotted in panel (c), and a temporal factor, plotted in panel (d).

boundary is line-tied to the flow. This was ensured by setting the magnetic field in the ghost zones to be anti-symmetric around the boundary value. The same anti-symmetric-around-boundary-value condition was applied on u_x in the ghost zones.

The numerical experiments span a 32×32 Mm² physical domain and were run for 40 min. In particular, we performed 44 different simulations grouped as follows: (1) the 2k simulations, that is, 24 cases with a resolution of 2048×2048 grid points, using either uniform, Syntelis-19, YS-94, or Gudiksen-11 resis-

Table 1: Simulations with their respective grid points, resistivity model, and resistivity peak values, η_p ($\text{km}^2 \text{s}^{-1}$).

Group	Resolution	Resistivity model	η_p ($\text{km}^2 \text{s}^{-1}$)
S1-5	2048×2048	Syntelis-19	125, 87.3, 62.4, 42.7, 24.8
Y1-8	2048×2048	YS-94	155, 89.2., 71.7, 57.4, 43.9, 34.2, 26.7, 21.7
G1-7	2048×2048	Gudiksen-11	650, 309, 211, 131, 68.3, 36.1, 19.9
U1-4	2048×2048	Uniform ($\eta = \eta_p$)	75.6, 37.8, 18.9, 15.1
4kU1-9	4096×4096	Uniform ($\eta = \eta_p$)	75.6, 37.8, 18.9, 15.1, 7.56, 3.78, 1.89, 0.945, 0.473
8kU1-11	8192×8192	Uniform ($\eta = \eta_p$)	75.6, 37.8, 18.9, 11.3, 7.56, 3.78, 1.89, 0.945, 0.473, 0.378, 0.189

tivity with various input values for the scaling parameters; (2) the 4k simulations, that is, nine experiments, each with a resolution of 4096×4096 grid points, all using a uniform resistivity with different values of η_0 ; and (3) the 8k simulations, that is, 11 runs with an 8192×8192 resolution, also using a uniform resistivity with different values of η_0 . The details of all the cases are listed in Table 1; models are labelled with a letter, which denotes the chosen resistivity model, and a number that decreases with increasing resistivity. The fourth column displays the peak value η_p , the meaning of which is as follows. For the uniform-resistivity cases, η_p is equal to the uniform value η_0 . For any of the anomalous resistivity cases (S1-5, Y1-8, G1-7), η_p denotes the maximum resistivity in the current sheet averaged over the time period $t \in [15, 35]$ min and is directly proportional to the input value of the scaling parameter of the resistivity model applied in the given case.

In the 2k simulations, the scaling parameter for each resistivity model varied from the minimum required for stability up to 1-2 orders of magnitude above, or to a level that entirely prevents plasmoid formation (resulting in a few cases of steady reconnection). Similar variations were applied in the 4k and 8k simulations. Notably, in these cases, the resistivity could be set considerably lower than in the 2k simulations while maintaining stability. On the other hand, if the resistivity terms are completely removed, the simulations become numerically unstable. This fact indicates that the numerical diffusion due to the discretisation of the equations is negligible with respect to the explicit resistivity terms in the small regions with large gradients or jumps in the variables, as in current sheets.

3. Results

3.1. Overview

In all simulations, the inner spine undergoes a positive x -directional displacement due to the boundary driving velocity. As a consequence, the null-point collapses, leading to a tilted current sheet between the inner and outer spine. Following the behaviour of the driver, the length of the current sheet increases during the first 15 minutes of the simulation; it then remains roughly constant for 20 minutes before finally decreasing during the final 5 minutes of the simulations. At the current sheet, reconnection occurs continuously, significantly heating the plasma. As a representative example, Fig. 2 shows the temperature of the 8kU6 case at $t = 26.7$ min with the magnetic field topology superimposed. An animation of the full time evolution of the map is available online. In all the simulations, the temperature profile has roughly the same shape as shown in the image, albeit with distinct peak temperatures, which range from 0.72 to 0.83 MK.

The differences between the simulations are more evident regarding other physical quantities such as mass density, which is displayed in Fig. 3 at $t = 26.7$ min for six of the 8k cases (see also associated animation). For instance, in case 8kU1, no evident

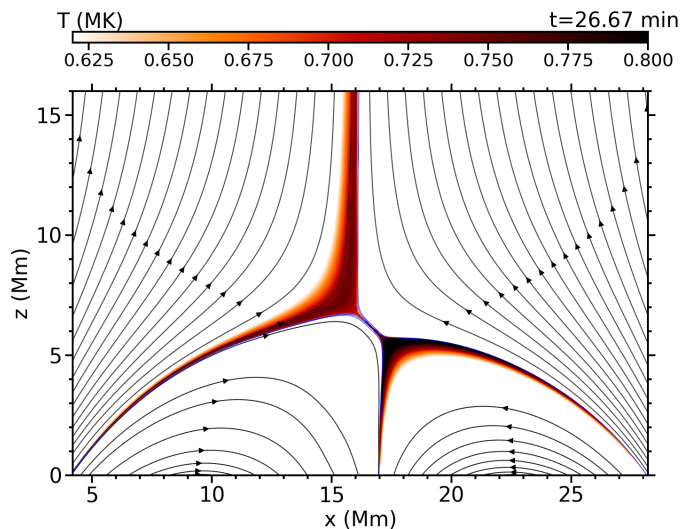


Fig. 2: Temperature and magnetic field topology taken from simulation case 8kU6. A movie of the time evolution of the map for $t \in [0, 40]$ min is available online.

plasmoids are seen, while plasmoids appear frequently in the other cases, moving in either direction along the current sheet. In some cases, several plasmoids merge together, a phenomenon referred to as coalescence instability (Finn & Kaw 1977). In the following, we analyse the characteristics of the reconnection in all simulation cases listed in Table 1.

3.2. Data analysis method

3.2.1. The current sheet

As a first step of our analysis, we define our current sheet as the region with a characteristic length $L_B \equiv (|\mathbf{J}|/|\mathbf{B}|)^{-1} \leq 20$ km, filtering away any cells that belong to the spines and fan surfaces. The $L_B \leq 20$ km threshold ensures that we consider elements with a characteristic length larger than the lowest resolution we have ($\Delta x = \Delta z = 15.6$ km in the 2k cases). As an example, the top panel of Fig. 4 contains a density map within the current sheet in the 8kU6 simulation. The current-sheet axis is found through a linear fit of the cells fulfilling the aforementioned condition, and the current-sheet length, L , is then measured as the distance between its extremes, labelled P_0 and P_1 , as shown in the figure. Having located the current-sheet axis, we define a coordinate system centred at the middle of the current sheet, using the distances along (d_{\parallel}) and perpendicular to the current sheet (d_{\perp}); see Fig. 4 for coordinate axes.

To measure the current-sheet width, we projected the magnetic field onto the coordinate system of the current sheet. Its component parallel to the sheet, B_{\parallel} , has a Harris (1962) current

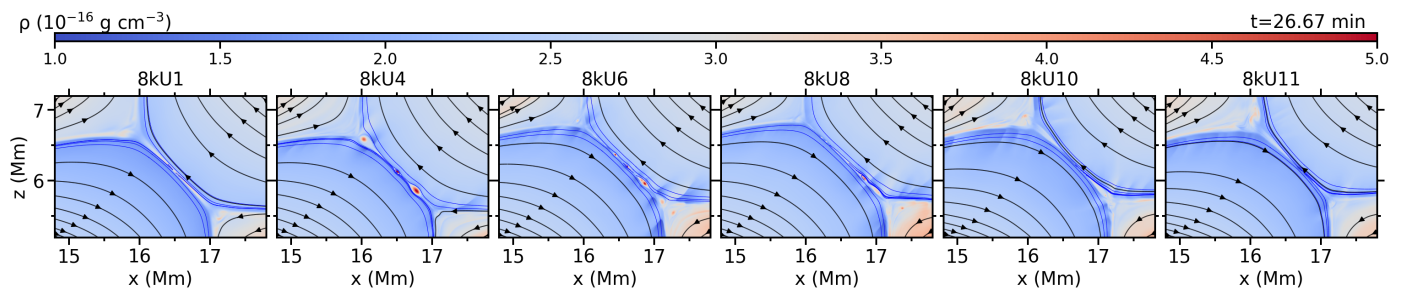


Fig. 3: Mass density and magnetic field topology around the current sheet for six of the 8k simulation cases. A movie of the time evolution of the maps for $t \in [25, 30]$ min is available online to show how plasmoids and shocks originate along the current sheet.

sheet-like profile in its variation with d_{\perp} , having nearly oppositely equal values on each side of the sheet. We therefore found the current-sheet width a by fitting B_{\parallel} with a hyperbolic tangent. Panel (c) of Fig. 4 depicts the method, showing B_{\parallel} (blue curve) at $d_{\parallel} = 0$, and its fit B_{fit} (red curve) as functions of d_{\perp} . The variation of the width along the current sheet is given in Panel (b) (green curve). The large peaks in this curve correspond to plasmoids, as evidenced by the density variations along the current sheet (ρ_{CS}) shown in black in the same panel. In subsequent sections, we use the average width over the whole current sheet \bar{a} to estimate the inverse aspect ratio \bar{a}/L (Sect. 3.4), as well as density variations along the current sheet to measure the frequency of plasmoids (Sect. 3.3).

To illustrate how the different anomalous resistivity models work on the current sheet, Fig. 5 maps the resistivity η_{CS} along the current sheet for three 2k simulation cases (S3, Y4, and G5), which all reach a peak value of around $60 \text{ km}^2 \text{ s}^{-1}$. The resistivity of S3 has a weaker variation along the current sheet than the other two cases here, which is due to the fact that the resistivity of the Syntelis-19 model is only linearly proportional to current density. Therefore, one might expect the results of this resistivity model to lie closer to those of uniform resistivity (for the same resolution). Case G5, on the other hand, shows by far the most variation in the resistivity along the sheet out of these three cases; this is due to the more dynamic behaviour of the Gudiksen-11 model.

3.2.2. The diffusion region

The diffusion region of the reconnection site was defined as the region around the current sheet delimited by $|d_{\parallel}| \leq 0.50L$ and $|d_{\perp}| \leq 60 \text{ km}$, marked by a magenta dashed rectangle in the top panel of Fig 4. We chose to set the diffusion region half-width to 60 km for two reasons: (a) this threshold is slightly bigger than the peak value of the sheet width a measured in the largest plasmoids in our simulation cases, and (b) it ensures that the magnetic Reynolds number $Re \equiv L_B |\mathbf{u}| / \eta$ is always larger than 100 outside this region. Thus, this diffusion region marks the area where the resistivity has a significant effect on the plasma. The mean resistivity of the diffusion region, η_d , is used when estimating the effective Lundquist number.

3.2.3. The inflow regions

The inflow regions of the reconnection site were defined as the areas delimited by $|d_{\parallel}| \leq 0.25L$ and $60 \text{ km} \leq |d_{\perp}| \leq 300 \text{ km}$, marked by green dotted rectangles in the top panel of Fig 4. This threshold ensures that the inflow regions lie just outside the diffusion region (so $Re > 100$), and the Alfvén speed here is more

or less constant with distance from the sheet. The delimitation of $|d_{\parallel}| \leq 0.25L$ is to avoid the areas near the endpoints of the current sheet where the Alfvén speed fluctuates more rapidly.

With this definition, the inflow Alfvén speed v_{Ai} was measured as the mean Alfvén speed within the green dotted rectangles. Similarly, the inflow velocity v_i was measured as the mean absolute value of the velocity u_{\perp} perpendicular to the current sheet within the inflow region. In panels (d) and (e) of Fig. 4, we show both quantities as a function of d_{\perp} . The black curve plots the average values taken over $|d_{\parallel}| \leq 0.25L$, while the blue area shows the ranges within one standard deviation. The estimated (equilibrium) values for the inflow Alfvén speed and the inflow velocity (at a given time and for a given case) is computed as the mean value of these black curves for $0.06 \text{ Mm} \leq |d_{\perp}| \leq 0.3 \text{ Mm}$, which is printed in the upper right corners of the panels.

Finally, the reconnection rate M_{Ai} in each simulation case can be estimated as the mean of v_i/v_{Ai} , which is analysed in Sect. 3.5. Similarly, the effective Lundquist number S_L is estimated as the mean of Lv_{Ai}/η_d , which is a central part of the analysis in the following sections. For both quantities, the mean values are time averages over $t \in [15, 35]$ min due to the fact that the current-sheet length is approximately stable during that time period.

3.3. Frequency of plasmoids along the current sheet

The frequency of plasmoids in the current sheet is studied here through the variation in mass density ρ_{CS} measured along the sheet (Fig. 4, panel b), which, for our case, was found to be easier than detecting null-points following the method described by Huang & Bhattacharjee (2010). To demonstrate this, ρ_{CS} is mapped against d_{\parallel} and time in Fig. 6 for (top panels) the same six 8k simulation cases as in Fig. 3, along with six 2k cases with the YS-94 resistivity (middle panels) and six with the Gudiksen-11 resistivity (bottom panels). Plasmoids are here identified as dark red stripes tilted either upwards to the left or to the right, depending on which way the plasmoids move along the current sheet. In agreement with the movie of Fig. 3, no plasmoids appear in case 8kU1. On the other hand, plasmoids appear frequently in cases 8kU4, 8kU6, and 8kU8. In case 8kU4, a roughly equal number of plasmoids move upwards to the left along the current sheet as those moving downward to the right, while in cases 8kU6 and 8kU8, the majority move in the latter direction. In cases 8kU10 and 8kU11, the dark stripes are very thin and barely visible, which indicates that most of the plasmoids have diminished and in such a way that they are only visible as outward-propagating shocks, which is also seen in the movie. These cases are not perfectly shock-mediated, as plasmoids still occur (though the larger plasmoids occur only rarely here), but they are signif-

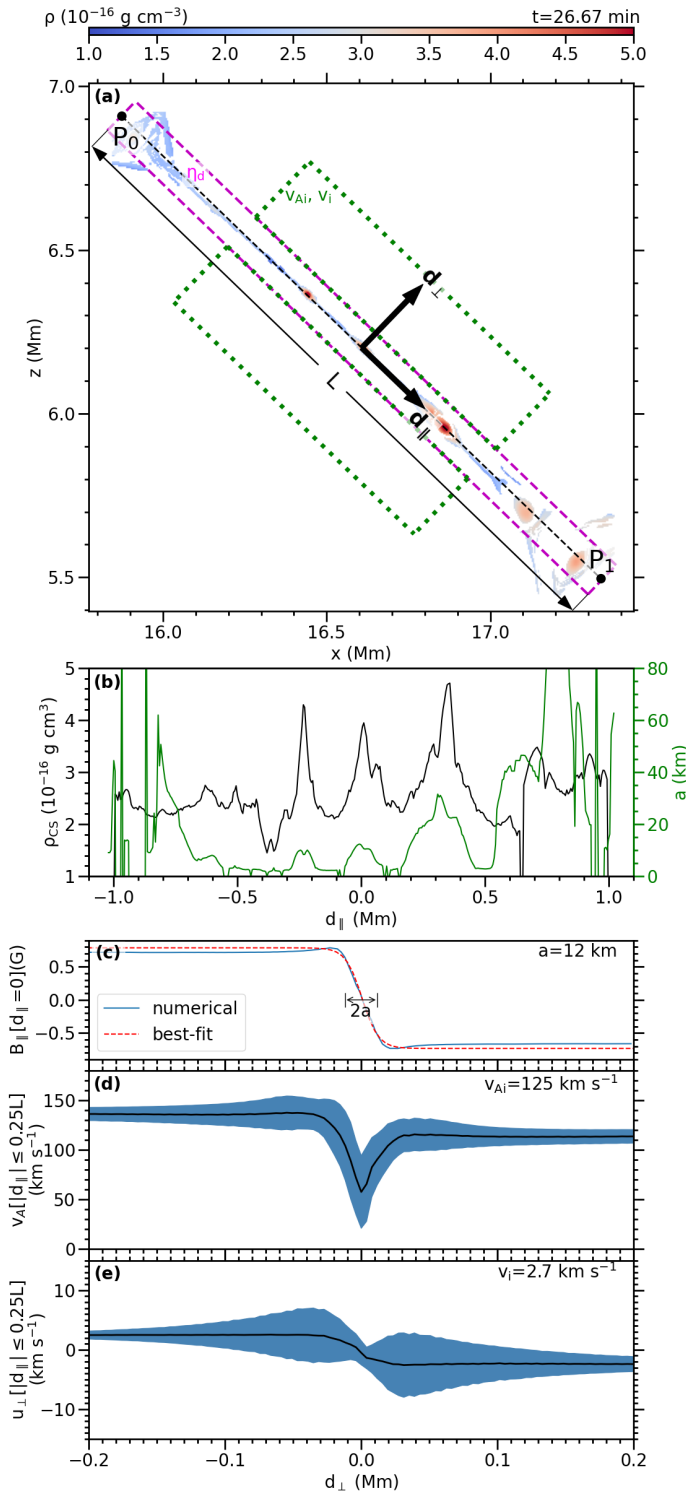


Fig. 4: Characteristics of the current sheet (case 8kU6). Panel (a): Mass density ρ in the current sheet, mapped for $L_B \leq 20$ km. The dashed line with endpoints P_0 to P_1 marks the current sheet, with coordinate axes d_{\parallel} and d_{\perp} plotted in. Diffusion and inflow regions are delimited by magenta and green rectangles, respectively. Panel (b): Average density ρ_{CS} (black curve) and width a (green curve) of the current sheet. Panel (c): Parallel component of magnetic field, B_{\parallel} (blue), across the current sheet and the best-fit (red) curve used to estimate a at $d_{\parallel} = 0$. Panels (d) and (e): Alfvén velocity v_A (d) and perpendicular velocity u_{\perp} (e) across the current sheet. Blue area maps the ranges of all values for $|d_{\parallel}| \leq 0.25L$, and black curve plots the average. Estimated inflow region mean values are printed in top right corner.

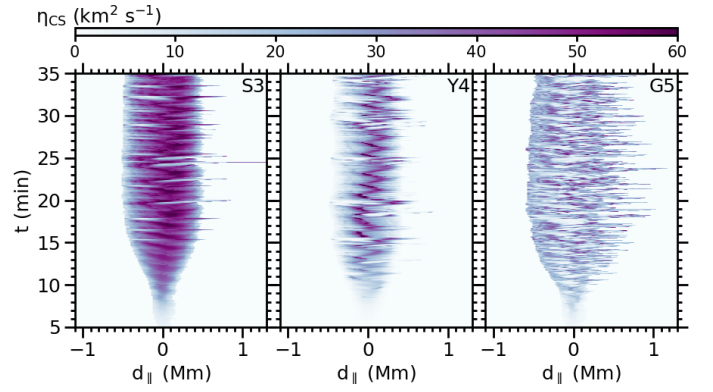


Fig. 5: Evolution of the resistivity η_{CS} along the current sheet for the S3, Y4, and G5 models. The three cases shown are 2k simulations with anomalous resistivity with $\eta_p = 60 \text{ km}^2 \text{ s}^{-1}$.

icantly closer to the shock-mediated regime than cases 8kU4-9. Therefore, the 8k cases seemingly cover three different types of reconnection: steady (Sweet-Parker-like), plasmoid-mediated, and (nearly) shock-mediated (Petschek-like) reconnection. In all 8k cases, the current-sheet length, as measured in the figure as the width of the coloured region, lies roughly around 2 Mm. The corresponding maps for the 4k cases (not shown in the figure) appear very similar to the 8k cases, though with a slightly shorter current-sheet length. Similar plasmoid patterns are also found in the 2k uniform resistivity cases for a narrower range of Lundquist numbers.

Among the YS-94 resistivity cases (see Fig. 6, middle row), the number of plasmoids (as seen as the dark stripes in the maps) clearly increases from Y3 to Y5. The plasmoids are more difficult to detect by eye in cases Y6-8, but a closer look reveals a significant number of very thin stripes. Hence, the plasmoids as reproduced with the YS-94 model seem to diminish in size (but not necessarily in number) as the resistivity gets sufficiently low. This indicates that reconnection reproduced with this resistivity model may approach steady Petschek reconnection—which is characterised by shocks instead of plasmoids—as the resistivity decreases. In all of the Gudiksen-11 cases, the plasmoids are relatively large in size, and are clearly more numerous in the lower-resistivity cases (especially in G5-7) than in the higher-resistivity cases. Among the Syntelis-19 cases, which are not shown in the figure, a minor decrease in plasmoid size is seen from cases S4 to S5, similar to that of the YS-94 cases, but of a lesser degree. All the 2k cases have a shorter current sheet than the 8k (and 4k) cases, which is due to a higher numerical diffusion that sets a stricter limit on the current-sheet length. The current-sheet length in the Gudiksen-11 cases increases as the resistivity decreases, in agreement with the discussion in Sect. 3.1.5 of F2023 on how current-sheet length depends on the scaling of the anomalous resistivity models. A similar but weaker scaling between current-sheet length and resistivity is found in the YS-94 and Syntelis-19 cases.

In order to measure the frequency of plasmoids for each simulation case, we picked specific locations along the current sheet where we measure the density as a function of time. These locations are marked with dashed vertical lines in each panel of Fig. 6. For most of the cases, plasmoids move in either direction, and so we picked two locations for measuring the density curves. These locations were picked in such a way that each plasmoid passes through one of the locations, but not both. Plasmoids passing through one of those points are then detected as

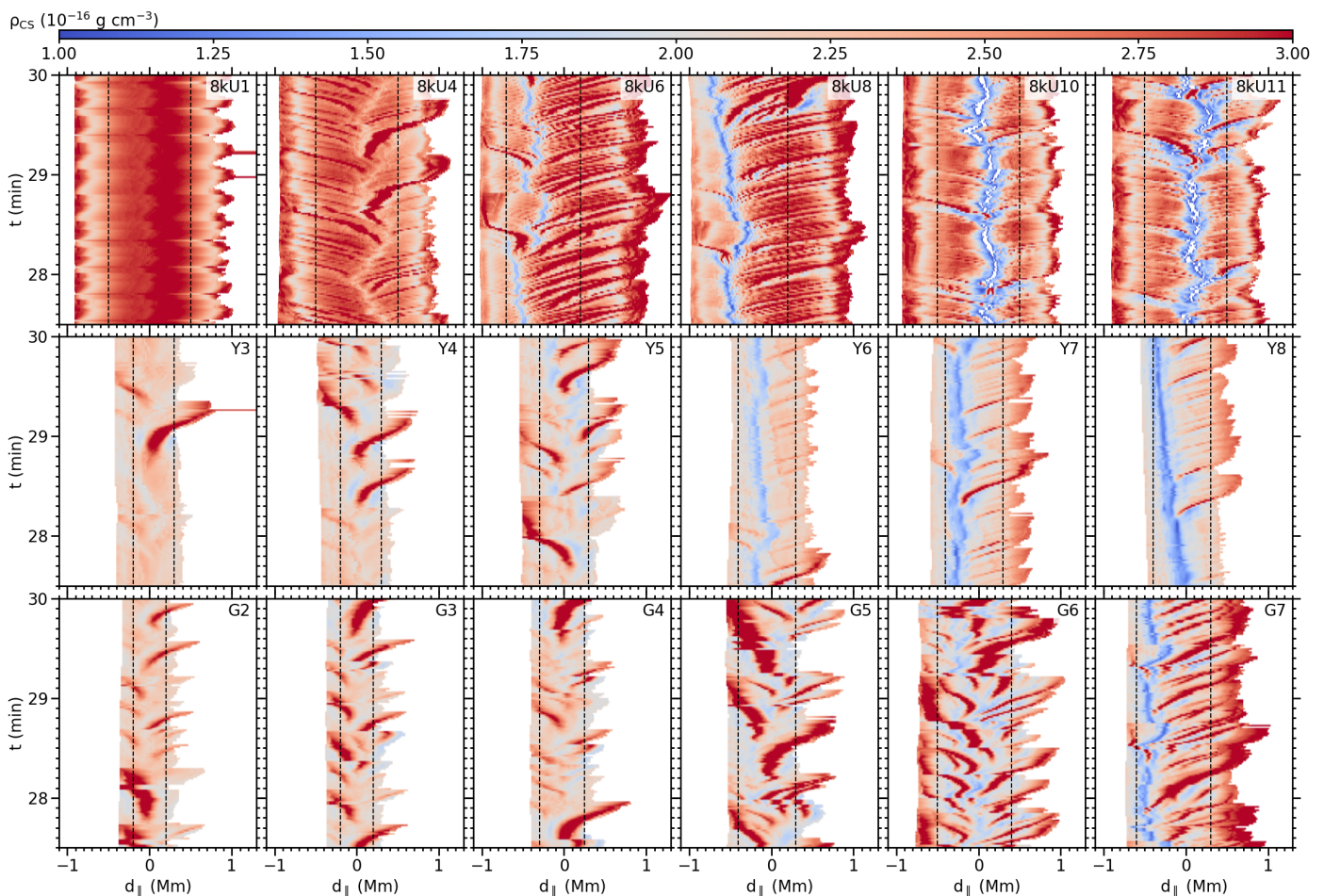


Fig. 6: Evolution of mass density ρ_{CS} along the current sheet over time for selected simulation cases. Dashed lines mark the locations where a peak detection algorithm was used to count the number of plasmoids occurring per time.

spikes in the density curves. Hence, the total number of plasmoids generated along the current sheet is given by the total number of spikes in the density curves. In the shock-mediated cases 8kU10-11 and Y6-8, the shocks are also seen as spikes in these curves.

The frequency of plasmoids for the different simulation cases—measured as the total number of plasmoids found in each case in the time interval $t \in [15, 35]$ min divided by 20 min—is plotted against Lundquist number in Fig. 7. The results are grouped into different panels by resistivity model and resolution. For a certain range of Lundquist number within each group of cases, the plasmoid frequency increases roughly with Lundquist number by a power law S_L^p , and we used curve fitting to find the best-fitting value of p , and the best-fit curves are plotted as dashed lines. For the shock-mediated cases, we use the term ‘shock frequency’ instead of ‘plasmoid frequency’, as the majority of the spikes found in the density curves in those cases are seen only as shocks propagating out of the reconnection site.

Among the uniform resistivity cases, as seen in the top panels of Fig. 7, cases U1, 4kU1-2, and 8kU1-2 follow steady reconnection, and therefore no plasmoids occur, as indicated by their label placed to the left of the vertical blue line in each panel. The other cases are plasmoid-mediated or shock-mediated (8kU10 and 8kU11). As for the 2k cases, plasmoid-mediated reconnection is reproduced only for a narrow range of Lundquist numbers given by $3.5 \leq \log S_L \leq 4.0$, below which steady reconnection occurs, and above which numerical instability oc-

urs. Within the plasmoid-mediated regime, given by cases U2-U4, the plasmoid frequency ranges from 2.0 to 4.7 plasmoids per minute, with a scaling with Lundquist number given by $S_L^{0.811}$, which is much stronger than the $S_L^{0.375}$ scaling found by Loureiro et al. (2007) for an adiabatic medium. Regarding the plasmoid-mediated 4k cases (4kU3-9), the plasmoid number ranges from 4.5 to 11 plasmoids per minute for Lundquist numbers of $3.9 \leq \log S_L \leq 5.6$ with a scaling of $S_L^{0.240}$, which is weaker than the above-mentioned adiabatic scaling, and is relatively close to the $S_L^{0.223}$ scaling found in the non-adiabatic cases of Sen & Keppens (2022). Regarding the 8k cases, the plasmoid frequency ranges from 6.9 to 12 plasmoids per minute for Lundquist numbers of $4.2 \leq \log S_L \leq 5.4$ with scaling of $S_L^{0.210}$, which is even weaker than the scaling of the plasmoid-mediated 4k cases and is even closer to the scaling of Sen & Keppens (2022). In the shock-mediated cases 8kU10 and 8kU11, the measured frequency of shocks is lower than the plasmoid frequencies of 8kU7-9. These two cases fit well to the (dotted) line for the $S_L^{0.375}$ scaling, indicating that the frequency of shocks generated in this type of (Petschek-like) reconnection scales adiabatically with Lundquist number. Case 8kU3 is seemingly in an intermediate state between the steady-reconnection regime and the plasmoid-mediated regime, and case 8kU9 is in an intermediate state between the plasmoid-mediated and shock-mediated regimes. By comparing the results for uniform resistivity with the three different resolutions, we see that the plasmoid frequency tends to converge towards higher values with a weaker

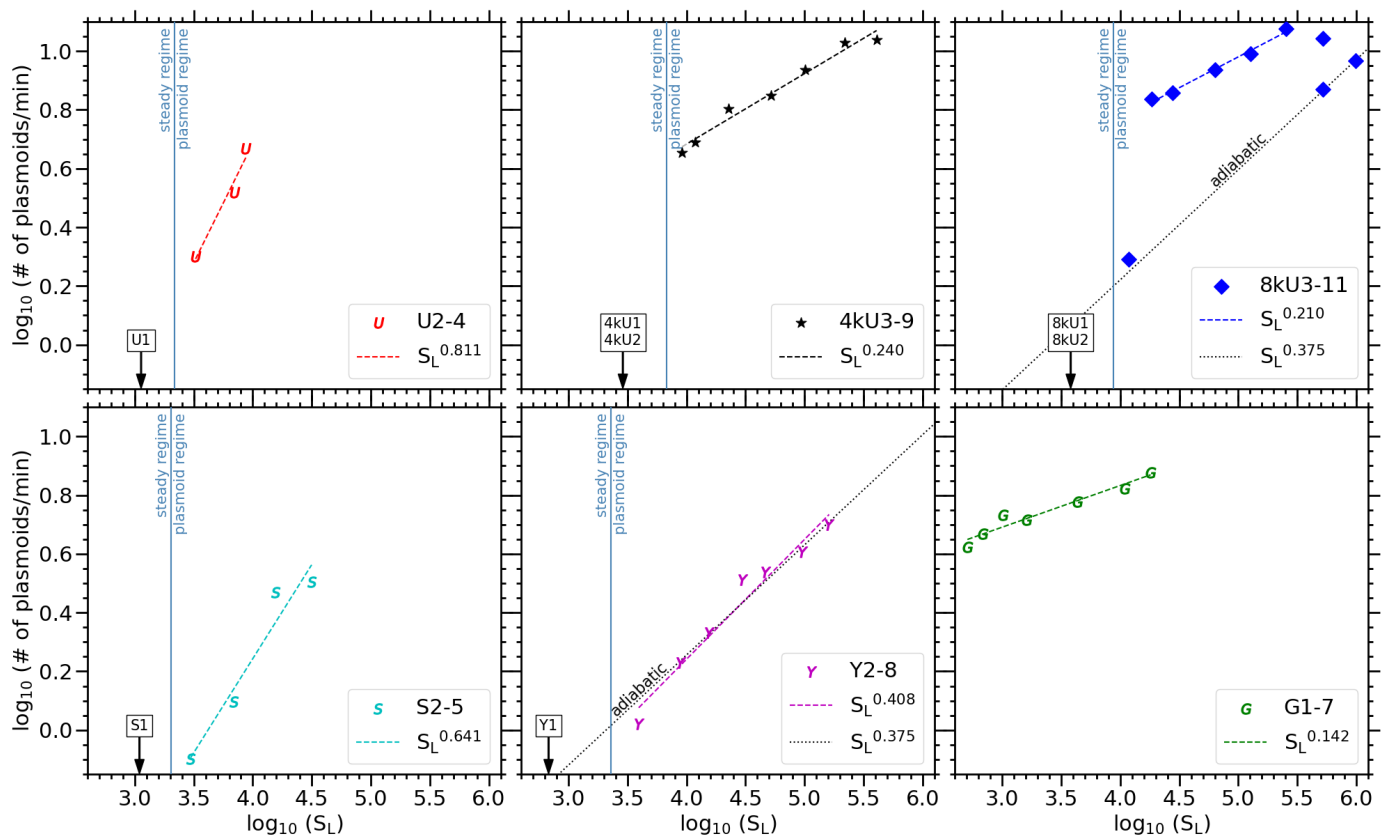


Fig. 7: Plasmoid frequency, measured as the number of plasmoids generated along the current sheet per minute, plotted against Lundquist number S_L for each simulation case. Results are displayed for cases with uniform resistivity (top panels, with 2k, 4k, and 8k cases in separate panels) and anomalous resistivity (bottom panels, with Syntelis-19, YS-94, and Gudiksen-11 cases in separate panels). For cases within a certain range of Lundquist numbers, the plasmoid frequency scales roughly with Lundquist number by a power law S_L^p , and best-fit curves for these cases are plotted as dashed lines in each panel. The curve for the adiabatic power law $S_L^{0.375}$ is plotted as a dotted line for the cases where a nearly adiabatic scaling between plasmoid number and Lundquist number occur. A vertical line marks the Lundquist number below which steady reconnection occurs and above which plasmoid-mediated reconnection occurs. Cases U1, 4kU1-2, 8kU1-2, S1, and Y1 have no plasmoids, as indicated by the label placed inside the steady-reconnection regime.

scaling with Lundquist number as the resolution is increased. The difference is smaller between the 4k and 8k cases than between the 2k and 4k cases.

Among the 2k cases with the Syntelis-19 resistivity model (bottom left panel), steady reconnection occurs for $\log S_L < 3.4$ (case S1). For $3.4 \leq \log S_L \leq 4.5$ (cases S2-5), the plasmoid frequency ranges from 0.8 to 3.2 plasmoids per minute with a scaling of $S_L^{0.641}$, a significantly stronger scaling than the adiabatic one, though weaker than the 2k cases with uniform resistivity (for higher Lundquist number, numerical instability occurs). Among the YS-94 cases (bottom centre panel), Y1 has steady reconnection, and in cases Y2-8, the plasmoid frequency (or shock frequency for Y6-8) ranges from 1.1 to 5.0 plasmoids (or shocks) per minute for $3.6 \leq \log S_L \leq 5.2$ with a scaling of $S_L^{0.408}$. With the (dotted) line for adiabatic scaling $S_L^{0.375}$ added to the panel, we see that the YS-94 resistivity model is capable of reproducing a nearly adiabatic scaling between plasmoid (or shock) frequency and Lundquist number. As for the Gudiksen-11 cases (bottom right panel), the plasmoid frequency ranges from 4.2 to 7.6 plasmoids per minute for $2.6 \leq \log S_L \leq 4.3$ with a scaling of $S_L^{0.142}$. Therefore, with the 2k resolution, the Gudiksen-11 model reproduces the highest plasmoid frequency with the weakest scaling to Lundquist number. Moreover, the

Gudiksen-11 cases are the only 2k cases where plasmoid frequency is found to scale more weakly with Lundquist number than the adiabatic scaling, and is closer to the scaling of Sen & Keppens (2022) than the other 2k cases.

The key findings of this plasmoid analysis are as follows: we observe that with uniform resistivity and a sufficiently high resolution (4k and 8k cases), the dependency between plasmoid formation and Lundquist number may be divided into three regimes: (1) a steady-reconnection regime, for Lundquist numbers lower than 10^4 ; (2) a plasmoid-mediated regime with a subadiabatic scaling between plasmoid number and Lundquist number similar to that of Sen & Keppens (2022) for Lundquist numbers between roughly 10^4 and 4×10^5 ; and (3) a shock-mediated regime for Lundquist numbers above roughly 4×10^5 , where the frequency of shocks follows an adiabatic scaling with Lundquist number similar to that predicted by Loureiro et al. (2007). With uniform resistivity, very high resolution (as in our 8k cases, $\Delta x = \Delta z = 3.9$ km) is needed to obtain numerically stable simulations with a Lundquist number high enough to reproduce the latter, shock-mediated regime.

For lower resolutions (as in our 2k cases, $\Delta x = \Delta z = 15.6$ km), uniform resistivity is not a suitable resistivity model for studying plasmoid formation, as plasmoid-mediated reconnection

tion is reproduced only within a narrow range of Lundquist numbers (between 3×10^3 and 10^4) without breaking numerical stability along the current sheet. Within this range, the plasmoid number increases rapidly with Lundquist number. The Syntelis-19 resistivity model allows numerically stable simulations with plasmoid-mediated reconnection for a slightly wider range, but still with a significantly strong scaling between plasmoid number and Lundquist number. The YS-94 model is capable of reproducing plasmoid- or shock-mediated reconnection for a relatively wide range of Lundquist numbers and shows an almost perfectly adiabatic scaling between plasmoid or shock frequency and Lundquist number. The Gudiksen-11 model is capable of reproducing plasmoid frequencies closer to those seen in the high-resolution high- S_L cases (G7 having ~ 7.6 plasmoids per minute, and the 8kU4-8 having about 7-12 plasmoids per minute), and the scaling between plasmoid number and Lundquist number is weaker than in the adiabatic case, which is in fair agreement with the scaling seen in our higher-resolution cases as well as with the scaling found by Sen & Kepens (2022).

3.4. Aspect ratio of the current sheet

In all of our simulation cases, the inverse aspect ratio \bar{a}/L is initially infinitely high, as the current sheet starts at zero length. During the first 15 minutes of the simulation, the aspect ratio decreases rapidly as the current sheet increases in length, reaches an equilibrium value of between 0.005 and 0.05 depending on the simulation case, and remains roughly constant throughout the reconnection phase. For the first 5-10 minutes of each simulation, \bar{a}/L is higher than the ideal tearing instability threshold value $S_L^{-1/3}$, and the current sheet is stable during this phase (i.e. no plasmoid instability occurs). Shortly after \bar{a}/L passes below $S_L^{-1/3}$, the current sheet becomes unstable in most of the simulation cases, and plasmoids therefore rapidly appear. However, in a few cases (S1, Y1, U1, 4kU1-2, and 8kU1-2, as discussed below) where the Lundquist number is sufficiently low ($< 10^4$), the current sheet remains stable even when $\bar{a}/L < S_L^{-1/3}$, allowing steady reconnection to occur. Amongst those cases, in the cases with uniform resistivity (U1, 4kU1-2, and 8kU1-2), \bar{a}/L reaches an equilibrium value of close to $S_L^{-1/2}$, indicating the occurrence of Sweet-Parker reconnection.

In Fig. 8, we show the equilibrium value that \bar{a}/L reaches in each case, which is computed as an average taken over the time interval $t \in [15, 35]$ min. The Sweet-Parker value $a_{SP}/L \equiv S_L^{-1/2}$ is plotted as a dashed line, and the ideal tearing instability threshold $a_{thr}/L \equiv S_L^{-1/3}$ as a dotted line. All the uniform resistivity cases (top panels) are scattered in a similar manner. The inverse aspect ratio clearly drops below the ideal tearing instability threshold, allowing plasmoids to appear rapidly in all cases except for those with a sufficiently low Lundquist number to maintain steady reconnection. Those steady-reconnection cases, namely U1, 4kU1, 4kU2, 8kU1, and 8kU2, all lie just below the Sweet-Parker value in the figure, confirming that these cases indeed follow Sweet-Parker reconnection. 8kU3 also lies just below this line, and U2 on this line, which is in fair agreement with the fact that they lie close to the threshold between the steady regime and the plasmoid-mediated regime. All of the cases that lie within the Sweet-Parker regime are scattered approximately along the Sweet-Parker line, confirming that the inverse aspect ratio is indeed proportional to $S_L^{-1/2}$ for Sweet-Parker reconnection. In the plasmoid-mediated cases (U2-3, 4kU3-9, 8kU4-11), the size of the plasmoids puts a limit on how small the mean

thickness \bar{a} of the current sheet can be, and therefore the inverse aspect ratio seems to be almost independent of Lundquist number for those cases. For the nearly shock-mediated cases, 8kU10 and 8kU11, we measured a significantly lower inverse aspect ratio than in the more heavily plasmoid-mediated cases, as the plasmoids here are diminished in size.

As for the anomalous resistivity cases seen in Fig. 8, the inverse aspect ratio decreases slowly with increasing Lundquist number because of a slowly increasing current-sheet length. In all of the Syntelis-19 cases (bottom left panel), the inverse aspect ratio decreases significantly below the ideal tearing instability threshold, which is in close agreement with the fact that plasmoids appear in all cases except S1 (where the sufficiently high resistivity enforces stability of the current sheet). The inverse aspect ratio of S1 is still significantly above the Sweet-Parker value. Therefore, this steady-reconnection case is not Sweet-Parker-like, which is expected given that the resistivity is non-uniform. Among the YS-94 cases (bottom centre panel), Y1-5 have an inverse aspect ratio far below $S_L^{-1/3}$, and cases Y2-5 are clearly plasmoid-mediated, as expected, while Y1 has sufficiently high resistivity to maintain steady reconnection, still with $\bar{a}/L > S_L^{-1/2}$ (therefore not a Sweet-Parker case). Regarding cases Y6-8, which are also plasmoid-mediated, the inverse aspect ratio drops only barely below $S_L^{-1/3}$ in Y6-7 and remains slightly above $S_L^{-1/3}$ in Y8. This may indeed explain why the plasmoids in these cases appear diminished in size, indicating a convergence towards shock-mediated reconnection for increasing Lundquist number. In all of the Gudiksen-11 cases (Fig. 8, bottom right panel), \bar{a}/L drops far below the ideal tearing instability threshold, in good agreement with the fact that plasmoids appear relatively large in size in all those cases (as seen in Fig. 6).

3.5. Reconnection rate

The reconnection rate $M_{Ai} \equiv v_i/v_{Ai}$ of each simulation case is plotted against Lundquist number in Fig. 9. The Sweet-Parker reconnection rate $M_{SP} \equiv S_L^{-1/2}$ is plotted as a dashed line, and the Petschek reconnection rate $M_{Pet} \equiv \pi/8 \ln S_L$ as a dotted curve. Among the uniform resistivity cases (top panels), the reconnection rates of U1, 4kU1, and 8kU1 lie near to the values predicted by the Sweet-Parker model, which is in good agreement with the previously observed Sweet-Parker-like aspect ratio and absence of plasmoids. These cases are therefore indeed in the Sweet-Parker regime. The steady-reconnection cases 4kU2 and 8kU2 are also close enough to the Sweet-Parker line to be characterised as Sweet-Parker reconnection. The plasmoid-mediated cases U2-4, 4kU3-9, and 8kU3-9 lie approximately along the same nearly horizontal line, meaning that the reconnection rate is almost independent of Lundquist number for those cases. A similar change of dependency between reconnection rate and Lundquist number from the Sweet-Parker regime to the plasmoid-mediated regime is seen in the simulations of Bhattacharjee et al. (2009). Cases 8kU10 and 8kU11 both have significantly higher reconnection rates, indeed close to that predicted by the Petschek model, which is in agreement with the fact that these cases are more shock-mediated. This is due to the fact that the resistivity in these two cases is low enough that the non-uniform viscosity term has a dominating effect on the dynamics of the current sheet. A similar Petschek-like reconnection was seen in the simulations by Baty et al. (2009), where a relatively low uniform resistivity was also applied, and that behaviour was mainly triggered by the non-linear viscosity.

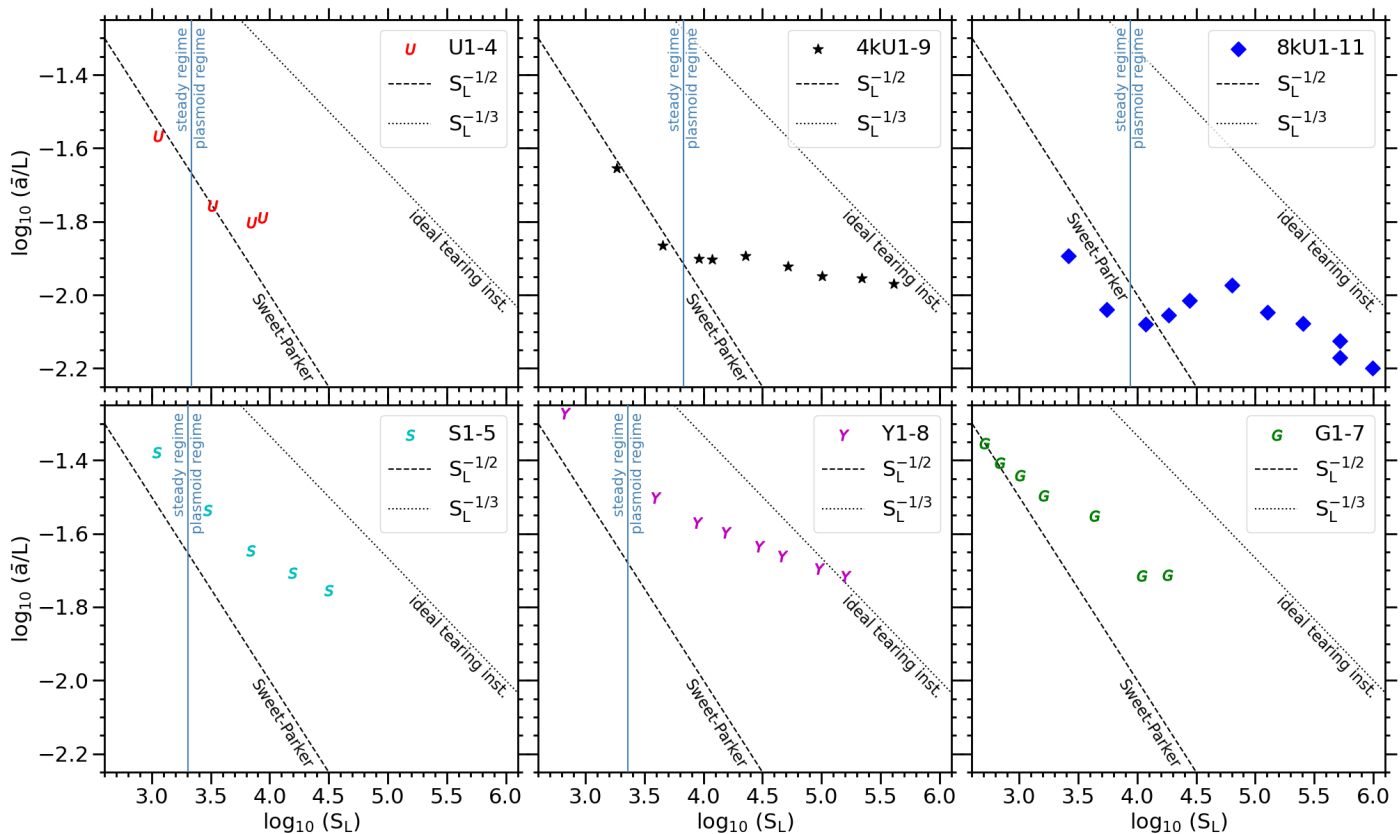


Fig. 8: Mean inverse aspect ratio averaged over $t \in [15, 35]$ min, plotted against Lundquist number S_L for each simulation case. The dashed line marks the Sweet-Parker value $a_{SP}/L \equiv S_L^{-1/2}$, and the dotted line shows the ideal tearing instability threshold $a_{thr}/L \equiv S_L^{-1/3}$.

Among the Syntelis-19 cases (Fig. 9, bottom left panel), the steady case S1 has a reconnection rate that is only slightly below the Petschek value, indicating that the reconnection here is nearly Petschek-like. The plasmoid-mediated cases S2 to S5 lie further below the Petschek curve, though the scaling between reconnection rate and Lundquist number is still similar to that of the Petschek model. Furthermore, all of the YS-94 cases (bottom centre panel) lie approximately along the Petschek curve, meaning that their reconnection rates roughly agree with Petschek theory, even though plasmoids are present in all of those cases except for Y1. This agrees perfectly with what Yokoyama & Shibata (1994) found in their 2D simulations of an emerging coronal loop, namely that this anomalous resistivity model is capable of reproducing a non-steady Petschek-like reconnection scheme. Regarding the Gudiksen-11 cases (bottom right panel), only G1 lies below the Sweet-Parker line. This is in agreement with the fact that the current sheet in this case also has a Sweet-Parker-like aspect ratio, which indicates that non-steady Sweet-Parker reconnection may be occurring here. G3-G5 all have reconnection rates that are slightly below the Petschek value (and G2 somewhere in between), while G6 and G7 have even lower reconnection rates.

In summary, the reconnection rates obtained with the anomalous resistivity models are in general higher than those obtained with uniform resistivity. The YS-94 model is the only one to reproduce reconnection rates that are approximately equal to the Petschek values. The Gudiksen-11 model, on the other hand, is capable of reproducing relatively high reconnection rates at the same time as reproducing high plasmoid frequencies, as seen in

cases G1-5; these latter are the only cases that show reconnection rates above 0.04 whilst also producing more than four plasmoids per minute.

3.6. Temperature increase in the reconnection site

As a final step in our analysis of the reconnection process, Fig. 10 displays the maximum temperature increase relative to the initial temperature, $\max \Delta T/T_0$, for all simulation cases, which is given by the maximum value of $(T - T_0)/T_0$ found in the computational domain averaged over $t \in [15, 35]$ min. This maximum temperature increase lies roughly around 27%-30% in the 8k cases, at about 25% in the 4k cases, and between 15% and 22% in the 2k cases. This shows that the total heating of the current sheet increases with resolution. The reason for this is that the simulation cases with higher resolution obtain significantly longer, though slightly narrower current sheets. Therefore, as the total heating of the current sheet is equal to the heat input per volume integrated over its area, this observed correlation between total heating and resolution is to be expected. Among the uniform resistivity cases, with the exception of 8kU10 and 8kU11, the total heating of the current sheet seems to be almost independent of Lundquist number. This is because the viscous heating of the plasma in the reconnection site, which, predictably, becomes dominant for high Prandtl numbers (Rempel 2017), is in our cases found to increase with Lundquist number in a way that balances the corresponding decrease in Joule heating. The nearly shock-mediated cases 8kU10 and 8kU11 have a lower heat input

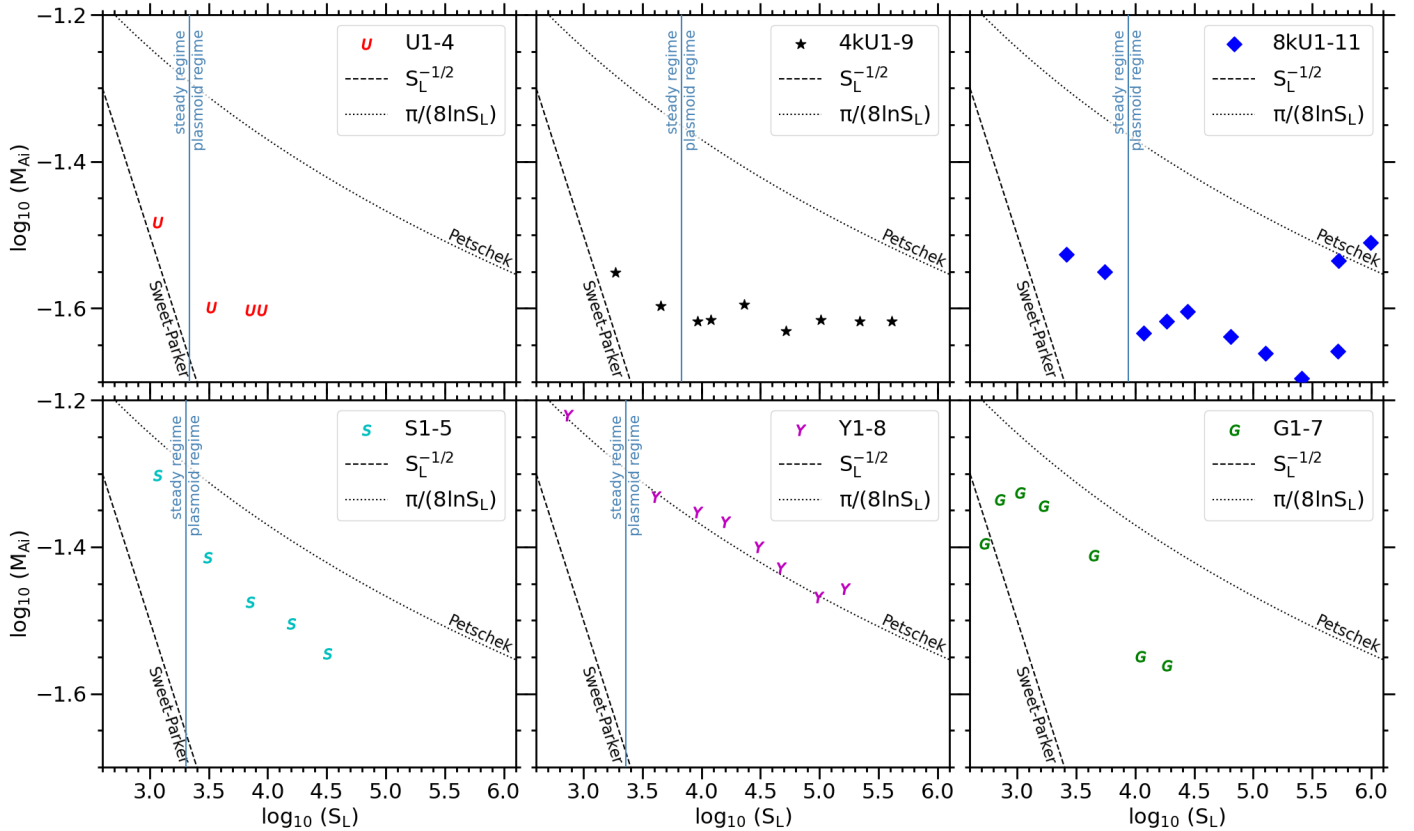


Fig. 9: Reconnection rate, averaged over $t \in [15, 35]$ min, plotted against Lundquist number S_L for each simulation case. The dashed line marks the Sweet-Parker value $M_{SP} \equiv S_L^{-1/2}$, and the dotted line the Petschek value $M_{Pet} \equiv \pi/8 \ln S_L$.

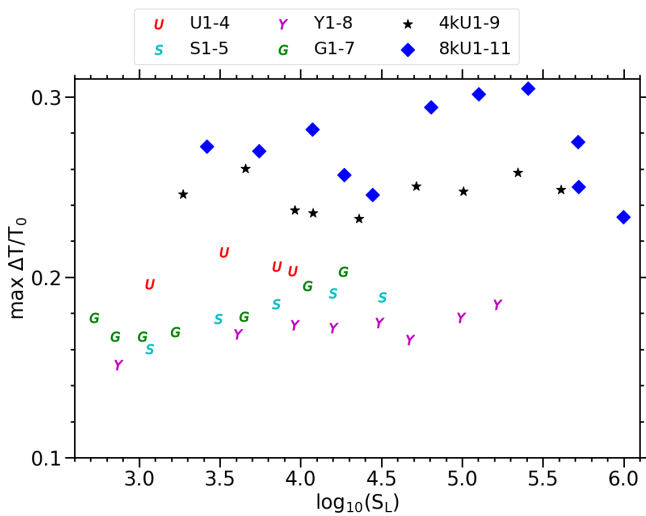


Fig. 10: Maximum temperature increase relative to initial temperature, averaged over $t \in [15, 35]$ min, plotted against Lundquist number S_L for all simulation cases.

than the other 8k cases because of a significantly shorter and thinner current sheet.

In all the anomalous resistivity cases, the total heating of the plasma increases weakly with Lundquist number because of the corresponding increase in current-sheet length, as seen in Fig. 6. The scaling between total heating and Lundquist number is strongest in the Gudiksen-11 cases, and G7 obtain a maximum

temperature increase of slightly above 20 %, reaching the highest temperatures of the anomalous resistivity cases. Among the 2k cases, only the uniform resistivity cases reach higher temperatures, but only at a significantly lower Lundquist number. Therefore, with the resolution of the 2k cases, the Gudiksen-11 resistivity model is the most suitable for reproducing satisfactorily high temperatures, that is, closer to those obtained in the higher resolution cases, at relatively high Lundquist numbers ($> 10^4$).

4. Discussion

Here, we expand on our previous comparative study of resistivity models (F2023) by performing numerical experiments of plasmoid-mediated reconnection in a 2D coronal fan-spine topology. We carried out a parametric study employing the same three anomalous resistivity models as in F2023 as well as a model with uniform resistivity. We varied the scaling parameters and the numerical resolution and analysed how the characteristics of the reconnection process depend on Lundquist number.

In all simulations, reconnection occurs along a tilted current sheet in the corona, causing a temperature increase of 15%-30 %. The majority of the experiments show plasmoid-mediated reconnection, regardless of the resistivity model used. Steady reconnection is only found in cases where the resistivity of the current sheet is high enough to prevent plasmoid instability. The minimum Lundquist number required to reproduce plasmoid instability lies around 2×10^3 in our lowest-resolution cases and converges towards 10^4 as the resolution reaches sufficiently high values, which is in good agreement with the findings of Loureiro et al. (2007). The hyper-diffusive resistivity model reproduces

plasmoid instability at significantly lower Lundquist numbers, which is due to its dynamic variation in the resistivity along the current sheet. We also see (in some cases with the drift-velocity-dependant resistivity) that the reconnection is shock-mediated rather than plasmoid-mediated if the inverse aspect ratio \bar{a}/L of the current sheet remains above or only slightly below $S_L^{-1/3}$, indicating that \bar{a}/L has to drop significantly below this threshold in order for the current sheet to become intrinsically unstable, as predicted by Pucci & Velli (2014).

The frequency of plasmoids generated along the current sheet scales with the Lundquist number, following a power law for a certain range of Lundquist numbers. With uniform resistivity, the plasmoid frequency converges towards higher values and a weaker scaling with Lundquist number as the resolution increases. The cases with the highest resolution, $\Delta x = \Delta z = 3.9$ km, reproduce a plasmoid frequency that ranges from 6.9 to 12 plasmoids per minute and scales as $S_L^{0.210}$ for $S_L \in [1.8 \times 10^4, 2.6 \times 10^5]$, which is close to the power law found by Sen & Keppens (2022) for the maximum plasmoid number on a Harris current sheet in a non-adiabatic medium. Our simulated plasma is also non-adiabatic, which explains why we reproduce a scaling law here that is similar to theirs rather than to those derived in the adiabatic cases of Loureiro et al. (2007) and Huang & Bhattacharjee (2010), where the plasmoid number was $\propto S_L^{0.375}$ in the linear reconnection phase and $\propto S_L$ in the non-linear phase. For $S_L < 10^4$, steady Sweet-Parker reconnection occurs that is characterised by the absence of plasmoids, a Sweet-Parker-like aspect ratio of the current sheet, and a reconnection rate similar to that predicted by the Sweet-Parker model. For sufficiently high Lundquist numbers ($S_L > 5 \times 10^5$), a rather shock-mediated Petschek reconnection occurs, which is similar to what was found by Baty et al. (2009), with a nearly adiabatic scaling between shock frequency and Lundquist number and a reconnection rate close to the Petschek value. This happens because the resistivity here is low enough to allow the non-uniform viscous term to dominate.

Among our simulation cases with the lowest resolution, $\Delta x = \Delta z = 15.6$ km, plasmoid-mediated reconnection is reproduced for only a narrow range of Lundquist numbers ($S_L \in [3 \times 10^3, 10^4]$) with uniform resistivity. The anomalous resistivity models help to increase this range. The drift-velocity-scaled model (YS-94) used by Yokoyama & Shibata (1994) reproduces Petschek reconnection for any Lundquist number (being steady for $S_L < 10^3$) with reconnection rates approximately equal to $\pi/(8 \ln S_L)$ and a nearly adiabatic scaling between plasmoid (or shock) frequency and Lundquist number. The model with resistivity proportional to current density (Syntelis-19) reproduces similar results, but on a narrower range of Lundquist numbers, with a lower plasmoid frequency that scales more closely with Lundquist number and a reconnection rate that is slightly lower than the Petschek value. The hyper-diffusive resistivity model of Bifrost (Gudiksen-11) reproduces higher plasmoid frequencies (4.2-7.6 plasmoids per minute) with a weaker scaling with Lundquist number ($\propto S_L^{0.142}$) than any of the other resistivity models applied on the same resolution; indeed, it is the only resistivity model that, for the given resolution, reproduces a plasmoid frequency with a weaker scaling to Lundquist number than the $S_L^{0.375}$ scaling predicted for adiabatic reconnection (Loureiro et al. 2007). This resistivity model therefore reproduces plasmoid characteristics that more closely resemble those seen in the higher-resolution cases. It is also the only resistivity model that reproduces both relatively high reconnection rates (> 0.04) and plasmoid frequencies (> 4 plasmoids per minute) at the

same time. Additionally, for significantly high Lundquist numbers ($> 10^4$), the hyper-diffusive resistivity model of Bifrost reproduces a higher total heating of the plasma than the other resistivity models applied on the same resolution, reaching temperatures closer to those of the higher-resolution cases. Therefore, this model indeed proves to be suitable for simulating dynamic plasmoid-mediated reconnection, and is also applicable for 3D models of the solar atmosphere without requiring extremely high resolution. Indeed, this model has been successfully used for simulations of flux emergence with plasmoid reconnection leading to EBs and UV bursts (Hansteen et al. 2019) as well as nanoflare-like events with synthesised line spectra detectable for the upcoming MUSE mission (Robinson & Carlsson 2023).

The most important result of this comparative study is that, out of the four resistivity models applied on the same reconnection experiment with the same numerical resolution, the plasmoid characteristics produced with the hyper-diffusive model most closely resemble those obtained with uniform resistivity with significantly higher resolution. Additionally, by taking into account scaling laws previously derived for spontaneous reconnection on Harris sheets (Loureiro et al. 2007; Bhattacharjee et al. 2009; Huang & Bhattacharjee 2010; Sen & Keppens 2022), we show that we are able to derive very similar scaling laws for a more driven reconnection process. This indicates that such scaling laws may apply on a wider range of reconnection processes, allowing us to better understand more complex scenarios such as reconnection driven by granular motion (Nóbrega-Siverio & Moreno-Insertis 2022).

The complex behaviours of plasmoid instability may only be fully understood through three-dimensional numerical studies; namely the turbulent splitting, kinking, and merging of plasmoids seen in the coronal mass ejection simulation of Ye et al. (2023), or the chaotic tearing-thermal instability leading to coronal condensation similar to prominences and coronal rain blobs simulated by Sen et al. (2023). Two-dimensional particle-in-cell (PIC) simulations of waves in plasmoid-mediated reconnection have provided new insights into the different natures of waves inside and outside current sheets as an effect of the tearing instability (Shahraki Pour & Hosseinpour 2022). High-resolution 2D MHD simulations with resistivity predicted from particle-collision probabilities including radiative cooling and partially ionised effects have provided detailed information on the energy balance in plasmoid reconnection in the chromosphere leading to EBs (Liu et al. 2023) and UV bursts (Ni et al. 2022). Though MHD simulations with anomalous resistivity may lead to a slightly more approximate representation of the reconnection process, this study proves that the hyper-diffusion model of Bifrost is indeed helpful in numerically studying phenomena on the Sun that would otherwise require a significantly higher resolution to simulate with a low, Spitzer-like resistivity.

Acknowledgements. This research has been supported by the European Research Council through the Synergy Grant number 810218 (“The Whole Sun”, ERC-2018-SyG) and by the Research Council of Norway through its Centres of Excellence scheme, project number 262622. The simulations were performed on resources provided by Sigma2 - the National Infrastructure for High Performance Computing and Data Storage in Norway. The authors are grateful to the referee for his/her constructive comments to improve the paper.

References

- Baty, H., Forbes, T. G., & Priest, E. R. 2009, *Physics of Plasmas*, 16, 012102
 Bhattacharjee, A., Huang, Y.-M., Yang, H., & Rogers, B. 2009, *Physics of Plasmas*, 16, 112102

- Danilovic, S. 2017, *A&A*, 601, A122
- Færder, Ø. H., Nóbrega-Siverio, D., & Carlsson, M. 2023, *A&A*, 675, A97
- Finn, J. M. & Kaw, P. K. 1977, *Physics of Fluids*, 20, 72
- Furth, H. P., Killeen, J., & Rosenbluth, M. N. 1963, *Physics of Fluids*, 6, 459
- Gudiksen, B. V., Carlsson, M., Hansteen, V. H., et al. 2011, *A&A*, 531, A154
- Guo, L. J., De Pontieu, B., Huang, Y. M., Peter, H., & Bhattacharjee, A. 2020, *ApJ*, 901, 148
- Hansteen, V., Ortiz, A., Archontis, V., et al. 2019, *A&A*, 626, A33
- Hansteen, V. H., Archontis, V., Pereira, T. M. D., et al. 2017, *ApJ*, 839, 22
- Harris, E. G. 1962, *Il Nuovo Cimento*, 23, 115
- Heyvaerts, J. & Priest, E. R. 1984, *A&A*, 137, 63
- Hofmeister, S. J., Utz, D., Heinemann, S. G., Veronig, A., & Temmer, M. 2019, *A&A*, 629, A22
- Huang, Y.-M. & Bhattacharjee, A. 2010, *Physics of Plasmas*, 17, 062104
- Kumar, P., Karpen, J. T., Antiochos, S. K., Wyper, P. F., & DeVore, C. R. 2019, *ApJ*, 885, L15
- Liu, M., Ni, L., Cheng, G.-C., Ziegler, U., & Lin, J. 2023, *Research in Astronomy and Astrophysics*, 23, 035006
- Loureiro, N. F., Schekochihin, A. A., & Cowley, S. C. 2007, *Physics of Plasmas*, 14, 100703
- Ni, L., Chen, Y., Peter, H., Tian, H., & Lin, J. 2021, *A&A*, 646, A88
- Ni, L., Cheng, G., & Lin, J. 2022, *A&A*, 665, A116
- Ni, L., Zhang, Q.-M., Murphy, N. A., & Lin, J. 2017, *ApJ*, 841, 27
- Nóbrega-Siverio, D., Martínez-Sykora, J., Moreno-Insertis, F., & Rouppe van der Voort, L. 2017, *ApJ*, 850, 153
- Nóbrega-Siverio, D. & Moreno-Insertis, F. 2022, *ApJ*, 935, L21
- Nóbrega-Siverio, D., Moreno-Insertis, F., & Martínez-Sykora, J. 2016, *ApJ*, 822, 18
- Nordlund, Å. & Galsgaard, K. 1995, *A 3D MHD Code for Parallel Computers*
- Parker, E. N. 1963, *ApJS*, 8, 177
- Parker, E. N. 1988, *ApJ*, 330, 474
- Peter, H., Huang, Y. M., Chitta, L. P., & Young, P. R. 2019, *A&A*, 628, A8
- Petschek, H. E. 1964, *Magnetic Field Annihilation*, Vol. 50, 425
- Priest, E. 2014, *Magnetohydrodynamics of the Sun*
- Pucci, F. & Velli, M. 2014, *ApJ*, 780, L19
- Rempel, M. 2017, *ApJ*, 834, 10
- Rempel, M., Chintzoglou, G., Cheung, M. C. M., Fan, Y., & Kleint, L. 2023, *ApJ*, 955, 105
- Robinson, R. A. & Carlsson, M. 2023, *A&A*, 677, A36
- Rouppe van der Voort, L., De Pontieu, B., Scharmer, G. B., et al. 2017, *ApJ*, 851, L6
- Rouppe van der Voort, L. H. M., van Noort, M., & de la Cruz Rodríguez, J. 2023, *A&A*, 673, A11
- Sen, S., Jenkins, J., & Keppens, R. 2023, *A&A*, 678, A132
- Sen, S. & Keppens, R. 2022, *A&A*, 666, A28
- Shahraki Pour, M. & Hosseinpour, M. 2022, *Frontiers in Astronomy and Space Sciences*, 8, 237
- Sweet, P. A. 1958a, in *Electromagnetic Phenomena in Cosmical Physics*, ed. B. Lehnert, Vol. 6, 123
- Sweet, P. A. 1958b, *Il Nuovo Cimento*, 8, 188
- Syntelis, P., Priest, E. R., & Chitta, L. P. 2019, *ApJ*, 872, 32
- Vaiana, G. S., Krieger, A. S., & Timothy, A. F. 1973, *Sol. Phys.*, 32, 81
- Wyper, P. F., Antiochos, S. K., & DeVore, C. R. 2017, *Nature*, 544, 452
- Wyper, P. F., DeVore, C. R., Karpen, J. T., & Lynch, B. J. 2016, *ApJ*, 827, 4
- Ye, J., Raymond, J. C., Mei, Z., et al. 2023, *ApJ*, 955, 88
- Yokoyama, T. & Shibata, K. 1994, *ApJ*, 436, L197
- Yokoyama, T. & Shibata, K. 1995, *Nature*, 375, 42
- Yokoyama, T. & Shibata, K. 1996, *PASJ*, 48, 353
- Yokoyama, T. & Shibata, K. 2001, *ApJ*, 549, 1160

Paper III

EUV observables of simulated plasmoid-mediated reconnection in the solar corona

**Øystein Håvard Færder, Daniel Nóbrega-Siverio, Mats Carlsson,
Juan Martínez-Sykora**

Forthcoming article in A&A

EUV observables of simulated plasmoid-mediated reconnection in the solar corona

Ø. H. Færder^{1,2}, D. Nóbrega-Siverio^{3,4,1,2}, M. Carlsson^{1,2}, and J. Martínez-Sykora^{5,6,1,2}

¹ Rosseland Centre for Solar Physics, University of Oslo, PO Box 1029, Blindern, NO-0315 Oslo, Norway
e-mail: o.h.farder@astro.uio.no

² Institute of Theoretical Astrophysics, University of Oslo, PO Box 1029, Blindern, NO-0315 Oslo, Norway

³ Instituto de Astrofísica de Canarias, E-38205 La Laguna, Tenerife, Spain

⁴ Universidad de La Laguna, Dept. Astrofísica, E-38206 La Laguna, Tenerife, Spain

⁵ Lockheed Martin Solar & Astrophysics Laboratory, 3251 Hanover Street, Palo Alto, CA 94304, USA

⁶ Bay Area Environmental Research Institute, NASA Research Park, Moffett Field, CA 94035, USA

January 26, 2024

ABSTRACT

Context. Understanding the role of magnetic reconnection in the heating and dynamics of the solar atmosphere requires detailed observational data of any observable aspect of the reconnection process, including small-scale features such as plasmoids.

Aims. We aim to examine the capability of active and upcoming instruments to detect plasmoids generated by reconnection in the corona including low-density regimes.

Methods. We performed two Bifrost simulations of plasmoid-mediated reconnection in a 2D fan-spine topology with different coronal densities. Through forward-modelling of extreme-ultraviolet (EUV) observables, we check whether the plasmoids in our simulations could be detected with the instruments of the Solar Dynamics Observatory (SDO) and Solar Orbiter (SO), as well as of the upcoming Multi-Slit Solar Explorer (MUSE) and Solar-C missions.

Results. Short-lived ($\sim 10 - 20$ s) small-scale ($\sim 0.2 - 0.5$ Mm) coronal plasmoids are not resolvable with the Atmospheric Imaging Assembly (AIA) onboard SDO. In contrast, they could be captured with the EUV High-Resolution Imager at the Extreme Ultraviolet Imager (EUI-HRI_{EUV}) of SO. The spatial and temporal high-resolution planned for the MUSE spectrograph (SG) is adequate to obtain full spectral information of these plasmoids. To achieve a sufficient signal-to-noise ratio for ~ 0.8 MK plasmoids in the MUSE/SG 171 Å channel, this should work on full-raster mode in regions with electron densities above 10^9 cm⁻³ whereas on sit-and-stare mode for lower-density regions. The future Solar-C mission could also capture these coronal plasmoids using the EUV High-Throughput Spectroscopic Telescope (EUVST), through rapid changes in Doppler shift and line width in different EUV lines caused by plasmoid motions along the current sheet.

Conclusions. With combined spectra of MUSE/SG and Solar-C/EUVST in multiple emission lines, along with high-resolution images from SO/EUI-HRI_{EUV} and MUSE/CI, it should be possible to gain new insights about plasmoid formation in the corona.

Key words. magnetohydrodynamics (MHD) – magnetic reconnection – methods: numerical – Sun: atmosphere – Sun: corona – Sun: magnetic fields

1. Introduction

Magnetic reconnection stands out as a candidate for solving the coronal heating problem (Vaiana et al. 1973; Heyvaerts & Priest 1984; Parker 1988). Numerical simulations have shown the ability of this process to generate a wide range of observable solar phenomena such as Ellerman Bombs (EBs), ultraviolet (UV) bursts, coronal bright points (CBPs), surges, coronal jets, and flares (Yokoyama & Shibata 1995, 1996, 2001; Nóbrega-Siverio et al. 2016, 2017, 2023; Wyper et al. 2016, 2017; Hansteen et al. 2017, 2019; Danilovic 2017; Peter et al. 2019; Ni et al. 2021; Nóbrega-Siverio & Moreno-Insertis 2022; Rempel et al. 2023). Furthermore, numerical simulations demonstrate the connection between magnetic reconnection and the formation of small features within current sheets, like plasmoids (Ni et al. 2017; Nóbrega-Siverio et al. 2017; Hansteen et al. 2019; Peter et al. 2019; Guo et al. 2020; Ni et al. 2022; Liu et al. 2023).

Plasmoids appear in any current sheet due to resistive tearing instability (Furth et al. 1963) as long as the Lundquist number is sufficiently high ($S_L > 10^4$, Loureiro et al. 2007) and the cur-

rent sheet width is below a critical value ($a/L < S_L^{-1/3}$, Pucci & Velli 2014). Plasmoid instability causes the characteristics of the reconnection process, including the reconnection rate, to be significantly different from what predicted with the Sweet-Parker (Sweet 1958a,b; Parker 1963) or the Petschek (Petschek 1964) model, which both assume steady reconnection. In particular on the Sun, they have been observationally reported related to EBs, UV bursts, surges, coronal jets, and flares (see, e.g., Rouppe van der Voort et al. 2017, 2023; Kumar et al. 2019; Guo et al. 2020; Yan et al. 2022).

In order to broaden our understanding about magnetic reconnection, further exploration about plasmoids is necessary. This could allow us not only to improve our theoretical models about plasmoid-mediated reconnection in the solar atmosphere, but also to establish constraints on the observational detection capabilities of such features using current and future missions. For instance, the Solar Dynamics Observatory (SDO, Pennell et al. 2012), with its Atmospheric Imaging Assembly (AIA, Lemen et al. 2012; Boerner et al. 2012), observes the corona through several EUV narrow-band filters, including one focused

on the Fe ix 171 Å line. However, its spatial resolution (1"5) makes it challenging for studying plasmoids and other small-scale (< 1 Mm) features. In contrast, the recently launched Solar Orbiter (SO) mission, through the Extreme Ultraviolet Imager instrument and its EUV High-Resolution Imager telescope (EUI-HRI_{EUV}, Rochus et al. 2020), can offer coronal images of appreciably improved spatial and temporal resolution focused on the Fe x 174 Å line, especially at its perihelion distance of 0.3 AU (Berghmans et al. 2023). The near-future launches of the Multi-slit Solar Explorer (MUSE, Cheung et al. 2019, 2022; De Pontieu et al. 2020, 2022) and the Solar-C (Suematsu et al. 2021) missions, are expected to open up more possibilities to delve further into the dynamics of the coronal plasma. In particular, MUSE, with its 35-slit spectrograph (SG), is designed to obtain solar spectra in four bright EUV lines, including Fe ix 171 Å, allowing us to study coronal plasma in temperature ranges all from 0.8 MK to 12 MK at unprecedented timescales. With a spatial pixel size of 0"167 × 0"4, it will provide an excellent opportunity for observing small-scale plasmoids in the corona. In addition, MUSE will have two context imagers (CI) set to observe the Sun with filters centered in the He ii 304 Å and Fe xii 195 Å lines. Solar-C is planned to have a better temperature coverage thanks to the single-slit EUV High-Throughput Spectroscopic Telescope (EUVST, Suematsu et al. 2021), which could scan a wide range of EUV wavelengths, including well-known coronal lines such as Fe ix 171 Å, Fe x 174 Å, and Fe xii 195 Å, among many others. Despite having only one slit, in contrast to MUSE, this spectrograph may provide detailed temperature and density diagnostics in the chosen location where the slit is aimed, with a slightly higher spatial (0"16) and spectral resolution than MUSE. Hence, these two upcoming spectrographs complement each other and can together be used to retrieve detailed information on relatively small structures in the corona.

Preparing for observational studies of plasmoids in the solar corona involves understanding the detectable signatures they may leave. In our previous paper (Færder et al. 2024, hereafter F2024), we carried out numerical simulations of reconnection in a fan-spine magnetic topology within a 2D coronal domain, showing how different resistivity models produced varying plasmoid characteristics. Therefore, characterising observed plasmoid properties could serve as an indicator of the most suitable resistivity model for reproducing coronal-like reconnection. In this paper, we use simulations akin to those in the F2024 paper as a foundation for spectral synthesis, aiming at determining the capability of each of the aforementioned space-borne instruments in detecting small (~ 0.2 – 0.5 Mm), short-lived (~ 10 – 20 s) plasmoids in coronal regions with ~ 0.8 MK. The structure of the paper is as follows. Section 2 describes the numerical model along with the methods applied for spectral synthesis. Section 3 gives a brief overview of the simulations and presents the results from the spectral synthesis. Finally, Sect. 4 gives a brief discussion of these results and summarises the conclusions.

2. Methods

In the following sections, we summarise briefly how we set up our numerical simulations and give some details on how we performed our forward-modelling of each synthetic observable studied in this paper.

2.1. Numerical simulations

The numerical simulations were performed with the Bifrost code (Gudiksen et al. 2011). This code solves the equations of magnetohydrodynamics (MHD) on a 3D Cartesian grid, applying a sixth-order operator for spatial derivatives and a third-order scheme for time derivatives, hence minimising the numerical diffusion due to the discretisation. In our special case, we focused on a 2D coronal domain, neglecting gravity and approximating the equation-of-state by an ideal gas law with a mean molecular weight of 0.616. Concerning the entropy terms, we included Joule heating, viscous heating, and Spitzer conductivity, while neglecting radiative heating/cooling terms. The latter assumption is justified by the fact that the characteristic time for optically thin losses in the corona and transition region (TR) is about 20–100 s (see, e.g., Nóbrega-Siverio et al. 2018), which is longer than the typical plasmoid lifetimes of our simulations.

We perform two simulations using the same initial condition as in the F2024 paper, namely, a fan-spine magnetic topology given by

$$B_x = B_1 e^{-kz} \sin(kx), \quad (1)$$

$$B_z = B_0 + B_1 e^{-kz} \cos(kx), \quad (2)$$

with $k = \pi/16 \text{ Mm}^{-1}$, imposed on a 2D coronal domain with an initial uniform temperature of 0.61 MK and different input values for B_0 , B_1 , and the initial mass density ρ_0 . The first simulation case, which is case G6 from the F2024 paper, has $\rho_0 = 3.0 \times 10^{-16} \text{ g cm}^{-3}$, $B_0 = 3 \text{ G}$, and $B_1 = 10 \text{ G}$, while the second one, referred to as case G6b, has $\rho_0 = 2.7 \times 10^{-15} \text{ g cm}^{-3}$, $B_0 = 9 \text{ G}$ and $B_1 = 30 \text{ G}$. With this, cases G6 and G6b have the same initial plasma- β (inflow value ~ 2), Alfvén speed (inflow value ~ 125 km s⁻¹), and null-point height ($z = 6.13 \text{ Mm}$). The configuration of case G6, with its relatively low mass density and low temperature (compared to the upper corona) and the given magnetic field strength, resembles that of quiet-Sun coronal holes (Hofmeister et al. 2019). Case G6b, with its substantially higher mass density, represents plasma in the lower corona (but not in coronal holes) with a magnetic field strength similar to that of coronal loops (Nakariakov & Ofman 2001; Van Doorselaere et al. 2008).

The boundary conditions of both cases are as given in F2024, with a velocity driver applied on the lower boundary. The experiments span a domain of 32×32 Mm² discretised over 2048×2048 grid points and were run for 40 min. The resistivity is given by the hyper-resistivity model of Bifrost. In F2024, we showed that this resistivity model reproduces plasmoid characteristics in better agreement with results obtained when using significantly higher resolution and uniform resistivity.

2.2. Forward-modelling

Our study focuses on synthetic observables of the Fe ix 171 Å, Fe x 174 Å, and Fe xii 195 Å lines, whose peak formation temperatures lie around 0.8 MK, 1.0 MK, and 1.5 MK, respectively. In the following, we explain the calculations of the corresponding emissivity as well as the total and specific intensities of these lines as received from the Sun without any instrumental effects. Furthermore, we describe the forward-modelling of these lines as observed with different instruments, including the currently active SDO/AIA and SO/EUI-HRI_{EUV} telescopes along with the upcoming MUSE/SG, MUSE/CI, and Solar-C/EUVST.

2.2.1. Emissivity

The emissivity of any optically thin emission line i from chemical element X produced in statistical equilibrium at a given temperature T is given by

$$\epsilon_i = A_X G_i(n_e, T) n_e n_H, \quad (3)$$

where $G_i(n_e, T)$ is the contribution function of the line, A_X the relative abundance of the atomic element X with respect to hydrogen, n_e the electron number density, and n_H the hydrogen number density. The product $n_e n_H$, defined as the emission measure, is already known from our simulations. To retrieve the gain function $A_X G_i(n_e, T)$ for each of the above-mentioned lines, we used the CHIANTI version 10.1 database (Dere et al. 2023, and references therein) with abundances given in the file `sun_coronal_2021_chianti.abund` provided by Del Zanna et al. (2023). Since the gain functions depend weakly on n_e , it is common to assume a fixed electron number density for forward-modelling in the corona (in our case, $n_e = 10^9 \text{ cm}^{-3}$).

2.2.2. Spectral synthesis: VDEM and spectral moments

The total intensity of a line is given by the integral of the emissivity along the line-of-sight (LOS). The intensity as received by a telescope in a given filter which comprises the same line (along with some neighbour lines) is similarly found by integrating the product of the temperature response function for the given filter—which depends on the gain function and the instrumental effects—and the emission measure along the LOS. Synthetic observables of spectrographs, on the other hand, are given by the specific intensity $I_{\lambda,i}$ (rather than just the total intensity). We computed this specific intensity by the following integral

$$I_{\lambda,i} = \iint R_i(T, v_{\text{LOS}}, \lambda) \text{VDEM}(T, v_{\text{LOS}}) dT dv_{\text{LOS}}. \quad (4)$$

where $R_i(T, v_{\text{LOS}}, \lambda)$ is the response function of line i depending of temperature T , LOS velocity v_{LOS} , and wavelength λ , and $\text{VDEM}(T, v_{\text{LOS}})$ is the velocity differential emission measure (VDEM, Cheung et al. 2019).

For our forward-modelling, we applied two different LOS: the vertical z -direction, integrating the whole box from the top and downwards to mimic an on-disk observation; and the horizontal y -direction, in order to mimic an off-limb observation, assuming to that end that our computational domain has a width of 0.2 Mm, which roughly represents the typical diameter of the larger plasmoids of our simulations. Response functions for the 171 Å, 174 Å, and 195 Å lines were computed using gain functions from CHIANTI as described above, assuming Gaussian line profiles with thermal broadening (initially neglecting instrumental broadening in order to study the pure line spectra as obtained from the Sun). The VDEM was calculated with routines developed by the MUSE team (Cheung et al. 2019), with a velocity sampling of 2.5 km s^{-1} and a $\log T(\text{K})$ sampling of 0.025.

With the specific intensity (of any line i) given by Eq. (4), we compute the zeroth, first, and second spectral moments, defined as follows,

$$M_0 = \int I_\lambda d\lambda, \quad (5)$$

$$M_1 = \frac{\int \lambda I_\lambda d\lambda}{M_0}, \quad (6)$$

$$M_2 = \frac{\int (\lambda - M_1)^2 I_\lambda d\lambda}{M_0}, \quad (7)$$

where the zeroth moment is the total intensity as integrated over the line profile, the first moment is the Doppler shift of the line profile, while the square root of the second moment gives the line width σ . The line width is related to the full width at half maximum (FWHM) of the line profile by $\sigma = \text{FWHM} / \sqrt{8 \ln 2}$. In our maps of spectral moments without instrumental effects, the intensities are given in CGS units ($\text{erg cm}^{-2} \text{ sr}^{-1} \text{ s}$), while the Doppler shifts and line widths are given in km s^{-1} .

2.2.3. SDO/AIA 171 Å

The synthetic SDO/AIA intensity in the 171 Å filter, for any chosen LOS-coordinate s_{LOS} , was estimated by the following integral,

$$I_{\text{SDO/AIA } 171 \text{ \AA}} = \int ds_{\text{LOS}} R_{\text{SDO/AIA } 171 \text{ \AA}}(T) n_e n_H, \quad (8)$$

where the temperature response function $R_{\text{SDO/AIA } 171 \text{ \AA}}(T)$ was acquired using the SolarSoft (Freeland & Handy 1998) routine `aia_get_response`. Since SDO/AIA is an Earth-bound instrument with a spatial pixel size of $0''.6$, one pixel on an AIA image covers a $\sim 0.44 \text{ Mm}$ wide region on the Sun. Therefore, we degraded the resolution on all our synthetic AIA images to this pixel size. We also added some Gaussian smoothing to account for the AIA spatial resolution of $1''.5$, or $\sim 1.1 \text{ Mm}$ (Lemen et al. 2012). Since the AIA is capable of taking images with a cadence of 12 seconds, we applied this cadence for the temporal resolution in the AIA intensity maps against time.

2.2.4. SO/EUI-HRI 174 Å

For the SO/EUI-HRI 174 Å filter, we used the SO/EUI-HRI 174 Å response function $R_{\text{SO/EUI-HRI } 174 \text{ \AA}}(T)$ —provided to us by Dr. Frédéric Auchère, member of the Solar Orbiter team (see also Gissot et al. 2023)—to compute the intensity

$$I_{\text{SO/EUI-HRI } 174 \text{ \AA}} = \int ds_{\text{LOS}} R_{\text{SO/EUI-HRI } 174 \text{ \AA}}(T) n_e n_H. \quad (9)$$

EUI-HRI_{EUV} has an spatial pixel size of $0''.5$ as seen from the location of the telescope. At its perihelion distance of 0.3 AU, a pixel, therefore, covers a $\sim 0.11 \text{ Mm}$ wide region of the Sun, which is the pixel size we degraded our synthetic EUI-HRI_{EUV} images to. The temporal resolution is given by a cadence of 1 second.

2.2.5. MUSE/SG Fe IX 171 Å and MUSE/CI 195 Å

Specific intensities for the MUSE/SG Fe IX 171 Å line were calculated by Eq. (4) using the same VDEMs as used for the pure line spectra (without instrumental effects), though degraded to fit a spatial pixel size of $0''.167 \times 0''.167$ ¹, and using a similar response function but with an instrumental broadening in addition to thermal broadening. Hence, the total line width of any line profile seen through the MUSE/SG is given by

$$\sigma = \sqrt{\sigma_{\text{th}}^2 + \sigma_{\text{instr}}^2 + \sigma_{\text{n-th}}^2}, \quad (10)$$

¹ Though the actual pixel size of MUSE/SG will be $0''.167 \times 0''.4$, we only consider the smallest pixel size, only for the xz field-of-view (FOV), when synthesising spectra to preserve the highest resolution achievable with MUSE/SG (De Pontieu et al. 2022).

where $\sigma_{\text{th}} \equiv \sqrt{k_{\text{B}}T/m_{\text{Fe}}}$ is the thermal width, given the iron mass m_{Fe} , σ_{instr} the instrumental width, and $\sigma_{\text{n-th}}$ the non-thermal width due to variations in the (LOS component of the) fluid velocity along the LOS. The MUSE/SG Fe IX 171 Å line has a spectral sampling of 14.6 mÅ and the instrumental FWHM is 2.9 times the spectral sampling, hence 43.34 mÅ or 74.25 km s⁻¹ in terms of Doppler velocity, found by multiplying the value in angstroms by c/λ_0 , where c is the speed of light, and $\lambda_0 = 171.073$ Å. This gives an instrumental width of $\sigma_{\text{instr}} = \text{FWHM}_{\text{instr}}/\sqrt{8 \ln 2} = 17.98$ mÅ or 31.53 km s⁻¹ in terms of Doppler velocity. We computed the total intensity, Doppler shift, and line width from the MUSE/SG Fe IX 171 Å specific intensities using Eqs. (5)-(7). For the temporal resolution, we assumed a cadence of 12 seconds, which is roughly the time needed to perform the densest raster—requiring a reading/moving time of 0.4 s for each of the 11 slit positions—to achieve the best spatial resolution (De Pontieu et al. 2020), assuming an exposure time of 0.6 s for each slit position. Such a high cadence is only needed for images with the highest-achievable resolution in both dimensions. If high resolution is only needed in one dimension, MUSE can provide sit-and-stare images with a cadence nearly equal to the exposure time. The intensity units for the synthetic MUSE/SG spectra are given in photon count per pixel per second (ph pix⁻¹ s⁻¹), whose conversion from units of erg cm⁻² sr⁻¹ s⁻¹ is as following:

$$I[\text{ph pix}^{-1} \text{s}^{-1}] = I[\text{erg cm}^{-2} \text{sr}^{-1} \text{s}^{-1}] \frac{\text{sr}}{\text{pix}} \epsilon_{\text{eff}} \frac{\lambda_0}{hc}, \quad (11)$$

where sr/pix denotes the size of the solid angle observed by one pixel, which for MUSE/SG is $0.167 \times 0.4 \times (2\pi/360/3600)^2$. The effective area ϵ_{eff} is 3.7 cm² for the 171 Å filter. Furthermore, hc/λ_0 is the energy per photon.

We also synthesised intensity maps for the MUSE/CI in the 195 Å filter. For this, we computed the emissivity of the Fe XII 195 Å line given by Eq. (3) with the gain function for the 195 Å line (acquired from CHIANTI), integrating the emissivity along the LOS and degrading to MUSE/CI spatial pixel size of $0''.33 \times 0''.33$. Again, units were converted to ph pix⁻¹ s⁻¹ by Eq. (11), with an effective area $\epsilon_{\text{eff}} = 5.0$ cm² for the 195 Å filter. For temporal resolution, we assumed a cadence of 4 s.

2.2.6. Solar-C/EUVST Fe X 174 Å and Fe XII 195 Å

Solar-C/EUVST Fe X 174 Å and Fe XII 195 Å specific intensities were computed from Eq. (4) the same way as for MUSE/SG Fe IX 171 Å using similar response functions assuming the given EUVST instrumental broadening of ($\text{FWHM}_{\text{instr}} = 40$ mÅ, hence) $\sigma_{\text{instr}} = 16.99$ mÅ and a VDEM resolution of $0''.16 \times 0''.16$ for preserving the highest possible resolution achievable along any chosen slit alignment. With spectral moments calculated from Eqs. (5)-(7), the intensity unit conversion into photons per pixel per second was found by using Eq. (11) with the given pixel dimensions of $0''.16$ along the slit and $0''.4$ across the slit, along with the EUVST effective areas, which for 174 Å and 195 Å is 0.61 cm² and 1.2 cm², respectively.

3. Results

In the following sections, we first summarise main events of our simulations with special emphasis on the plasmoid dynamics

along with the overall evolution of the temperature and velocity in the simulated fan-spine structure. Furthermore, we study each of our synthetic observables in detail in order to determine to which extent the different currently-active and upcoming instruments may provide observational diagnostics on plasmoids in the solar corona.

3.1. Simulation summary

Our simulations evolve similarly to the ones described in F2024. To give a quick overview, Fig. 1 contains the temperature, T , emission measure, $n_e n_H$, vertical velocity component, u_z , and velocity divergence, $\nabla \cdot \mathbf{u}$, with the magnetic field lines superimposed for both simulations. Here, u_z is defined to be positive for velocities pointing out from the Sun, in agreement with the z -axis which is defined to point outwards as well.

In each simulation, the null-point collapses as soon as the inner spine starts moving in positive x -direction, and a tilted current sheet is formed between the inner and outer spine. Reconnection occurs along the current sheet throughout the simulation as the inner spine keeps moving. During the reconnection process, plasmoids frequently appear along the current sheet, about 6-7 plasmoids per minute, moving either upwards to the left or downwards to the right. The plasmoids have sizes between $\sim 0.2 - 0.5$ Mm and lifetimes around 10 - 20 s. These lifetimes are shorter than the typical characteristic time scales for optically thin losses, hence justifying our choice to neglect them in our simulation cases since they would not affect the dynamics. The advection of plasmoids along the current sheet triggers shocks, seen in the velocity-divergence panels (lower right) as a wavy pattern of short pulses where $\nabla \cdot \mathbf{u}$ oscillates roughly between -0.3 and 0.3 s⁻¹. The velocity panels (lower left) clearly illustrate the reconnection inflows and outflows, which are particularly prominent around the spines of the structure. The temperature panels (upper left) show that the plasma is heated due to the reconnection to temperatures up to ~ 0.73 MK in case G6 and ~ 0.84 MK in case G6b. However, the plasmoids in G6b occasionally reach temperatures close to 1 MK. The emission measure (upper right panels) is nearly two orders of magnitude higher in case G6b than in G6 due to the density difference of almost one order of magnitude. This difference has a noticeable impact on the observable traceability of the magnetic reconnection features, as seen in the following sections.

3.2. Fe IX 171 Å observables

In this section, we study how our simulated fan-spine topology looks like in the Fe IX 171 Å line, whose peak formation temperature lies within the temperature ranges of the simulated fan-spine structure. First, we analyse the pure Fe IX 171 Å spectra as obtained from the Sun without any instrumental effects. Furthermore, we look at the Fe IX 171 Å intensity as retrieved with the currently-active SDO/AIA telescope. Finally, we examine how the Fe IX 171 Å spectra will look like with the upcoming MUSE/SG.

3.2.1. Fe IX 171 Å line spectra

Figure 2 and associated animation show the synthetic Fe IX 171 Å line spectra as obtained without any instrumental effects for both simulations. The first column contains the off-limb intensity. In both simulations, the plasmoid (marked by a grey arrow), the spines, and the fan surfaces are considerably brighter

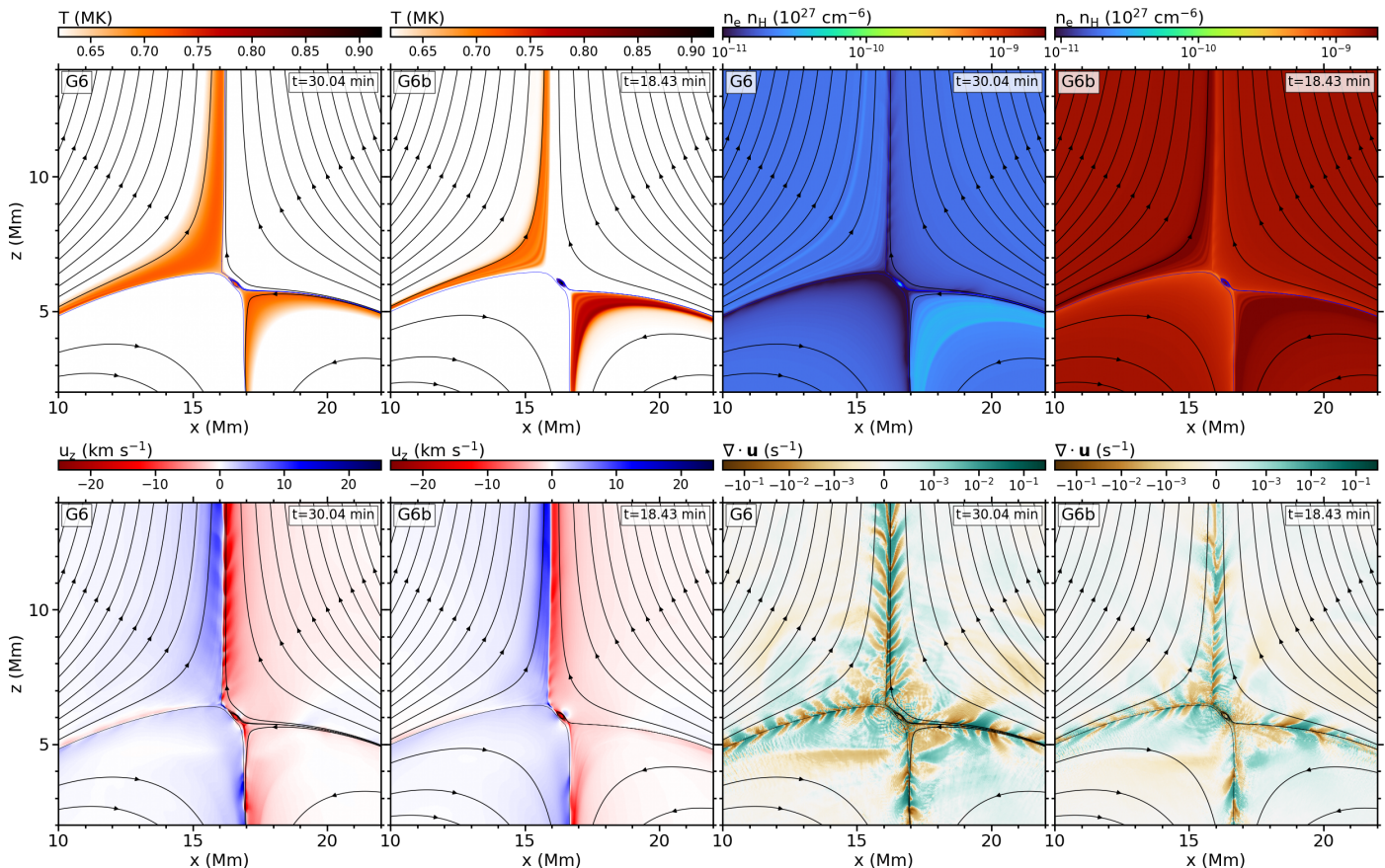


Fig. 1: Temperature T , emission measure $n_e n_H$, vertical velocity component u_z (defined to be positive for velocities out of the Sun), and velocity divergence $\nabla \cdot \mathbf{u}$ with magnetic field topology superimposed in cases G6 and G6b. A movie of the full time evolution for $t \in [0, 40]$ min is available online.

than the surrounding medium. This is due to the temperature here being closer to the peak formation temperature for this line as well as the emission measure being slightly higher than the surroundings. The overall intensity in case G6b is nearly of two orders of magnitude higher than in case G6 as a direct consequence of the similar difference in emission measure seen in Fig. 1.

The second column of Fig. 2 shows the on-disk intensity. In these maps, and all the following figures with similar maps, the range of the colorbar is intentionally set to highlight the plasmoid imprints, even though the intensity map gets saturated in the regions outside the current sheet. With this, the current sheet region is here easily located as the non-white area, being darker than the surroundings due to the slightly decreased temperature and emission measure of the above-lying plasma. Plasmoids are seen as tiny, bright, and tilted stripes, a few of them being marked by arrows to ease their localisation. The intensity signatures of the plasmoids approaching the outer spine appear darker than of those approaching the inner spine. This is because the region above the current sheet is darker in the areas closer to the outer spine, and the plasma above the current sheet covers a larger fraction of the LOS integration path. Therefore, the areas above the current sheet which lies closer to the outer spine obtains a considerably lower total intensity contribution than the areas further away. As a consequence, the outer-spine-bound plasmoids are in this map essentially less enlightened than the inner-spine-bound plasmoids, so that only the latter ones are seen in this map. Again, the overall intensity is nearly of two orders of magnitude higher in G6b than in G6.

The third column of Fig. 2 illustrates the Doppler shift of the line, also as observed on-disk. In this map, and all following Doppler shift maps, positive Doppler shift (redshift) corresponds to plasma moving away from the observer (i.e., inwards to the Sun). With this definition, negative values of u_z (downflows) contributes positively to the Doppler shift. In both simulations, the line is redshifted in the region to the right of the outer spine and blueshifted in the region to the left, in good agreement with the vertical velocity distribution mapped in Fig. 1. The outer spine can easily be located as the distinct white, nearly-vertical stripe between the blue and red area. The inner spine appears less distinct but can be identified as the boundary between a tilted red-white stripe and a darker red stripe. The x -position of both spines are marked by dashed, curved arrows (only for this figure) to ease their identification. In the current sheet region (located between the dashed arrows), plasmoids can be seen as weak, thin stripes. For the same reason as for the on-disk intensity map, we mainly see the signatures of plasmoids that move downwards (towards the inner spine), appearing as slightly darker, red stripes (see arrows). Signatures of the upward-moving, outer-spine-bound plasmoids, on the other hand, are almost not seen at all, as their intensity contribution is overshadowed by the above-lying, downward-moving plasma.

The fourth column shows the line width, σ , of the Fe ix 171 Å line profile. Far from the current-sheet region, where the line broadening is mainly dominated by thermal broadening, the line width is $\sim 9.5 \text{ km s}^{-1}$, as expected, since this is approximately equal to the thermal width $\sigma_{\text{th}} \equiv \sqrt{k_B T / m_{\text{Fe}}}$ for $T = 0.61 \text{ MK}$.

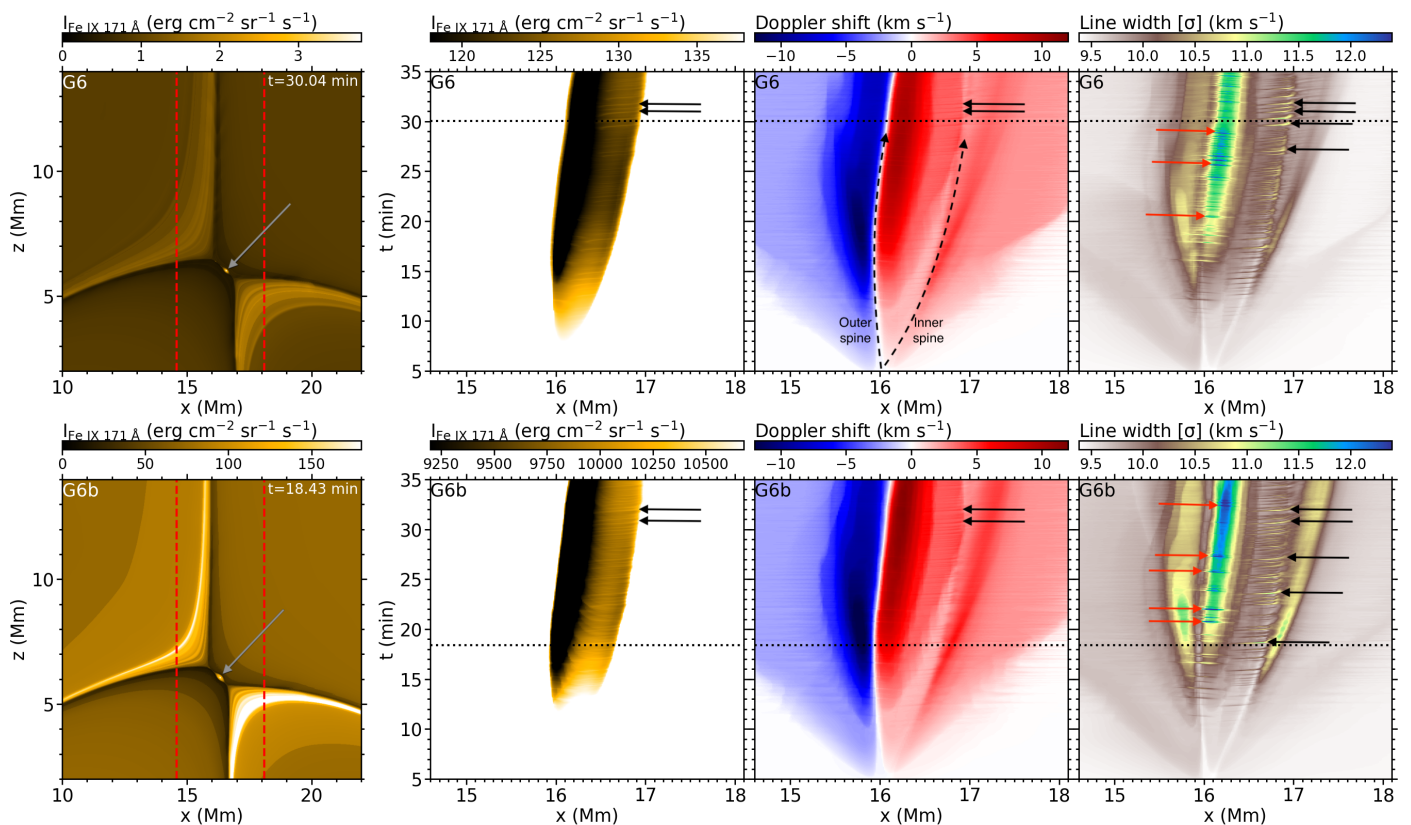


Fig. 2: Synthetic spectral moments of the Fe IX 171 Å line with no instrumental effects for the simulations G6 (top) and G6b (bottom). The first column contains the off-limb intensity at a given time. The other three columns show the on-disk observables for the intensity, Doppler shift, and line width, respectively, as functions of x and t . The red dashed lines in the first column delimit the x range shown in the other three columns. The black dotted lines on the latter three columns mark the time illustrated in the first column. The solid arrows point at the location of some plasmoids: red ones for those upward-moving; black or grey for downward-moving. The dashed (curved) arrows mark the inner an outer spine location (upper third panel only). A movie of the full-time evolution of the figure for $t \in [0, 40]$ min is available online.

Closer to the current sheet, the line width is increased to values ranging from 10 to 13 km s⁻¹. The line broadening is especially high in the (green) area above the current-sheet which lies closer to the outer spine ($x \in [16.1, 16.4]$ Mm for $t > 20$ min), due to a strong non-thermal broadening caused by large oppositely-directed bulk velocities below and above the current sheet. In fact, non-thermal broadening is the main contributor of the additional broadening effects around the current sheet, as the thermal broadening contributions from the heated plasma is nearly negligible except for the region to the left of the outer spine and to the right of the inner spine (seen clearly as large yellow areas in G6b), where the heated plasma covers a larger LOS integration. Especially, one may note that the region $x \in [17.5, 18.0]$ Mm, which lies above the strongly heated right fan-surface, has here nearly the same total line broadening as any region far from the fan-spine structure. In our simulations, non-thermal broadening is exclusively caused by variations in the LOS velocity along the LOS. Signatures of the plasmoids can be seen in this map, both close to the inner and outer spines. The upward-moving, outer-spine-bound plasmoids, marked by red arrows, appear as thin, blue stripes, and the downward-moving, inner-spine-bound plasmoids, marked by black arrows, appear as thin, yellow stripes. These stripes get thicker near the end of the current sheet, where the plasmoids collide into the spine, which also causes a further enhancement in the line broadening. The largest line width measured in the plasmoids is about 13.3 km s⁻¹ in case G6b. Since

the plasmoids' contribution to thermal broadening is negligible here (being smaller in width than the fan-surface, where the line width is nearly unaffected by the heated plasma), one may conclude that the visible signatures of the plasmoids here are caused by non-thermal broadening due to the motion of the plasmoids along the current sheet. The thermal width above the plasmoids is therefore still roughly around $\sigma_{\text{th}} \approx 9.5$ km s⁻¹. Hence, since $\sigma = \sqrt{\sigma_{\text{th}}^2 + \sigma_{\text{n-th}}^2}$, one may estimate that the non-thermal width is around $\sigma_{\text{n-th}} \approx 9.3$ km s⁻¹, that is, nearly-equal to the thermal width.

3.2.2. SDO/AIA 171 Å intensities

The SDO/AIA 171 Å intensity maps are shown in Fig. 3. The two leftmost panels clearly show that the AIA instrument lacks enough resolution to resolve the plasmoids that are generated along the current sheet. The fan-spine topology is still resolvable in both cases. In G6, however, the count rate (< 1 DN pix⁻¹s⁻¹) indicates that the outer spine emits barely one photon every two seconds. The photon count per pixel need to be above ~ 100 in order for the signal-to-noise ratio to be satisfactorily high. It would therefore require an exposure time of at least two minutes in order for the fan-spine topology of G6 to become visible on an observational image. For case G6b, the count rate is above the desirable level for the fan-spine topology to be detectable in

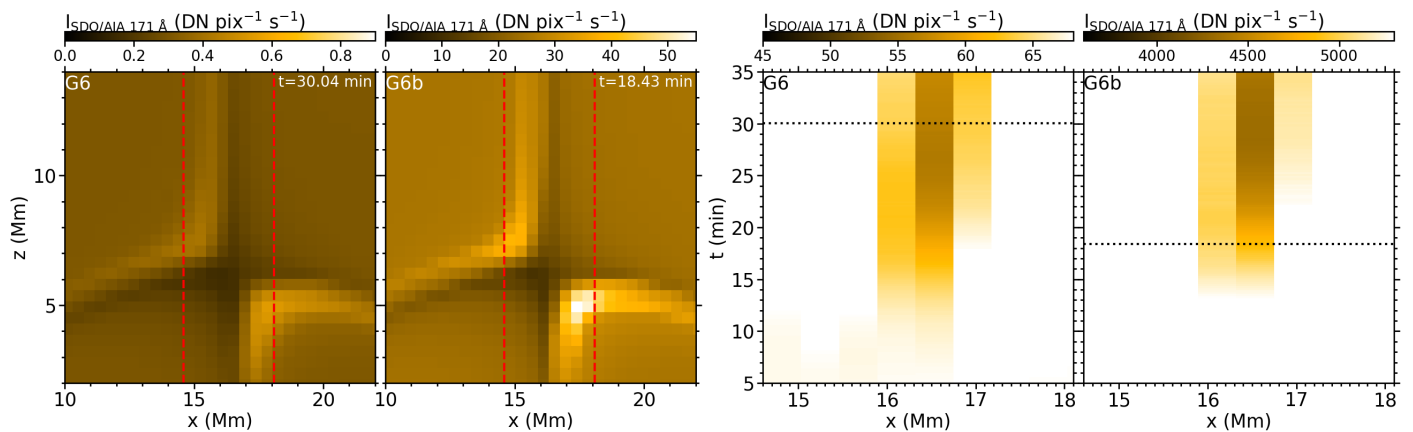


Fig. 3: Synthetic SDO/AIA 171 Å response for the simulations G6 and G6b as seen off-limb (two leftmost panels) and on-disk (two rightmost panels). The red dashed lines in the two leftmost panels delimit the x -range for the other two panels. The black dotted line in the two rightmost panels marks the time shown in the two leftmost panels.

the off-limb view, even with an exposure time of a few seconds. As seen from the count rate in the right-side panels, the on-disk SDO/AIA 171 Å response is slightly dimmer above the current sheet than in the surroundings, in agreement with what is seen in Fig. 2, though the current sheet here is no more than three pixels wide when viewed with AIA. The post-reconnection loops (though difficult to see in the on-disk intensity maps due to the chosen colorbar range) are still substantially brighter than the surroundings and can easily be detected with this instrument.

3.2.3. MUSE/SG Fe IX 171 Å spectra

To study the capabilities of MUSE, Fig. 4 (and the associated movie) contains the synthetic spectral moments of the MUSE/SG Fe IX 171 Å line for simulations G6 and G6b. It is similar to Fig. 2 but includes MUSE/SG instrumental effects. The first column shows that our plasmoids are clearly well-resolved with MUSE/SG in the off-limb view. The photon count rate for the low-density case G6, however, is below the required threshold for plasmoid detection. Even with an exposure time of 10–20 seconds, which corresponds to the typical lifetime of our simulated plasmoids, barely 1–2 photons per pixel will be received from the plasmoid, which is not enough to make the signals brighter than the noise. As for case G6b, both the fan, spines, and plasmoids have a remarkably higher photon count rate (> 5 ph pix $^{-1}$ s $^{-1}$) and can be possible to detect, for instance by taking sit-and-stare images with the slit aligned with the current sheet and an exposure time between 10 and 20 seconds.

The on-disk MUSE/SG Fe IX 171 Å intensity (second column of Fig. 4) is noticeably dimmer in the region above the current sheet than in the surroundings. Plasmoids are here seen as thin, white, stripes (see arrows). The photon count rates indicate that plasmoids of both cases G6b and G6 should be visible through the MUSE/SG Fe IX 171 Å line in this on-disk view, at least with sit-and-stare images for case G6 (to allow for an exposure time of 10–20 s) and even with full-raster images for case G6b.

The corresponding Doppler shift maps (third column) look nearly the same for both simulation cases. The line is blueshifted on left side of the spine and redshifted on the right side due to plasma moving vertically in opposite directions on each side of the spine, in a similar fashion to what is seen in Fig. 2. Plasmoid signatures appear as thin, blue stripes (marked by red arrows) along the outer spine and as slightly darker red stripes (marked

by black arrows) along the inner spine. The maximum change in Doppler shift due to the plasmoids are of order $\sim 2 - 3$ km s $^{-1}$.

The evolution of the line width (Fig. 4, fourth column) is also very similar for both simulations. The line width stays roughly around ~ 33 km s $^{-1}$ due to the instrumental width of $\sigma_{\text{instr}} = 31.5$ km s $^{-1}$ which makes the thermal and non-thermal broadening effects small in comparison. In the regions far from the spines, the plasma is at rest and not essentially heated, leaving the temperature barely above 0.61 MK. Therefore, we have $\sigma_{\text{th}} = 9.53$ km s $^{-1}$ and $\sigma_{\text{n-th}} \approx 0$, which, together with the above-mentioned instrumental broadening, agrees with the total line width of $\sigma \approx 32.9$ km s $^{-1}$, seen in the line width maps far from the spines. At the centre of the outer spine, the line width is enhanced by $\sim 0.5 - 0.7$ km s $^{-1}$. Imprints of plasmoids are seen as blue stripes (marked by red arrows) along the outer spine and yellow stripes (marked by black arrows) along the inner spine. As discussed in Sect. 3.2.1, these plasmoid signatures in the line width map are mainly due to non-thermal broadening, caused by the motion of plasmoids along the current sheet, and not by the heating of the plasmoids. Here, the total line width reaches values up to 33.8 km s $^{-1}$, in good agreement with the previously-estimated non-thermal broadening of about ~ 9.3 km s $^{-1}$. This maximum line width (seen in the plasmoids) is still only about 1% higher than the average line width measured in the same region when no plasmoids are present, and consequently, one can expect that these plasmoids will not leave any visible trace in the observed MUSE/SG Fe IX 171 Å line width with observational noise taken into consideration.

Synthetic Solar-C/EUVST Fe IX 171 Å spectra are not included here since its response function is very similar to that of MUSE/SG Fe IX 171 Å. With only slightly higher spatial and spectral resolution than MUSE/SG, this one-slit spectrograph can be expected to produce a nearly identical on-disk observation of the simulated fan-spine topologies of cases G6b and G6 as seen in the latter three panels of Fig. 4. Besides, producing a two-dimensional image mimicking the off-limb images of MUSE/SG Fe IX 171 Å would take longer time for Solar-C/EUVST, which only has one slit, hence achieving a considerably lower cadence.

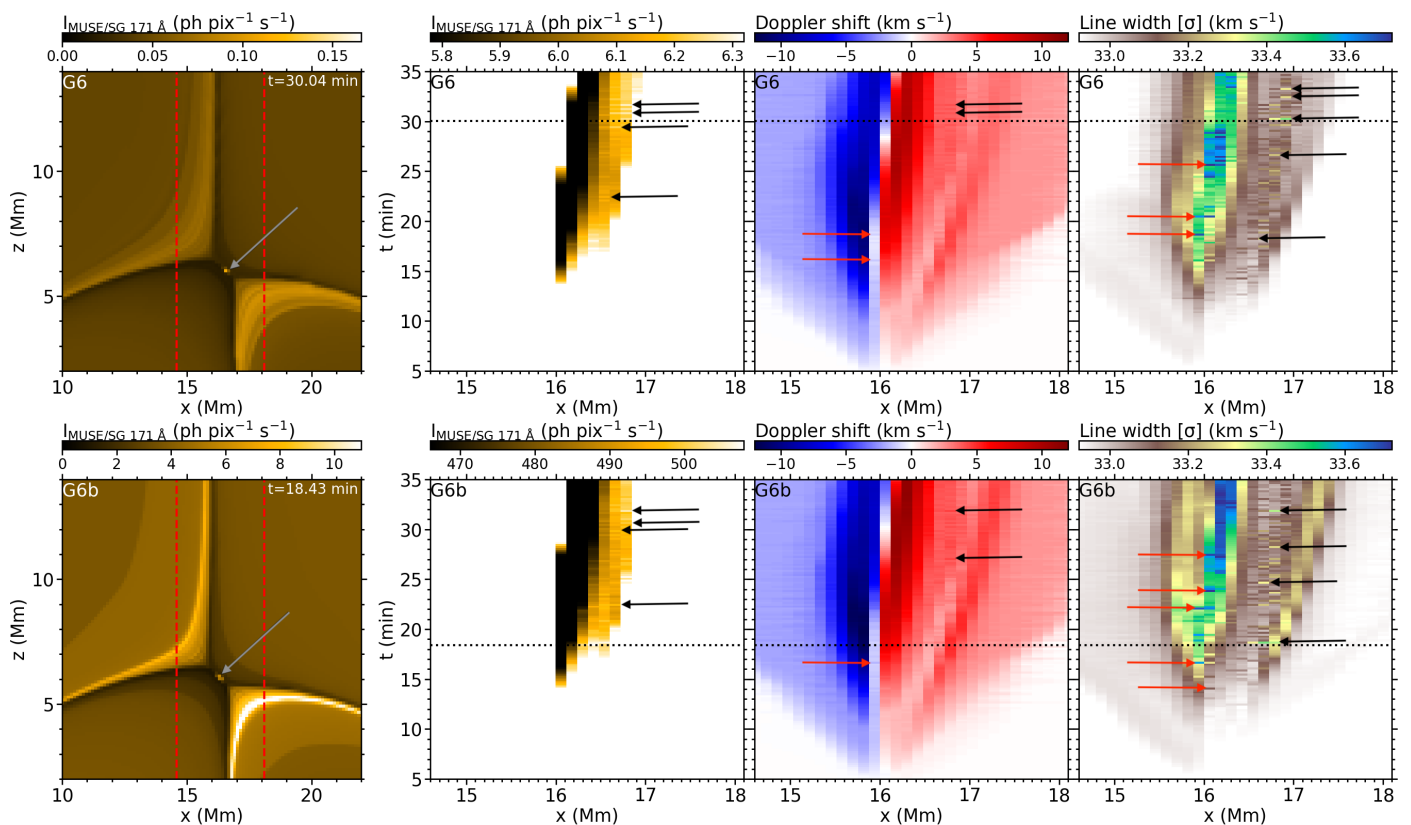


Fig. 4: Synthetic MUSE/SG Fe IX 171 Å spectral moments for the simulations G6 (top) and G6b (bottom). Layout is the same as for Fig. 2. A movie of the full-time evolution of the figure for $t \in [0, 40]$ min is available online.

3.3. Fe x 174 Å observables

Similarly to the previous section, we here study synthetic observables of the Fe x 174 Å line. While its peak formation temperature of 1 MK is slightly above the typical temperatures of our simulated fan-spine structure, the plasmoids of G6b occasionally reach such high temperatures. Like the previous section, we start by looking at the pure spectra without instrumental effects before delving into the Fe x 174 Å observables as retrieved with the following instruments: 1) the EUH-RES-EUV telescope onboard the recently-launched SO mission; and 2) the EUVST spectrograph onboard the upcoming Solar-C mission.

3.3.1. Fe x 174 Å line spectra

Figure 5 and associated animation map the Fe x 174 Å line spectra without instrumental effects in a similar manner as Fig. 2 for the Fe IX 171 Å line. The mapped spectral moments of the Fe x 174 Å line are similar to those of the Fe IX 171 Å line with the following differences. The fan-spine intensity is about one order of magnitude weaker here because: 1) the Fe x 174 Å peak formation temperature is higher than that of Fe IX 171 Å, hence slightly more outside the temperature ranges of our simulated fan-spine structures; and 2) the Fe x 174 Å gain function has a lower peak value as well. Furthermore, the Fe x 174 Å intensity maps have larger contrasts, with the intensity being close to zero in the non-heated regions. Because of this, the plasmoids are more distinguishable in this line, making them more visible in the on-disk intensity maps (second columns) as well, as the total intensity here depends less on contributions from above the current sheet. Though the downward-moving, inner-spine-bound

plasmoids (marked by black arrows) are still easiest to spot here for the same reasons as for the Fe IX 171 Å case, a few upward-moving, outer-spine-bound plasmoids (marked by red arrows) are visible here as well. The Doppler shift maps (third column) are very similar to those of the Fe IX 171 Å line, as expected, except for the imprints of the plasmoids being slightly more visible here. The inner-spine-bound plasmoids (see black arrows) are seen as dark red stripes because they move inwards, away from the observer, hence contributing in increasing the total redshift. Similarly, the outer-spine-bound plasmoids (see red arrows) are seen as light red stripes as they move outwards, towards the observer, hence contributing in decreasing the total redshift. The Fe IX 174 Å line width (fourth column) are also more strongly enhanced in the signatures of the plasmoids, along with the spines and fan surfaces—compared to the Fe IX 171 Å line—since the main intensity contributions for this line lie in those features (while the contributions from the surroundings are more negligible). Consequently, the imprints of the plasmoids (see arrows) are more distinct here as well. These additional line-width-increases caused by the plasmoids are still mainly from non-thermal broadening due to the motion of plasmoids along the current sheet. The regions next to the outer (blue-green) and inner (green) spines are clearly marked here by their considerably increased line widths. Hence, the low-line-width region which lies between these two regions of increased line width provides a good proxy for localising the null-point.

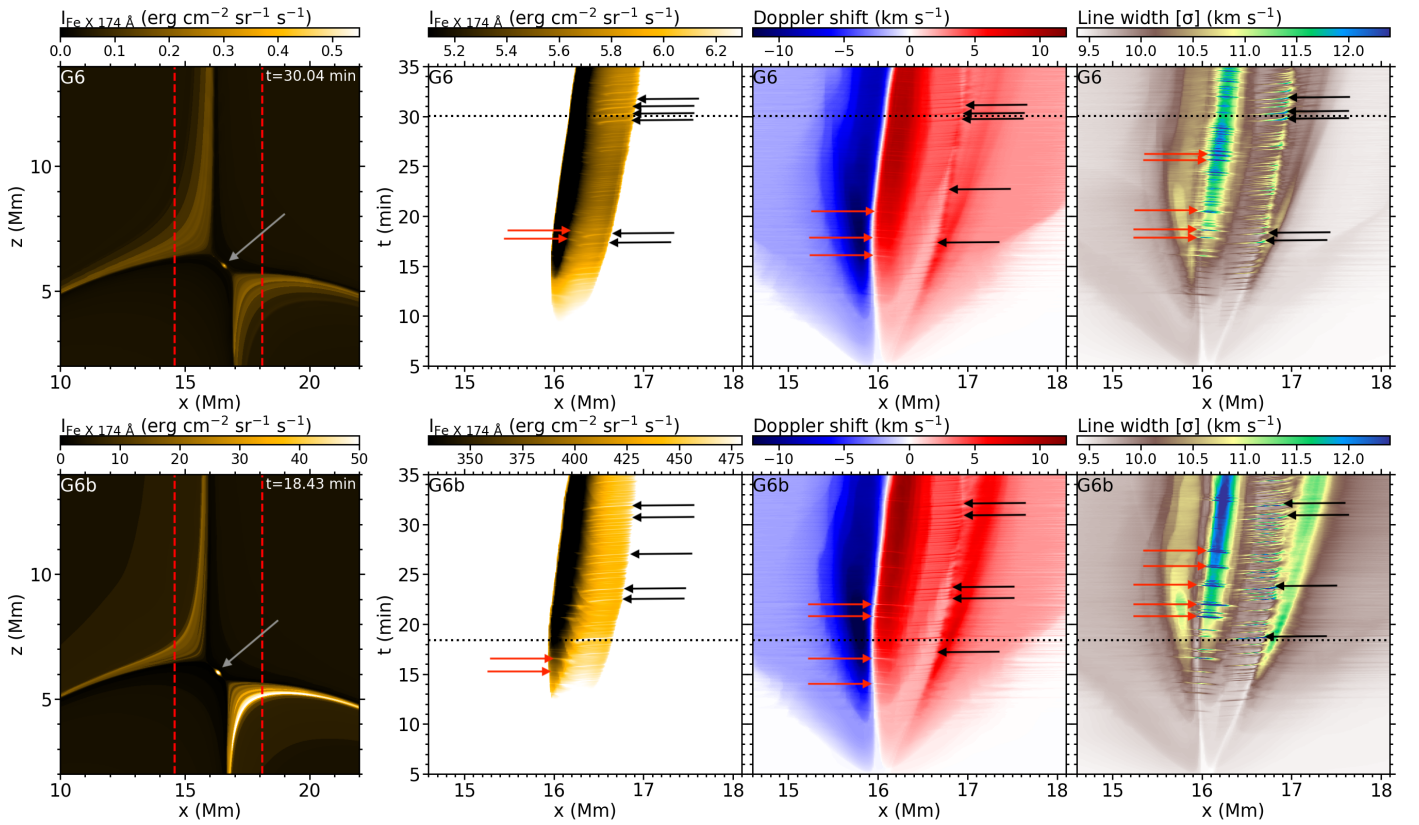


Fig. 5: Synthetic spectral moments of the Fe x 174 Å line with no instrumental effects for cases G6 (top) and G6b (bottom). Layout is the same as for Fig. 2. A movie of the full-time evolution of the figure for $t \in [0, 40]$ min is available online.

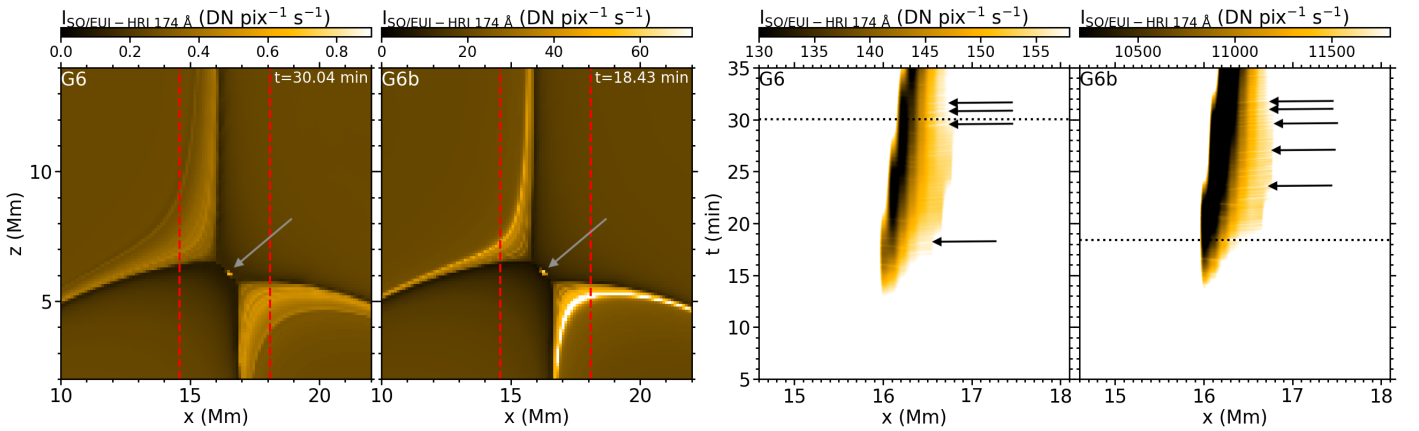


Fig. 6: Synthetic SO/EUI-HRI 174 Å response for the simulations G6 and G6b as seen off-limb (two leftmost panels) and on-disk (two rightmost panels). Layout is the same as for Fig. 3, with the addition of arrows pointing at the location of some plasmoids.

3.3.2. SO/EUI-HRI 174 Å intensities

The SO/EUI-HRI 174 Å intensities are mapped in Fig. 6 in a similar manner as in Fig. 3 for SDO/AIA 171 Å. From the two leftmost panels, we see that the contrast in the intensity maps is smaller than in the intensity maps of the isolated 174 Å line. This is because the SO/EUI-HRI 174 Å filter comprises several emission lines that lie near the 174 Å line in the spectrum, hence its total intensity has non-negligible contributions from these lesser lines in addition to the main line. Therefore, the regions outside the fan-spine-topology are not completely dark in this filter. The count rates do actually have similar values as in the SDO/AIA

171 Å intensity maps, but the resolution is remarkably better. Plasmoids are resolvable both in G6 and G6b. In the latter case, these plasmoids reach a count rate beyond the level required for detection, given an exposure time of a few seconds. In the on-disk view (two rightmost panels), plasmoids are again seen as bright stripes in the current sheet region (see arrows), and their photon count rates are above the lower limit for detection in both cases.

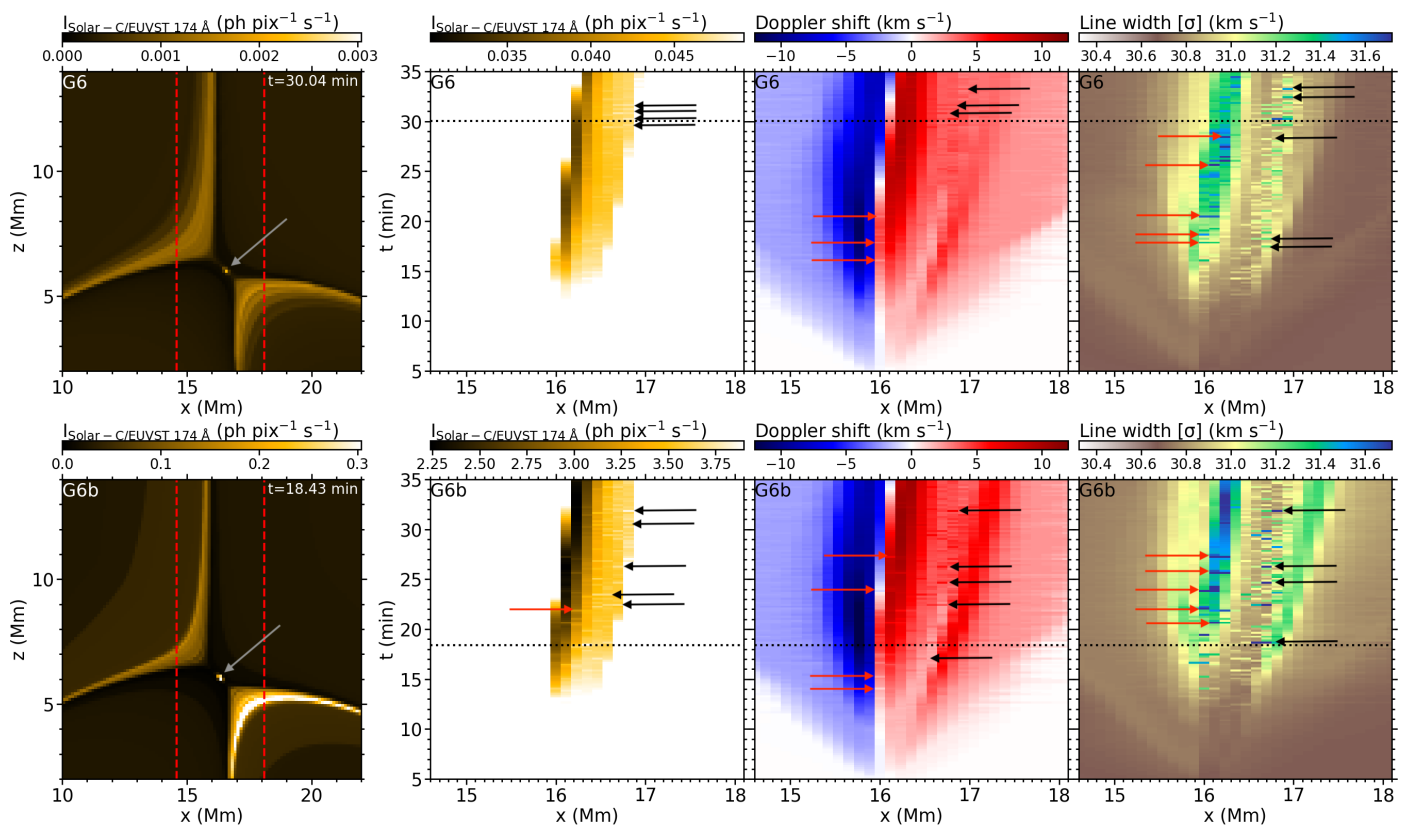


Fig. 7: Synthetic Solar-C/EUVST 174 Å spectral moments for cases G6 (top) and G6b (bottom). Layout is the same as for Fig. 2. A movie of the full-time evolution of the figure for $t \in [0, 40]$ min is available online.

3.3.3. Solar-C/EUVST Fe x 174 Å spectra

The spectral moments of the Solar-C/EUVST Fe x 174 Å line are shown in Fig. 7 and its associated movie in a similar manner as Fig. 4 for MUSE/SG Fe ix 171 Å. Even though EUVST is a single-slit spectrograph, we still choose to include a 2D map (first column) of the synthetic off-limb intensity for the sake of context and consistency with previous figures since the slit may be placed in any location above the fan-spine topology to produce a 1D projection of this map. In our cases, the photon count rates are below the desired level to detect the plasmoids in this view. The mapped on-disk spectral moments, as seen in the latter three columns, may be reproduced observationally with EUVST if the slit is aligned properly with the current sheet. In the on-disk intensity maps (second column), the plasmoids are seen as bright dots in the current sheet. The imprints of the plasmoids (see arrows) in G6b reach a photon count rate satisfactory for detection given an exposure time of $\sim 10 - 20$ s. The Doppler shift maps (third columns) show an increased redshift for the inner-spine-bound plasmoids (see black arrows), akin to the corresponding MUSE/SG Fe ix 171 Å spectra, and a decreased redshift for the outer-spine-bound plasmoids (see red arrows). The increases in redshift due to the downwards-moving (inner-spine-bound) plasmoids seen in the Solar-C/EUVST Fe x 174 Å spectra are of order ~ 5 km s $^{-1}$, which is higher than the corresponding increases in the MUSE/SG Fe ix 171 Å Doppler shift and in agreement with the (non-instrumental) Fe x 174 Å line Doppler shift (Fig. 5). The decreases in redshift due to the upwards-moving plasmoids are of the same order or weaker. Also, similarly to the MUSE/SG Fe ix 171 Å spectra, the instrumental broadening of EUVST (which is about 29.2 km s $^{-1}$ for the Fe x 174 Å line)

substantially overshadows the thermal and non-thermal broadening, resulting in a line width lying around 30 – 31 km s $^{-1}$. Still, since the major contributions to the Fe x 174 Å line intensity come from the plasmoids and spines, the imprints of the plasmoids (see arrows) in the line-width maps are slightly more visible here than for MUSE/SG Fe ix 171 Å, with the line width being enhanced by up to 3 % when a plasmoid hits one of the spines. In this case, the line width in the imprints of the plasmoids increases as the plasmoids hit the spines, reaching a maximum line width of 31.9 km s $^{-1}$. The regions around the spines also have a more distinct line broadening which are directly related to thermal broadening due to the increased temperatures. This indicates that the Solar-C/EUVST Fe x 174 Å line may be more suitable for temperature diagnostics than MUSE/SG Fe ix 171 Å, especially for the regions outside the current sheet where the thermal broadening is not overshadowed by the variations in the LOS velocity along the LOS.

3.4. Fe xii 195 Å observables

In this section, we look into synthetic observables of the Fe xii 195 Å line. Despite the fact that this line has a peak formation temperature quite far above the highest plasmoid temperatures of our simulations, we still want to check for any possibility of seeing plasmoid signatures in this line, even if it should turn out that a higher temperature is needed to achieve detectability. Similarly to the previous sections, we take a look at the pure Fe xii 195 Å line spectra before delving into the corresponding observables seen in different instruments, in this case the upcoming MUSE/CI and Solar-C/EUVST.

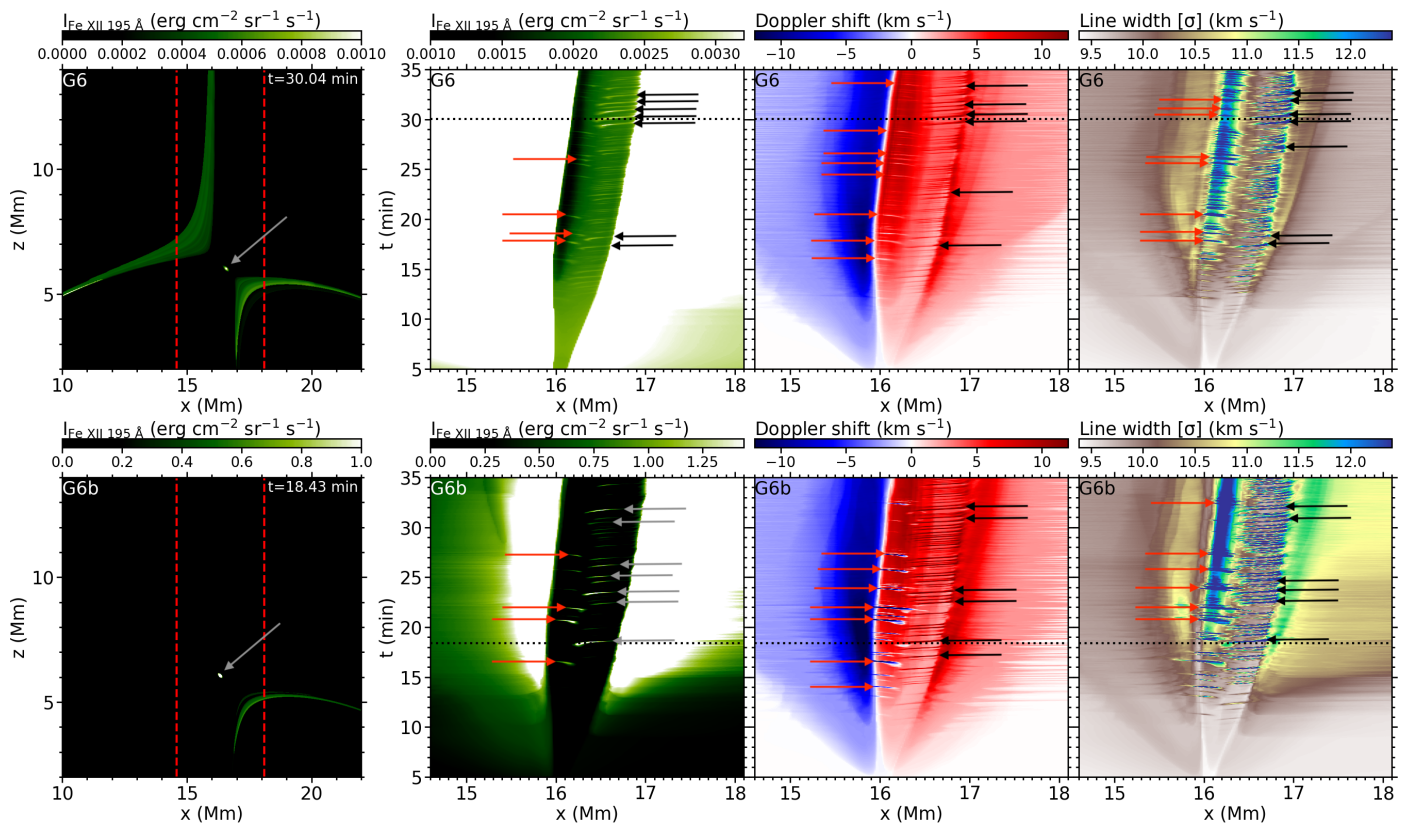


Fig. 8: Synthetic spectral moments of the Fe XII 195 Å line with no instrumental effects for cases G6 (top) and G6b (bottom). Layout is the same as for Fig. 2. A movie of the full-time evolution of the figure for $t \in [0, 40]$ min is available online.

3.4.1. Fe XII 195 Å line spectra

Figure 8 (and associated movie) shows the synthetic Fe XII 195 Å line spectra without instrumental effects in a similar manner as Figs. 2 and 5. The mapped intensities here (first and second columns) are of several orders of magnitude lower than for Fe IX 171 Å, because the Fe XII 195 Å peak formation temperature lies at ~ 1.5 MK, which is far outside the temperature ranges of our simulations. The brightness contrast between the plasmoids and surrounding matter is larger, though, making the plasmoids here more distinguishable from the surroundings in the on-disk view (second columns), where we can now easily see the plasmoids moving in both directions (see red and black/grey arrows). Furthermore, since the plasmoids are the dominant components here, they are also more distinct in the Doppler shift maps (third columns). Especially in the G6b case, the upward-moving, outer-spine-bound plasmoids (see red arrows) appear as strong blueshifts—in contrast to the surrounding redshift—instead of just decreased redshifts. The redshift enhancements caused by the downward-moving, inner-spine-bound plasmoids (see black arrows) are also stronger here than in the corresponding maps for Fe IX 171 Å and Fe X 174 Å. Finally, the plasmoids here also have a considerably higher impact on the line width (fourth column). This is because the heated plasma in the plasmoids here contributes more to the total thermal broadening, since the major contributions to the line intensity come from the plasmoids, along with the spines and fan-surfaces. For the same reasons, the line-width in the region above the fan surfaces is also noticeably enhanced, especially above the right fan-surface where the highest temperatures are reached (seen as a large yellow area in G6b).

3.4.2. MUSE/CI 195 Å intensities

Synthetic MUSE/CI 195 Å intensities are shown in Fig. 9 in a similar manner as in Figs. 3 and 6. All four panels show that plasmoids are resolvable with the MUSE/CI (in the 195 Å filter) both in the on-disk view and the off-limb view. In our cases, far below the peak formation temperature of this line, the correspondingly low photon count rates do not allow for any detection at all. The plasmoids would need to be heated up to temperatures closer to the 195 Å peak formation temperature (1.5 MK) in order to be detectable, and even then, only the G6b on-disk plasmoids (fourth column) would probably be possible to detect, given an exposure time of ~ 10 s.

3.4.3. Solar-C/EUVST Fe XII 195 Å spectra

Solar-C/EUVST Fe XII 195 Å spectral moments are mapped in Fig. 10 in a similar manner as Figs. 4 and 7. The intensity maps (first and second columns) show that the plasmoids are resolvable and clearly distinguishable from the surroundings when viewing the topology both off-limb and on-disk. The photon count rates of our cases are far below the required level for detection. As already concluded from the MUSE/CI 195 Å intensity maps, the plasmoids would need to be heated up to temperatures closer to 1.5 MK in order to be seen in this line on-disk for the G6b case (and would still not be detectable for the G6 case). The plasmoids give stronger imprints on the Doppler shift and line width (third and fourth columns, see arrows) for this line than for the Fe X 174 Å line, especially for case G6b, where the plasmoids hitting the spines lead to changes of up to 10 km s⁻¹ in the Doppler shift and up to 3 km s⁻¹ in the line width. Akin to what

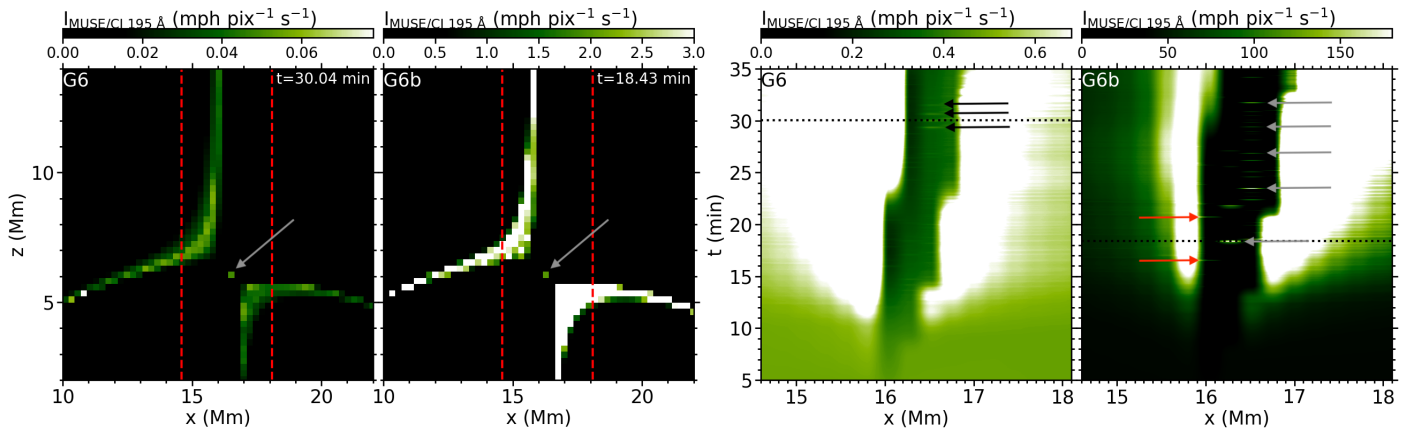


Fig. 9: Synthetic MUSE/CI 195 Å response for the simulations G6 and G6b as seen off-limb (two leftmost panels) and on-disk (two rightmost panels). Layout is the same as for Fig. 3, with the addition of arrows pointing at the location of some plasmoids: red ones for those upward-moving; black or grey for downward-moving.

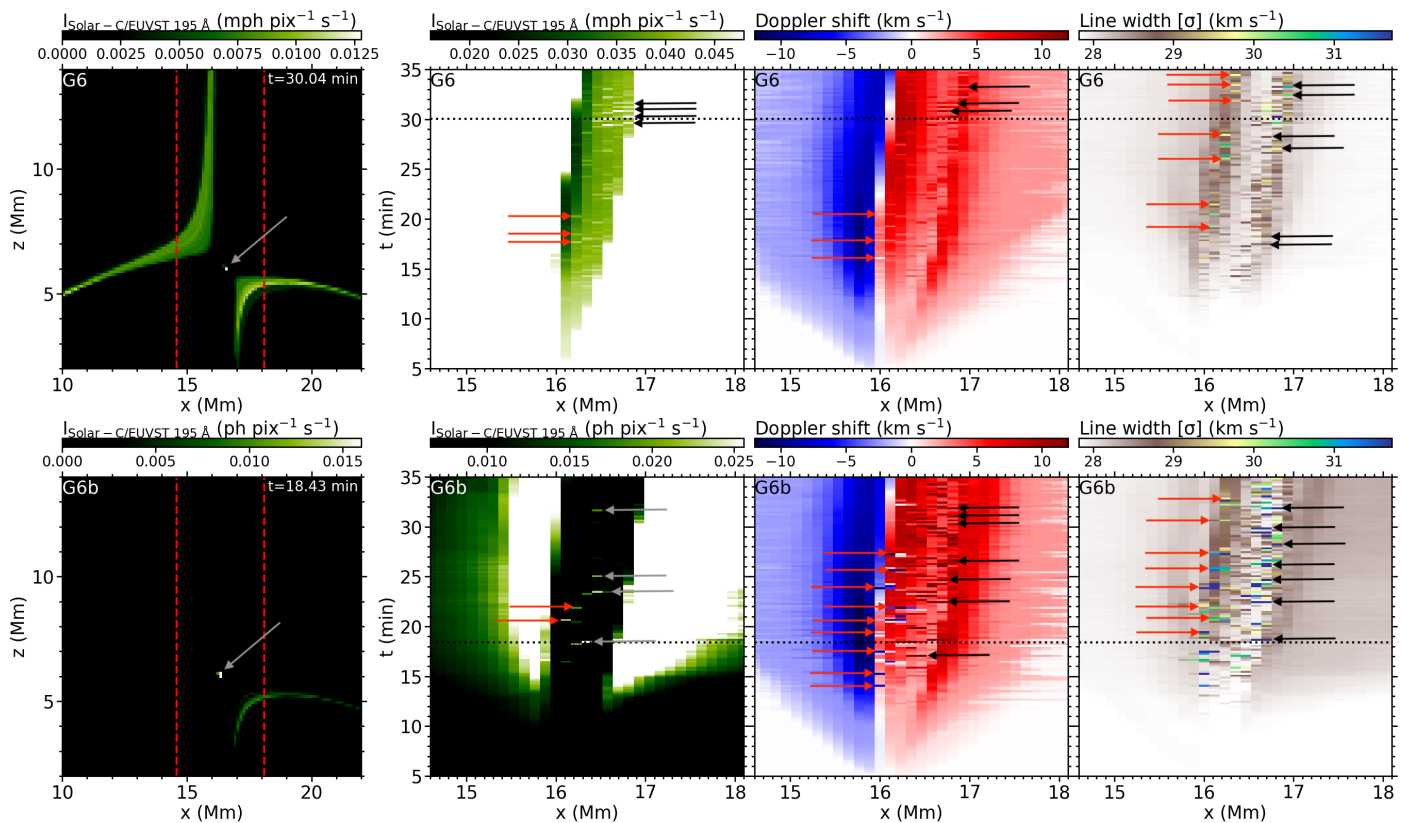


Fig. 10: Synthetic EUVST 195 Å spectral moments for cases G6 (top) and G6b (bottom). Layout is the same as for Fig. 2. A movie of the full-time evolution of the figure for $t \in [0, 40]$ min is available online.

we saw in the non-instrumental Fe II 195 Å line Doppler shift map, the outer-spine-bound plasmoids leave strong blueprints in EUVST Fe II 195 Å Doppler shift maps as well, while the inner-spine-bound plasmoids are seen as strong red stripes. Especially for case G6b, a significant line broadening is seen in the region that coincides with the fan surfaces (especially the right one), indicating that this observable may potentially be used for temperature diagnostics of fan-spine topologies similar to our simulated ones.

3.5. Spectral line profiles

To complete our study, we now focus on examining the synthetic spectral profiles from the G6b simulation: the one with more emission measure. Specifically, the top panels of Fig. 11 show the line width, for context purposes, for the Fe IX 171 Å, Fe X 174 Å, and Fe X 174 Å lines, from left to right. The bottom panels contain the synthetic profiles as observed on-disk for the locations marked in the top panels, using the same colour coding. In particular, the red line profile is extracted from a location near the outer spine, the black curve is obtained close to the in-

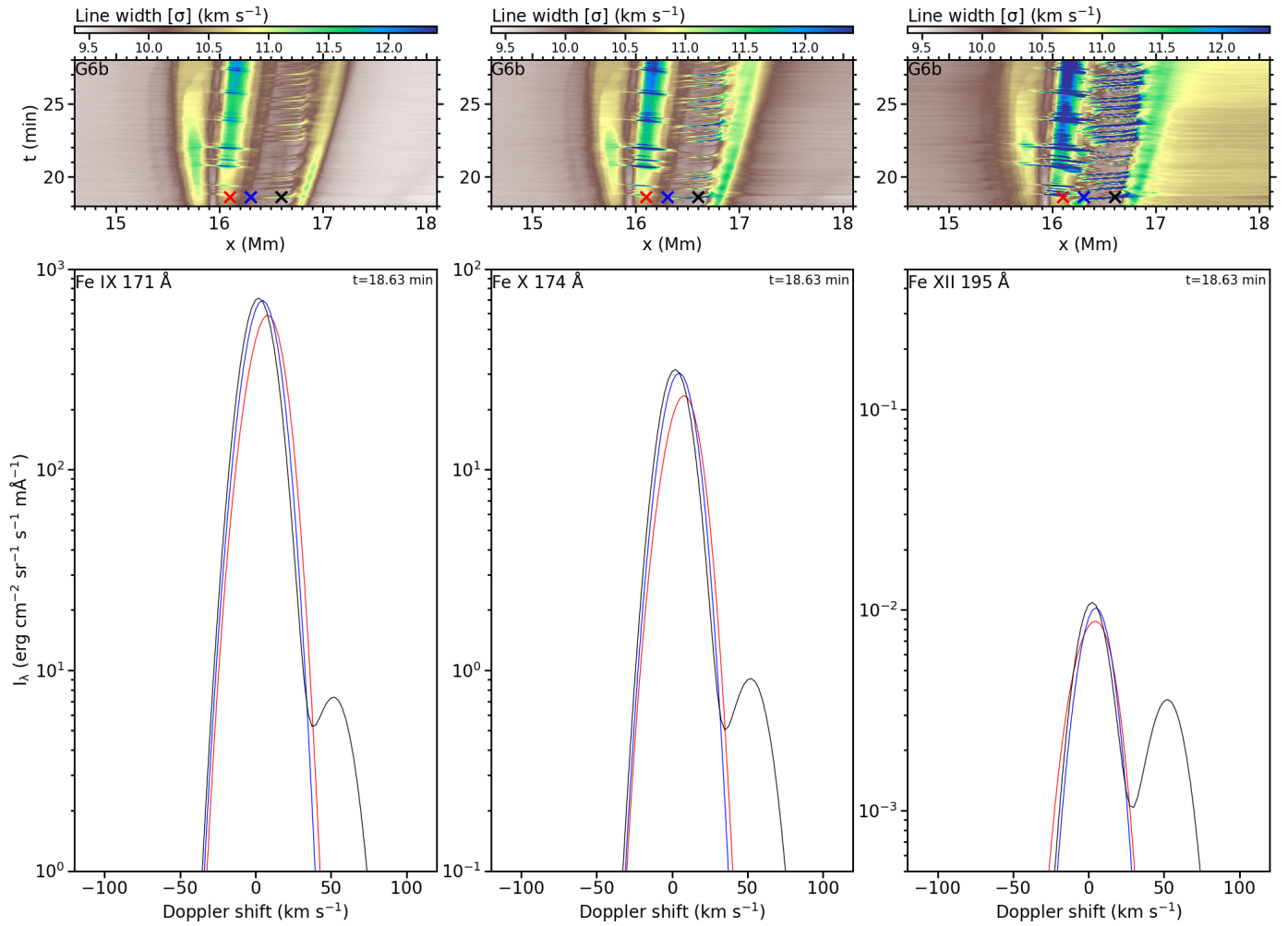


Fig. 11: Spectral line profiles for the Fe IX 171 Å, Fe X 174 Å, and Fe XII 195 Å lines without instrumental effects, taken from case G6b with z -axis as LOS, at selected positions along x -axis. For context, the top panels show maps of the line width against x and time, where the "x"s mark the positions from where the corresponding line profiles with the same color (in bottom panels) are taken. A movie of the time evolution for $t \in [18, 23]$ min is available online.

ner spine, and the blue curve represents an intermediate position. An associated animation of the figure is available online.

The line profiles exhibit a nearly-perfect Gaussian shape when plasmoids are not present. However, when plasmoids pass through the marked locations, secondary peaks emerge in the line profile. This is due to the distinct vertical velocities of plasmoids compared to the surrounding plasma, which contributes to the primary peak. In the black curve, the secondary peaks appear redshifted regarding the primary peak, as the inner-spine plasmoids move downwards. Similarly, the secondary peaks in the red curve, which correspond to outer-spine-bound plasmoids, appear blueshifted. The Doppler shift of the secondary peaks reach values up to 50 km s⁻¹, which is a consequence of the plasmoids being accelerated up to such high velocities. The amplitude of the secondary peaks is typically 2-3 orders of magnitude lower than the primary peaks for the Fe IX 171 Å line and 1-2 orders of magnitude lower in the Fe X 174 Å line. Therefore, these secondary peaks will be extremely difficult to detect for those lines. With respect to the Fe XII 195 Å line profile, on the other hand, the secondary peaks caused by the plasmoids get comparable in size with the primary peaks, in some occasions larger. The challenge here, though, is the fact that the peak intensity is

very low, about five orders of magnitude lower than for the Fe IX 171 Å line.

To analyse how the instrumental effects affect the particular spectral profiles, Figure 12 (and associated movie) represents an equivalent figure to the previous one for MUSE/SG Fe IX 171 Å, Solar-C/EUVST Fe X 174 Å, and Solar-C/EUVST Fe XII 195 Å. When plasmoids are not present, the profiles also have, in general, nearly-Gaussian shapes, similar to the corresponding non-instrumental line profiles. Nevertheless, the secondary peaks caused by the plasmoid motions are here mostly hidden behind the instrumental broadening. Consequently, we only perceive one peak in each of the profiles at any time. For the cases of MUSE/SG Fe IX 171 Å and Solar-C/EUVST Fe X 174 Å, the appearance of plasmoids leads to a minor broadening of the total line profile, which results in a slight increase in the total intensity, as seen in the intensity maps shown in the second column of Figs. 4 and 7, respectively. Concerning the Solar-C/EUVST Fe XII 195 Å line profile, the instrumental broadening also makes the secondary peak indistinguishable from the primary peak, and, interestingly, the maximum of the Gaussian profile increases essentially when plasmoids are passing by. However, given the temperature of our plasmoids, the intensity of this line profile is too faint to be detected at all.

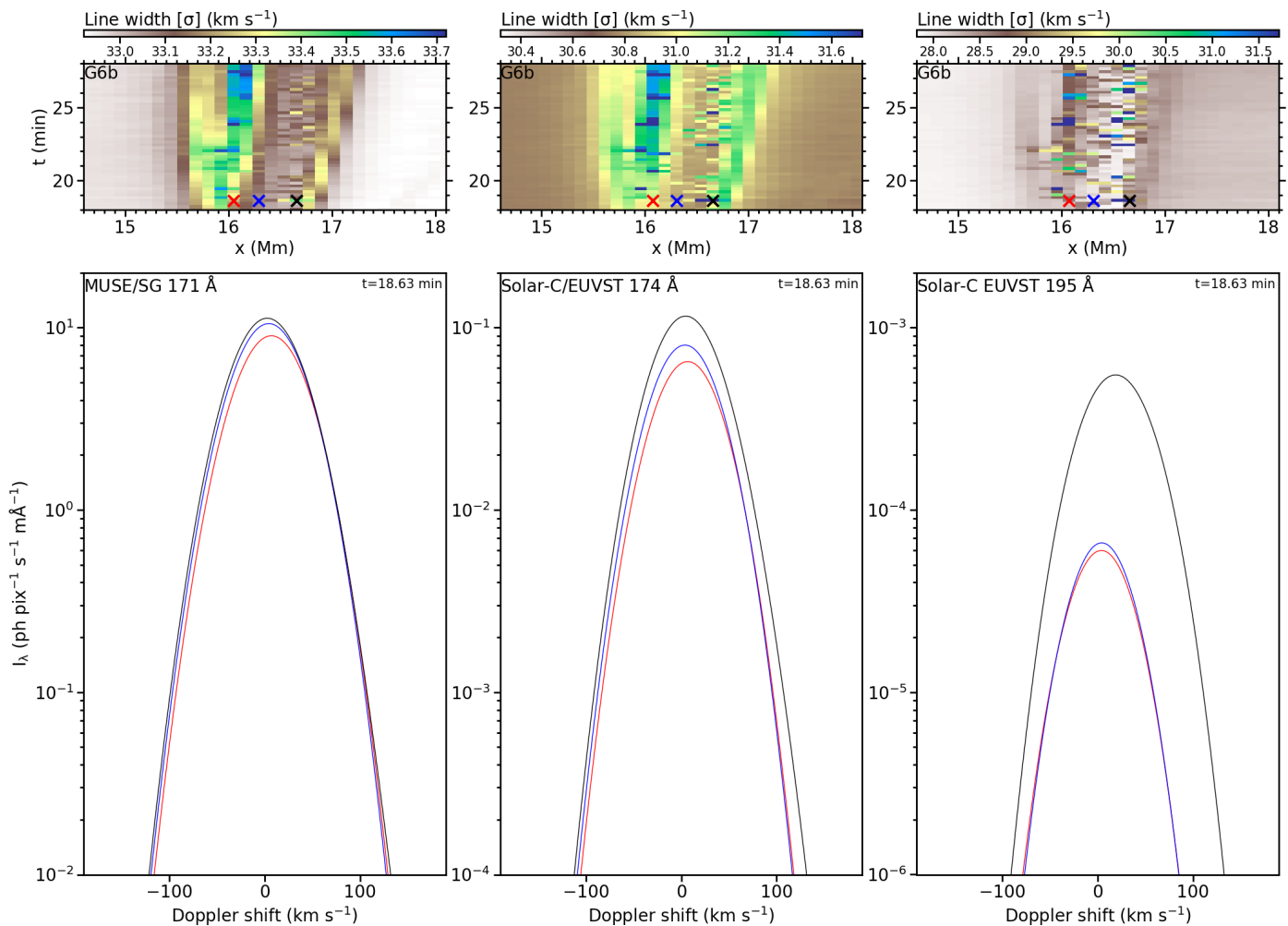


Fig. 12: Spectral line profiles for the MUSE/SG Fe ix 171 Å, Solar-C/EUVST Fe x 174 Å, and Solar-C/EUVST Fe xii 195 Å lines, taken from case G6b. Layout is the same as for Fig. 11. A movie of the time evolution for $t \in [18, 28]$ min is available online.

4. Discussion

In this paper, we have performed EUV forward-modelling from numerical simulations of plasmoid-mediated reconnection in the solar corona. In particular, we have synthesised observables for SDO/AIA 171 Å, SO/EUI-HRI 174 Å, MUSE/SG Fe ix 171 Å, MUSE/CI 195 Å, as well as for Solar-C/EUVST Fe x 174 Å and Fe xii 195 Å to determine the capability of currently active and upcoming observational instruments for detecting small-scale plasmoids. By employing two simulations with distinct mass density parameters, we have gained preliminary insights into the lower limits of density that still allow for plasmoid detectability.

The plasmoids in our simulations show the following characteristics: during their typical lifetimes of 10 – 20 s, they reach sizes of 0.2 – 0.5 Mm, get heated up to temperatures ranging between 0.73 and 1.0 MK, and are accelerated to velocities of up to $\sim 50 \text{ km s}^{-1}$. As a consequence of these particular properties, a widely-used instrument such as SDO/AIA is insufficient for capturing them through EUV imaging due to its moderate resolution, although the heated plasma around the fan-spine topology may still be seen in AIA 171 Å, as shown in Sect. 3.2.2. Likewise, other currently-active space instruments like the Spectral Imaging of the Coronal Environment (SPICE, [SPICE Consortium et al. 2020](#)), onboard the SO mission, and the EUV Imaging Spectrometer (EIS, [Culhane et al. 2007](#)), onboard the Hinode

satellite ([Kosugi et al. 2007](#)), also offer limited spatial resolution ($1''2$ and $2''0$, respectively) for the detection of plasmoids akin to those we are investigating, so we discarded performing forward-modelling for them. In contrast, in this paper we show that SO/EUI-HRI 174 Å can be a suitable option for detecting such small-scale plasmoids in EUV images. In fact, recent observations have already demonstrated the SO/EUI-HRI 174 Å capacity to detect brightenings with sizes down to 0.3 Mm ([Berghmans et al. 2021](#); [Mandal et al. 2023](#)).

Concerning future instruments, the MUSE and Solar-C missions provide a promising perspective for observing and analysing plasmoids in the corona through EUV spectrography and imaging. The design of MUSE/SG is suitable for observing plasmoids with properties resembling those from our simulations, particularly in Fe ix 171 Å. With its considerably high spatial and temporal resolution, it should directly detect such plasmoids through tiny, short-lived peaks in the intensity maps. In on-disk observations with the line of sight nearly parallel to the inner and outer spines, plasmoids in coronal higher-density regions (e.g., $n_e \sim 10^9 \text{ cm}^{-3}$, represented in case G6b) can be detected in full-raster images with short exposure times of $\sim 0.6 \text{ s}$. In lower-density regions like coronal holes (e.g., $n_e \sim 10^8 \text{ cm}^{-3}$, case G6), despite smaller photon count rates, plasmoids may still be discernible through sit-and-stare images with exposure times of $\sim 10 \text{ s}$. However, for off-limb observations, the lower pho-

ton count rates indicate visibility of plasmoids only in higher-density regions, requiring exposure times of ≥ 10 s, making a full-raster image impractical due to the extended time exceeding two minutes. It is also noteworthy that our plasmoids induce short-lived fluctuations of $2 - 3 \text{ km s}^{-1}$ in the Doppler shift and $0.5 - 0.7 \text{ km s}^{-1}$ in the line width of the MUSE/SG Fe IX 171 Å spectra. This additional line broadening is due to the plasmoids moving with a velocity distinctly different from the bulk velocity of the surrounding plasma, giving rise to a secondary peak in the line profile. The secondary peak can only be distinguished from the main peak in the non-instrumental line profile, as it is overshadowed by the instrumental broadening in the MUSE/SG Fe IX 171 Å line profile, but still contributes in increasing the total line width. Since the MUSE/SG's specified maximum uncertainties are 5 km s^{-1} for Doppler shift and 10 km s^{-1} for line width (De Pontieu et al. 2020), it is quite likely that these plasmoid imprints could be overshadowed by Gaussian noise. Consequently, for undoubtedly detection, plasmoids would need velocities at least twice as fast as in our cases.

In the case of Solar-C/EUVST, we obtain similar results to those from MUSE/SG. In particular, focusing on the Fe X 174 Å line, the largest Doppler shift caused by our plasmoids is $\sim 5 \text{ km s}^{-1}$, which could be resolved with the EUVST instrument whose maximum uncertainty is expected to be 2 km s^{-1} . However, the line width broadening we obtain is still small to discern the plasmoids separately from the background, given the expected maximum instrumental uncertainty of 4 km s^{-1} for the line width. Consequently, plasmoids would need to move at least 1.5 times faster than those from our simulations to lead clear distinguishable imprints in the line width.

With respect to diagnostics focused on Fe XII 195 Å, the typical temperature of our simulated plasmoids ($\sim 0.8 \text{ MK}$) is far below the peak formation temperature of this line ($\sim 1.5 \text{ MK}$). Therefore, we do not obtain detectable signals for either MUSE/CI 195 Å or Solar-C/EUVST Fe XII 195 Å. Nonetheless, it is interesting to see that if the plasmoid temperature was around 1.5 MK , Solar-C/EUVST could reveal more distinct imprints of the plasmoids, particularly in changes of the Doppler width and line shift of up to, approximately, 10 km s^{-1} and 3 km s^{-1} , respectively.

Our results highlight the potential of Solar Orbiter, along with the forthcoming MUSE and Solar-C missions, to study small-scale plasmoids in the solar corona. This is a crucial step in advancing our understanding of plasmoid-mediated reconnection in the solar atmosphere, complementing existing research on transition-region and chromospheric small-scale plasmoids (e.g., Rouppe van der Voort et al. 2017; Guo et al. 2020; Rouppe van der Voort et al. 2023).

Acknowledgements. This research has been supported by the European Research Council through the Synergy Grant number 810218 (“The Whole Sun”, ERC-2018-SyG) and by the Research Council of Norway through its Centres of Excellence scheme, project number 262622. The simulations were performed on resources provided by Sigma2 - the National Infrastructure for High Performance Computing and Data Storage in Norway. Juan Martínez-Sykora gratefully acknowledges support by NASA grants 80NSSC20K1272, 80NSSC23K0093, 80NSSC21K0737, 80NSSC21K1684, and contract NNG09FA40C (IRIS) and 80GSFC21C0011 (MUSE) and NSF ANSWERS grant 2149781.

References

Berghmans, D., Antolin, P., Auchère, F., et al. 2023, A&A, 675, A110
 Berghmans, D., Auchère, F., Long, D. M., et al. 2021, A&A, 656, L4
 Boerner, P., Edwards, C., Lemen, J., et al. 2012, Sol. Phys., 275, 41
 Cheung, M. C. M., De Pontieu, B., Martínez-Sykora, J., et al. 2019, ApJ, 882, 13

Cheung, M. C. M., Martínez-Sykora, J., Testa, P., et al. 2022, ApJ, 926, 53
 Culhane, J. L., Harra, L. K., James, A. M., et al. 2007, Sol. Phys., 243, 19
 Danilovic, S. 2017, A&A, 601, A122
 De Pontieu, B., Martínez-Sykora, J., Testa, P., et al. 2020, ApJ, 888, 3
 De Pontieu, B., Testa, P., Martínez-Sykora, J., et al. 2022, ApJ, 926, 52
 Del Zanna, G., Samra, J., Monaghan, A., et al. 2023, ApJS, 265, 11
 Dere, K. P., Del Zanna, G., Young, P. R., & Landi, E. 2023, ApJS, 268, 52
 Færder, Ø. H., Nóbrega-Siverio, D., & Carlsson, M. 2024, arXiv e-prints, arXiv:2401.01177
 Freeland, S. L. & Handy, B. N. 1998, Sol. Phys., 182, 497
 Furth, H. P., Killeen, J., & Rosenbluth, M. N. 1963, Physics of Fluids, 6, 459
 Gissot, S., Auchère, F., Berghmans, D., et al. 2023, arXiv e-prints, arXiv:2307.14182
 Gudiksen, B. V., Carlsson, M., Hansteen, V. H., et al. 2011, A&A, 531, A154
 Guo, L. J., De Pontieu, B., Huang, Y. M., Peter, H., & Bhattacharjee, A. 2020, ApJ, 901, 148
 Hansteen, V., Ortiz, A., Archontis, V., et al. 2019, A&A, 626, A33
 Hansteen, V. H., Archontis, V., Pereira, T. M. D., et al. 2017, ApJ, 839, 22
 Heyvaerts, J. & Priest, E. R. 1984, A&A, 137, 63
 Hofmeister, S. J., Utz, D., Heinemann, S. G., Veronig, A., & Temmer, M. 2019, A&A, 629, A22
 Kosugi, T., Matsuzaki, K., Sakao, T., et al. 2007, Sol. Phys., 243, 3
 Kumar, P., Karpen, J. T., Antiochos, S. K., Wyper, P. F., & DeVore, C. R. 2019, ApJ, 885, L15
 Lemen, J. R., Title, A. M., Akin, D. J., et al. 2012, Sol. Phys., 275, 17
 Liu, M., Ni, L., Cheng, G.-C., Ziegler, U., & Lin, J. 2023, Research in Astronomy and Astrophysics, 23, 035006
 Loureiro, N. F., Schekochihin, A. A., & Cowley, S. C. 2007, Physics of Plasmas, 14, 100703
 Mandal, S., Peter, H., Chitta, L. P., et al. 2023, A&A, 670, L3
 Nakariakov, V. M. & Ofman, L. 2001, A&A, 372, L53
 Ni, L., Chen, Y., Peter, H., Tian, H., & Lin, J. 2021, A&A, 646, A88
 Ni, L., Cheng, G., & Lin, J. 2022, A&A, 665, A116
 Ni, L., Zhang, Q.-M., Murphy, N. A., & Lin, J. 2017, ApJ, 841, 27
 Nóbrega-Siverio, D., Martínez-Sykora, J., Moreno-Insertis, F., & Rouppe van der Voort, L. 2017, ApJ, 850, 153
 Nóbrega-Siverio, D. & Moreno-Insertis, F. 2022, ApJ, 935, L21
 Nóbrega-Siverio, D., Moreno-Insertis, F., Galsgaard, K., et al. 2023, ApJ, 958, L38
 Nóbrega-Siverio, D., Moreno-Insertis, F., & Martínez-Sykora, J. 2016, ApJ, 822, 18
 Nóbrega-Siverio, D., Moreno-Insertis, F., & Martínez-Sykora, J. 2018, ApJ, 858, 8
 Parker, E. N. 1963, ApJS, 8, 177
 Parker, E. N. 1988, ApJ, 330, 474
 Pesnell, W. D., Thompson, B. J., & Chamberlin, P. C. 2012, Sol. Phys., 275, 3
 Peter, H., Huang, Y. M., Chitta, L. P., & Young, P. R. 2019, A&A, 628, A8
 Petschek, H. E. 1964, Magnetic Field Annihilation, Vol. 50, 425
 Pucci, F. & Velli, M. 2014, ApJ, 780, L19
 Rempel, M., Chintzoglou, G., Cheung, M. C. M., Fan, Y., & Kleint, L. 2023, ApJ, 955, 105
 Rochus, P., Auchère, F., Berghmans, D., et al. 2020, A&A, 642, A8
 Rouppe van der Voort, L., De Pontieu, B., Scharmer, G. B., et al. 2017, ApJ, 851, L6
 Rouppe van der Voort, L. H. M., van Noort, M., & de la Cruz Rodríguez, J. 2023, A&A, 673, A11
 SPIE Consortium, Anderson, M., Appourchaux, T., et al. 2020, A&A, 642, A14
 Suematsu, Y., Shimizu, T., Hara, H., et al. 2021, in Society of Photo-Optical Instrumentation Engineers (SPIE) Conference Series, Vol. 11852, International Conference on Space Optics & ICSO 2020, ed. B. Cugny, Z. Sodnik, & N. Karafolas, 118523K
 Sweet, P. A. 1958a, in Electromagnetic Phenomena in Cosmical Physics, ed. B. Lehnert, Vol. 6, 123
 Sweet, P. A. 1958b, Il Nuovo Cimento, 8, 188
 Vaiana, G. S., Krieger, A. S., & Timothy, A. F. 1973, Sol. Phys., 32, 81
 Van Doorselaere, T., Nakariakov, V. M., Young, P. R., & Verwichte, E. 2008, A&A, 487, L17
 Wyper, P. F., Antiochos, S. K., & DeVore, C. R. 2017, Nature, 544, 452
 Wyper, P. F., DeVore, C. R., Karpen, J. T., & Lynch, B. J. 2016, ApJ, 827, 4
 Yan, X., Xue, Z., Jiang, C., et al. 2022, Nature Communications, 13, 640
 Yokoyama, T. & Shibata, K. 1995, Nature, 375, 42
 Yokoyama, T. & Shibata, K. 1996, PASJ, 48, 353
 Yokoyama, T. & Shibata, K. 2001, ApJ, 549, 1160

